Helical waves in Earth's outer core

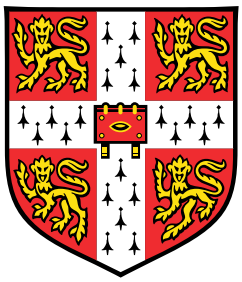

Ben R McDermott

Supervisor: Prof. P. A. Davidson

Department of Engineering
University of Cambridge

This dissertation is submitted for the degree of
Doctor of Philosophy

Wolfson College

March 2021

Declaration

I hereby declare that except where specific reference is made to the work of others, the contents of this dissertation are original and have not been submitted in whole or in part for consideration for any other degree or qualification in this, or any other university. This dissertation is my own work and contains nothing which is the outcome of work done in collaboration with others, except as specified in the text and Acknowledgements. This dissertation contains fewer than 65,000 words including appendices, bibliography, footnotes, tables and equations and has fewer than 150 figures.

Ben R McDermott
March 2021

Acknowledgements

Above all, I would like to thank my supervisor, Peter Davidson; the help and guidance he has given me has been indispensable throughout my PhD. His scientific insight, and endeavour to explain the most complex ideas in the simplest terms possible, has been crucial to the progression of this work. I am grateful for the scientific freedom he has allowed me, the assistance with writing articles, and practical advice. I would like to thank Peter for his guidance, encouragement and, most importantly, his friendship.

Thanks to PK Yeung for sharing his PSDNS code and providing assistance with the numerical nitty-gritties. Also, I thank Andrea Maffioli and Avishek Ranjan for their help understanding the code early on. The GHOST code is written by Pablo Mininni, who was a pleasure to collaborate with in making adjustments for the set-up required in chapter 5.

I am also grateful to my friends and colleagues in the fluids group for providing at times much needed technical guidance and beer-flavoured distractions. The geophysical fluids group: Oli Bardsley, Jack Atkinson, and Avishek Ranjan, have provided numerous helpful contributions in group meetings and off-the-clock discussions. Coffee breaks with our neighbours in the acoustics group – Amélie, Ben, Andy, Max, Alastair, and Ed – and the recent resurgence of our weekly cake meetings, have been grand.

I greatly appreciate the financial support from the Leverhulme Trust UK, who have provided my maintenance and made these studies possible. Funding from Leverhulme, the Department of Engineering and the Royal Astronomical Society has allowed me to attend international conferences and workshops, which have been enriching and enjoyable. Noteable mentions go to: Colin and Rob from Leeds, and the Zürich group – Daria, Felix, and Fabian – who made WITGAF and AGU particularly memorable. Friends from my time at Leeds University have always provided a welcome weekend distraction, and I count myself lucky to remain in contact with so many of you.

My parents have always given me endless love and support, and for this I can never be grateful enough. Last, but by no means least, to my partner Jess, for her continued dedication over the past five years.

Abstract

This thesis addresses the generation and dispersion of wave packets in Earth's outer core. The waves of interest feed off the buoyancy field, and are supported by strong rotation and/or a large-scale magnetic field, two key features of the dynamics in Earth's core. We aim to better understand the role of wave packets in shaping the turbulent convection, the process of magnetic induction, and maintaining Earth's magnetic field. Our numerical experiments focus on the emission of wave packets from localised sources, on the small length-scales of the convection, which stirs the fluid iron.

The fluid flow in Earth's outer core is characterised by a small Rossby number, the ratio of nonlinear inertia and the Coriolis acceleration. However, due to computational constraints, many geodynamo simulations lie in a regime where the convective structures have a moderate Rossby number. These simulations, that over-estimate the influence of nonlinear inertia, undergo an abrupt transition from a columnar flow structure with a strongly dipolar magnetic field, to a state of disorganised flow accompanied by a multipolar field. This transition is commonly termed the *dipolar-multipolar* transition, and the collapse of the dipole occurs when the *'local'* Rossby number (as introduced by Christensen & Aubert, 2006) is greater than 0.1. Separately, in the rotating turbulence literature, there is preliminary evidence of a similarly sharp transition from a columnar flow structure to incoherent turbulence when the Rossby number is $Ro \sim 0.2 - 0.6$. We show, that when $Ro > Ro^{\text{crit}} \approx 0.4$, inertial wave packets are suppressed, and columnar flow structures break down. Furthermore, we highlight a relationship between the 'local' Rossby number used to describe the dipolar-multipolar transition and our Ro, which places both transitions at approximately Ro^{crit}. Based on this evidence, we conjecture that the breakdown of columnar structures, followed by the dipole collapse, is caused by the suppression of inertial wave packets at the critical threshold.

In the following series of simulations, we study the effects of an ambient magnetic field on the dispersion of inertial wave packets. In the presence of an large-scale field, inertial waves are modified into a spectrum of waves called *magnetic-Coriolis* waves, which present in a variety of forms depending on the wave-frequency. We focus on the Earth-like regime of rapid rotation and a small Lehnert number, Le, the ratio of

the Alfvén and inertial frequencies. Our simulations initiated with a single buoyant blob yield an excellent comparison to the diffusion-less analytical results of Bardsley & Davidson (2016) at $Ro \to 0$ and $Le = 0.1$. We identify three wave-types, predicted by linear theory, based on the waves' group velocity, helicity characteristics, and magnetic to kinetic energy ratio. At Earth-like values of Le, we observe that magnetic-Coriolis wave packets distribute helicity in a way that is beneficial to planetary magnetic field generation. Furthermore, the emf induced by the wave packets is coherent for Earth-like values of Le, suggesting than an α-effect associated with the waves has the potential to drive a *helical wave dynamo* (Davidson, 2014).

Table of contents

List of figures

List of tables

Nomenclature

Roman Symbols

$\boldsymbol{a}$	Solenoidal vector potential: $\boldsymbol{\nabla} \times \boldsymbol{a} = \boldsymbol{b}$
$\boldsymbol{B}$, $\boldsymbol{b}$	Magnetic field in velocity units
$\boldsymbol{B}_0$	Large-scale magnetic field (in velocity units)
$\mathcal{B} = c\mathrm{g}$	Buoyancy
$\tilde{B}$	Magnetic field in units of Tesla
$c = \rho'/\rho$	Nondimensional density perturbation
C	CFL number
Δt	Time-step
Δx	Grid spacing in direction x
$\boldsymbol{e}_i$	Unit vector in the direction i
$\mathbf{g}$	Gravitational acceleration
h_c	Cross helicity density
h_k	Kinetic helicity density
h_m	Magnetic helicity density
i	Unit imaginary number $\sqrt{-1}$
$\boldsymbol{j}$	Fluctuating current density: $\boldsymbol{\nabla} \times \boldsymbol{b} = \boldsymbol{j}$
$\boldsymbol{k}$	Wavevector

ℓ	Length-scale
L	A large length-scale
m	Spherical harmonic order
n	Spherical harmonic degree
p	Pressure modified by centrifugal effects
S_{ij}	Rate of strain tensor
$\square_\perp$	Perpendicular to the rotation vector
$\square^*$	Relative or normalised quantity
$\hat{\square}$	Fourier transform
t	Dimensional time
$\boldsymbol{u}$	Velocity field
$\boldsymbol{x}$	Position vector
x, y	Cartesian coordinates perpendicular to the rotation vector
z	Cartesian coordinate parallel to the rotation vector

Greek Symbols

α	Isotropic alpha
α_{ij}	Alpha tensor
δ	Size of a buoyant blob
$\boldsymbol{\mathcal{E}}$	Electromotive force: $\boldsymbol{\mathcal{E}} = \boldsymbol{u} \times \boldsymbol{b}$
ϵ	Dissipation of kinetic energy: $\epsilon \approx \nu \lvert\boldsymbol{\omega}\rvert^2$
ϖ	Wave frequency
κ	Diffusivity of density perturbations
λ	$(\boldsymbol{u}^2 - \boldsymbol{b}^2)/(\boldsymbol{u}^2 + \boldsymbol{b}^2)$
μ	Magnetic permeability

η	Magnetic diffusivity
ν	Kinematic viscosity
$\boldsymbol{\omega}$	Vorticity field: : $\boldsymbol{\nabla} \times \boldsymbol{u} = \boldsymbol{\omega}$
Ω	Rotation rate
Π	Pressure modified by centrifugal and magnetic effects
π	$\simeq 3.14\ldots$
ρ	Background density
ρ'	Density perturbation
σ	Electrical conductivity

Acronyms / Abbreviations

CFL	Courant–Friedrichs–Lewy
CMB	Core-mantle boundary
CPU	Central Processing Unit
DFT	Discrete Fourier Transform
DNS	Direct Numerical Simulation
emf	Electromotive force
FFT	Fast Fourier Transform
MC	Magnetic-Coriolis
MHD	Magnetohydrodynamic(s)
ODE	Ordinary Differential Equation
PDE	Partial Differential Equation
PDF	Probability Density Function
QG	Quasi-Geostrophic
r.m.s.	Root-mean-square
TC	Tangent Cylinder

Chapter 1

Introduction

Planet Earth has a dynamic magnetic field which shields all life from harmful solar radiation. The field originates in the outer core of the planet, where iron alloy at high temperatures and pressures is a good conductor with a viscosity similar to that of water. Persistent convection of the liquid iron sustains the magnetic field through the *dynamo* process, against its natural tendency to decay. It is this process, through which potential energy drives convection in an electrically conducting fluid, and the kinetic energy of the fluid motion is converted to magnetic energy, which has maintained the field for Billions of years (Roberts & King, 2013).

1.1 Earth's core and the geodynamo

Earth's fluid core lies almost 3000 km beneath its surface, and the interface between the core and the mantle is at a radius of ≈ 3485 km (Dziewonski & Anderson, 1981). The solid inner core, which occupies Earth's centre, and the silicate mantle can be assumed to be stationary with respect to outer core convection. The iron-nickel alloy which fills the outer core is under immense pressures $\sim 200 - 300$ GPa and temperatures ~ 5000 K (Dziewonski & Anderson, 1981). The outer core is 6-10 % less dense than iron under the same conditions with no additives (Nimmo, 2015). This implies that there must be some light element content in the core, and the most favoured light elements are oxygen, sulphur and silicon. For the present day dynamo, it is the release of such light elements as the inner core grows which is thought to be the main source of convection (Roberts & King, 2013). The secular cooling of the Earth complements the compositional convective driving; on the other hand, in the absence of an inner core, secular cooling must be the main source of convection. Recent estimates of core conductivities estimate the age of inner core nucleation at $0.5 - 1$ billion years ago (Pozzo *et al.*, 2012).

Outer core convection is vigorous, as measured by the temperature difference across the core, which is approximately $\sim 10^4 - 10^6$ times that of the temperature contrast needed for convection to first onset (Gubbins, 2001). Although, the supercriticality of outer core convection remains fiercely debated. (To estimate the strength of the convection based on compositional driving is much more uncertain). Nevertheless, with respect to time-scales experienced in everyday life, the fluid motion and magnetic field variations are rather slow (at least those which we can observe, see §1.1.3). A fluid parcel released at the inner core boundary is expected to reach the core-mantle boundary (CMB) in approximately 300 years, at a slow pace of 0.2 mm/s. However, this is $\sim 10^5$ times faster than motions in the mantle above (Foulger *et al.*, 2005).

The problem of magnetic field generation in Earth's core is often called the *geodynamo* problem, and geodynamo theory is the modern theory of how Earth's field is sustained. The attempt to explain the maintenance of the field against its natural tendency to decay sets the current theory apart from the previous, incomplete theories. For example, William Gilbert thought that Earth was a permanent magnet (Gilbert, 1600), however this is inconceivable as we now know that the deep Earth is much hotter than the Curie temperature[1] of iron. Further, observations of the field reveal that it is dynamic, and it exhibits variations on a large range of time-scales, from millions of years to months (see §1.1.3). Another suggestion was that Earth's field is a primordial field left over from planetary formation. However, observations from magnetic minerals suggest Earth had a planetary magnetic field over 4 Billion years ago, and this is equivalent to many magnetic diffusion (decay) times. Geodynamo theory seeks to explain the mechanisms through which the cooling Earth has generated and maintained a coherent magnetic field in its outer core for Billions of years.

1.1.1 Dominant effects in Earth's core

A closer look at the outer core suggests that some effects are much more important than others. We will not introduce the equations now, but they express the conservation of energy, momentum, and mass, along with a modified version of Ohm's law for the magnetic field, and they can be found in Roberts & King (2013). The relevant equations are fairly well agreed upon, and the observational data (although limited, see §1.1.3) guide us in the estimation of the parameter values. We list the most important effects first:

[1] The Curie temperature is the temperature above which remnant magnetism is lost.

Buoyancy

Simply put, there would be no dynamo without the buoyant driving, whether it be thermal or compositional. As mentioned above, the release of light elements at the inner core boundary combined with the temperature difference across the outer core drives chaotic, persistent convection. In fact, it is only the deviations away from the adiabatic reference state which drive convection, and these deviations are rather small, i.e. perturbations in temperature on the order of $\sim 10^{-5}$ K (compared to the average temperature of the outer core ~ 4500 K). Nevertheless, the deviations are sufficient to power chaotic core flow.

The Coriolis force

Earth is a rapidly rotating planet. Its angular rate Ω, of approximately 2π radians per day, defines by far the shortest relevant time-scale effecting the dynamics in the outer core. In the rotating reference frame of the core, the fluid is subject to the Coriolis force, which is a fictitious force (Vallis, 2017). The Coriolis force does no work, as it always acts perpendicular to the direction of motion of a fluid parcel, however it leaves an overwhelming imprint on the structure of core convection (see §1.1.2). Indeed, the dipole representation of Earth's magnetic field is closely aligned with the rotation axis, and this is no coincidence.

Magnetic induction

The motion of a conducting fluid tends to drag any permeating magnetic lines with it, an idea related to Alfvén's theorem (Alfvén, 1942). Alfvén's theorem states that in a fluid that is a perfect conductor, magnetic field lines are frozen into the fluid, as if they were material lines. It follows that, in a finitely conducting fluid, the fluid motion can twist and contort magnetic field lines in such a way that the magnetic energy is amplified (Moffatt, 1978).

The Lorentz force

Just as the motion of the fluid can distort magnetic field lines, magnetic field lines also tend to resist being bent by the fluid motion, and this is the action of the Lorentz force (Davidson, 2017). Thus, the fluid motions may be shaped by the magnetic field, as it can be much easier for a fluid parcel to move in the direction of the magnetic field lines, rather than across them.

Ohmic dissipation

The liquid iron at outer core conditions has a finite electrical conductivity, which means

that any currents flowing through it dissipate energy through Ohmic heating. The electrical conductivity σ, relates to a magnetic diffusivity of $\eta = 1/\mu\sigma \sim 1$ m^{2}s^{-1} (Pozzo *et al.*, 2014). This means that if convection ceased, Earth's field would decay in a time similar to $R_c^2/\eta \sim 4 \times 10^5$ years, where R_c is the radius of the CMB. We note here the vast discrepancy between this magnetic diffusion time-scale and the time-scale of observed changes in the magnetic field (10–100 years – Jackson & Finlay, 2015). Thus, these changes must be a result of other core processes than magnetic diffusion, although smaller features in the magnetic field have shorter characteristic diffusion times.

At this stage it might seem like something is amiss, as we have neglected to mention two fundamental effects in conventional fluid dynamics: fluid inertia and viscous dissipation. This is no mistake, as in Earth's core we argue that these effects play a minor role (Davidson, 2013*a*). First, the kinematic viscosity of fluid iron at Earth's core conditions is $\nu \sim 10^{-6}$ m^{2}s^{-1}, little different to that of water, and 10^6 times smaller than the aforementioned magnetic diffusivity. This means that hydrodynamic fluid motions with gradients that scale with the dimensions of the outer core, with this value of ν, would take a time longer than the age of the universe to decay due to viscous dissipation. In fact, the ratio of the kinematic viscosity to the magnetic diffusivity is the nondimensional magnetic Prandtl number, which is $Pm = \nu/\eta \sim 10^{-6}$ for Earth's outer core. The smallness of Pm implies that the large majority of dissipation in the core is expected to be Ohmic, and that the magnetic field is expected to be smoother than the velocity field.

We must be careful with the definition of inertia. Fluid speeds u, as mentioned above, are slow, so the magnitude of nonlinear advection $(\boldsymbol{u}\cdot\boldsymbol{\nabla})\boldsymbol{u} \sim u^2/R_c$ is expected to be a small quantity. As we shall see, even selecting a more appropriate length scale for this scaling does not lift advection into the leading order force balance. However, the same cannot be said of the acceleration term $\partial_t \boldsymbol{u}$, as this involves selecting a characteristic frequency for the dynamics, which may not be small with respect to Ω. Indeed, this thesis will concentrate on waves which are principally supported by the Coriolis force, and these waves have frequencies in the range $0 \to 2\Omega$; thus we make no assumptions about the size of $\partial_t \boldsymbol{u}$ in the core.

Nondimensional groups

In order to quantify some of these claims, we introduce some relevant nondimensional groups given in table 1.2. We denote the magnetic field in units of Tesla as $\tilde{B}$, and introduce the magnetic field in velocity units as $B = \tilde{B}/\sqrt{\mu\rho}$, which is equivalent to the Alfvén speed (see §2.3.1). The physical parameters pertaining to Earth's outer core,

and used to construct these numbers, are given in table 1.1. The first thing to notice is that all the balances listed in table 1.2 have the Coriolis force in the denominator, and that most of the numbers are much less than 1. The Ekman number is minuscule. This suggests that rotation completely dominates over viscous forces. The Rossby number is also tiny, indicating that rotation dominates nonlinear advection. Another interpretation of the Rossby number is that it compares the velocity of the fluid to the group speed of waves supported by the Coriolis force (see §2.2); its smallness indicating that the wave packets travel much faster than advective speeds. Analogously, the Lehnert number measures the ratio of the frequencies of oscillations supported by the magnetic tension in the field lines and by the Coriolis force. The Lehnert number is a little larger than the Rossby number, although it is still much less than 1. These 'oscillations' and waves occupy much of the content of this thesis, and we will elaborate on the importance of the Rossby and Lehnert numbers in chapter 2.

The outlier it seems, is the Elsasser number, usually denoted by Λ. It is marginally less than 1, indicating the possibility of a large-scale balance between the Coriolis force, the Lorentz force and buoyancy, often referred to as a *magnetostrophic* or MAC balance (where the acronym stands for magnetic-'Archimedian'-Coriolis). However, there are two problems with this definition of the Elsasser number. First, this traditional definition implicitly defines the velocity scale $u \sim \eta/L$, which removes any length-scale from Λ, but inflates its magnitude by 10^3 compared to that obtained if we used u from table 1.1. Further, a large portion of the Coriolis force is balanced by pressure gradients, which forms a zero-order *geostophic* balance. This leaves, at first-order, the rotational parts of the Coriolis, Lorentz and buoyancy forces. Obtaining parameter regimes which satisfy a zero-order geostrophic balance, that form a base for first-order magnetostrophic perturbations is the subject of current research (Schwaiger *et al.*, 2019).

1.1.2 The dominance of rotation

The smallness of the nondimensional numbers in table 1.2, and indeed the alignment of the dipole component of Earth's magnetic field with the rotation axis, provide convincing evidence that rotation is a key player in the geodynamo. Rotating fluids often behave in a manner which is counter intuitive. The Coriolis force acts on any fluid parcel with components of velocity perpendicular to the direction of the rotation axis (Greenspan, 1968). The effect is to deflect horizontal motions in curved paths, in turn spiralling up the velocity field. These motions are commonly seen in Earth's atmosphere, where migrating storms are deflected clockwise (anti-clockwise) in the northern (southern) hemisphere. In general, rapid rotation tends to inhibit motions in the plane perpendicular to the rotation

Table 1.1 Physical parameters for Earth's outer core. Density, rotation rate and fluid velocity from Roberts & King (2013), core radius from Henderson & Henderson (2009), magnetic diffusivity from Pozzo *et al.* (2014), viscosity from de Wijs *et al.* (1998) and magnetic field strength from Davidson (2017).

Quantity	Symbol	Value
Density	ρ	$\sim 1.1 \times 10^4$ kg m^{-3}
Kinematic viscosity	ν	$\sim 10^{-6}$ m^2 s^{-1}
Rotation rate	Ω	7.29×10^{-5} s^{-1}
Large length-scale	L	$R_c \approx 3.485 \times 10^6$ m
Fluid velocity	u	$\sim 5 \times 10^{-4}$ m s^{-1}
Magnetic field strength	$\tilde{B}$	$\gtrsim 4 \times 10^{-4}$ T
Magnetic diffusivity	η	~ 1 m^2 s^{-1}

Table 1.2 Nondimensional numbers for Earth's outer core.

Dimensionless number	Definition	Balance	Order of magnitude
Rossby	$\frac{u}{\Omega L}$	$\frac{\lvert(\boldsymbol{u}\cdot\boldsymbol{\nabla})\boldsymbol{u}\rvert}{\lvert 2\boldsymbol{\Omega}\times\boldsymbol{u}\rvert}$	10^{-6}
Elsasser	$\frac{B^2}{\eta\Omega}$	$\frac{\lvert(\boldsymbol{\nabla}\times\boldsymbol{B})\times\boldsymbol{B}\rvert}{\lvert 2\boldsymbol{\Omega}\times\boldsymbol{u}\rvert}$	0.1
Ekman	$\frac{\nu}{\Omega L^2}$	$\frac{\lvert\nu\boldsymbol{\nabla}^2\boldsymbol{u}\rvert}{\lvert 2\boldsymbol{\Omega}\times\boldsymbol{u}\rvert}$	10^{-15}
Magnetic Ekman	$\frac{\eta}{\Omega L^2}$	-	10^{-9}
Lehnert	$\frac{B}{\Omega L}$	-	10^{-5}

vector, and this can lead to columnar structures in the velocity field. Such columnar structures can be seen in figure 1.1, a visualisation of a rapidly rotating turbulence simulation. This effect can be understood either in terms of the dispersion of inertial wave packets (Davidson *et al.*, 2006), or in terms of the Taylor-Proudman theorem (Proudman, 1916; Taylor, 1922).

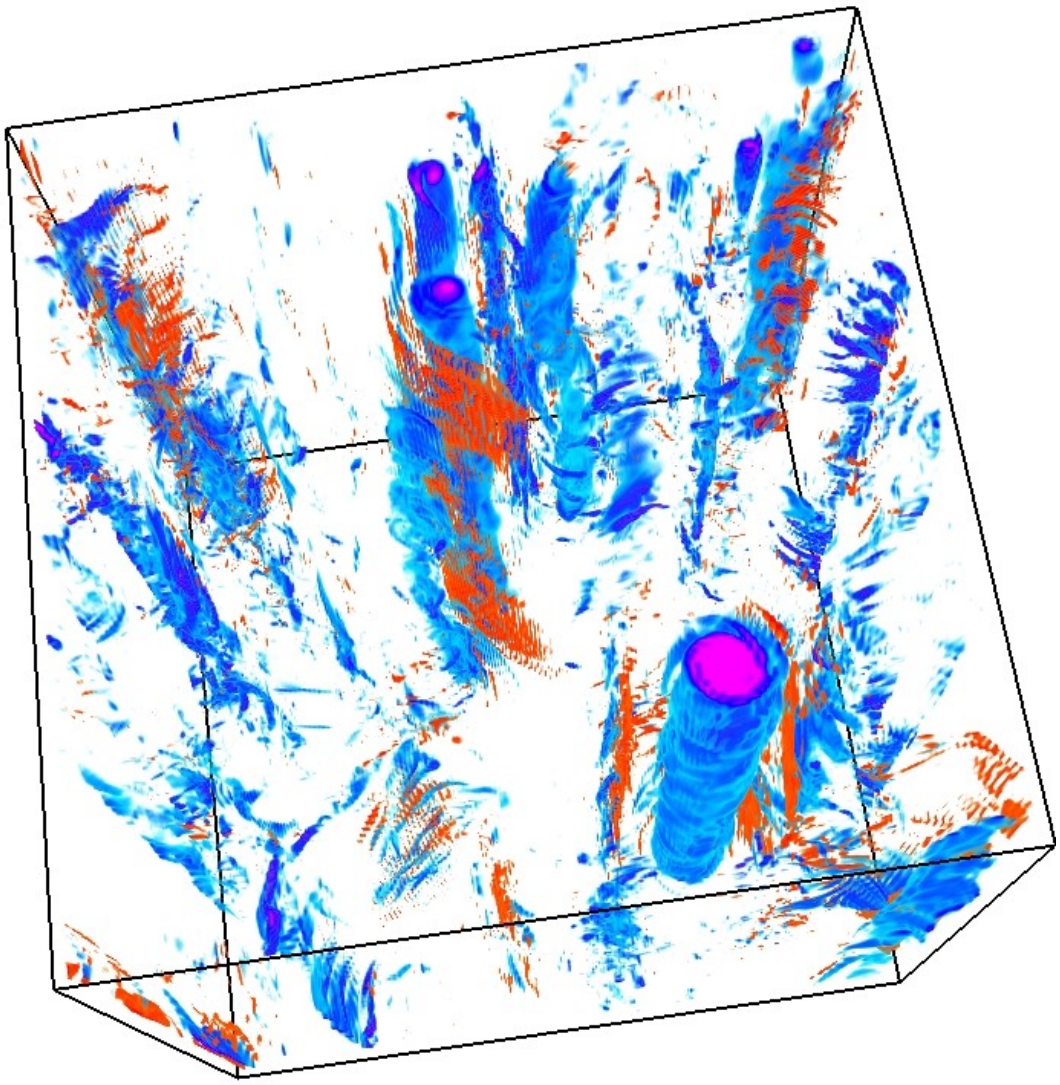

Fig. 1.1 Columnar structures in rapidly rotating turbulence. The image shows vorticity in the direction of the rotation vector from https://sites.google.com/site/pouquetannick/some-figures.

The Taylor-Proudman theorem

Consider a steady, inviscid, rapidly rotating, neutral fluid described by the force balance

$$2\Omega(\hat{\boldsymbol{e}}_z \times \boldsymbol{u}) \approx -\nabla p\,, \tag{1.1}$$

where p is the pressure field and $\boldsymbol{\Omega} = \Omega\hat{\boldsymbol{e}}_z$. If we take the curl to remove the pressure term this reduces to

$$\partial_z \boldsymbol{u} \approx 0\,. \tag{1.2}$$

So slow motions in a rapidly rotating inviscid fluid tend to be invariant in the direction of rotation. This is the Taylor-Proudman theorem, and we will revisit this peculiar phenomenon in the next chapter.

1.1.3 Observations of the geomagnetic field

Having reviewed some of the theoretical evidence on the fluid motions in Earth's outer core, we now turn to observations of the geomagnetic field. Possibly the earliest observations of Earth's magnetic field were reported by Chinese scholars in $\sim$ 1000 AD (Mitchell, 1946). These observations were in relation to lodestones, slender rocks which harbor permanent magnetism. The lodestones, placed on floating 'boats' in a bath of water, consistently aligned with the local direction of Earth's magnetic field, similar to the motion of the needle in modern compasses. The first measurements of declination (the horizontal angle between true north and the magnetic field vector) were taken in the 16th century, and in 1700, Edmund Halley created a map of declination across the western and southern (now the north and south Atlantic) oceans. In 1834, Gauss founded the 'Göttingen Magnetic Union' which formed a global network of stations to observe Earth's magnetic field (Mitchell, 1946). Shortly after, he applied spherical harmonic analysis to the scalar magnetic potential of the field, a procedure which remains the foundation of geomagnetic field models today. He performed the analysis up to spherical harmonic degree 4, and he noted that:

- The source of Earth's main field lies within Earth's deep interior.
- The dipole components are dominant.
- The field is well approximated by a low degree expansion.

Modern magnetic field models are consistent with these conclusions (e.g. Jackson *et al.*, 2000). One particular benefit of the potential field approach is that, as the mantle is assumed to be an electrical insulator, we are permitted to 'downward continue' the observed surface field to reveal the structure of the field at the CMB.

Humans have used the geomagnetic field to aid navigation for centuries, and as a consequence there is reliable directional data for the past 400 years. Since the formation of the Göttingen Magnetic Union in 1834 there is also some reliable intensity data, becoming increasingly more numerous towards the present day. Continuous monitoring of Earth's field using low Earth orbit satellites began in 1999[2], and higher resolution

[2]For details on the Ørsted satellite, see https://www.space.dtu.dk/english/research/projects/project-descriptions/oersted

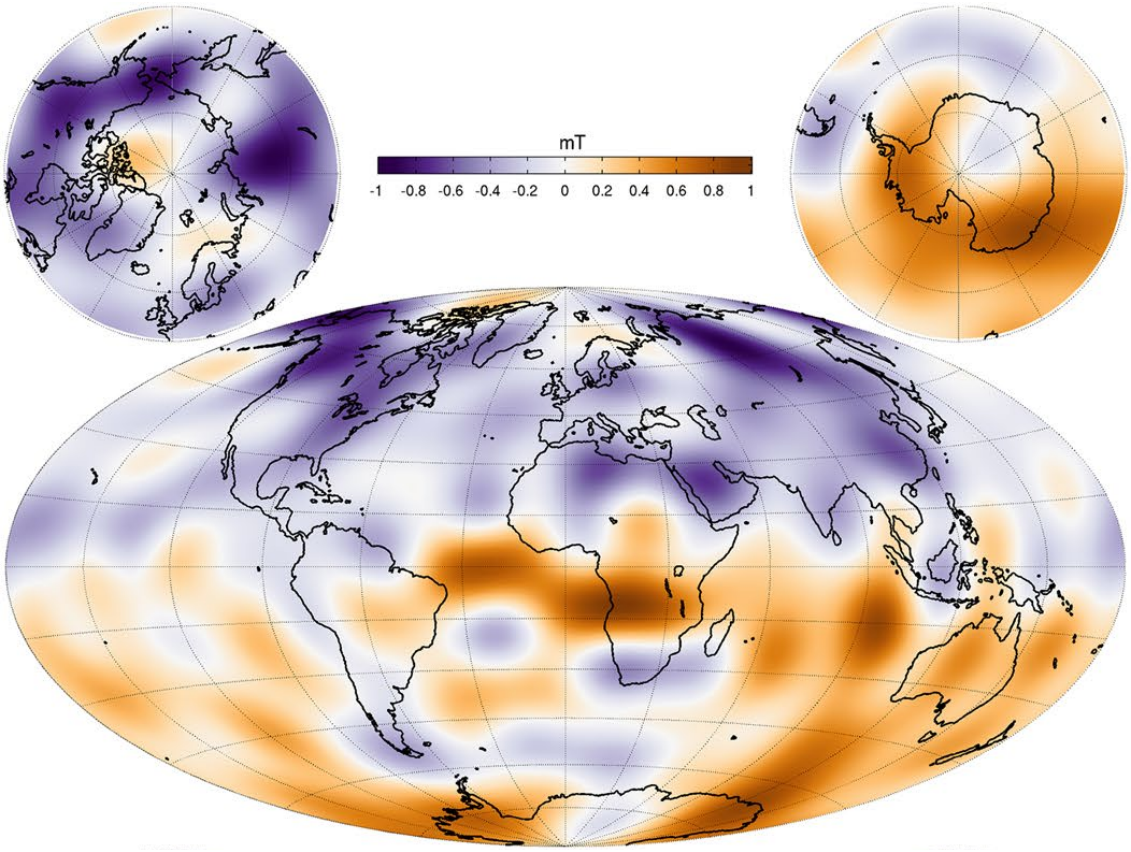

Fig. 1.2 The radial component of the geomagnetic field at the CMB in the year 2015, according to the CHAOS-6 geomagnetic field model (Finlay *et al.*, 2016).

measurements with better coverage (particularly in the southern hemisphere) have been available for the past 20 years.

Figure 1.2 shows the radial component of the geomagnetic field at the CMB in the year 2015. This particular model is called CHAOS-6 (Finlay *et al.*, 2016) and spans the years 1999-2016.5, utilising data from the Swarm constellation of satellites. As already mentioned, the field is fairly well approximated by an axially aligned dipole, with magnetic flux leaving the core in the southern hemisphere and re-entering in the north. This snapshot also shows significant variations from dipolarity, notably the *south Atlantic anomaly* to the east of Brazil in figure 1.2, where there is a substantial amount of opposite polarity flux. Another prominent feature is the presence of four *high latitude flux patches* (two near the Arctic, two near Antarctica), which are approximately symmetric about the equator. The geomagnetic model *gufm1*, which covers the years 1590–1990, shows that the the mid-to-low latitude field has been drifting westward at an approximate rate

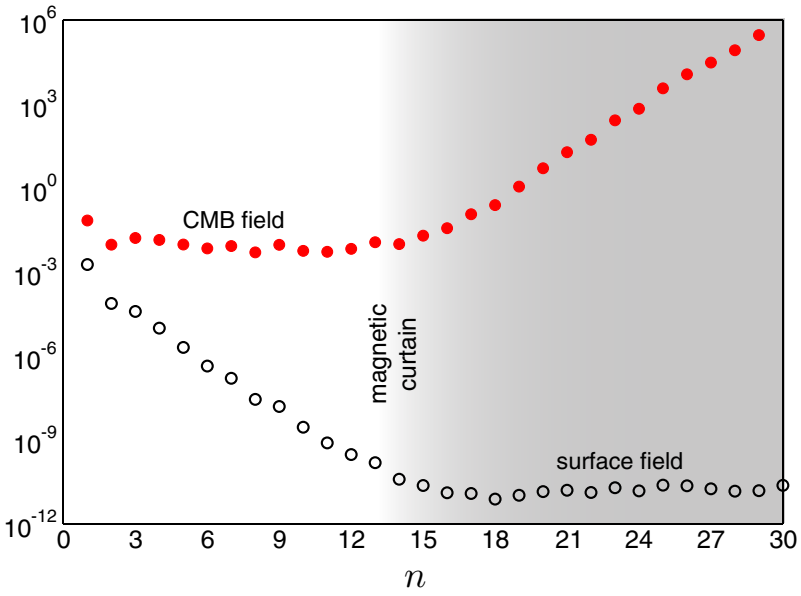

Fig. 1.3 The spatial power spectrum for the geomagnetic field as a function of spherical harmonic degree, highlighting the 'magnetic curtain' (after Roberts & King, 2013).

of $0.3\,^\circ\,\mathrm{yr}^{-1}$ (or $17\,\mathrm{km\,yr}^{-1}$ at the core surface) (Finlay & Jackson, 2003). These features have been fairly robust for the past 400 years (Jackson *et al.*, 2000).

Unfortunately, any small-scale features of the observed field are tarnished by the so-called *magnetic curtain*. Earth's crust has an associated permanent magnetism due to magnetic minerals, and this crustal magnetism contaminates observations of the internal field. Meaningful information about features described by spherical harmonic degrees 13 and above is lost (Roberts & King, 2013) (corresponding to patches of size ~ 1000 km at the CMB and ~ 1500 km at Earth's surface). This is clear from the geomagnetic power spectrum, shown at Earth's surface and at the CMB as a function of spherical harmonic degree n in figure 1.3 (the magnetic curtain is highlighted in grey). This is not to say that any length scales smaller than those associated with $n = 13$ are unimportant, in fact the spectrum at the CMB shows that although the field is dipole dominated, the power shows no sign of falling off with n. Holme *et al.* (2011) find that the power spectrum of the secular variation at the CMB is 'blue' — that power increases with n.

What we can observe of the secular variation exhibits a wide variety of dynamics. Magnetic field variations with a 5–10 year time-scale are thought to be linked to torsional waves supported by the cylindrical radial field in the interior of the outer core (Gillet *et al.*, 2010). The westward migration of flux patches at low latitudes have been linked to hydromagnetic wave motions (Finlay & Jackson, 2003). Abrupt changes in the time derivative of the magnetic field (or rapid accelerations), known as geomagnetic jerks,

occur on time-scales of months (Brown *et al.*, 2013). These observations suggest that wave activity and rapid variations are central to understanding core dynamics. Indeed, the increase in power of the secular variation spectrum with spherical harmonic degree suggests that some of the key dynamics may be hidden.

1.1.4 Numerical dynamos

Numerical simulations of the geodynamo have made impressive progress over the past 20 years, however their relevance to the real geodynamo has recently been called into question. The general framework is a spherical shell domain under uniform rotation, within which the equations for conservation of momentum and energy are solved, coupled to the induction equation for the magnetic field. The simulations attempt to replicate the cooling Earth by using a hot inner boundary and a cooler outer boundary to drive convection within the spherical shell. Boundary conditions vary, either no-slip or free-slip for the velocity field, along with fixed temperature or fixed heat-flux for the temperature field, depending on the object of the study. The most commonly reported dynamos are perhaps the most basic in their set-up, featuring: no-slip velocity conditions, insulating temperature conditions, an insulating inner core and mantle, with the magnetic field matched to a potential field at both boundaries (Christensen & Aubert, 2006).

The nondimensional parameters used in geodynamo simulations are vastly different to those which describe Earth's outer core. This is commonplace in computational fluid dynamics; Reynolds numbers in reality are large, whereas they are only moderate in simulations. The reasons for this are two-fold. First, wherever the flow meets a boundary, sharp gradients in the velocity field are created, which require extreme resolution to realise. Second, as the Reynolds number increases, large fluctuations in the flow become more frequent and more intense. These intermittent events place severe restrictions on the time-step and spatial resolution. For the geodynamo, the Reynolds number based on the values in table 1.1 is large $uL/\nu \sim 10^9$. But remember rotation is king in Earth's core, and it is the effects due to the Coriolis force which place the most prohibitive restrictions on numerical simulations.

The Ekman number, the ratio of the viscous force to the Coriolis force, is $E \sim 10^{-15}$ for Earth's core (using the values in table 1.1). The boundary layers that are expected to develop in a rotating spherical shell are called Ekman layers, and they have a theoretical thickness that scales as $\sim LE^{1/2}$ (Greenspan, 1968). Evidently, the Ekman layers for Earth's core would be tiny, on the order of ~ 10 cm, and it is unlikely that they play a role in the magnetic field generation. In reality, most geodynamo simulations span the range $E \sim 10^{-4} - 10^{-6}$ (Christensen & Aubert, 2006), and for the latter value millions of

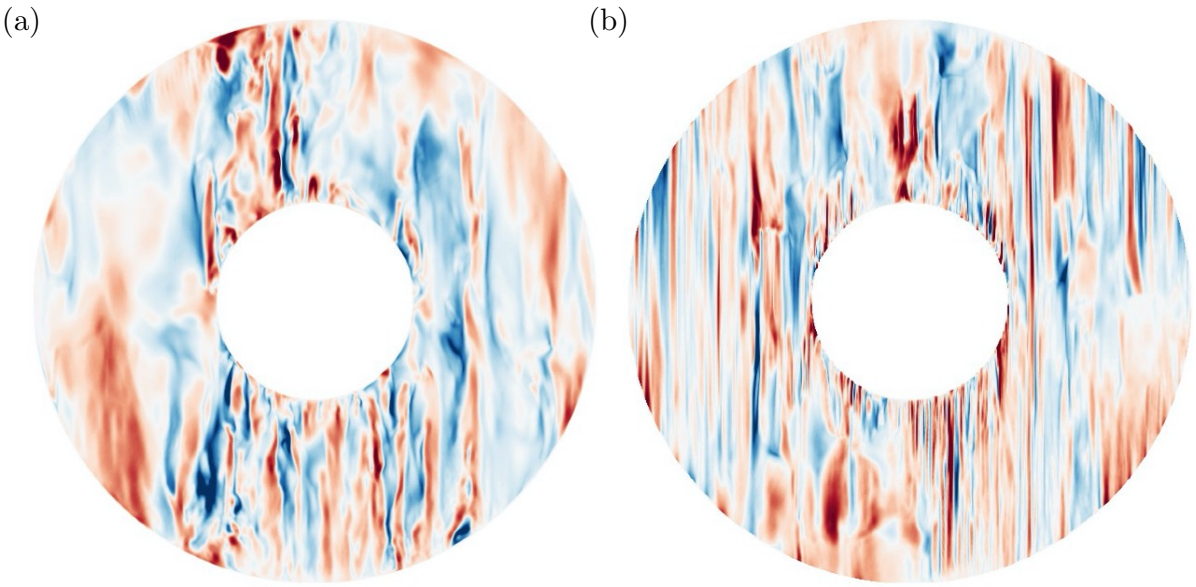

Fig. 1.4 Meridional slices of instantaneous azimuthal velocity in two simulations from Schaeffer *et al.* (2017), blue - negative, red - positive. (a) $E = 10^{-5}$ (b) $E = 10^{-7}$.

degrees of freedom are needed to resolve the dynamics. Also, a radial grid that is more dense near the inner and outer boundaries is needed to resolve the boundary layers. We mentioned earlier that internal waves are supported by the Coriolis force, with frequencies on the order of the planetary rotation rate Ω. These waves also impose severe restrictions on the time-step of geodynamo simulations, as they have a characteristic time-scale of Ω^{-1} ($\lesssim 1$ day), and ideally the dynamo should be integrated for a few magnetic diffusion times (~ 1 million years) to ensure the field is not decaying. These constraints indicate that if you want to integrate a dynamo for one magnetic diffusion time, you must compromise on the extremity of the parameters, and if you want to run at more realistic parameters, computational requirements permit only a short integration time. The limitations of fully consistent numerical modelling provide motivation for reduced models (Calkins *et al.*, 2015), laboratory experiments (Aurnou & Olson, 2001), and local investigations similar to those presented in this thesis (Bardsley & Davidson, 2016; Davidson & Ranjan, 2015; Davidson & Siso-Nadal, 2002; Moffatt & Loper, 1994; St. Pierre, 1996).

Two examples of the velocity field in numerical dynamos taken from Schaeffer *et al.* (2017) are shown in figure 1.4. The two simulations are at different Ekman numbers: (a) is at $E = 10^{-5}$ and (b) at $E = 10^{-7}$, the latter simulation is one of the most extreme to date. Meridional slices of the instantaneous axial velocity are shown, where the rotation vector points upwards – the effect of rapid rotation on the flow structures is clear. The flow is comprised of filamentary vortices which are aligned with the rotation axis, and these

features become more filamentary at lower E. You could compare these flow structures to the columnar features in figure 1.1. The flow length-scale perpendicular to the rotation axis reduces as the velocity field becomes more fine scale at low-E. Near convective onset (in a system with no magnetic field), the width of the convection columns theoretically scales as $\sim LE^{1/3}$ (~ 30 m for Earth's core), a length-scale which is set by viscous effects. For the highly supercritical convection expected within Earth's core, this length-scale is not thought to be relevant, as all other effects are more influential than viscosity. Indeed, the dominant convective length-scale perpendicular to the rotation axis in the simulation shown in figure 1.4b is larger than the length-scale predicted at onset. However, this is not true for the more viscous, weakly rotating simulations (King & Buffett, 2013).

A more realistic way to set this small length-scale is to assert that any structures with $Rm = u\ell/\eta < 1$ are susceptible to large Ohmic dissipation (Davidson, 2014). The magnetic field evolves according to two effects, the stretching and twisting of field lines by the flow and the diffusion of magnetic field. The magnetic Reynolds number Rm, measures the ratio of these two effects. Thus the scales with $Rm \approx 1$ are the smallest relevant scales, which results in $\ell \sim 2$ km. Using results from non-magnetic quasi-geostrophic (QG) simulations, Guervilly *et al.* (2019) suggested that ℓ is set by a balance between nonlinear inertia and the Coriolis force, resulting in the scaling $\ell \sim Ro^{1/2}$. Extrapolating their results down to Earth-like conditions yields $\ell \sim 30$ km, although this estimate does not include magnetic effects, and the smallness of the Rossby number suggests that it is unlikely that inertia plays an important role at this scale. Based on these results we take $\ell \sim 10$ km as a reasonable estimate for small-scale convective structures.

In the more rapidly rotating simulations, strong, axially aligned dipolar magnetic fields are generated (Kutzner & Christensen, 2002). This implies that the columnar convection, due to the dominance of the Coriolis force, organises the magnetic field so that its dipole is aligned with the rotation axis. If the strength of the buoyant forcing is increased, for the equivalent Ekman number, nonlinear inertia enters the force balance and the convection becomes less columnar (Christensen & Aubert, 2006). The main consequence of the reduction of coherence in the velocity field is that the magnetic field becomes multi-polar, with a broadband spectrum. An example of this phenomena is illustrated in figure 1.5, where axial vorticity isosurfaces and the radial magnetic field at the outer boundary are shown. The flow is columnar and coherent and the magnetic field is very dipolar in (a) whereas the flow is disorganised and the field is multi-polar in (b). This transition is governed by the competition between nonlinear inertia and the Coriolis force, and can be described by a 'local' Rossby number, which measures the ratio of the

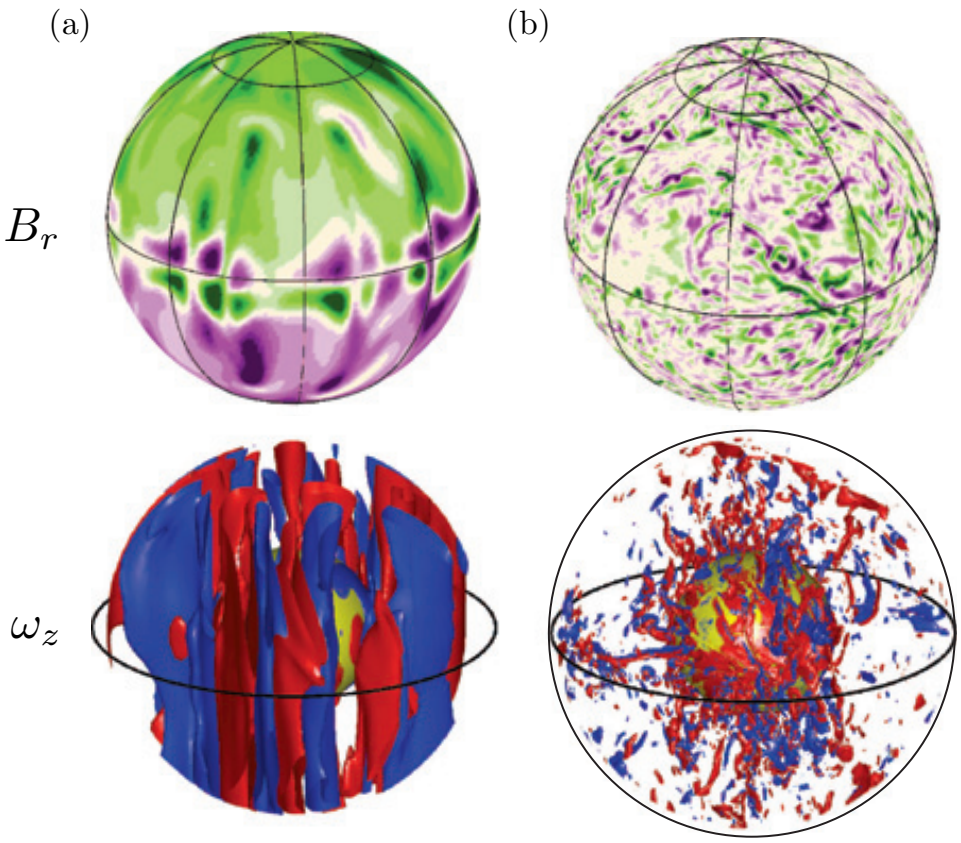

Fig. 1.5 Radial magnetic field at the outer boundary (top) and isosurfaces of axial vorticity (bottom) from Soderlund *et al.* (2012). The convection is much more strongly forced in (b) than in (a).

forces at the scale of the convection (Christensen & Aubert, 2006; Soderlund *et al.*, 2012, 2014). The physical mechanism underlying this transition is the focus of chapter 4.

We have explored properties of the velocity and magnetic field in numerical dynamo simulations, however it is the buoyancy field which is the driver of the system. The distribution of buoyancy in the outer core will shape the rotating convection, and this will have consequences for the dynamo mechanism. Figure 1.6 shows four meridional sections from geodynamo simulations, highlighting either the temperature/density perturbation or a component of the velocity field perpendicular to the rotation vector. The vertical dashed lines highlight the tangent cylinder (TC), the imaginary cylinder that is aligned with the rotation axis and circumscribes the inner core. The time and azimuthally averaged temperature perturbations shown in (a) (from Sheyko *et al.*, 2018) show that much of the heat within the TC is trapped, where in this image red signifies hot material. Outside of the TC in (a), there is an identifiable preference for hot material in and around the equational plane. The concentration of heat transport near the equatorial plane is a

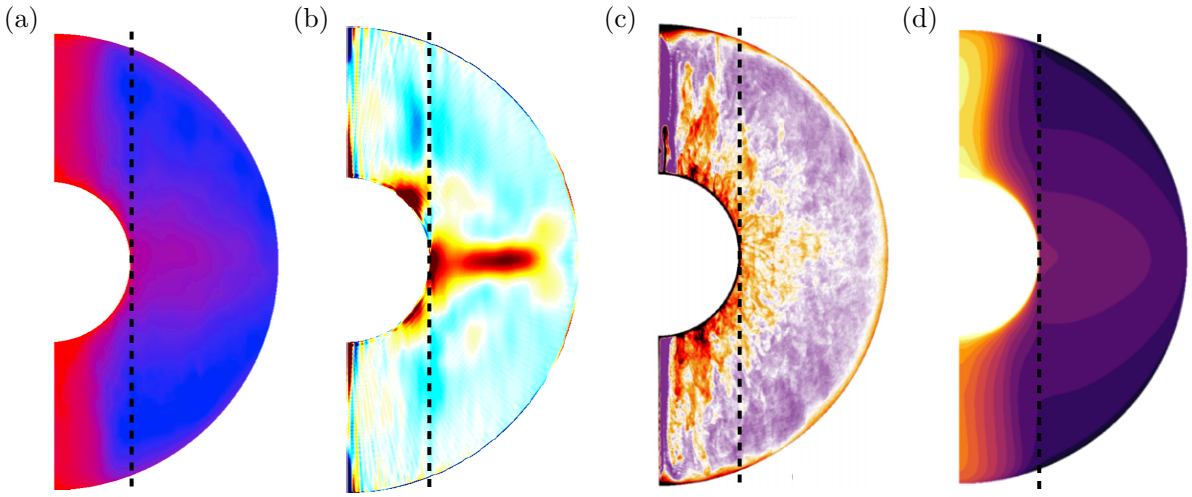

Fig. 1.6 Equatorial bias of the heat flux in spherical simulations. (a) Time and azimuthally averaged temperature perturbations from Sheyko *et al.* (2018) (b) Azimuthal average of cylindrical radial velocity from Sakuraba & Roberts (2009) (c) Azimuthal average of the concentration field in a meridional section from Bouffard *et al.* (2019) (d) Time and azimuthally averaged density/temperature fluctuations from Schaeffer *et al.* (2017). The vertical dashed lines highlight the tangent cylinder.

relatively frequent observation in geodynamo simulations. In perhaps the most extreme case, figure 1.6b shows an azimuthal average of the cylindrical radial velocity from Sakuraba & Roberts (2009), where red (blue) denotes positive (negative) velocity. There is a markedly strong equatorial jet of fluid which originates at the inner core boundary, and is directed outwards. This particularly strong jet develops when there are fixed-flux boundary conditions on the temperature field (as opposed to fixed temperature), which is arguably the more geophysical choice. Figure 1.6c shows the azimuthally averaged concentration field from a hydrodynamic simulation by Bouffard *et al.* (2019) driven by purely compositional convection. Even with no time-averaging the spatial bias outside of the TC is apparent. The combination of a radial jet and the presence of anomalously hot/light material (see also figure 1.6d), constitutes an equatorially biased heat-flux from the inner to the outer boundary. As shown in figure 1.6, the bias is observed in rotating hydrodynamic and MHD convection for both constant temperature and heat-flux boundary conditions, and for thermal and compositional convection.

Three of the images shown in figure 1.6 are azimuthal averages, and two of those have also been time averaged. The averaging results in a smooth, global view of the simulations, which is instructive when the dynamics are chaotic with a range of spatial and temporal scales. However, we would also like to examine the structure of the instantaneous temperature/density perturbations, and an example of this is shown in

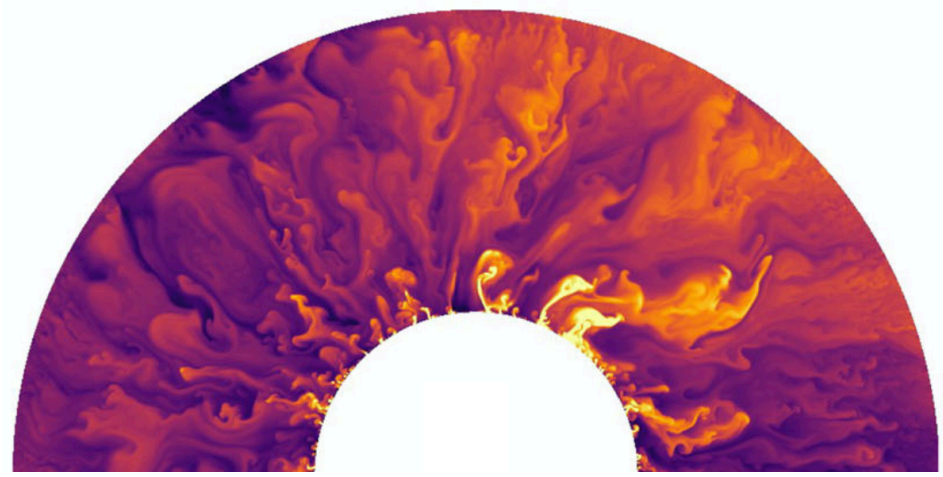

Fig. 1.7 Instantaneous temperature fluctuations in an equatorial slice from Schaeffer *et al.* (2017).

figure 1.7. The image shown is an instantaneous equatorial slice from the same simulation as in figure 1.6d, the intricate detail of the temperature field is evident. There are small-scale buoyant plumes released at the inner core boundary, some of a size 200 times smaller than the core radius. A movie corresponding to this snapshot (which can be accessed at https://figshare.com/authors/Nathanael_Schaeffer/474534) shows that the subsequent rise of the buoyant plumes through the core is chaotic, with a large time-dependence.

1.1.5 Planetary magnetic fields in our solar system

Most of the planets in our solar system are thought to have a dynamo generated magnetic field, with the exception of Mars and Venus. We list some properties of the planets in table 1.3. The first thing to notice is that the terrestrial planets and the gas giants all have magnetic fields that are roughly aligned with their rotation axis, measured by the inclination. On the other hand, the ice giants have fields which are highly inclined, suggesting a different dynamo mechanism. The field strength (in velocity units), given in column four, is obtained from an estimate of the planetary dipole moment which can be related to the integral of the field over the spherical volume within which it is generated (Griffiths, 2014).

Traditionally it is thought that the Elsasser number Λ, should approach ~ 1 for planetary dynamos, in which a global scale magnetostrophic balance is satisfied. However, the estimates of Λ in table 1.3 vary by almost a factor of 10^6. Davidson (2013*a*) introduced the nondimensional group $\bar{B}_z/\Omega R_c$, which is a type of Lehnert number, and showed that

this number is remarkably similar for the planets listed in table 1.3. This is despite the objects varying in size, rotation rate and field strength. The gas giants have dipolar fields, and seem to fit the same scaling as the terrestrial planets, however the cores of gas giants have no solid outer boundary. This supports the idea that viscous boundary layers play no role in the generation or organisation of the magnetic field.

It is thought that the dynamos of young fully convective M-stars might operate in a similar way to those of the planets (Brun & Browning, 2017), so as an interesting comparison we examine V374 Pegasi, an M-star of this type. These stars are huge and they rotate rapidly — V374 Pegasi has a rotation period of 0.44 days and a radius ~ 200 km, and its magnetic field has been imaged in detail to reveal a strong dipole (Gastine *et al.*, 2013). The observed values result in $\bar{B}_z/\Omega R \sim 17 \times 10^{-6}$, an estimate which compares favourably with the planets (Davidson, 2017). We note that $\Lambda \sim 10^4$ for V374 Pegasi, which provides more evidence that the assumption of $\Lambda \sim 1$ is far from universal.

Table 1.3 Properties of planetary dynamos, data from Davidson & Ranjan (2015) and references therein. The magnetic field has been normalised by $\sqrt{\mu\rho}$, and we use $\rho \sim 10^4$, 10^3, 4×10^3 kg m^{-3} and $\eta \sim 1$, 3, 300 m^2 s^{-1} for the terrestrial planets, gas giants and ice giants.

Object	$2\pi/\Omega$	R_c (10^3 km)	$\bar{B}_z$ (m s^{-1})	Inclination	$\bar{B}_z/\Omega R_c$ $\times 10^6$	$\Lambda = \bar{B}_z{}^2/\Omega\eta$
Mercury	58.6	1.8	1.25×10^{-5}	5°	5.5	2×10^{-4}
Venus	243	3.2	-	-	-	-
Earth	1	3.48	3.1×10^{-3}	11°	13	0.2
Mars	1.03	1.8	-	-	-	-
Jupiter	0.413	55	5.1×10^{-2}	9.6°	5.2	5
Saturn	0.440	29	1.1×10^{-2}	$< 0.1°$	2.3	0.2
Uranus	0.718	~ 18	$\sim 1.8 \times 10^{-3}$	59°	~ 1.0	$\sim 10^{-4}$
Neptune	0.671	~ 20	$\sim 7.1 \times 10^{-4}$	47°	~ 0.3	$\sim 10^{-5}$

1.2 The α-effect

All working dynamos need mechanisms through which to convert *toroidal* field into *poloidal* field, and vice-versa, to complete the dynamo cycle (Moffatt, 1978). Any divergence-free vector field, such as the magnetic field, may be decomposed into its

poloidal and toroidal components. Examples of poloidal and toroidal fields are shown in figure 1.8[3].

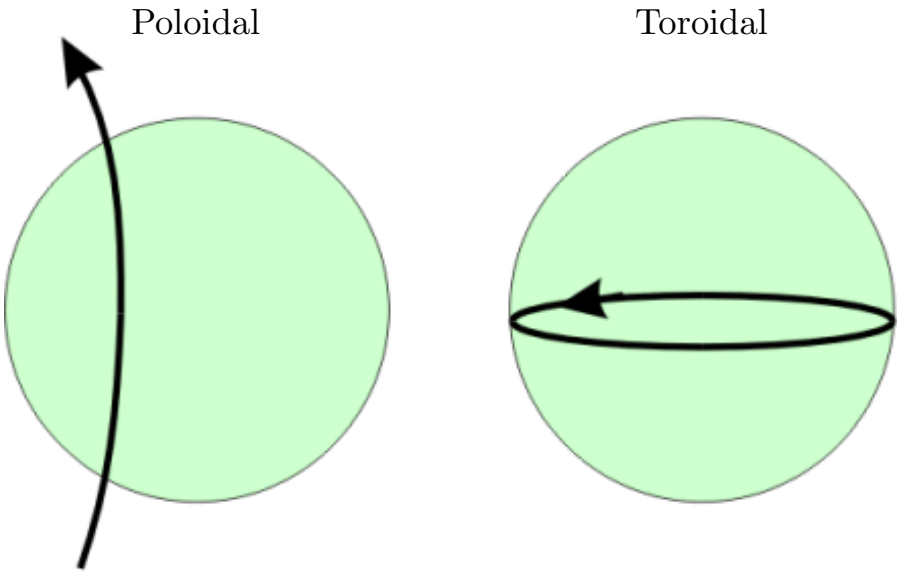

Fig. 1.8 Poloidal and toroidal components of a divergence-free vector field.

One mechanism to generate poloidal field from toroidal field is the α-effect, originally proposed by Parker (1955), and mathematically developed by Steenbeck *et al.* (1966). The α-effect is an inherently small-scale phenomenon, whereby 'cyclonic events' in the velocity field lift and twist large-scale magnetic field lines in a manner which generates an average current that is parallel or anti-parallel to the original magnetic field direction (figure 1.9). By Ampère's law, the resulting mean current is associated with a poloidal magnetic field, thus through this process poloidal field may be generated from toroidal field (and vice-versa). We note that this is only possible in a fluid of finite conductivity, as the mechanism by which the field loop pinches off is diffusive.

The fluid flow in figure 1.9 is positively helical; namely, the velocity, $\boldsymbol{u}$ and vorticity, $\boldsymbol{\omega} = \boldsymbol{\nabla} \times \boldsymbol{u}$ are positively correlated ($\boldsymbol{u} \cdot \boldsymbol{\omega} > 0$). (Had the helicity been negative, the induced current would have been parallel to $\boldsymbol{B}$). Helicity is highly beneficial for dynamo action (Moffatt, 1978; Tobias, 2019), and many natural fluid systems possess helicity. Indeed, numerical simulations of rotating fluids often exhibit highly helical velocity fields (Mininni & Pouquet, 2010), and the spiralling up of the flow through the action of the Coriolis force appears to be central to helicity generation.

[3]Original figure produced by Natural Resources Canada, and can be accessed at https://www.geomag.nrcan.gc.ca/mag_fld/fld2-en.php

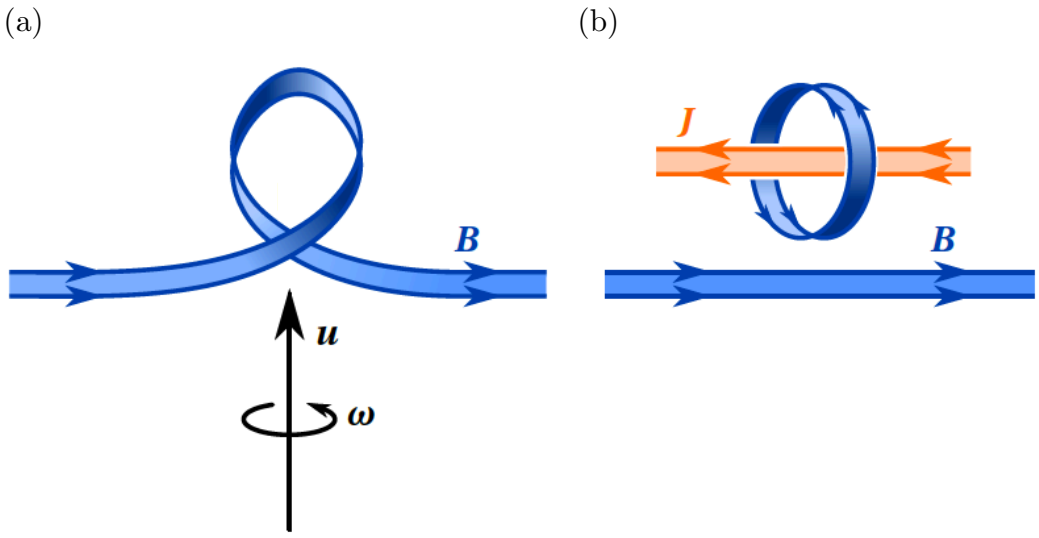

Fig. 1.9 The α-effect: (a) a positively helical flow lifts and twists originally horizontal magnetic field lines and (b) the finite electrical conductivity of the fluid allows a field loop to pinch off, with an associated current density that is anti-parallel to the initial magnetic field direction. Courtesy of Oli Bardsley (2019).

1.2.1 α^2 dynamos

Many of the published numerical dynamos can be classified as of the α^2 type, in a zero-order sense (Christensen & Aubert, 2006; Roberts & King, 2013). An α^2 dynamo converts toroidal field to poloidal field and back again through the α-effect. This is not true of the solar dynamo, in which the shearing of poloidal field by differential rotation (also called the Ω-effect) is thought to play a key role (Weiss & Proctor, 2014, pp. 322). One implication of an α^2 dynamo mechanism is that the resulting poloidal and toroidal magnetic field components are of approximately equal magnitudes, and this is what is observed in the numerics.

Figure 1.10 indicates the sufficient ingredients for an α^2 dynamo which operates outside of the TC. In this schematic B is the magnetic field, J is the current density, the subscripts p, ϕ and s correspond to poloidal, toroidal (azimuthal) and cylindrical radial components, h_k is the helicity of the flow and 'Ampère' signifies the use of Ampère's law. This cartoon describes many of the published dynamo simulations in a zero-order sense (Olson *et al.*, 1999). However, the source of the flow helicity and its subsequent distribution — negative (positive) in the northern (southern) hemisphere — is a matter of current debate (Davidson & Ranjan, 2015).

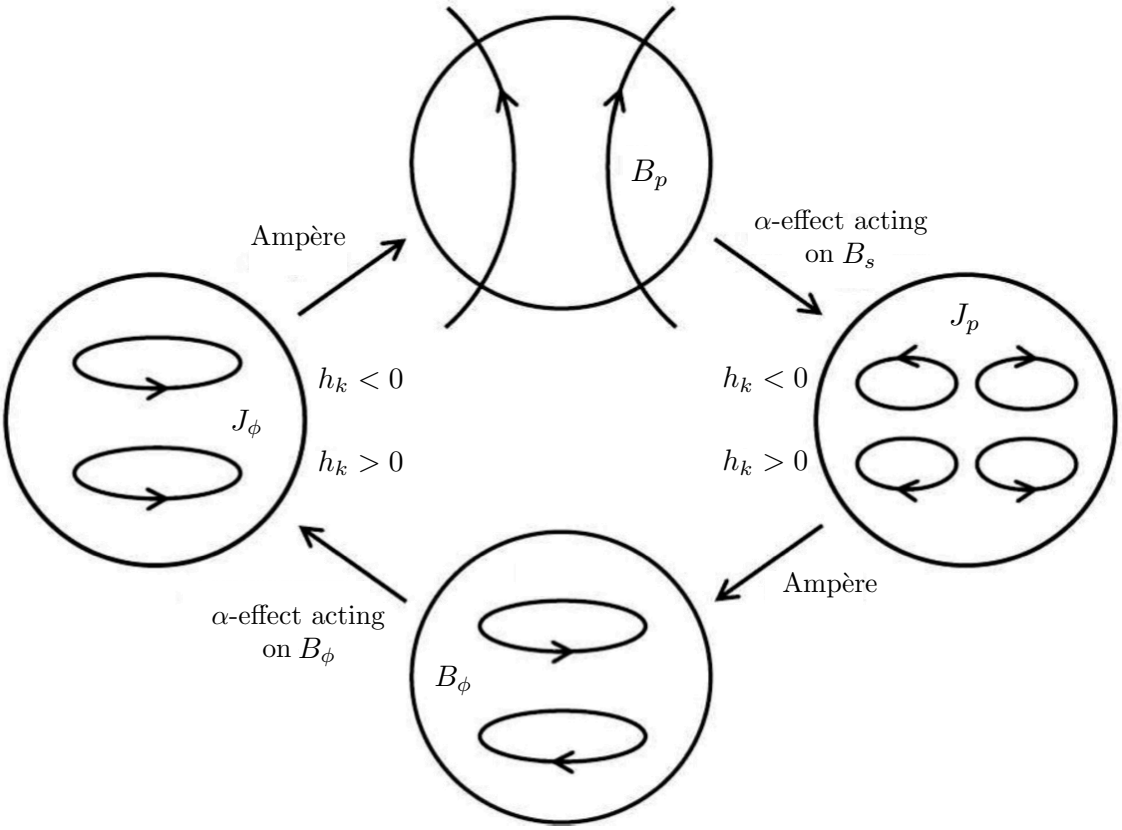

Fig. 1.10 α^2 dynamo cartoon with net flow helicity negative (positive) in the northern (southern) hemisphere; adapted from Davidson & Ranjan (2015).

1.2.2 Helicity segregation

As mentioned in §1.1.1, it is unlikely that viscosity plays an important role in a planetary core, owing to the smallness of the Ekman number. However, this cannot be said of many of the numerical dynamos (King & Buffett, 2013). The generation and organisation of kinetic helicity in the overly viscous numerical dynamos is often controlled by Ekman pumping at the outer boundary. The interaction of the columnar cyclone/anti-cyclone pairs with the viscous boundary layer generates a helicity distribution which is negative (positive) in the northern (southern) hemisphere (e.g. Roberts & King, 2013, pp. 34), exactly as is necessary for the α^2 dynamo cartoon above.

However, in the core of a planet, any helicity generation mechanism must be independent of viscosity and the outer boundary condition (see §1.1.5). An attractive alternative is the spontaneous emission of inertial wave packets from buoyant anomalies, first suggested in Davidson (2014). Inertial wave packets carry large amounts of kinetic helicity, and they propagate negative (positive) helicity above (below) their source (with

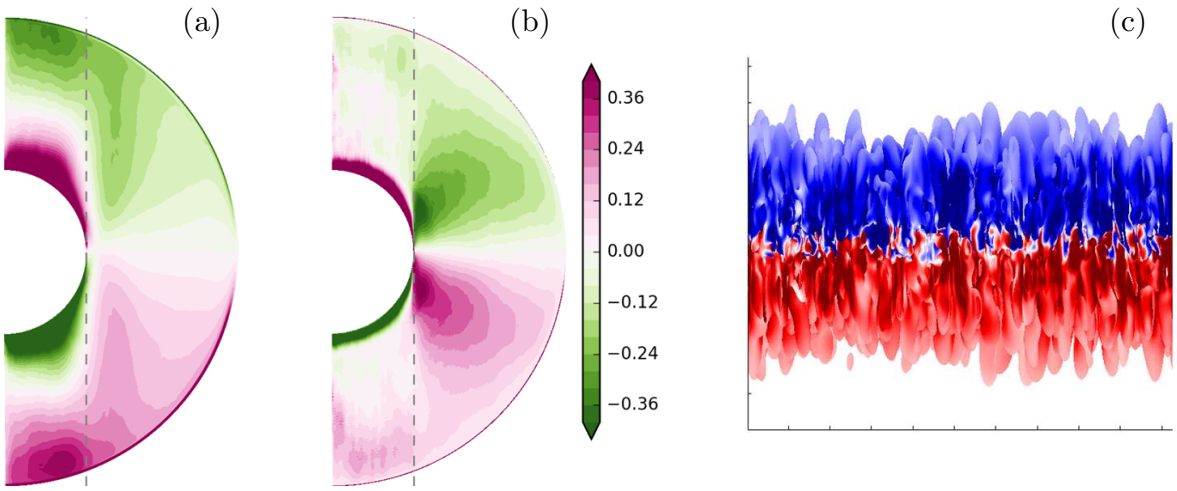

Fig. 1.11 Azimuthally averaged relative kinetic helicity from Schaeffer *et al.* (2017) (a) $E = 10^{-5}$ (b) $E = 10^{-7}$. (c) Inertial wave packets emitted from a buoyant cloud from Davidson & Ranjan (2015), showing axial velocity coloured by relative kinetic helicity (blue - negative, red - positive).

respect to the rotation vector). Thus, if inertial wave packets are preferentially generated near the equatorial plane, they could yield the helicity distribution required for an α^2 dynamo. (We will discuss the theory of inertial waves in chapter 2.)

These ideas are illustrated in figure 1.11, where (a) and (b) show relative helicity distributions in numerical dynamos at $E = 10^{-5}$ and $E = 10^{-7}$ respectively (Schaeffer *et al.*, 2017). In both (a) and (b) we observe the required helicity segregation outside of the TC (marked with a vertical dashed line): negative (positive) in the north (south). However, in (a) the helicity appears to originate at the outer boundary, which suggests that it is generated in the Ekman layer. Whereas in (b), at a smaller Ekman number, the helicity looks like it is generated in the interior, possibly by the emission of inertial wave packets from buoyant anomalies. Indeed, the segregation of helicity in (b) is similar to that in (c), which shows isosurfaces of axial velocity coloured by kinetic helicity from a numerical experiment by Davidson & Ranjan (2015). The simulation is initialised with a layer of buoyant anomalies confined to the mid-plane of the box, and $\boldsymbol{u} = \boldsymbol{0}$. The non-conducting fluid is rapidly rotating about the vertical axis, and viscous effects are negligible as there are no solid boundaries. The columnar flow structures are in fact low-frequency inertial wave packets, and this is confirmed by their axial propagation speed and the observed helicity distribution. It is clear that inertial wave packets, when launched by an equatorially biased heat-flux, provide an appealing inviscid mechanism for the generation and segregation of helicity in planetary cores.

1.2.3 Helical wave dynamos

Moffatt (1970) first suggested that a sea of inertial waves could act as a dynamo. He concluded that for dynamo action to occur, it is necessary for there to be a net wave flux parallel or anti-parallel to the rotation vector. Such a situation is only possible if the source of the waves, for example the distribution of buoyancy, is spatially inhomogeneous in the axial coordinate. This type of buoyancy distribution is evidenced in figure 1.6, where the distribution of heat-flux is shown to be biased towards the equatorial plane. This idea was explored further in Davidson (2014), where the *helical wave model* is introduced. The details of the helical wave model are summarised in the recent review paper Davidson & Ranjan (2018), and we will give a brief description here. This dynamo cartoon provides motivation for the work presented in this thesis, however our results also have a more general applicability.

To summarise the helical wave dynamo model, we begin with the equatorially biased heat-flux (figure 1.6). If the radial heat-flux is greater near the equatorial plane, or indeed there is greater agitation in that region, then waves are preferentially launched at low-latitudes which then axially propagate to the north and south (figure 1.11c). Buoyant anomalies, like those seen in figure 1.7, are sources of inertial waves (Davidson & Ranjan, 2015). Inertial wave packets are fast, and if launched by buoyant anomalies near the equatorial plane with a length-scale $\ell \sim 10$ km, they will reach the CMB in a couple of months. On their way they distribute kinetic helicity negative (positive) above (below) their source, as is required for a dynamo of α^2-type (figure 1.10). We note that the generation and segregation of helicity by inertial waves is entirely independent of viscosity. Inertial waves are modified by a large-scale magnetic field (§2), however all the resulting wave types segregate helicity in the same way as pure inertial waves (Bardsley, 2019).

1.3 Thesis Outline

In this study, we approach two problems whereby the propagation of inertial wave packets is inhibited and/or modified by nonlinear inertia (chapter 4) and by a large-scale magnetic field (chapter 5). The first of these problems is motivated by an observation from the numerical dynamos, where columnar structures are disrupted as the buoyant forcing is increased, and inevitably the dipole collapses (see §1.1.4). We explore the idea that the propagation of inertial wave packets is essential to the maintenance of columnar flow structures, which in turn organise the magnetic field into a strongly dipolar state. If the wave packets cannot freely propagate as nonlinear inertia becomes more intense, then the

columnar structures may break down and the field will disorganise. The second of the studies focuses on the variety of wave-types which are uncovered when a rapidly rotating conducting fluid is influenced by a large-scale magnetic field. We investigate the effects of the strength of an imposed transverse field on: columnar structure formation, the kinetic, magnetic and cross helicity carried by the waves, and on the emf induced by the wave packets and the related α-effect. Implications for the numerical dynamos and the helical wave dynamo model are discussed. We seek to answer the following questions.

The influence of non-linear inertia on inertial waves (chapter 4)

- What is the effect of an increase in Ro from 0.01 to 1?
- Does the segregation of kinetic helicity persist for larger Rossby numbers?
- Does the increase in Ro affect the axial coherence of any columnar structures?
- Can we reproduce the transition between inertial wave propagation and incoherent turbulence at $Ro = 0.2 - 0.6$, when the dynamics are driven by a buoyancy field?
- Can we provide evidence for a link between the dipolar-multipolar transition observed in the numerical dynamos and the transition in rotating turbulence?
- What is the explanation for the discrepancy between the critical Rossby number observed in the numerical dynamos ~ 0.1 and the critical Ro in rotating turbulence ~ 0.4?

Magnetic-Coriolis waves in a uniform transverse field (chapter 5)

- Can we verify the diffusionless analytical solutions at $Ro \to 0$ of Bardsley (2019) for a single buoyant blob?
- What are the differences between the single blob case and the multiple blob case with regard to the induced emf?
- What is the effect of the strength of the applied field on the coherence of the emf?
- At Earth-like Lehnert numbers is there a significant α-effect?
- What are the possible consequences for the helical wave dynamo model?

In chapter 2 we lay out some of the theory of inertial and magnetic-Coriolis waves, which is necessary to interpret the results in the later chapters. In this chapter we also briefly review the literature on experiments and simulations of rapidly rotating flows and turbulence, and explore the link between inertial waves, Taylor columns and quasi-geostrophy. Chapter 3 contains details of the codes used in this work and the numerical methods that they employ. The codes are validated against analytical solutions of simplified problems, and we give detail on the generation of initial conditions. Thereafter, the main body of work is presented in chapters 4 & 5, where we exhibit the contents of two papers published from this thesis (McDermott & Davidson, 2019, 2020). These chapters begin with a short, detailed review of literature that is particularly relevant to the work, followed by the results and a discussion. Finally, we end with concluding remarks (chapter 6) which place the results of the previous chapters into the broader research context of planetary magnetic field generation.

Chapter 2

Inertial and magnetic-Coriolis wave theory

2.1 Introduction

Inertial waves are a recurrent theme throughout this thesis. They are ubiquitous in rapidly rotating fluids, and are thought to be constantly forced by the buoyancy field within Earth's outer core (Davidson & Ranjan, 2015). The fact that planetary magnetic fields are often dipolar, and aligned with the rotation axis, suggests that columnar structures in the flow are central to the organisation of the field. It has been shown that the initial formation of columnar structures in rotating fluids is explained by the propagation of low-frequency inertial wave packets (Davidson *et al.*, 2006). The question is: how can the geomagnetic field be organised and quasi-steady over millions of years, when the source of the dynamo, the buoyancy field, is chaotic, time dependent and has a large range of scales? Inertial waves provide a robust means of organising the velocity field, which in turn may generate a coherent magnetic field. This is an attractive proposition, however the details of how this dynamo could operate are far from agreed upon.

The importance of inertial waves is two-fold. They provide a means by which columnar vortices are generated in rotating turbulence (Davidson *et al.*, 2006), and as they carry intense helicity, they have the potential to drive a dynamo (Moffatt, 1970). Although, this rests upon there being an inhomogeneity in the buoyant driving; namely, that there is a concentration of hot/light material near the equatorial plane (figure 1.6). There are some effects due to inertial waves that are far from obvious, so first we briefly review the theory of these waves. Second, we consider the effects of an imposed magnetic field on the wave dispersion, motivated by the dynamics in planetary cores.

2.1.1 Small scales in Earth's outer core

This study concentrates on small scale dynamics in dynamo simulations and in Earth's core, however there is no consensus in the field on the size of the small scales in the geodynamo. This leads to the question of what sets the small length-scale in Earth's core? We briefly addressed this question in chapter 1, and we will elaborate on it here. Two plausible ways in which the small length-scale could be set are as follows. At the origin of the convective driving—the inner core boundary—the partitioning of heavy and light elements into the inner and outer core leads to compositional convection. This type of convection is much less well studied than purely thermal convection, or convection driven by a so-called co-density field. The non-magnetic compositional convection simulations of Bouffard *et al.* (2019) reveal a very fine-scale structure to the concentration field, where plumes of light material destabilise near the inner core boundary and rise through the core. Deguen *et al.* (2007) suggest that the chimneys generated in the mushy layer at the inner core boundary could have a length-scale on the order of $10 - 1000$ m. However, what sets the scale of compositionally buoyant plumes released at the inner core boundary remains an open question.

Davidson (2014) considered the Ohmic dissipation of structures in the bulk of the outer core. He argued that structures with $Rm = u\ell/\eta \lesssim 1$, based on the length-scale of the structure perpendicular to the rotation axis, are expected to be subject to large Ohmic dissipation. This results in (for $Rm = 1$) a lower bound of $\ell \approx 2$ km for the energy carrying scales. Therefore a reasonable estimate for the length-scale of small convective structures is $\ell \sim 10$ km. Figure 1.7 shows the buoyancy field in a highly supercritical, rapidly rotating dynamo simulation, as is expected for Earth's core. The vast range of scales is prevalent, and we see small scale plumes released near the inner core boundary that slowly yet chaotically migrate toward the CMB. We shall see in §2.2 that each of these buoyant plumes is obliged to emit inertial wave packets, and in the outer core these waves disperse energy much faster than the rate at which the plume itself rises.

To get a sense for the relevant time-scales of the dynamics on the global scale $L \sim 2000$ km and the local scale $\ell \sim 10$ km, we consider some nondimensional numbers. First, the Rossby number is the ratio of the rotation period to the advective time-scale, and using the two given length-scales we have $Ro(\ell) \sim 5 \times 10^{-4}$ and $Ro(L) \sim 10^{-6}$. Thus, for the energy containing scales, rotation far outstrips the time-scale of overturning eddies. Viscosity is unimportant for the bulk of Earth's core, and this is evidenced by the Ekman number, which measures the ratio of the rotation period to the viscous diffusion time. For the length-scales considered we have $E(\ell) \sim 10^{-10}$ and $E(L) \sim 10^{-15}$. Now, the time-scale that is most similar to the rotation period is the time-scale of magnetic

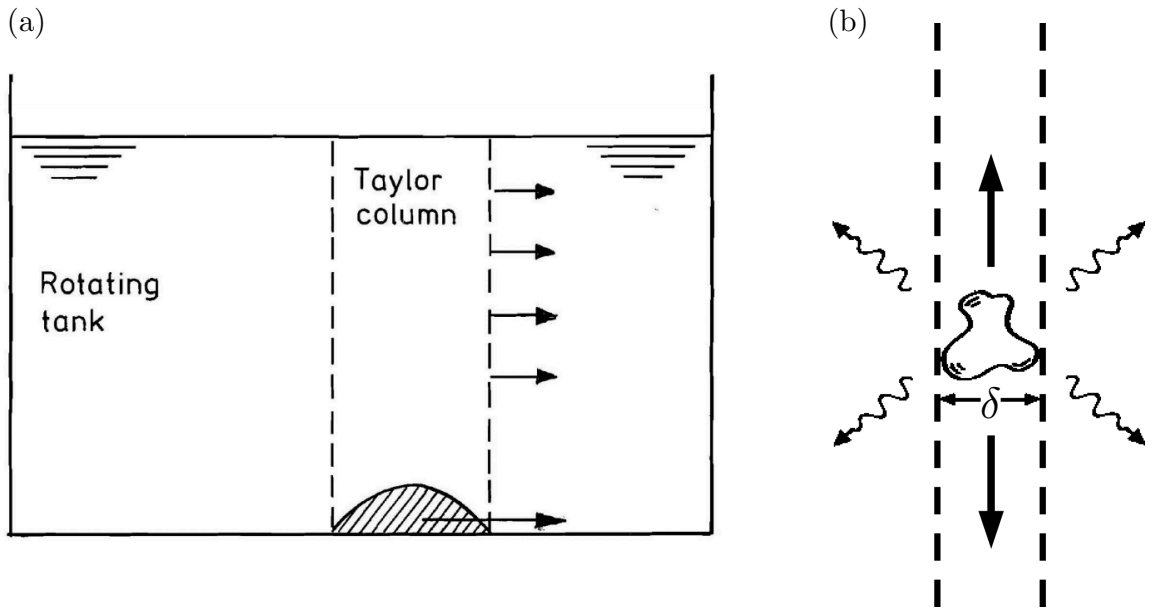

Fig. 2.1 The importance of inertial waves for transient Taylor columns, figures from chapter 3 of Davidson (2017). (a) A Taylor column is formed above an object at the base of a rotating tank when the object is slowly moved. (b) Radiation of angular momentum (straight arrows) and kinetic energy (curly arrows) from a localised disturbance in a rapidly rotating fluid.

oscillations (or Alfvén waves, §2.3.1), and this time-scale separation is measured by the Lehnert number Le. The small- and large-scale Lehnert numbers are $Le(\ell) \sim 0.03$ and $Le(L) \sim 10^{-4}$, indicating that on the small-scales magnetic oscillations may become entwined with inertial waves, but rotation is dominant. Indeed, in §2.3 the combination of rotation and a large-scale magnetic field gives rise to waves whose dispersion pattern is controlled by the value of the Lehnert number.

2.1.2 Rotating fluids

The Taylor-Proudman theorem, as presented in §1.1.2, is the first port of call in our discussion of the effects of uniform rotation on fluid motion. Figure 2.1a illustrates a rotating tank with a solid object at the base. The flow attempts to be invariant along the rotation axis despite the presence of the object, and thus a column of fluid forms above the object, called a Taylor column. That is, if we slowly drag the object along the bottom of the tank, the Taylor column follows, and this phenomenon raises an interesting question. How does the fluid at the top of the tank know what the fluid at the bottom of the tank is doing?

This question reveals a problem with the Taylor-Proudman theorem (1.2), in that there is no way for information to travel through the fluid, as we have neglected the time derivative. In the next section we will re-instate time dependence in the linearised conservation of momentum equation to explore the adjustment of the Taylor column as the object moves. A glimpse of how information is propagated in a rotating fluid is illustrated in figure 2.1b. This diagram shows a localised disturbance in a rapidly rotating fluid, the straight arrows represent the radiation of angular momentum, and the curly arrows represent the radiation of kinetic energy. Angular momentum is dispersed quickly away from the disturbance, but only within the column of fluid above and below the disturbance (Davidson *et al.*, 2006). Kinetic energy radiates in all directions, although, as we shall see, the *energy density* is highest on-axis.

2.2 Inertial waves

2.2.1 Theory

The linearised equation for vorticity in a rapidly rotating inviscid fluid is

$$\partial_t \boldsymbol{\omega} = 2(\boldsymbol{\Omega} \cdot \boldsymbol{\nabla})\boldsymbol{u}\,. \tag{2.1}$$

If we operate on (2.1) with $\boldsymbol{\nabla} \times \partial_t$, this yields the wave-like equation (Greenspan, 1968)

$$\frac{\partial^2}{\partial t^2}\left(\boldsymbol{\nabla}^2 \boldsymbol{u}\right) + 4(\boldsymbol{\Omega} \cdot \boldsymbol{\nabla})^2 \boldsymbol{u} = \boldsymbol{0}\,. \tag{2.2}$$

Seeking plane wave solutions of the form $\boldsymbol{u} = \hat{\boldsymbol{u}} \exp[\mathrm{i}(\boldsymbol{k} \cdot \boldsymbol{x} - \varpi t)]$, we arrive at the dispersion relation for inertial waves

$$\varpi = \pm \frac{2(\boldsymbol{\Omega} \cdot \boldsymbol{k})}{k}\,, \tag{2.3}$$

where ϖ is the angular frequency of the wave, $\boldsymbol{k}$ is the wavevector and $k = |\boldsymbol{k}|$. Notice that the frequency is independent of k, and depends on the orientation between $\boldsymbol{k}$ and $\boldsymbol{\Omega}$. If the sign of $\boldsymbol{k}$ and ϖ is changed in (2.3), then there is no change to the solution, thus in this work we make the choice that frequencies are non-negative: $\varpi \geq 0$. This enforces that one choice of $\boldsymbol{k}$ corresponds to a single frequency ϖ. The range of realisable frequencies is evidently $0 \leq \varpi \leq 2\Omega$, so that any disturbance with a frequency greater than 2Ω will not excite inertial waves.

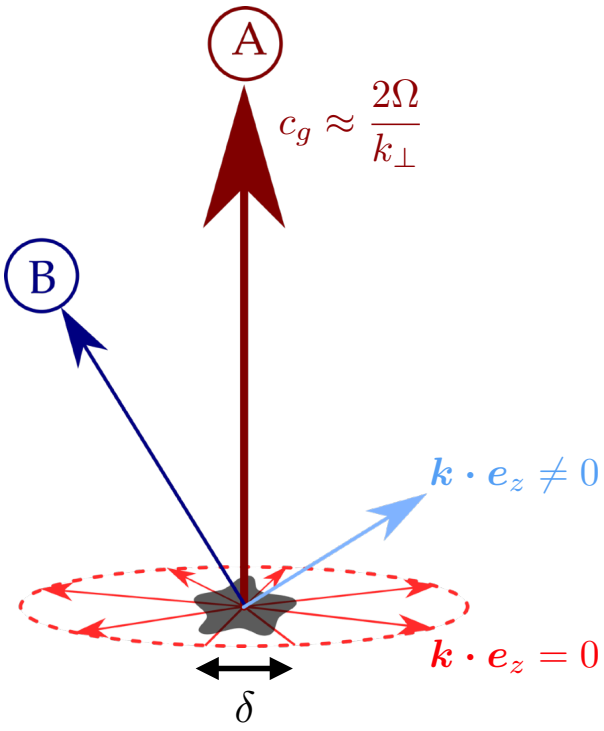

Fig. 2.2 Geometric focusing of energy by inertial waves (Davidson, 2013*b*, pp. 389). Energy propagated to the off-axis location B is associated with only one wavevector, however energy is propagated to the on-axis location A at the maximum possible speed $2\Omega/k$, and is associated with the multitude of wavevectors that satisfy $\boldsymbol{\Omega} \cdot \boldsymbol{k} \approx 0$.

The speed at which the crests and troughs of the wave propagate is the phase velocity

$$\boldsymbol{c}_p = \frac{\varpi}{k}\boldsymbol{e}_k = \pm\frac{\boldsymbol{\Omega} \cdot \boldsymbol{k}}{k^2}\boldsymbol{e}_k \,, \tag{2.4}$$

(where $\boldsymbol{k} = k\boldsymbol{e}_k$) and as the magnitude and direction of $\boldsymbol{c}_p$ depend on $\boldsymbol{k}$, inertial waves are dispersive (Lighthill, 1978). It is well known that energy is not propagated at the phase velocity, but at the group velocity, defined as the gradient in $\boldsymbol{k}$-space of ϖ. For inertial waves this is

$$\boldsymbol{c}_g = \pm 2\,\frac{\boldsymbol{k} \times (\boldsymbol{\Omega} \times \boldsymbol{k})}{k^3} = \pm 2\,\frac{\boldsymbol{\Omega} - (\boldsymbol{e}_k \cdot \boldsymbol{\Omega})\boldsymbol{e}_k}{k} \,, \tag{2.5}$$

thus the magnitude and direction of $\boldsymbol{c}_g$ also depend on the wavevector. From (2.5), the first thing to note is that larger wavelengths (smaller wavenumbers) propagate energy at a faster speed. Further, if we take $\boldsymbol{\Omega} \cdot$ (2.5), we find that the positive (negative) sign corresponds to energy propagating upwards (downwards), with respect to the rotation vector. The phase velocity and the group velocity are always perpendicular, and when

one is maximal (with respect to the angle between $\boldsymbol{\Omega}$ and $\boldsymbol{k}$), the other is zero. Moreover, the waves with the maximum possible group velocity are directed along the rotation axis with a speed $2\Omega/k$, and the wavevectors associated with these waves all lie in the plane $\boldsymbol{\Omega}\cdot\boldsymbol{k}=0$. In fact, these waves have zero frequency, as can be seen from the dispersion relation (2.3). The consequence of $\boldsymbol{c}_p\cdot\boldsymbol{c}_g=0$ is that inertial waves with $\boldsymbol{\Omega}\cdot\boldsymbol{k}\approx 0$ propagate energy at the maximal speed $2\Omega/k$, while the wave crests are stationary.

Now, there are strong consequences for the low-frequency waves with $\boldsymbol{\Omega}\cdot\boldsymbol{k}\approx 0$, and this may be seen from figure 2.2. This figure shows a localised disturbance in a rapidly rotating fluid that excites a spectrum of wavevectors. Energy is dispersed in all directions by inertial waves, but we focus on the two cases of energy propagated to the on-axis location A, and to the arbitrary off-axis location B. The energy propagated to location B is associated with only one wavevector, which is characterised by $\boldsymbol{\Omega}\cdot\boldsymbol{k}\neq 0$. This energy travels at a speed that is slower than $2\Omega/k$, by virtue of (2.5). Whereas, energy is propagated to the on-axis location A at the maximum possible speed $2\Omega/k$, and this energy is associated with the multitude of wavevectors that satisfy $\boldsymbol{\Omega}\cdot\boldsymbol{k}\approx 0$. The fact that the source typically has no preferred direction ensures that there is much greater energy associated with the wavevectors in the plane $\boldsymbol{\Omega}\cdot\boldsymbol{k}\approx 0$ than with some arbitrary $\boldsymbol{k}$. Thus, the energy is concentrated in the axially propagating waves. This unique behaviour—that low-frequency inertial waves are especially potent at distributing energy in the direction of the rotation axis—stems from the observation that $\boldsymbol{c}_g$ is perpendicular to $\boldsymbol{k}$ (Davidson, 2013*b*, pp. 389).

Let us now revisit the adjustment of the Taylor column in figure 2.1. As the object is slowly dragged across the bottom of the tank, low-frequency inertial waves are excited in the neighbouring fluid. These waves propagate kinetic energy through the column of fluid above the object at the maximum permissible speed $\sim\Omega\delta$ (where δ is the size of the object). It is through this process, the propagation of low-frequency inertial waves, that information is relayed to the fluid at the top of the tank. Of course, the wave fronts propagate until they reach the free surface, and leave behind the Taylor column. Thus, even though the Taylor-Proudman theorem presented in §1.1.2 assumes a quasi-steady state, the mechanism behind the transfer of information is inertial wave propagation.

Kinetic helicity is highly beneficial for dynamo action (see chapter 1), so it is interesting to explore the helicity of inertial waves (Moffatt, 1970). We substitute the ansatz $\boldsymbol{\omega}=\hat{\boldsymbol{\omega}}\exp[\mathrm{i}(\boldsymbol{k}\cdot\boldsymbol{x}-\varpi t)]$ into (2.1), and after substitution of the dispersion relation (2.3) we find

$$\hat{\boldsymbol{\omega}}=\mp k\hat{\boldsymbol{u}}\,. \tag{2.6}$$

Therefore, the velocity and vorticity vectors are aligned, and inertial waves have maximal kinetic helicity. This property of inertial waves frames them as a possible means of driving a dynamo in a rapidly rotating planetary core (Moffatt, 1978), where the Rossby number is small. Further, it can be shown that inertial waves propagate negative (positive) helicity above (below) their source (Davidson, 2014), as is required for the helical wave dynamo outlined in chapter 1.

The discussion so far has utilised plane-wave solutions of the linearised momentum equation to gain insight into the characteristics of inertial waves, but are these properties observed in practice? In a laboratory experiment or a numerical simulation, inertial wave packets are multi-chromatic, and nonlinear and viscous effects could influence the dispersion of energy and momentum. The ratio of nonlinear inertia to the Coriolis acceleration is described by the Rossby number, often defined as $Ro = u/2\Omega\ell_\perp$ in rotating turbulence experiments, where u is the root-mean-square (r.m.s.) of the fluctuating velocity field and $\ell_\perp$ is an integral length-scale perpendicular to the rotation axis. We will now briefly summarise some experiments and simulations of rotating turbulence.

2.2.2 Structure formation in rotating turbulence

As we have seen, inertial waves are the means by which Taylor columns initially form, and the focusing argument implies that low-frequency inertial waves will dominate the dispersion pattern (figure 2.2). The source of waves need not be the motion of a solid object; indeed, in rotating turbulence eddies can also excite inertial waves Davidson *et al.* (2006), and in the context of planetary cores buoyant anomalies provide a localised forcing (Davidson, 2014). In low Rossby number turbulence, one can imagine the continuous emission of inertial wave packets by eddies, which continually redistribute energy and momentum. As we have seen above, inertial waves are particularly efficacious in the dispersal of energy in the direction of the rotation vector, and this will shape the turbulence in a number of ways.

The experiments and simulations subject to strong rotation all reasonably agree on three observations:

1. The length-scale in the direction of the rotation vector grows to be substantially larger than the length-scales in the perpendicular directions. In other words, columnar structures are prevalent.

2. In decaying turbulence experiments, where the Rossby number is initially large and quickly falls to values $\lesssim 1$, elongated structures emerge at $Ro \sim 0.2 - 0.6$, and grow in time at a linear rate consistent with inertial wave propagation.

3. Strong rotation delays the decay of kinetic energy, in comparison to the non-rotating case.

The first of these may be understood in terms of low-frequency inertial wave propagation on the fast time-scale Ω^{-1} (Davidson *et al.*, 2006), as the second observation might suggest. However, there are a group of researchers who prefer a description on the nonlinear time-scale $\sim \ell_\perp/u$ (which is considerably larger than Ω^{-1} at low-Ro), that is built around the concept of *resonant triad interactions*. In some circumstances, these nonlinear interactions can allow a transfer of kinetic energy toward structures with large wavelengths in the direction of the rotation vector. We will not provide any detail on the theory of resonant triads, as they bare little relevance to the results presented in the later chapters, however we direct the curious reader to Godeferd & Moisy (2015).

Experiments

There were some impressive early experiments in rotating turbulence, however possibly the first to provide precise data were the experiments of Ibbetson & Tritton (1975). Their hot wire anemometry observations showed an increase in dissipation with rotation, and they speculated that this was linked to inertial wave propagation. In fact this increase was later attributed to viscous dissipation in the Ekman layers in their tank (Jacquin *et al.*, 1990). Importantly, Ibbetson & Tritton (1975) note an anisotropy in the direction of the rotation vector, quantified by a linear increase in the axial integral length-scale. In later experiments, Hopfinger *et al.* (1982) and Dickinson & Long (1983) generated flow visualisations, and they observed the spontaneous emergence of columnar vortices roughly aligned with the rotation axis. It will be important to note that in the oscillating grid experiments of Hopfinger *et al.* (1982), there are two distinct regions of the flow: a turbulent region at large Rossby number in the neighbourhood of the grid, and a region of elongated vortices where $Ro \lesssim 0.25$. Dickinson & Long (1983) also forced their flow with an oscillating grid, and they tracked a turbulent front as it advanced away from the grid. They find that for $Ro < 1$, the advancement of the front is consistent with the speed of low-frequency inertial waves. One problem with this experiment was that the grid itself may have been a greater source of inertial waves than the turbulent eddies, which questions the applicability of the results.

More recent experiments by Davidson *et al.* (2006) study a similar problem, however here an initial cloud of turbulence is created with a single stroke of the grid confined to the top of a rotating tank of water. To begin with, the turbulence has a large Rossby number, but this rapidly decreases due to viscous dissipation and an increase in the perpendicular length-scale. As the fluid motion decays, columnar structures emerge from

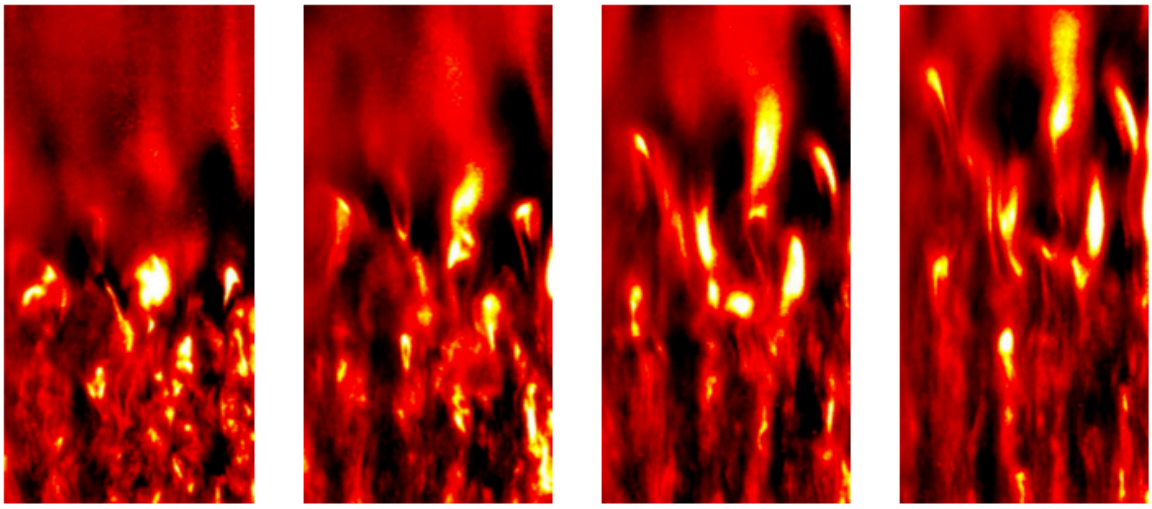

Fig. 2.3 Images from the inhomogeneous experiments of Davidson *et al.* (2006). A cloud of turbulence is created at the bottom of the rotating tank, which is left to decay. Time increases from left to right, where $\Omega t = 11.0$, 13.4, 15.9, 18.4. The initial Rossby number was ~ 2, which drops to $\lesssim 0.5$ at the times shown. The images are 30 cm x 60 cm.

the cloud of turbulence, and these structures can be seen in figure 2.3. The structures propagate through the quiescent fluid at a rate $\sim \Omega a$ (where a is the grid spacing), and elongate in the direction of the rotation vector. These observations are in line with low-frequency inertial wave propagation.

The experiments conducted by Davidson *et al.* (2006) are inhomogeneous, however Staplehurst *et al.* (2008) conducted homogeneous experiments of a similar style. Here, the entire tank is disturbed with a single grid stroke, and the $Ro \gtrsim 1$ turbulence is again left to decay under the influence of rotation. As the energy decays, and interestingly as Ro drops below ~ 0.4, columnar structures are seen to emerge (figure 2.4), whose axial growth is monitored by two-point vorticity correlations. The linear axial growth observed in the experiments is consistent with columnar structure formation by inertial wave propagation.

Simulations

In purely hydrodynamic direct numerical simulations (DNS) of decaying, statistically homogeneous, rotating turbulence, a number of authors have observed a similar change in flow morphology with varying Rossby number. For example, Baqui & Davidson (2015) performed DNS with an initial Rossby number ~ 1. The turbulence is unforced and so the kinetic energy rapidly decays, thus causing the Rossby number to fall. At the

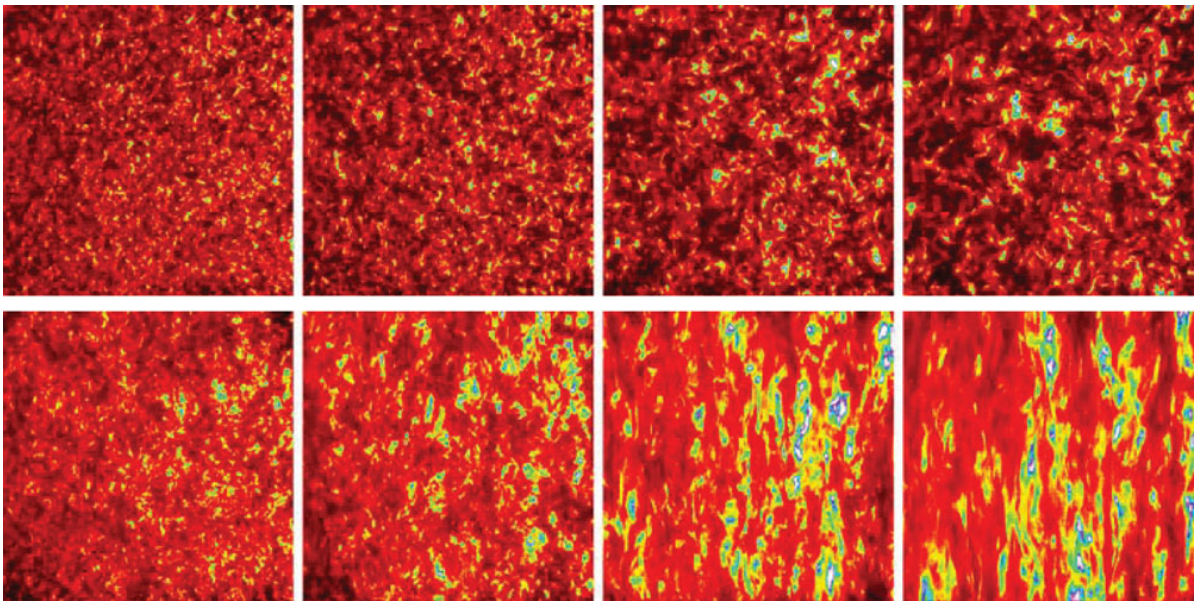

Fig. 2.4 Images from the homogeneous experiments of Staplehurst *et al.* (2008). The (top) bottom row is the (non-)rotating case and time increases from left to right.

time when $Ro \sim 0.4$, there is a rapid growth of the length scale parallel to the rotation vector, which grows linearly at the rate $\sim \Omega \ell_\perp$. In contrast, the perpendicular length scale $\ell_\perp$ remains approximately constant for the duration of the simulations. The linear increase in the axial length-scale is well described by internal inertial wave propagation. Note that the axial extension observed here occurs on a time-scale much shorter than the nonlinear time-scale. Thus, it is unlikely that nonlinear effects play a role. The inhomogeneous DNS of Ranjan & Davidson (2014) are initialised with a slab of turbulence in the centre of a periodic cube, and the box begins rotating so that the Rossby number is $\sim 0.1 - 0.5$. Columnar structures emerge from the slab of turbulence, akin to the laboratory experiments of Davidson *et al.* (2006), and the advancement of the front is consistent with the speed of low-frequency inertial waves based on the integral scale of the turbulence. The simulations are stopped when the wave packets reach the domain edge, to avoid error due to the periodicity. In the DNS, it is possible to calculate the point-wise kinetic helicity density, and this reveals that negative (positive) helicity is dispersed above (below) the initial turbulent slab. This observation is in line with the distribution of helicity by inertial wave propagation.

In buoyantly forced rotating turbulence we may expect inertial waves to be continually launched at the scale of the forcing, provided the Rossby number based on this length scale is small enough. In analogy to the numerical experiments initialised with a slab of turbulence, Davidson & Ranjan (2015) conducted Boussinesq rotating DNS initialised

with null velocities, but with a layer of buoyant anomalies confined to the vertical centre of the periodic cube. Inertial wave packets are emitted from the buoyant anomalies in a very similar way to their emission in the turbulence experiments, only now the speed of the wave packets is set by $\sim \Omega\delta$, where δ is the mean size of the anomalies which constitute the buoyant layer. The Rossby number is small, so the buoyancy field is advected a negligible amount at the time the wave packets reach the box edge. This time-scale separation is thought to be characteristic of the convection in Earth's outer core.

Inertial waves are helical waves (2.6), and they are an important source of helicity in a rotating fluid (Moffatt, 1978). Davidson & Ranjan (2015) find that even in their multi-chromatic simulations with finite Rossby and Ekman numbers, the kinetic helicity holds high relative values. The properties of monochromatic inertial waves appear to be approximately preserved in inertial wave packets (Ranjan, 2017).

2.3 Magnetic-Coriolis waves

In a planetary core, however, there often lies a dynamic magnetic field. The introduction of a mean magnetic field $\boldsymbol{B}_0$ modifies inertial waves into what we term magnetic-Coriolis (MC) waves, which encompasses a large variety of wave dynamics. The tension in the magnetic field allows waves to propagate along the field lines. The larger the field strength, the greater the tension and the higher the speed of the wave, analogous to the classic problem of waves on a taught string. We have reliable measurements of the radial component of the field at the CMB, applicable up to degree 13, and these yield an average field strength of 1 mT (Jackson & Finlay, 2015). Another method, which uses Earth's axial dipole moment to estimate the volume averaged axial field strength, results in a magnitude of 0.37 mT (Moffatt, 1978). Direct measurements of the internal field are impossible, and knowledge is particularly scarce for the azimuthal component of the field, as this component is confined to the core. However, slight variations in the length of day were interrogated in Gillet *et al.* (2010), and this led to an estimate of the internal cylindrical radial field of ~ 2 mT. They then used an argument based on isotropy to suggest an r.m.s. field strength of ~ 4 mT. These values are consistent with the theoretical arguments of Starchenko & Jones (2002). The scaling laws developed by Christensen & Aubert (2006) from their suite of simulations predict the slightly smaller value of 1.2 mT, however remember that the dynamo mechanism in many of the simulations may be unrealistic. Although there have been larger estimates for the azimuthal field strength, 5 mT (Zhang & Fearn, 1993, an upper bound) or even ~ 12 mT

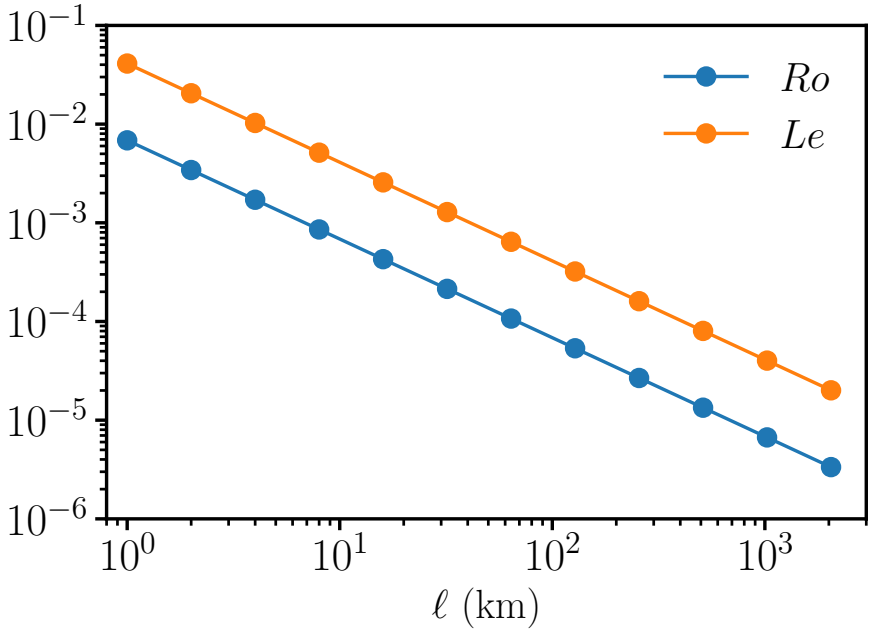

Fig. 2.5 Variation of Ro and Le with length-scale. Here we take $u \sim 0.5$ mm s^{-1}, $\tilde{B} \sim 3$ mT and $\rho \sim 11000$ kg m^{-3}.

(Hori *et al.*, 2015, to support slow QG waves), most modern estimates lie in the range 2–4 mT.

These estimates suggest that the components of Earth's field perpendicular to the rotation axis, and in the bulk of the core, are an order of magnitude larger than the volume averaged B_z. The Lehnert number reported in table 1.2 is inflated by a stronger field and a smaller length-scale, and figure 2.5 shows the variation of Le with length-scale where we have taken $\tilde{B} = 3$ mT. We argued in chapter 1 that scales with a magnetic Reynolds number $Rm \lesssim 1$ would be subject to intense magnetic diffusion, leading to an estimate for the small-scales of the dynamics on the order of $\ell \sim 10$ km. Figure 2.5 shows that at this scale $Le \approx 0.01$, indicating that axial low-frequency inertial wave packets transport energy much faster than the magnetic oscillations propagate along field lines. Also shown is the variation of Ro, where we take $u \sim 0.5$ mm s^{-1}. The fact that $Ro << 1$ for all scales (1 km $\leq \ell \leq$ 2000 km) suggests that inertial wave packets will freely propagate at Earth-like conditions, largely unhindered by advective motions. We now concentrate on the effects of a large-scale magnetic field on the propagation of inertial waves, motivated by small-scale disturbances in Earth's outer core. First we briefly discuss the magnetic oscillations in isolation, and build in the effect of rotation in §2.3.2.

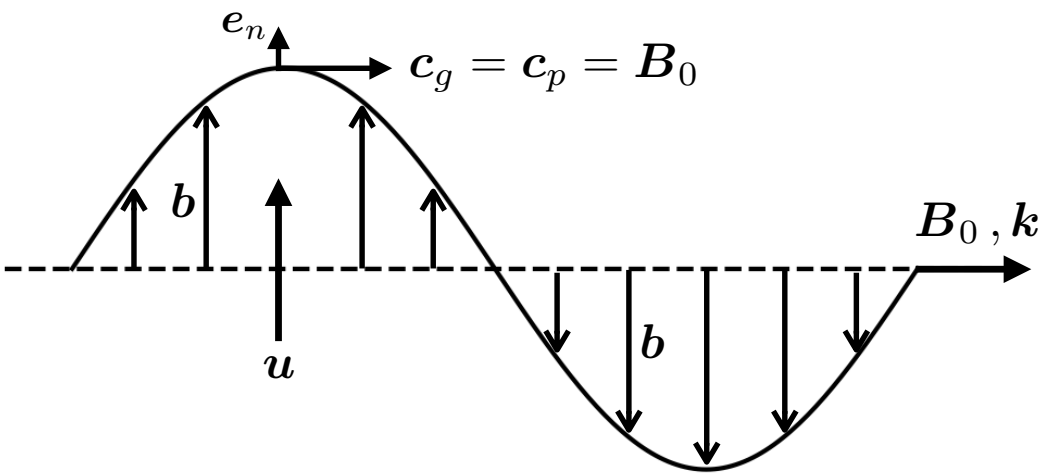

Fig. 2.6 An Alfvén wave is excited by the fluid motion $\boldsymbol{u}$ across the large-scale field $\boldsymbol{B}_0$; $\boldsymbol{b}$ is the perturbation to the large-scale field. The wave travels in the direction of $\boldsymbol{B}_0$ at the speed B_0.

2.3.1 Alfvén waves

First, we forgo rotation to examine the behaviour of waves due to the tension in magnetic field lines permeating a conducting fluid. These waves are called Alfvén waves (after Alfvén, 1942), and they are non-dispersive. The Lorentz force acts in two ways: when a field line is bent there is a restoring force similar to a taught string, and there is a pressure due to the magnetic field. We can write the (specific) Lorentz force as the sum of these two effects

$$(\boldsymbol{\nabla} \times \boldsymbol{B}) \times \boldsymbol{B} = (\boldsymbol{B} \cdot \boldsymbol{\nabla})\boldsymbol{B} + \boldsymbol{\nabla}\left(\frac{|\boldsymbol{B}|^2}{2}\right), \tag{2.7}$$

where the second term is the magnetic pressure which can be absorbed into a modified pressure term. The first term is due to the magnetic tension in the field lines, and can be written in field line coordinates s, n as

$$(\boldsymbol{B} \cdot \boldsymbol{\nabla})\boldsymbol{B} = \partial_s\left(\frac{|\boldsymbol{B}|^2}{2}\right)\boldsymbol{e}_s - \frac{|\boldsymbol{B}|^2}{R}\boldsymbol{e}_n\,, \tag{2.8}$$

where s is directed along the field line and n is normal to it, and R is the local radius of curvature of the field line. The first term is directed along the field line, and the second is normal to it and is proportional to the local curvature of the field line. Now, magnetic field lines are dragged by the fluid motion, and this is illustrated in figure 2.6. In this figure, $\boldsymbol{B}_0$ is the large-scale field, $\boldsymbol{u}$ is a localised flow and $\boldsymbol{b}$ is the magnetic perturbation

to $\boldsymbol{B}_0$. The flow pulls the field line upwards, bending it, and the tension in the magnetic field resists the motion. When the fluid parcel is arrested it is pulled downwards by the Lorentz force, inertia causes the parcel to overshoot its original position, and oscillatory motion follows.

These oscillatory perturbations in the velocity and magnetic fields are called Alfvén waves. The dispersion relation for Alfvén waves is (Moffatt, 1978)

$$\varpi = \boldsymbol{B}_0 \cdot \boldsymbol{k}\,, \tag{2.9}$$

and this results in an equal phase and group velocity

$$\boldsymbol{c}_p = \boldsymbol{c}_g = \pm \boldsymbol{B}_0\,. \tag{2.10}$$

So Alfvén waves travel parallel and anti-parallel to the large-scale magnetic field at the speed B_0[1]. The phase and group velocity do not depend on $\boldsymbol{k}$, so all disturbances excite waves of the same speed. Alfvén waves transport energy in equipartition, i.e. $|\boldsymbol{u}| = |\boldsymbol{b}|$, and they are characterised by maximal cross helicity $h_c = \boldsymbol{u} \cdot \boldsymbol{b}$. In the context of Earth's outer core, we expect Alfvén waves to traverse the core in approximately 3–4 years, so they are much slower than inertial waves. However, the effects of a large-scale magnetic field and background rotation are likely to act in concert in a planetary core, and the combined effects are considered in the next section.

2.3.2 MC wave theory

The combined effects of rotation and a background magnetic field may be explored through considering (2.1) with the addition of a mean magnetic field $\boldsymbol{B}_0$, coupled to the induction equation for the fluctuating field. The linearised diffusion-less equations removed from a localised disturbance are now

$$\partial_t \boldsymbol{b} = (\boldsymbol{B}_0 \cdot \boldsymbol{\nabla})\boldsymbol{u}\,, \qquad \partial_t \boldsymbol{\omega} = (\boldsymbol{B}_0 \cdot \boldsymbol{\nabla})\boldsymbol{j} + 2(\boldsymbol{\Omega} \cdot \boldsymbol{\nabla})\boldsymbol{u}\,, \tag{2.11}$$

$$\boldsymbol{\omega} = \boldsymbol{\nabla} \times \boldsymbol{u}\,, \qquad \boldsymbol{j} = \boldsymbol{\nabla} \times \boldsymbol{b}\,, \tag{2.12}$$

where $\boldsymbol{j}$ is the current density field, and all lower-case vectors are understood to be fluctuating fields. We also introduce a solenoidal vector potential through $\boldsymbol{\nabla} \times \boldsymbol{a} = \boldsymbol{b}$, $\boldsymbol{\nabla} \cdot \boldsymbol{a} = 0$, commonly referred to as the Coulomb gauge (Griffiths, 2014). These equations

[1] In this chapter, and for the remainder of the thesis, the magnetic field is in Alfvén units i.e. normalised by $\sqrt{\mu\rho}$.

combine to give the wave-like equation (Davidson, 2005, pp. 531)

$$\left[\frac{\partial^2}{\partial t^2} - (\boldsymbol{B}_0 \cdot \boldsymbol{\nabla})^2\right]^2 \boldsymbol{\nabla}^2 \boldsymbol{u} + 4(\boldsymbol{\Omega} \cdot \boldsymbol{\nabla})^2 \frac{\partial^2 \boldsymbol{u}}{\partial t^2} = \boldsymbol{0}\,. \tag{2.13}$$

We now apply the same machinery as in §2.2.1. If we apply the plane-wave ansatz $\boldsymbol{f} = \hat{\boldsymbol{f}} \exp[\mathrm{i}(\boldsymbol{k} \cdot \boldsymbol{x} - \varpi t)]$ (where $\boldsymbol{f} \sim \boldsymbol{u}\,, \boldsymbol{\omega}\,, \boldsymbol{a}\,, \boldsymbol{b}\,, \boldsymbol{j}$) to (2.13) we arrive at the relations

$$\hat{\boldsymbol{\omega}} = \mp k \hat{\boldsymbol{u}}\,, \qquad \hat{\boldsymbol{j}} = \mp k \hat{\boldsymbol{b}}\,, \qquad \hat{\boldsymbol{b}} = -\frac{\varpi_B}{\varpi} \hat{\boldsymbol{u}}\,, \qquad \hat{\boldsymbol{b}} = \mp k \hat{\boldsymbol{a}}\,, \tag{2.14}$$

and the dispersion relationship becomes

$$\varpi^2 \mp \varpi_I \varpi - \varpi_B^2 = 0\,, \tag{2.15}$$

where $\varpi_B = \boldsymbol{B}_0 \cdot \boldsymbol{k}$ and $\varpi_I = 2(\boldsymbol{\Omega} \cdot \boldsymbol{k})/k$ are the Alfvén and inertial wave frequencies (Davidson, 2013*b*, pp. 150). It is clear from (2.14) that all plane-wave solutions to (2.13) have maximal kinetic and magnetic helicity, $h_k = \boldsymbol{u} \cdot \boldsymbol{\omega}$ and $h_m = \boldsymbol{a} \cdot \boldsymbol{b}$ respectively, though this need not be true for a wave packet (Davidson & Ranjan, 2015). Further, as h_k is maximal irrespective of the presence of a mean field, this tells us that all monochromatic MC waves have an identical structure for the velocity field – a circularly polarised transverse wave (Moffatt, 1978).

The group velocity for these waves, acquired from (2.15), can be expressed in the form

$$\left[1 + \left(\frac{\varpi_B}{\varpi}\right)^2\right] \boldsymbol{c}_g = \frac{2\varpi_B}{\varpi} \boldsymbol{B}_0 + \boldsymbol{c}_{g_I}\,, \tag{2.16}$$

where $\boldsymbol{c}_{g_I} = \pm 2[\boldsymbol{k} \times (\boldsymbol{\Omega} \times \boldsymbol{k})]/k^3$ is the inertial wave group velocity (2.5). From (2.16), we see that energy with $\boldsymbol{k}$ perpendicular to $\boldsymbol{\Omega}$ is still focused onto the rotation axis (as it is for pure inertial waves), however we now have a component of the group velocity in the direction of the mean field.

In the rapidly rotating regime of Earth's outer core, the conventional wisdom states that on large-scales we might expect $\varpi_I \gg \varpi_B$, as suggested by the smallness of Le (figure 2.5). This assumption produces a splitting of the wave frequencies: $\varpi \approx |\varpi_I|$ and $\varpi \approx \varpi_B^2/|\varpi_I|$, and these two solutions correspond to very different wave types. The former corresponds to weakly modified off-axis inertial waves, which might traverse the core on a time-scale of weeks, and the latter to magnetostrophic waves, perturbations which predominantly migrate along the mean-field on a time-scale of centuries (Moffatt, 1978) (see the end members in figure 2.7). Due to their low frequencies and slow group velocities, magnetostrophic waves have been covered at length in the literature in efforts

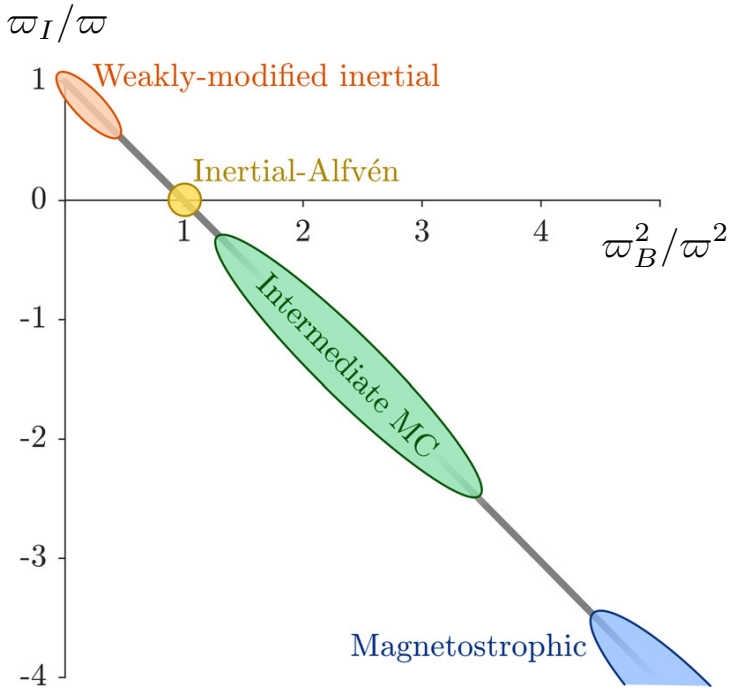

Fig. 2.7 The classes of waves derived from the MC wave dispersion relation (2.15); from Bardsley & Davidson (2017).

to explain the secular variation of the geomagnetic field (Hide, 1966; Malkus, 1967). In the general case, exactly how the energy is dispersed depends strongly on the orientation of $\boldsymbol{\Omega}$, $\boldsymbol{k}$, and $\boldsymbol{B}_0$. However, as it became clear for pure inertial waves, we might expect that there is a special role for those waves with $\boldsymbol{k}$ perpendicular to $\boldsymbol{\Omega}$. Indeed, this is a degenerate case for the magnetostrophic wave analysis (Bardsley & Davidson, 2016).

If we now look closer at the waves with $\boldsymbol{k} \cdot \boldsymbol{\Omega} \approx 0$, from (2.15) we find that their frequency matches the Alfvén frequency: $\varpi \approx \pm \varpi_B$. The leading order expression for the group velocity, for upward propagating waves, becomes

$$\boldsymbol{c}_g = \pm \boldsymbol{B}_0 + \frac{\boldsymbol{\Omega}}{k} \,. \tag{2.17}$$

We note there is an Alfvén-like propagation along magnetic field lines, and the wave-energy is propagated axially at half the speed of low-frequency inertial waves. These waves are termed Inertial-Alfvén (IA) waves, and were first highlighted by Bardsley & Davidson (2016) as a possible means of establishing quasi-geostrophy in planetary cores. The self-focusing property of pure inertial waves is passed over to IA waves in the presence of a mean magnetic field (with a component perpendicular to $\boldsymbol{\Omega}$), as all waves with $\boldsymbol{k} \cdot \boldsymbol{\Omega} \approx 0$, which may be initially launched as inertial waves, are converted to IA

waves as they feel the effects of the field. Any weakly modified inertial waves emitted must be off-axis waves, which have a lower energy density. From (2.14), all MC waves have maximal h_k, h_m and h_c, however IA waves propagate energy in equipartition i.e. $\boldsymbol{u}^2 = \boldsymbol{b}^2$. This is in contrast to weakly modified inertial waves that are characterised by maximal h_k, but $h_m \approx 0$, $h_c \approx 0$ and $\boldsymbol{b}^2/\boldsymbol{u}^2 \approx 0$, and slow magnetostrophic waves with maximal h_m, but $h_k \approx 0$, $h_c \approx 0$ and $\boldsymbol{u}^2/\boldsymbol{b}^2 \approx 0$. The wave types derived from the dispersion relation (2.15) are summarised in figure 2.7. Here, the 'intermediate MC' region characterises those wave packets which sit between the self-focusing IA waves and slow magnetostrophic waves. The dispersion properties of intermediate MC waves depend strongly on the ratio of the Alfvén and inertial frequencies – at Earth-like values of this ratio the intermediate waves predominantly radiate information along the direction of the rotation axis (Bardsley & Davidson, 2017). The properties of MC waves are summarised in table 2.1.

One final point arises from taking the dot product of (2.16) with $\boldsymbol{\Omega}$. Using (2.14), it can be shown that the segregation of h_k for pure inertial waves—negative (positive) above (below) the disturbance—extends to MC waves, only now h_m is segregated in exactly the same way. Evidently this is true for weakly modified inertial waves, magnetostrophic waves and IA waves alike. Cross helicity is maximal for IA waves, however there is no such segregation of h_c above/below the source, there is a left–right asymmetry which may be seen from (2.14) and the fact that the sign of ϖ_B depends on $\boldsymbol{B}_0 \cdot \boldsymbol{k}$.

Torsional oscillations

A class of Alfvén waves, thought to be important in Earth's core, are torsional oscillations. These waves are the oscillations of whole geostrophic cylinders, which ride on the cylindrical radial component of the field, and have been linked to changes in the length of day. Torsional Alfvén waves are thought to take approximately 3–4 years to traverse the core (Gillet *et al.*, 2010). Inertial-Alfvén waves provide a glimpse into the variety of Alfvén-like waves that could be present in Earth's core. They can propagate along the cylindrical radial or azimuthal field, and they are localised phenomena which may be excited by turbulent eddies or buoyant plumes within the chaotic convection. The fact that Le is small in Earth's core also indicates that IA waves are expected to be columnar, so along with inertial waves, they could contribute to the maintenance of quasi-geostrophy – a prerequisite for torsional waves.

Table 2.1 Properties of MC waves.

Wave	ϖ	$\boldsymbol{c}_g$	$\boldsymbol{c}_{g\Omega}$	$\boldsymbol{c}_{gB}$	$\boldsymbol{b}^2/\boldsymbol{u}^2$
Inertial	ϖ_I	$\approx 2\boldsymbol{\Omega}/k$	$2\boldsymbol{\Omega}/k$	0	0
Inertial-Alfvén	ϖ_B	$\boldsymbol{B_0} + \boldsymbol{\Omega}/k$	$\boldsymbol{\Omega}/k$	$\boldsymbol{B}_0$	1
Magnetostrophic	$\varpi_B^2/\lvert\varpi_I\rvert$	$\varpi\left[\frac{2\boldsymbol{B}_0}{\boldsymbol{B}_0\cdot\boldsymbol{k}} + \frac{\boldsymbol{k}\times(\boldsymbol{k}\times\boldsymbol{\Omega})}{k^2(\boldsymbol{k}\cdot\boldsymbol{\Omega})}\right]$	$\varpi\left[\frac{\boldsymbol{k}\times(\boldsymbol{k}\times\boldsymbol{\Omega})}{k^2(\boldsymbol{k}\cdot\boldsymbol{\Omega})}\right]$	$\varpi\left[\frac{2\boldsymbol{B}_0}{\boldsymbol{B}_0\cdot\boldsymbol{k}}\right]$	$\sim Le^{-2}$

Chapter 3

Numerical methods

The results presented in the following chapters are numerical solutions of idealised problems. This approach differs from analytical methods in that no terms in the given model are neglected, the full equations are solved and we try to push parameters toward the relevant physical regime. For example, to approach Earth's core conditions we wish to make the Ekman and Rossby numbers very small. All the simulations presented are forced by a buoyancy field, as is relevant to a planetary core, however we neglect any mean flows or boundary effects. The simulations in chapter 4 are purely hydrodynamic, whereas those in chapter 5 include the evolution of the magnetic field and the back-reaction due to the Lorentz force.

In §3.1 we introduce pseudospectral methods, the preferred numerical methods for fundamental investigations in fluid dynamics and MHD. The governing equations for the hydrodynamic simulations are given in §3.2, and relevant details of the numerical algorithm and resolution requirements are given. The code and set-up for rotating MHD is detailed in §3.3. (Additional details of the numerical algorithms for both codes are given in the appendix.) The generation of the initial conditions is reported in §3.4, where we introduce the 'buoyant blob' and 'buoyant cloud' fields (Davidson & Ranjan, 2015). Last, we present validation of the hydrodynamic and MHD codes in §3.5, utilising the analytical solutions given in Bardsley (2019).

3.1 Pseudospectral methods

Pseudospectral methods utilise spectral transforms to convert partial differential equations (PDEs) into ordinary differential equations (ODEs) in time for the coefficients of the transformed variables. The resulting ODEs may be integrated forward in time using well-established methods e.g. Runge-Kutta (Canuto, 1988). Pseudospectral methods

have been incredibly successful in the integration of equations encountered in geophysical and astrophysical fluid dynamics. Since the pioneering work of Orszag & Patterson Jr (1972), who solved the 3D Navier-Stokes equations in a periodic cube with 32 points in each dimension, turbulence simulations have rapidly increased in size. Indeed, Yeung *et al.* (2015) recently published a turbulence simulation with 8192 points in each direction, that is 5.5×10^{11} degrees of freedom. But, why do we need to push the limits of our computational resources?

For conventional turbulence, we have an estimate for the number of grid points in one dimension $\sim (L_{\rm box}/\ell)Re^{3/4}$ (Davidson, 2005). Thus, for a modest simulation at $Re = 1000$, with an integral length-scale ℓ ten times smaller than the box size $L_{\rm box}$, it is recommended that there are 1800 points in each direction. A simulation of this size requires a significant amount of resources even with modern computer architectures. The Reynolds numbers in industrial applications or in geophysics/astrophysics are routinely greater than 10^6, so to simulate reality is often impossible[1]. The Reynolds number is huge in Earth's core due to its size, but it is the Ekman number which is the most important for the numerical resolution of geodynamo simulations, as Ekman layers of thickness $E^{1/2}L$ are produced at the outer boundary. Roughly 10 radial grid points inside the boundary layer are necessary to safely resolve the dynamics, and at $E = 10^{-4}$ the layer is 1% of the shell thickness. For smaller Ekman numbers, the required spatial resolution becomes prohibitive, and enormous amounts CPU time are needed. Further, the time-step must be small enough to resolve the propagation of information by inertial waves, which have a group velocity $\sim \Omega/k$.

3.1.1 The Fourier transform

Spectral methods often use the spatial Fourier transform

$$\hat{\boldsymbol{u}}(\boldsymbol{k}) = \frac{1}{(2\pi)^3} \int \boldsymbol{u}(\boldsymbol{x}) \exp[-\mathrm{i}\, \boldsymbol{k}\cdot\boldsymbol{x}]\ \mathrm{d}^3\boldsymbol{x} \tag{3.1}$$

and its inverse

$$\boldsymbol{u}(\boldsymbol{x}) = \int \hat{\boldsymbol{u}}(\boldsymbol{k}) \exp[\mathrm{i}\, \boldsymbol{k}\cdot\boldsymbol{x}]\ \mathrm{d}^3\boldsymbol{k}\,. \tag{3.2}$$

Here, $\hat{\boldsymbol{u}}$ is the Fourier transform of the vector field $\boldsymbol{u}$. In practice the discrete Fourier transform (DFT) is used to perform the transforms, up to some desired level of truncation. In three-dimensional Cartesian space sampled by a uniform grid (as is the case in all the

[1] It was claimed at the recent WITGAF meeting in Cargèse that to simulate a star, you need the power output of a star!

simulations presented here) the discrete transforms are

$$\hat{\boldsymbol{u}}(k_x, k_y, k_z) = \frac{1}{N_x N_y N_z} \sum_{i=1}^{N_x} \sum_{j=1}^{N_y} \sum_{k=1}^{N_z} \boldsymbol{u}(i,j,k) \exp[-\mathrm{i}\, \boldsymbol{k} \cdot \boldsymbol{x}] \,, \tag{3.3}$$

$$\boldsymbol{u}(i,j,k) = \sum_{k_x=-N_x/2+1}^{N_x/2} \sum_{k_y=-N_y/2+1}^{N_y/2} \sum_{k_z=-N_z/2+1}^{N_z/2} \hat{\boldsymbol{u}}(k_x, k_y, k_z) \exp[\mathrm{i}\, \boldsymbol{k} \cdot \boldsymbol{x}] \,. \tag{3.4}$$

Here, $\boldsymbol{k}$ and $\boldsymbol{x}$ are now discrete grids and N_γ are the grid points in each direction, which need not be equal. To speed up the transforms the fast Fourier transform (FFT) is utilised. The number of operations necessary to complete a uni-directional DFT is $O(N^2)$, whereas the FFT achieves the equivalent result with a complexity of $O(N \log N)$. On our three-dimensional Cartesian grid this corresponds to a complexity of $O(N^3 \log N)$. For moderate values of N, the use of the FFT yields a significant saving.

It is readily shown that spatial differentiation in physical space relates to multiplication by $\mathrm{i}\boldsymbol{k}$ in wavenumber space, and this is how spatial derivatives are computed in a pseudospectral scheme. Note these relations for a scalar field ϕ and vector field $\boldsymbol{f}$ (operation in physical space $\rightarrow$ operation in $\boldsymbol{k}$-space)

$$\boldsymbol{\nabla}\phi \rightarrow \mathrm{i}\boldsymbol{k}\hat{\phi} \tag{3.5}$$

$$\boldsymbol{\nabla} \cdot \boldsymbol{f} \rightarrow \mathrm{i}\boldsymbol{k} \cdot \hat{\boldsymbol{f}} \tag{3.6}$$

$$\boldsymbol{\nabla} \times \boldsymbol{f} \rightarrow \mathrm{i}\boldsymbol{k} \times \hat{\boldsymbol{f}} \tag{3.7}$$

$$\boldsymbol{\nabla}^2 \boldsymbol{f} \rightarrow -|\boldsymbol{k}|^2 \hat{\boldsymbol{f}} \,. \tag{3.8}$$

These relations greatly simplify spatial differentiation, however to compute a quadratic nonlinear term in spectral space is very costly. This is due to the equivalence of multiplication in physical space and convolution in spectral space; sometimes termed the convolution theorem (Gubbins, 2004). Therefore, to reduce CPU time, nonlinear products are formed in physical space, then transformed back to $\boldsymbol{k}$-space to be differentiated by multiplication by $\mathrm{i}\boldsymbol{k}$. This method of multiple transforms is central to the success of pseudospectral methods, and has proved to be highly efficient for the numerical integration of nonlinear PDEs (Canuto, 1988; Fornberg, 1998).

3.1.2 Aliasing

The DFT and FFT are prone to aliasing error due to their discretisation (Gubbins, 2004), and this can be explained through a simple one-dimensional example. We are interested

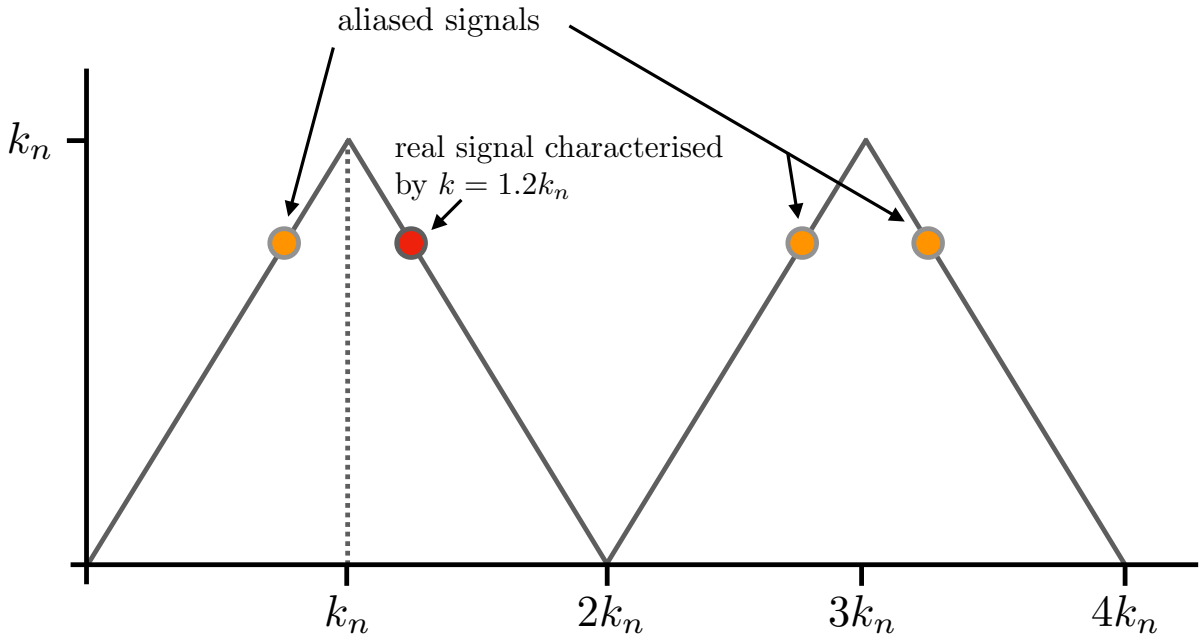

Fig. 3.1 Aliasing of a signal recorded with a Nyquist wavenumber k_n. The red dot marks the physical signal of interest and the orange dots highlight the aliased artefacts.

in a signal u whose continuous transform is $\hat{u}$. Suppose we now sample this signal on the interval $x_j = 2\pi j/N$ where $j = 1, \ldots, N$. The digitisation to form the discrete transform, denoted $\tilde{\hat{u}}_j$, yields the following result

$$\tilde{\hat{u}}_j = \hat{u}_j + \sum_{q \neq 0} \hat{u}_{j+qN} \,, \tag{3.9}$$

for integer q. The discrete transform is equal to the continuous one, plus unwanted artefacts from other wavenumbers. This introduces the spurious effect known as aliasing, which is a consequence of the fact that $\exp[\mathrm{i}jx]$ and $\exp[\mathrm{i}(j+qN)x]$ are indistinguishable when evaluated on x_j. This effect is illustrated in figure 3.1, where $k_n = 1/(2\Delta x)$ is the Nyquist wavenumber and Δx is the grid spacing. The Nyquist wavenumber represents the highest wavenumber a signal may contain that can be truthfully represented by the digitisation. The real signal contains information with a wavenumber slightly past k_n, and this can produce unwanted artefacts, both at low- and high-wavenumber, in the digitised signal. Examples of aliasing are commonly observed in digital photography and music production.

In the Navier-Stokes equations: linear terms do not couple modes of different wavenumber, so they cannot amplify energy with wavenumbers larger than k_n, however this is not true of nonlinear terms. The coupling of modes through the nonlinear term $(\boldsymbol{u} \cdot \boldsymbol{\nabla})\boldsymbol{u}$

is the source of the forward cascade of kinetic energy in conventional turbulence. It is known that an effective method to remove any error due to aliasing is the 2/3-rule, where the energy in all modes with $k > N/3$ is set to zero, so that the effective maximum wavenumber is $k_{\max} = N/3$ (Canuto, 1988). This procedure ensures that the error due to aliasing in the solution is zero.

We use two codes in this thesis: PSDNS (Yeung & Zhou, 1998, and others) for the hydrodynamic investigation in chapter 4, and GHOST (Gómez *et al.*, 2005) for the simulations with a mean magnetic field in chapter 5. The latter code, GHOST, uses the simple 2/3-rule, however PSDNS opts for a more complex dealiasing method in order to retain several more usable wavenumbers; this method is outlined in §3.2.

3.2 Rotating hydrodynamics (PSDNS)

Chapter 4 contains results obtained from rotating hydrodynamic simulations where the fluid motion is forced by a spatially localised buoyancy field (figure 3.2). The system is within the Boussinesq approximation, in which acoustic waves are filtered out the equations and the velocity field is divergence-free. Any density perturbations are only included in the buoyancy term, and are not taken into account elsewhere in the equations (Vallis, 2017, pp. 71). This is to say that density perturbations are small, yet the gravitational acceleration may be large. The rotating turbulence code was originally developed by Yeung & Zhou (1998), and buoyancy effects were later added by Maffioli (2012).

We set the rotation vector $\boldsymbol{\Omega} = \Omega \boldsymbol{e}_z$ and the gravitational acceleration $\mathbf{g} = \mathrm{g}\boldsymbol{e}_y$ so that they are orthogonal, an orientation which is reminiscent of the equatorial regions in a planetary core. The equations for a rotating Boussinesq fluid are

$$\partial_t \boldsymbol{u} + (\boldsymbol{u}\cdot\boldsymbol{\nabla})\boldsymbol{u} + 2\Omega(\boldsymbol{e}_z \times \boldsymbol{u}) = -\boldsymbol{\nabla} p + c\mathrm{g}\boldsymbol{e}_y + \nu\boldsymbol{\nabla}^2\boldsymbol{u}\,, \tag{3.10}$$

$$\partial_t c + (\boldsymbol{u}\cdot\boldsymbol{\nabla})c = \kappa\nabla^2 c\,, \tag{3.11}$$

$$\boldsymbol{\nabla}\cdot\boldsymbol{u} = 0\,. \tag{3.12}$$

Here $c = \rho'/\rho$ is the dimensionless density perturbation, κ is the diffusivity of the density perturbation and p is the pressure modified by the centrifugal acceleration.

The equations are solved using a pseudospectral method based on Rogallo's algorithm (Rogallo, 1981; Yeung & Zhou, 1998). The details of the algorithm are included in the appendix. The procedure results in a system of first-order ODEs in time, which are time-stepped using an order-2 Runge-Kutta predictor-corrector scheme. The computational

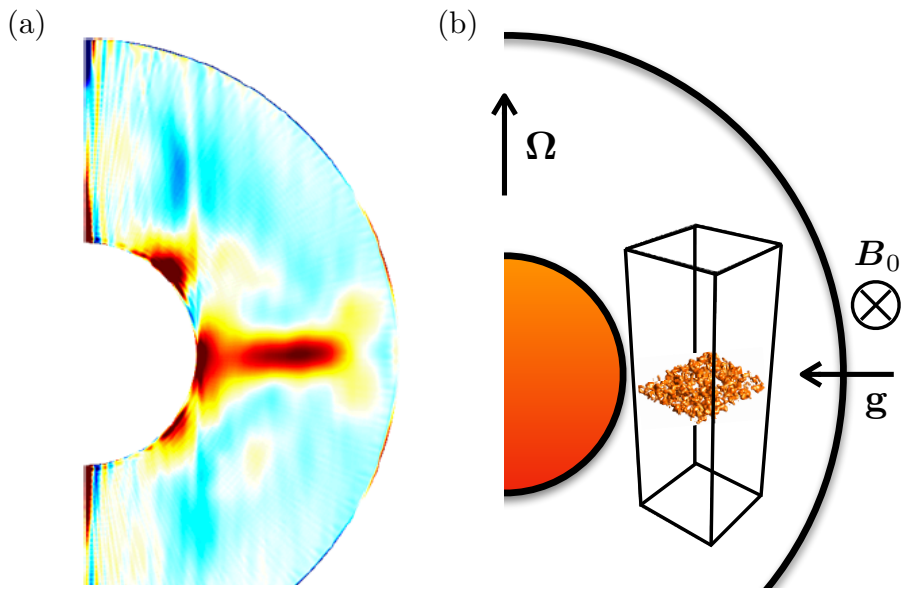

Fig. 3.2 The numerical set-up and its motivation. (a) An image from Sakuraba & Roberts (2009) showing an equatorially biased heat-flux. (b) We approximate the equatorial regions of a spherical shell with $\mathbf{\Omega} \perp \mathbf{g}$, and the equatorially biased heat-flux is modelled as a layer of buoyant anomalies. The large-scale azimuthal magnetic field $\boldsymbol{B}_0$ is included in §3.3.

domain is triply periodic, and is extended in the z-direction so that the box is three times taller than it is in the other two equal directions. The viscous and diffusive terms are integrated exactly by using integrating factors over a small time-step.

To ensure the stability of the time-stepping scheme, the code uses an adaptive time-step that satisfies the Courant-Friedrichs-Lewy (CFL) condition. The CFL condition states that information cannot propagate across a grid-cell at a larger speed than can be resolved by $\Delta x/\Delta t$, where Δt is the time-step. The condition on the time-step due to advection is

$$\Delta t_a = \frac{C\Delta x}{\max[|u_x| + |u_y| + |u_z|]}\,, \tag{3.13}$$

where $C \leq 1$ is the CFL number. The simulations are rapidly rotating, so we expect inertial waves to be present. This introduces another restriction on the time-step

$$\Delta t_w = \frac{C\Delta x}{|c_{gz}|}\,, \tag{3.14}$$

where c_{gz} is the group velocity of axially propagating inertial waves. The code advances in time according to the condition $\Delta t = \min[\Delta t_a, \Delta t_w]$. Note that the simulations are initialised with $\boldsymbol{u} = 0$, so for the first few time-steps the consideration of (3.14)

is particularly important. At low Rossby number we typically observe $\Delta t_w < \Delta t_a$, however as nonlinear inertia becomes more important more extreme velocity fluctuations are permitted, and Δt_a reduces. For the simulations in chapter 4 we typically use $C = 0.05 - 0.1$.

To reduce aliasing error, phase-shifts at each time-step are used in conjunction with a less restrictive truncation. Phase-shifting constitutes shifting the grid by an amount Δ_1, and evaluating the nonlinear terms on the shifted grid, then shifting the result back to the original grid. If the nonlinear terms are evaluated twice on two different grids such that $\Delta_2 - \Delta_1 = \Delta x/2$, a result that is alias-free may be obtained by summing the two evaluations (Rogallo, 1981). The code takes advantage of the two-stage time-stepping scheme to evaluate the shifted terms at each predictor and corrector step (though the solutions are slightly different at each substep). This results in a residual alias error on the same order as the uncertainty in the time-stepping scheme – $(\Delta t)^2$. In combination with the phase shifts, all wavenumbers with $|\boldsymbol{k}| > \sqrt{2}N/3$ are eliminated to properly ensure any spurious effects are removed (Orszag & Patterson Jr, 1972).

3.3 Rotating MHD (GHOST)

The results presented in chapter 5 are obtained from rotating MHD simulations with an imposed mean-field. The system is still Boussinesq, and the dynamics are forced by the buoyancy field, however there are now magnetic fluctuations instigated through the induction equation. The GHOST code[2] is a general framework for solving the PDEs associated with geophysical and astrophysical fluid dynamics, including hydrodynamics and MHD with and without rotation or buoyancy/stratification (Gómez *et al.*, 2005). The code is accurate and highly scalable up to 100,000 processing units (Mininni *et al.*, 2011).

The set-up is similar to as described in §3.2, however now we impose a uniform magnetic field $\boldsymbol{B}_0 = B_0\boldsymbol{e}_x$, which in our local approximation is analogous to a large-scale east-west field in a planetary core. The equations for momentum, the fluctuating field $\boldsymbol{b}$

[2]The Geophysical High-Order Suite for Turbulence (GHOST) is maintained by Pablo Mininni and Duane Rosenberg, and is available at https://github.com/pmininni/GHOST.

and the density perturbations are now

$$\partial_t \boldsymbol{u} + (\boldsymbol{u}\cdot\boldsymbol{\nabla})\boldsymbol{u} + 2\Omega(\boldsymbol{e}_z \times \boldsymbol{u}) = -\boldsymbol{\nabla}\Pi + B_0\partial_x\boldsymbol{b} + (\boldsymbol{b}\cdot\boldsymbol{\nabla})\boldsymbol{b} + cg\boldsymbol{e}_y + \nu\boldsymbol{\nabla}^2\boldsymbol{u}\,, \tag{3.15}$$

$$\partial_t \boldsymbol{b} + (\boldsymbol{u}\cdot\boldsymbol{\nabla})\boldsymbol{b} = (\boldsymbol{b}\cdot\boldsymbol{\nabla})\boldsymbol{u} + B_0\partial_x\boldsymbol{u} + \eta\boldsymbol{\nabla}^2\boldsymbol{b}\,, \tag{3.16}$$

$$\partial_t c + (\boldsymbol{u}\cdot\boldsymbol{\nabla})c = \kappa\nabla^2 c\,, \tag{3.17}$$

$$\boldsymbol{\nabla}\cdot\boldsymbol{u} = \boldsymbol{\nabla}\cdot\boldsymbol{b} = \boldsymbol{\nabla}\cdot\boldsymbol{a} = 0\,. \tag{3.18}$$

Here $\boldsymbol{b} = \boldsymbol{\nabla}\times\boldsymbol{a}$ and Π is the pressure modified by both the centrifugal acceleration and the magnetic pressure.

The equations are solved using the standard pseudospectral method, whereby nonlinear terms are calculated in physical space and differentiated in spectral space. The computational domain is the same as described in §3.2, and we use a similar 2nd-order Runge-Kutta time-stepping scheme. In GHOST the diffusive terms are evaluated explicitly, with no use of integrating factors. The details of the algorithm are included in the appendix.

To enforce the divergence-free condition on the magnetic field, the 'un-curled' version of the induction equation is solved for the vector potential

$$\partial_t\boldsymbol{a} = \boldsymbol{u}\times\boldsymbol{b} - \boldsymbol{\nabla}\phi + \eta\boldsymbol{\nabla}^2\boldsymbol{a}\,. \tag{3.19}$$

The gauge is chosen such that $\boldsymbol{\nabla}\cdot\boldsymbol{a} = 0$ (which implicitly sets ϕ) and this is easily enforced in $\boldsymbol{k}$-space. Recovering $\boldsymbol{b}$ from $\boldsymbol{a}$ does not introduce any extra computational effort as the nonlinear term in (3.19) is no longer differentiated. The GHOST code uses a constant timestep, and this is estimated through the consideration of wave speeds and advective velocities. In rotating MHD there are inertial waves, Alfvén waves and MC waves (chapter 2), however in our simulations the inertial waves are the fastest, as is thought to be relevant for Earth's core. Therefore, the timestep is still determined by the smaller of (3.13) and (3.14). The results in chapter 5 are in the rapidly rotating regime, so when the magnetic field is weak we have the balance

$$(\boldsymbol{\Omega}\cdot\boldsymbol{\nabla})\boldsymbol{u} \sim \boldsymbol{\nabla}c\times\mathbf{g}\,, \tag{3.20}$$

$$\frac{\Omega u}{\delta} \sim \frac{\mathrm{g}c}{\delta}\,, \tag{3.21}$$

$$u \sim \frac{\mathrm{g}c}{\Omega}\,. \tag{3.22}$$

This estimate guides our choice of timestep, coupled with lower resolution simulations to gauge the distribution of $|\boldsymbol{u}|$. Although, for the simulations in chapter 5 it is typical that $\Delta t_w < \Delta t_a$, and we generally have $C \approx 0.07$ (based on Δt_w).

3.4 Initial conditions

All the simulations presented in this thesis are forced by a localised buoyancy field, whether this field contains a single buoyant anomaly or a layer composed of many buoyant anomalies. The initial velocities and fluctuating magnetic field (in chapter 5) are null, and the prevailing dynamics are due to the conversion of potential energy in the buoyancy field into kinetic and/or magnetic energy. The isolated buoyant blob is a convenient simple case to test our understanding of the wave dynamics, whereas the buoyant cloud introduces more complexity, and perhaps may be seen as a stepping-stone toward the initiation of wave packets in a planetary core.

Our initial conditions are motivated by observations of an equatorially biased heat-flux in dynamo simulations, as explained in §1.1.4 (figure 1.6). Buoyant anomalies are concentrated in the equatorial regions, and a radial jet is sometimes observed, resulting in a greater source of waves at low-latitudes. The wave source, as evidenced in figure 1.7, is not large-scale nor smooth; it comprises multiple buoyant blobs of varying sizes and it has a characteristic time-scale that is much longer than the typical time-scale of the wave packets it emits.

3.4.1 Buoyant blob

The buoyant blob initial condition is a single spherical blob with a Gaussian radial profile

$$c\left(\boldsymbol{x}, 0\right) \sim \exp\left[-|\boldsymbol{x}|^2/\delta^2\right] , \tag{3.23}$$

where $\boldsymbol{x}$ is the position vector (whose origin is at the box centre) and δ is the blob size. The blob size is kept much smaller than the box side-length in the horizontal directions L_{box} – we set $L_{\text{box}}/\delta = 50$. The amplitude of the buoyant blob may be tuned in order to set the desired Reynolds and Rossby numbers.

3.4.2 Buoyant cloud

The buoyant cloud initial condition comprises many buoyant blobs similar to the one defined in (3.23). However, for the buoyant cloud we wish to vary the blob positions and

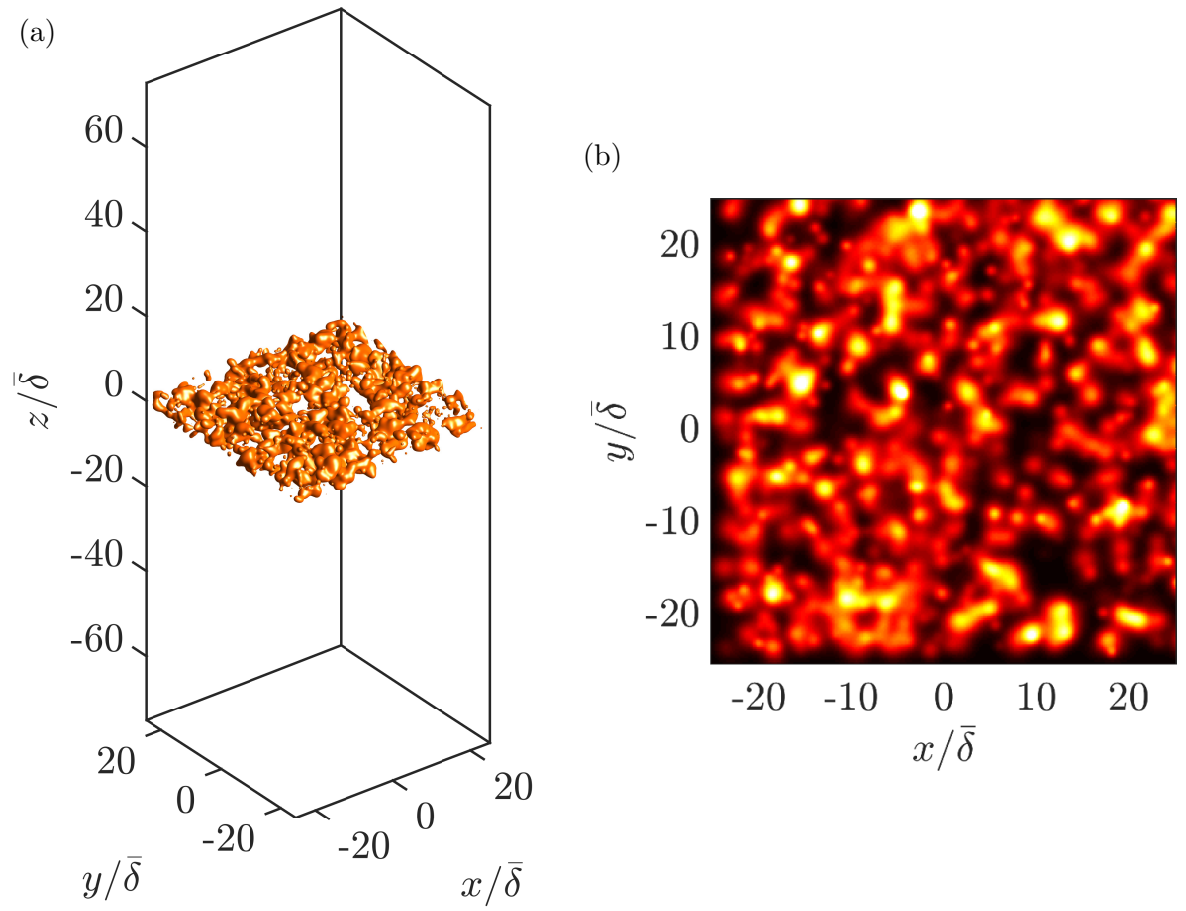

Fig. 3.3 Buoyant cloud initial condition: (a) 3D rendering showing the full extent of the domain (b) the slice at $z = 0$.

sizes. This is accomplished through the field

$$c(\boldsymbol{x}, 0) \sim \sum_{n_b} \exp\left[-\left((x - X_i)^2 + (y - Y_i)^2 + (z - Z_i)^2\right)/\delta_i^2\right], \tag{3.24}$$

where n_b is the number of blobs, (X_i, Y_i, Z_i) defines the blob centre and δ_i is the blob size. The blob sizes are randomly chosen from the uniform distribution $\delta_i/2 \leq \bar{\delta} \leq 3\delta_i/2$, where $\bar{\delta} = L_{\text{box}}/50$ is the mean blob size. The positions are also uniformly distributed: X_i and Y_i are chosen from the full box width, whereas Z_i is restricted to the layer $|z| < 3\bar{\delta}$.

The resulting buoyancy field (with $n_b = 2000$) is shown in figure 3.3, where (a) is a 3D rendering showing the full computational domain and (b) highlights the slice through the mid-plane. The result is a random and varied buoyancy field, localised about the mid-plane of the box. The choice $n_b = 2000$ corresponds to a filling factor of roughly 50 %, and this was found to be sufficient to preserve the blob-scale, yet provide adequate

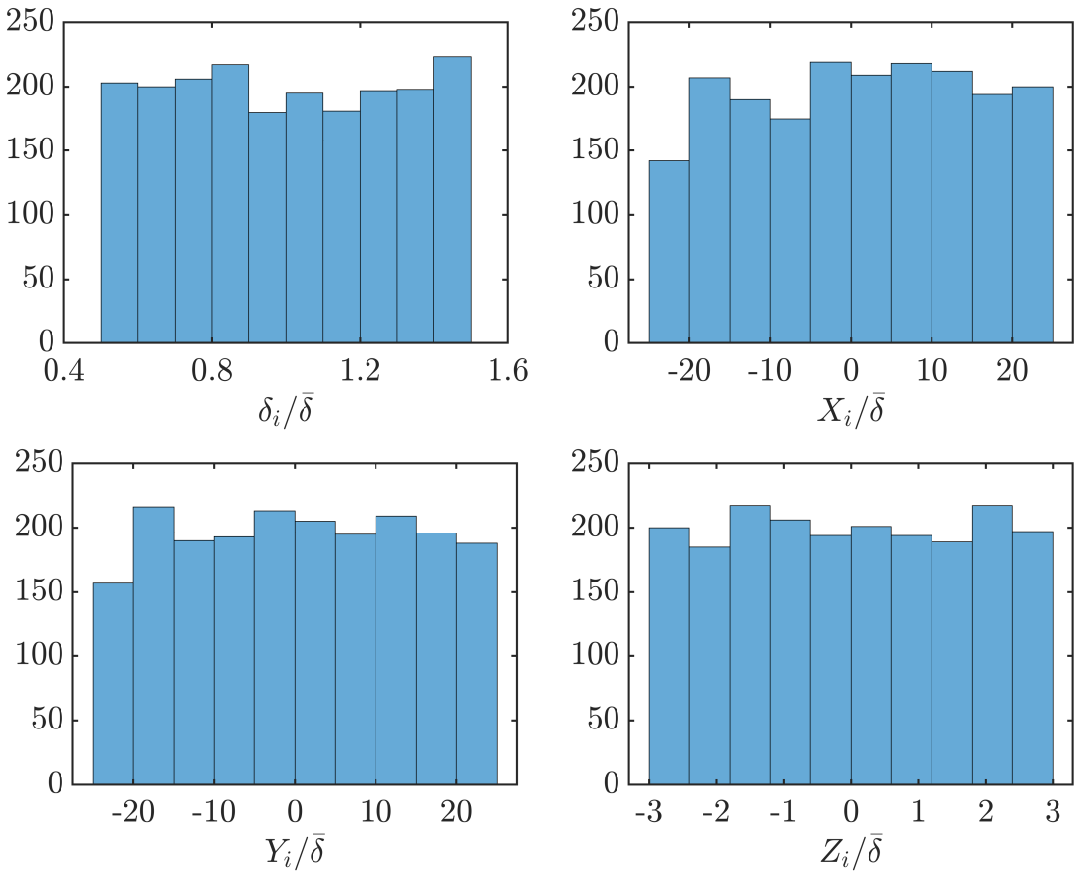

Fig. 3.4 Histograms of the blob positions (X_i, Y_i, Z_i) and sizes δ_i for the buoyant cloud initial condition.

homogeneity in the horizontal plane (Ranjan, 2015). Histograms of the blob positions and sizes are shown in figure 3.4; the distributions are reasonably uniform. We note that if $\bar{\delta} = 10$ km, then the total box height would correspond to 1500 km, providing a comparison to Earth's core.

3.5 Validation

For both PSDNS and GHOST, a hydrodynamic Taylor-Green vortex test case was calculated at $Re = 100$. The resulting r.m.s. velocity and the r.m.s. viscous dissipation were within 1% of accepted solutions in the literature (Brachet *et al.*, 1983). A corresponding 'magnetic Taylor-Green vortex' solution was computed for GHOST at $Re = Rm = 100$. The r.m.s. velocity and magnetic field fluctuations were in line with reports in the literature (Pouquet *et al.*, 2010).

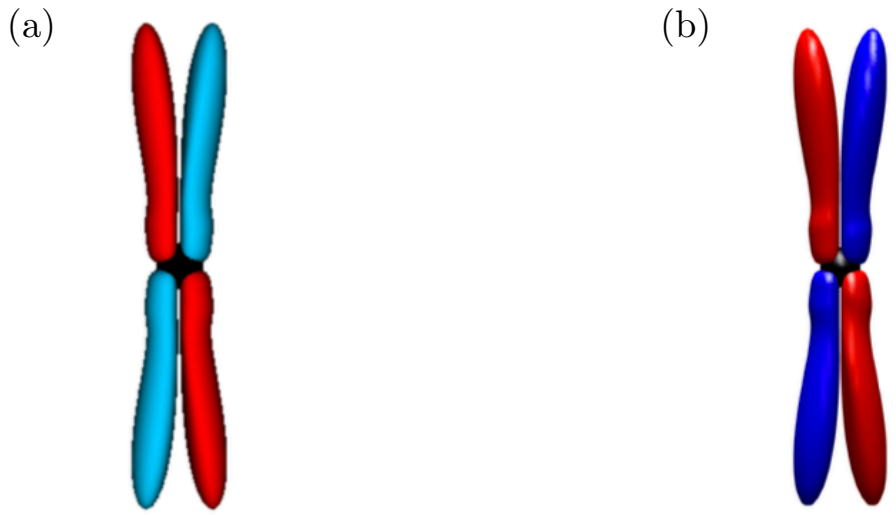

Fig. 3.5 Axial velocity induced by a buoyant blob (a) simulation at $Ro \approx 0.01$ and (b) analytical solution at $Ro \to 0$, both at $\Omega t = 8$. Gravity acts into the page and rotation is vertical. Analytical solution courtesy of Bardsley (2019). The colours used for rendering the two objects are not the same.

Hydrodynamics

To validate the rotating hydrodynamics code (PSDNS), we compare the numerical solution of the buoyant blob problem at $Ro \approx 0.01$ with an inviscid analytical solution at $Ro \to 0$ (Bardsley, 2019). The initial condition is a single buoyant blob at the origin, as described in §3.4.1, and all velocities are null. The diffusivities are equal and small, and the Ekman number $E = \nu/2\Omega\delta^2 \approx 10^{-4}$. The axial velocity at $\Omega t = 8$ is shown in figure 3.5 for both the simulation and for the analytical solution, and the comparison is very favourable. Moreover, figure 3.6 shows the comparison of a buoyant cloud simulation in a periodic cube with an inviscid analytical solution at $Ro \to 0$. The middle row shows axial velocity and the bottom row shows isosurfaces of u_z^2 coloured by kinetic helicity; again, there is a good comparison. It was shown in chapter 2 that inertial waves propagate negative (positive) kinetic helicity above (below) their source, and this is verified by the DNS.

MHD

Another diffusionless analytical solution[3] at $Ro \to 0$ is employed in the validation of the rotating MHD code (GHOST). Gravity and rotation remain perpendicular, with

[3]Detailed solutions of the diffusionless equations at $Ro \to 0$ are given in Bardsley (2019).

the addition of a mutually orthogonal uniform imposed magnetic field $B_0\boldsymbol{e}_x$ (as detailed in §3.3). Both the analytical solution and the simulation have a Lehnert number $Le = B_0/\Omega\delta = 0.1$, and the DNS uses small and equal diffusivities. A comparison is shown in figures 3.7 & 3.8 where the components of $\boldsymbol{u}$ and $\boldsymbol{b}$ are illustrated in the plane $y = 0$ at $\Omega t = 30$ (the subsection [0,15]x[0.60] is shown for clarity). The analytical solution and the DNS match very well.

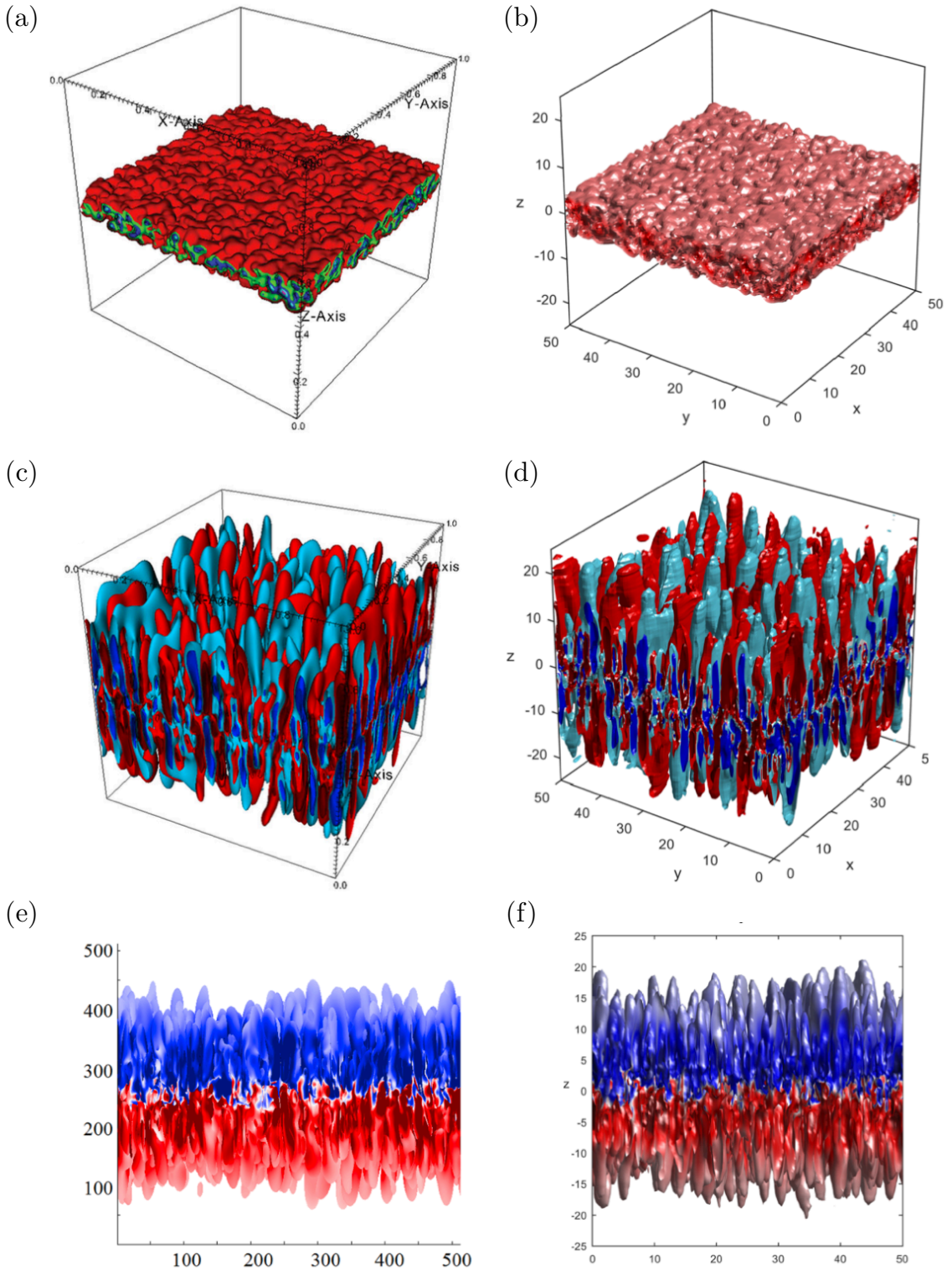

Fig. 3.6 Comparison of a buoyant cloud simulation at $Ro \approx 0.01$ (Davidson & Ranjan, 2015) (a,c,e) and the analytical solution at $Ro \to 0$ (b,d,f), both at $\Omega t = 10$. (a,b) the buoyancy field, (c,d) isosurfaces of axial velocity, (e,f) isosurfaces of u_z^2 coloured by kinetic helicity (red positive, blue negative). Analytical solution courtesy of Bardsley (2019).

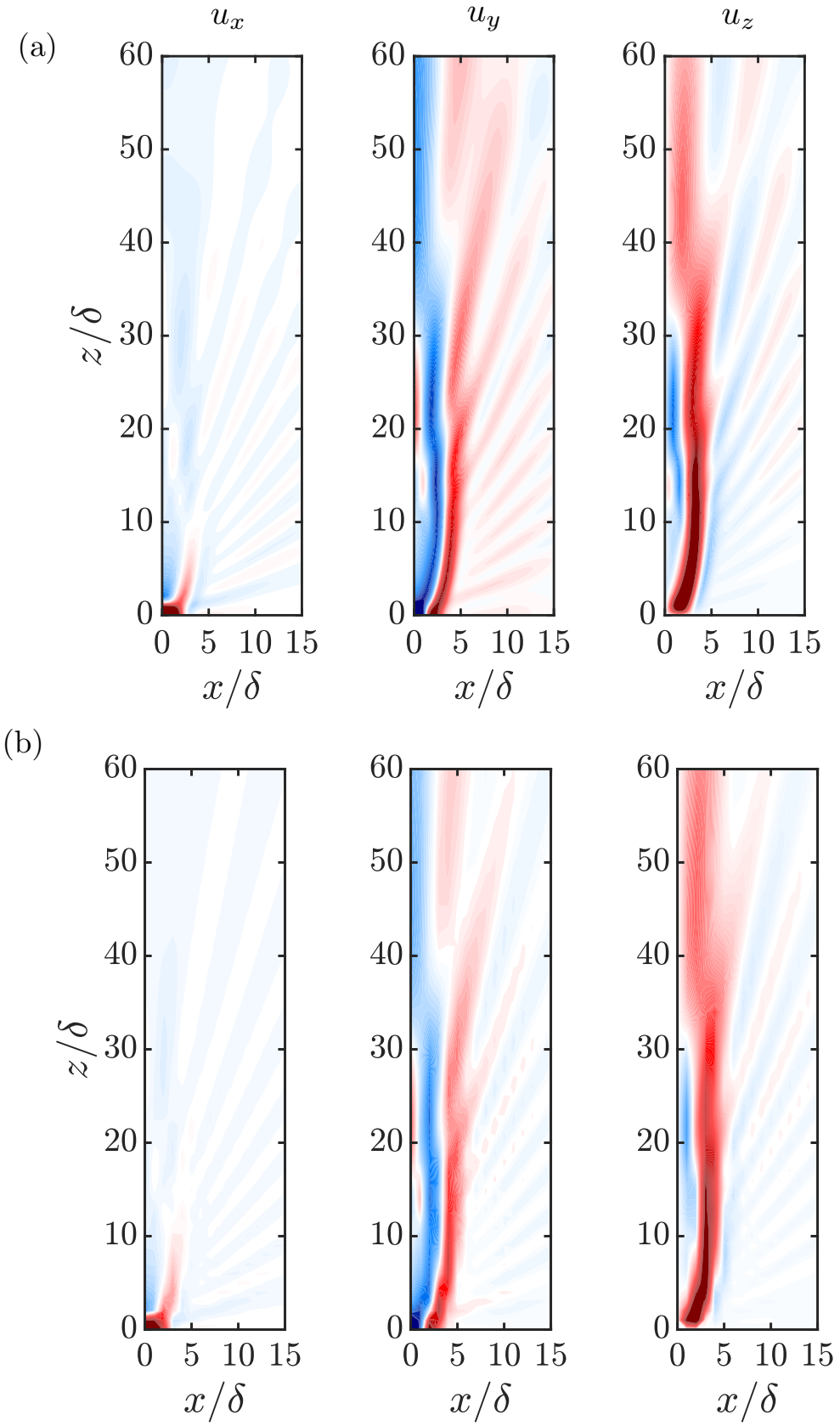

Fig. 3.7 Comparison of a buoyant blob (a) simulation at $Ro \approx 0.01$ with (b) the analytical solution at $Ro \to 0$, both at $Le = 0.1$ and $\Omega t = 30$. The three components of velocity are shown from left to right, in the plane $y = 0$. Analytical solution courtesy of Bardsley (2019).

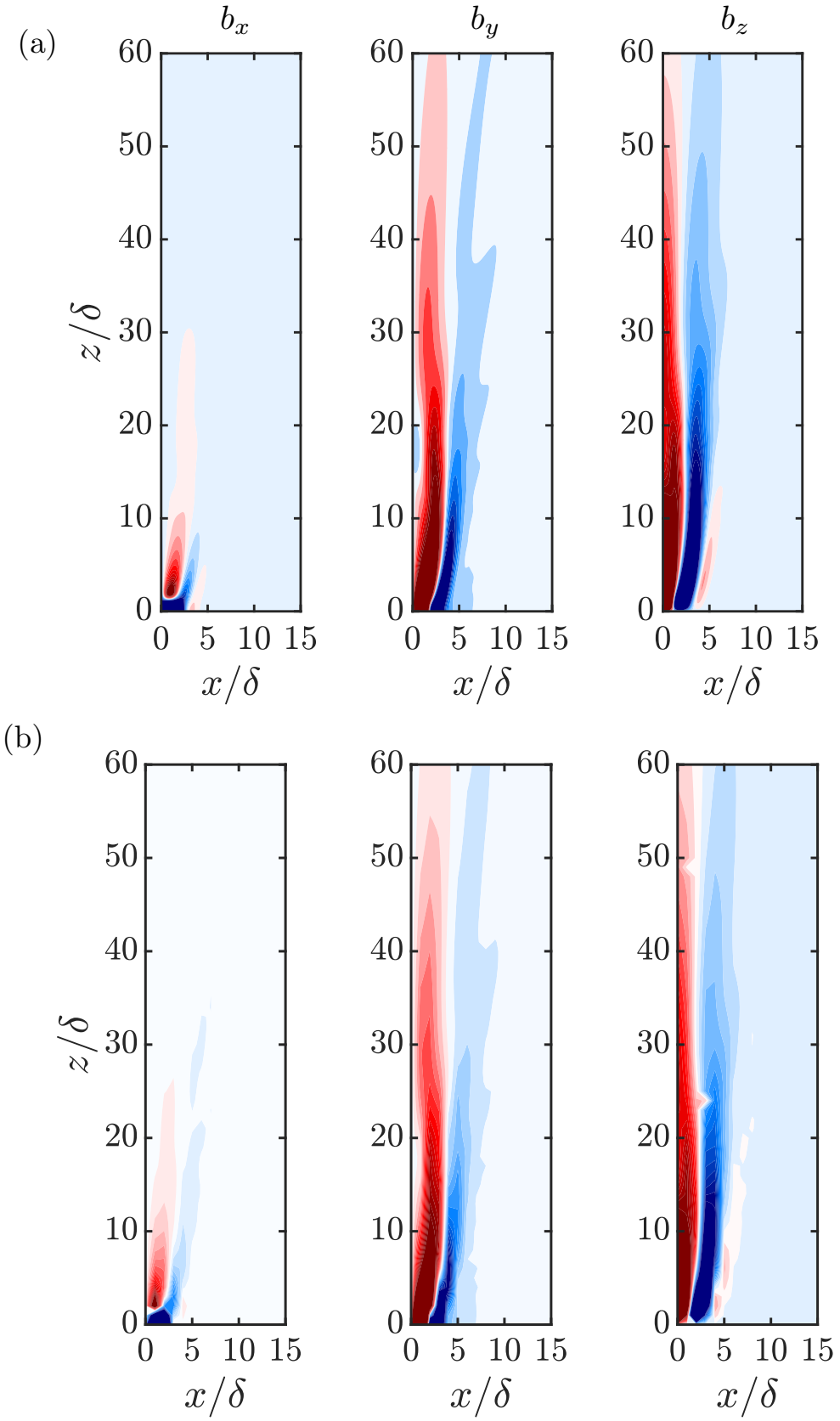

Fig. 3.8 The same as in figure 3.7, but showing the three fluctuating components of the magnetic field.

3.6 Numerical parameters

Hydrodynamics

The numerical parameters for simulations R1–6 presented in chapter 4 (table 3.1). All simulations were computed on a Cartesian grid with $N_x = N_y = 256$ and $N_z = 768$. The viscosity and thermal diffusivity are $\nu = \kappa = 10^{-4}$ so that the Prandtl number $Pr = 1$. On 64 Intel Skylake processing cores, the simulations take from 2 hours (R1) to 7 hours (R6).

Table 3.1 Numerical parameters for the simulations presented in chapter 4. The timestep Δt here is an average over the simulation, as PSDNS uses an adaptive timestep.

Simulation	$\bar{b}$	Ω	Δt
R1	0.077	8.0	4.5×10^{-4}
R2	0.501	7.0	2.3×10^{-4}
R3	0.501	5.0	2.0×10^{-4}
R4	0.501	4.0	2.0×10^{-4}
R5	0.501	3.5	1.9×10^{-4}
R6	0.501	3.0	1.6×10^{-4}

MHD

The numerical parameters for simulations S1–6 presented in chapter 5 (table 3.2). The timestep here is constant: $\Delta t = 1.0 \times 10^{-4}$, and the Cartesian numerical grid has $N_x = N_y = 512$ and $N_z = 1024$. The viscosity, thermal diffusivity and magnetic diffusivity are $\nu = \kappa = \eta = 10^{-4}$, so that $Pr = Pm = 1$. On 128 Intel Skylake processing cores, the simulations take 12 hours to run for 40 Ωt.

Table 3.2 Numerical parameters for the simulations presented in chapter 5.

Simulation	$\bar{b}$	Ω	B_0
S1	0.077	10.0	1.25×10^{-8}
S2	0.077	10.0	0.0125
S3	0.077	10.0	0.0625
S4	0.077	10.0	0.125
S5	0.077	10.0	0.250
S6	0.077	10.0	0.625

Chapter 4

The influence of nonlinear inertia on inertial waves

In this chapter, which covers work published in McDermott & Davidson (2019), we address the influence of nonlinear inertia on the propagation of inertial wave packets. In Earth's core the Rossby number is small at all conceivable convective scales, however this is not true of many of the dynamo simulations. In some of the simulations with a more intense buoyant forcing, nonlinear inertia becomes as important as the Coriolis acceleration at the scale of the convective structures. Robust columnar structures at low Rossby number are broken down when nonlinear inertia is influential, and we suggest from the evidence given in chapter 2 that this is due to the fact that inertial waves cannot propagate when $Ro = u/2\Omega\ell_\perp \gtrsim 0.2 - 0.6$.

In geodynamo simulations, the columnar flow structures are thought to organise the magnetic field into a strongly dipolar state. For stronger forcing, the loss of columnar structures in the velocity field inevitably results in the disorganisation of the magnetic field. The curious link between the suppression of inertial waves at $Ro \sim 0.4$ and the transition in flow and magnetic field morphology in dynamo simulations motivates the work presented in this chapter. We first set the scene here, then briefly review the relevant literature from geodynamo simulations and from rotating turbulence (some of which is discussed in chapter 2) in §4.1. The results from six simulations of increasing Rossby number are presented in §4.2, where we inspect the flow morphology, length-scales, velocity magnitude, helicity, and finally Ro. We discuss and interpret our results in §4.3.

4.1 Literature review

The morphology of the flow in Earth's outer core and its magnetic field are thought to be intimately related. Columnar flow outside the TC usually results in a predominantly dipolar field, as evidenced from geodynamo simulations (Roberts & King, 2013). The convection columns assume the form of alternating cyclones and anti-cyclones, and carry a large degree of kinetic helicity $\boldsymbol{u} \cdot \boldsymbol{\omega}$ (Sreenivasan & Jones, 2011).

4.1.1 An observed dipole-multipole transition in numerical dynamos

Simulations attempting to mimic the geodynamo have been surprisingly successful, in the sense that many of the published simulations produce large scale magnetic fields which are predominantly dipolar. However, an abrupt transition between dipolar and multi-polar dynamos has been observed in many numerical datasets of spherical shell MHD convection, that appears to be robust with respect to boundary conditions or the source of convection.

The transition was initially reported by Kutzner & Christensen (2002) for convection driven dynamos in a spherical shell. In these numerical experiments the Ekman number is $E \sim 10^{-3} - 10^{-4}$ while the largest Rayleigh number is $Ra \approx 40 Ra_c$, where Ra_c is the critical Rayleigh number at which hydrodynamic convection first appears. Two distinct regimes of convection and magnetic field configuration were observed. When the buoyant forcing is supercritical but relatively weak, there is stable columnar convection, the magnetic field has a large dipolarity (as defined below), and there are no polarity reversals. However, when the convection is forced more strongly—for the same Ekman number—the flow becomes strongly three-dimensional and the dipole quickly breaks down. Thermal and compositional convection were considered in this work, with a variety of boundary conditions, and no dependence was found on the type of convective driving.

With a suite of numerical experiments, Christensen & Aubert (2006) showed that the transition persists for more highly forced simulations. They made the link to a *local* Rossby number defined as $Ro_\ell = Ro(\bar{n}/\pi)$, where the *global* scale Rossby number is $Ro = u/2\Omega L$ and $\bar{n}$ is the mean spherical harmonic degree in the time-averaged kinetic energy spectrum (which is a dimensionless wavelength on spherical surfaces). The local Rossby number attempts to measure the ratio of inertial to Coriolis forces at the scale of the columnar convection. Stable columnar convection and dipolar magnetic fields were found for $Ro_\ell \lesssim 0.1$, whereas columnarity is lost and multi-polar fields dominate for $Ro_\ell \gtrsim 0.1$.

For a series of MHD and purely hydrodynamic spherical shell simulations (driven by a temperature difference), Soderlund *et al.* (2012) (see also the corrigendum, Soderlund *et al.*, 2014) observe a similar transition at $Ro_\ell = Ro(\bar{k}/\pi) \sim 0.1$. Here $\bar{k} = (\bar{n}^2 + \bar{m}^2)^{1/2}$, where $\bar{m}$ is the mean spherical harmonic order in the time-averaged kinetic energy spectrum. The transition at $Ro_\ell \sim 0.1$ occurs when there is a reduction in the helicity of the flow. The change in helicity is found to be independent of magnetic field strength, suggesting that there is a purely hydrodynamic mechanism behind the transition in flow structure and hence magnetic field morphology. Further, the three-dimensional convection observed for the more strongly forced simulations approximately follows the non-rotating, non-magnetic, turbulent convection scaling $Re \sim Ra^{1/2}$ (Sano *et al.*, 1989), suggesting that in this regime rotation and magnetic fields do not strongly influence the flow.

Using the given values of Re, E, and $\bar{k}$ (Soderlund, 2011), we have calculated the local Rossby number for this dataset. Figure 4.1a shows the local Rossby number dependence of dipolarity f_d, the ratio of the energy in the dipole coefficients of the magnetic field to the energy in the full magnetic spectrum at the outer boundary. Also shown is the average relative axial helicity H_z (using the corrected data from Soderlund *et al.*, 2014). This is calculated as $H_z = \langle u_z \omega_z \rangle / (\langle |u_z|^2 \rangle \langle |\omega_z|^2 \rangle)^{1/2}$, where the angle brackets denote averaging over a hemisphere, as the helicity distribution tends to be antisymmetric across the equatorial plane for the rapidly rotating simulations. An abrupt decrease in the average relative axial helicity is found to correlate well with the loss of dipolarity of the magnetic field. The decrease in axial helicity is attributed to increases in thermal forcing, which causes the flow to lose its columnar structure, as measured by the columnarity (defined below).

It is noted in Soderlund *et al.* (2012) that the columnarity of the flow decreases less sharply than the dipolarity and axial helicity (figure 4.1b), however, there remains a clear correlation between all three measures. Besides, the columnarity measure introduced by Soderlund *et al.* (2012) is somewhat arbitrary, and their regime boundary between columnar and non-columnar flow is chosen on a visual basis. Moreover, they calculate the dipolarity of the magnetic field as a ratio of the energy in the dipole components to the full magnetic spectrum, where authors in the past have only integrated to a degree of $n = 12$ (Christensen & Aubert, 2006). This choice will weakly affect the value of dipolarity for strongly dipolar magnetic fields (with a steep magnetic spectrum). However, once small magnetic scales are excited in the multi-polar dynamos (with a broader magnetic spectrum), this choice will exaggerate the decrease in dipolarity. Given these concerns, we conjecture that the transition in flow and magnetic field morphology

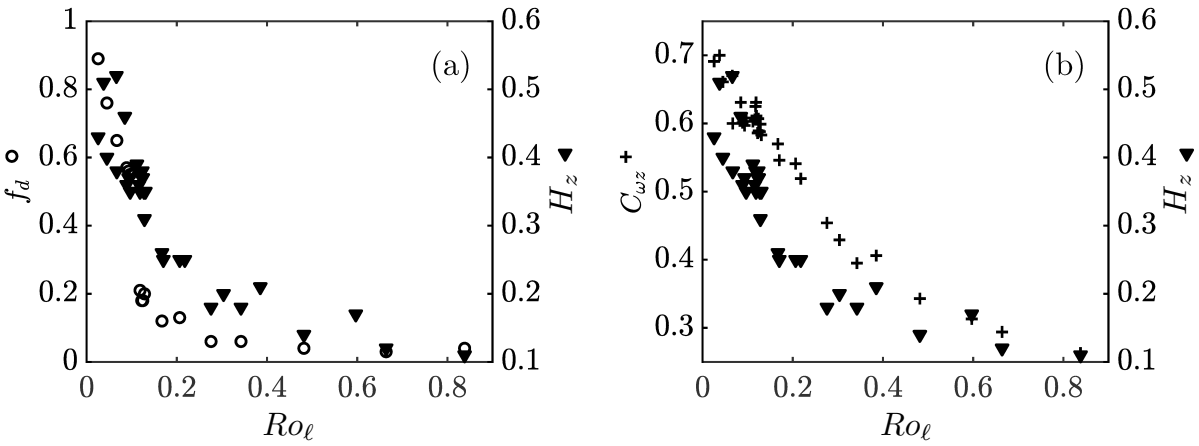

Fig. 4.1 Data from Soderlund *et al.* (2012) and Soderlund *et al.* (2014) as a function of local Rossby number. The symbol for each quantity is shown above the corresponding axis label. (a) Dipolarity and relative axial helicity. (b) Columnarity and relative axial helicity.

are closely linked, and we seek an explanation for the correlation between columnarity, relative helicity and dipolarity.

In summary, as the forcing is increased, inertia becomes more significant in the force balance. The length scale at which inertial effects are in contention with the effects of global rotation shifts into the energy-containing scales. This causes a loss of columnar structures and flow helicity, which results in the dipole collapse (Christensen & Aubert, 2006; Dormy *et al.*, 2018; Soderlund *et al.*, 2012). This chapter addresses the question: what mechanism causes the transition from columnar to three-dimensional flow?

Flow in Earth's core is often characterised by $Ro = u/2\Omega\ell \approx 10^{-6} - 10^{-3}$, using the estimates $\ell \sim 1 - 10^3$ km and $u \sim 5$ mm s^{-1} (chapter 2). Now it is observed in the purely hydrodynamic literature that inertial waves can propagate when $Ro \lesssim 0.1$ (Baqui & Davidson, 2015; Sreenivasan & Davidson, 2008; Yarom & Sharon, 2014). Moreover, such waves are responsible for the initial formation of columnar vortices in a rapidly rotating fluid (Ranjan & Davidson, 2014; Staplehurst *et al.*, 2008). It might be expected, therefore, that at all conceivable scales in Earth's outer core, columnar structures will be sustained by inertial waves (or some magnetically modified version of inertial waves, see Bardsley & Davidson, 2016, & §5).

Despite these low Rossby number estimates, some authors have suggested the geodynamo lies close to the transition at $Ro_\ell \sim 0.1$ (Olson & Christensen, 2006), in an attempt to explain geomagnetic excursions and reversals. For dynamos driven by compositional convection, Driscoll & Olson (2009) observe a reduction in dipolarity at $Ro_\ell \sim 0.1$, which coincides with the onset of magnetic polarity reversals. However, for this style of

convection, the decrease in dipolarity is much less abrupt. An alternate mechanism for polarity reversals was recently observed by Sheyko *et al.* (2016), with a more Earth-like dynamo model. They find periodic reversals consistent with the propagation of dynamo waves, in which $Ro_\ell = 0.06$, contradicting the previously established regime boundary.

4.1.2 A transition in inertial wave propagation and in rotating turbulence

Modern studies into rotating turbulence reveal a similar transition in axially elongated flow structures. Numerical simulations of a vortical eddy, with characteristic velocity u and length scale ℓ, subject to background rotation Ω (Sreenivasan & Davidson, 2008) show that for $Ro = u/2\Omega\ell \lesssim 0.5$ the eddy rapidly elongates along the rotation axis. This behaviour is attributed to inertial wave packets propagating along the axis. However, for $Ro \gtrsim 1$ the eddy spreads radially under the action of its own centrifugal force, with no preferential axial growth. These Rossby number limits differ slightly for different eddies, with lower (higher) bounds for anticyclonic (cyclonic) eddies, although this asymmetry is not the subject of the current work.

Experiments of inhomogeneous rotating turbulence at $Ro \lesssim 1$ show that, on time-scales of the order Ω^{-1}, the growth of columnar structures is consistent with inertial wave propagation (Davidson *et al.*, 2006). In a follow-up study (Staplehurst *et al.*, 2008), this result is extended to homogeneous turbulence with a further set of experiments where turbulence was generated at $Ro \sim 1$ and left to decay. As the energy decays, and interestingly as Ro drops below ~ 0.4, columnar structures are seen to emerge, whose axial growth is monitored by two-point vorticity correlations. The linear axial growth seen in the experiments is consistent with columnar structure formation by inertial wave propagation.

In purely hydrodynamic DNS of decaying, statistically homogeneous, rotating turbulence, a number of authors have observed a similar change in flow morphology with varying Rossby number. For example, Baqui & Davidson (2015) performed DNS with an initial Rossby number of $O(1)$, defined as $Ro = u_\perp/2\Omega\ell_\perp$, where $u_\perp$ is the root-mean-square (r.m.s.) perpendicular velocity and $\ell_\perp$ is the integral length scale perpendicular to the rotation axis. The turbulence is unforced and so the kinetic energy rapidly decays, thus causing the Rossby number to fall. At the time when $Ro \sim 0.4$, there is a rapid growth of the length scale parallel to the rotation vector characterised by $\sim \ell_\perp \Omega t$. In contrast, the perpendicular length scale remains approximately constant for the duration of the simulations. The linear increase in axial length-scale is explained by internal

inertial wave propagation. Note that the axial extension observed here occurs on a time-scale much shorter than the nonlinear time-scale.

In buoyantly forced rotating turbulence we may expect inertial waves to be continually launched at the scale of the forcing, provided the Rossby number based on this length scale is small enough. Inertial waves are helical waves (see the next section), and they are an important source of helicity in a rotating fluid. Dallas & Tobias (2016) find that for a sufficiently time-independent random forcing, large amounts of relative helicity may be generated in a rotating fluid. For $Ro \lesssim 0.2$, defined using the forcing modes, they find a bifurcation to a state of non-zero helicity whereas for larger values of $Ro \gtrsim 0.2$ there is an abrupt drop to zero helicity. Here several simulations are spread across a large range of Ro, so any transition cannot be tied to some critical Ro value. Even so, the Rossby number dependence of helicity is markedly abrupt.

In this chapter we attempt to bridge the gap between the transition in hydrodynamic rotating turbulence and the dipolar-multipolar dynamo transition. We conjecture that the discrepancy between the dynamo transition (local) Rossby number $Ro^{\text{crit}} \approx 0.1$ and the rotating turbulence $Ro^{\text{crit}} \sim 0.2 - 0.6$ is merely one of definition, i.e. which length scale is used; this will be discussed further in §4.3.

4.1.3 The suppression of inertial waves in dynamo simulations

Columnar flow structures spanning much of the core are a robust feature of most geodynamo simulations with rapid rotation. These are often interpreted in terms of boundary-driven columnar eigenmodes, i.e. steady solutions of a boundary-value problem in a rotating, internally heated spherical shell (Busse, 1975); although this relies on weak supercriticality. Convection in Earth's outer core, on the other hand, is expected to be highly supercritical, where we expect $Ra/Ra_c \sim 10^6$ (Gubbins, 2001). This necessitates an alternate mechanism to explain the columnar structure formation. An alternative source of columnar structures in a system where the velocity and buoyancy fields are highly time dependent, as we saw in chapter 2, are internally driven inertial waves (Davidson & Ranjan, 2015).

Internally driven inertial waves have recently been identified in a moderately supercritical dynamo simulation (Ranjan *et al.*, 2018). These waves are thought to be important for sustaining columnar structures and for helicity transport in planetary cores. Further, when preferentially agitated near the equatorial plane, inertial wave packets yield a helicity distribution which could maintain an α^2 dynamo (Davidson & Ranjan, 2015, 2018). On this basis, Davidson (2016) proposed and tested the hypothesis that the transition from dipolar to multipolar fields in the numerical dynamos is triggered

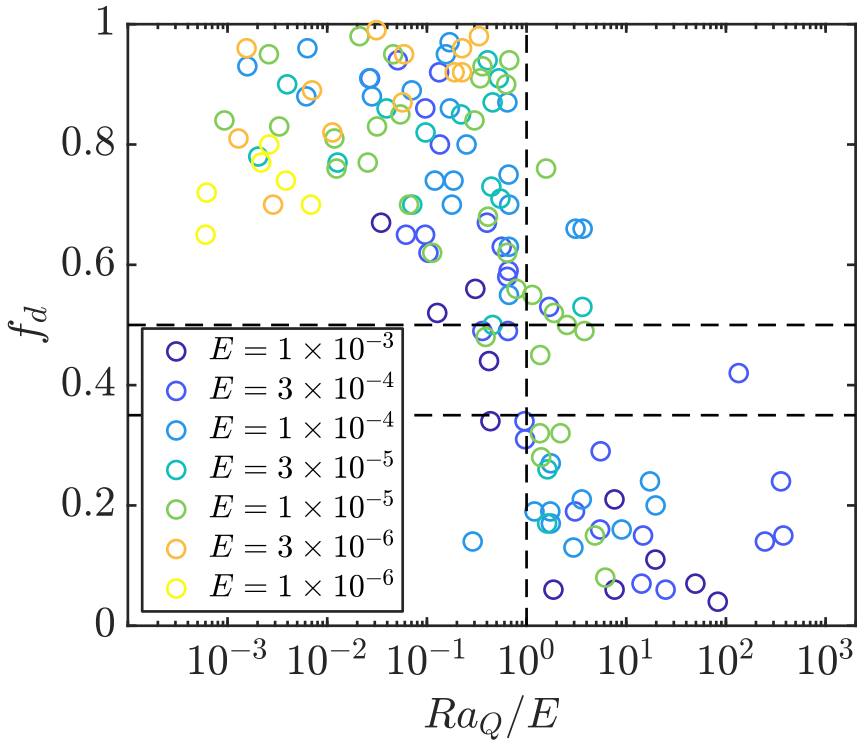

Fig. 4.2 Dipolarity against the $Ro \sim Ra_Q/E$ scaling from Davidson (2016). The horizontal dashed lines mark the region $f_d = 0.35-0.5$, and the vertical dashed line is at $Ra_Q/E = 1$. Data courtesy of Uli Christensen.

by the suppression of inertial waves at the critical threshold $Ro \sim 0.4$. He developed a scaling for the local Rossby number $\sim Ra_Q/E$ (where Ra_Q is a Rayleigh number based on the heat-flux), based on the fact that the column width in many of the published simulations is on the order of $E^{1/3}L$. The dipolarity is plotted against Ra_Q/E for dynamos in Uli Christensen's dataset in figure 4.2. It is conventional to characterise dynamos with $f_d > 0.5$ as dipolar and those with $f_d < 0.35$ as multipolar, and these values are highlighted by horizontal dashed lines. The vertical dashed line at $Ra_Q/E = 1$, corresponding to $Ro \sim 0.5$, separates the two regimes reasonably well. The results, while consistent with the hypothesis, are not entirely conclusive.

In a series of hydrodynamic and dynamo simulations, Garcia *et al.* (2017) observe that the equatorial symmetry of the flow is a key indicator for the dipolar-multipolar transition. Interestingly, a high degree of flow symmetry is associated with the picture outlined by Davidson (2016), in the rapidly rotating regime. As the Rossby number is increased, and the system passes the critical threshold at $Ro \sim 0.4$, a reduction in flow symmetry is expected. Thus, the relation of the dynamo transition to the symmetry of the velocity field is not inconsistent with Davidson's hypothesis.

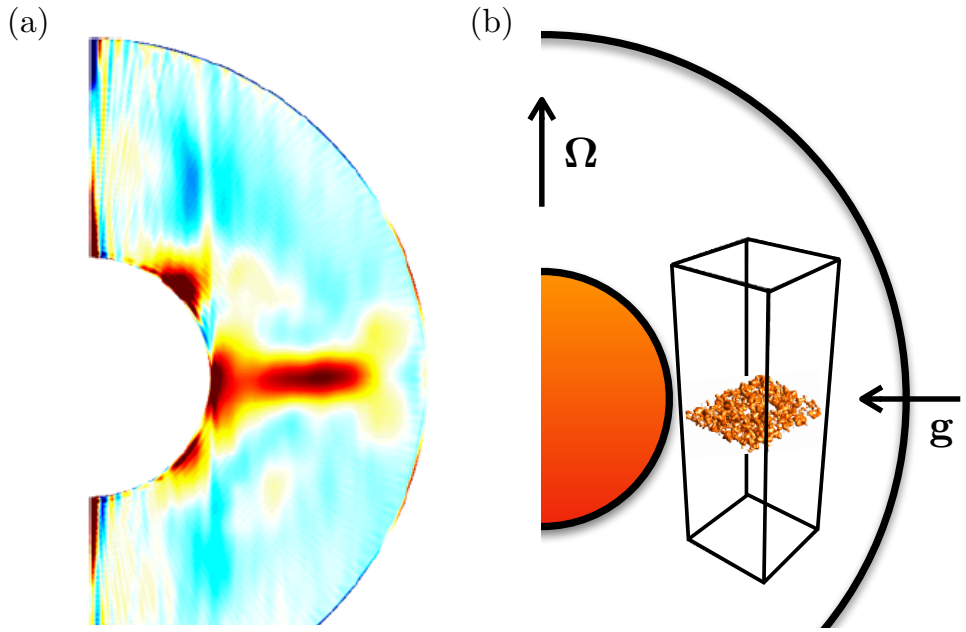

Fig. 4.3 The numerical set-up and its motivation. (a) An image from Sakuraba & Roberts (2009) showing an equatorially biased heat-flux. (b) We approximate the equatorial regions of a spherical shell with $\boldsymbol{\Omega} \perp \mathbf{g}$, and the equatorially biased heat-flux is modelled as a layer of buoyant anomalies. This figure is a reproduction of figure 3.2.

4.2 Results

4.2.1 Rationale

We perform DNS of a rapidly rotating Boussinesq fluid in a box elongated in the direction of the rotation vector. We use Cartesian coordinates where the rotation vector points in the z-direction and gravity is in the y-direction, with the origin at the centre of the box. The initial condition is a layer of buoyant anomalies confined to the vertical centre of the box (as described in chapter 3), and for the velocity field: $\boldsymbol{u} = \mathbf{0}$. The buoyancy field initial condition is motivated by the equatorially biased heat-flux, as described in chapter 1. For example, figure 4.3a shows a dynamo simulation from Sakuraba & Roberts (2009), where the heat-flux is concentrated in and around the equatorial plane. The set-up for this chapter is shown in figure 4.3b, where the layer of buoyant anomalies models the equatorially biased heat-flux. We are interested in the launching of inertial wave packets from the layer of buoyant anomalies, as is observed at low Rossby number (Davidson & Ranjan, 2015).

The influence of nonlinear inertia on inertial wave propagation is investigated through increasing the magnitude of the buoyant forcing, and this is done by increasing the

magnitudes of the buoyant anomalies which constitute the layer. The increase in the forcing results in larger velocities and a larger Rossby number. As will soon be clear, when the buoyant forcing is large enough, the Rossby number in the centre of the box passes a critical threshold, and there is a localised transition to turbulence in the neighbourhood of the buoyant layer. There are two distinct regions of the flow. The wave-field is a sea of inertial wave packets, characterised by a low Rossby number, that extends towards the top/bottom of the box at the speed of low-frequency inertial waves. Also, we identify the buoyancy/turbulence region, which is in the neighbourhood of the buoyant layer, and is characterised by a larger Rossby number and incoherent flow. The wave-field and the buoyancy/turbulence region will be illustrated and defined in the next section. We seek to understand the differences in the dynamics of these regions, and to investigate the value of a critical Rossby number which delineates the boundary between the two regions.

Six simulations of increasing Rossby number are performed (R1–R6), as documented in table 4.1, with R1 having the lowest Rossby number and R6 the highest. As the simulations are inhomogeneous, we calculate the r.m.s. velocity (denoted u) in the mid-plane of the box, where it is highest in magnitude. The r.m.s. velocity is shown in two normalised forms in figure 4.4: (a) as a Reynolds number and (b) as a Rossby number, both based on the mean blob size $\bar{\delta}$. For R1, both measures initially rise due to the conversion of potential energy contained in the buoyant cloud to kinetic energy of the fluid motion. As expected, inertial waves begin to propagate away from the buoyant cloud (see §4.2.2), and the r.m.s. velocity saturates at the point when the flux of wave energy balances the energy conversion rate. For R3–6 however, the picture is different: u rises by the same process and waves carry energy away from the buoyant region, but now there is a decrease due to dissipation. For R1 we have a typical Reynolds number $Re = u\bar{\delta}/\nu \approx 30$, whereas for R2–6, $Re \sim 250$ (see the dashed lines, figure 4.4a).

To investigate the effect of nonlinear inertial forces on wave dispersion, we increase the Rossby number by increasing the amplitude of the buoyancy source, which increases the peak value of Ro (figure 4.4b). The Ekman number is kept low at all times. If we balance the inertial and buoyancy terms in the curl of the momentum equation, we find a characteristic velocity based on the initial buoyancy field is $v_0 = (c_0 g \bar{\delta})^{1/2}$. However this procedure is only valid for runs R2–6, as it is in these runs that inertia substantially effects the solution. We find it convenient to introduce two different Rossby numbers, one based on the initial (prescribed) buoyancy field and one based on the observed r.m.s.

Table 4.1 Parameters for all runs. Subscripts b and w denote the buoyancy/turbulence region and the wave region respectively.

Run	$\tilde{Ro}$	E	$\overline{Ro}_b$	$\overline{Ro}_w$	Symbol
R1	–	4.0×10^{-4}	0.02	0.01	✻
R2	0.10	4.6×10^{-4}	0.28	0.13	×
R3	0.13	6.4×10^{-4}	0.41	0.17	○
R4	0.17	8.0×10^{-4}	0.47	0.19	△
R5	0.19	9.1×10^{-4}	0.52	0.20	▽
R6	0.22	1.1×10^{-3}	0.56	0.22	□

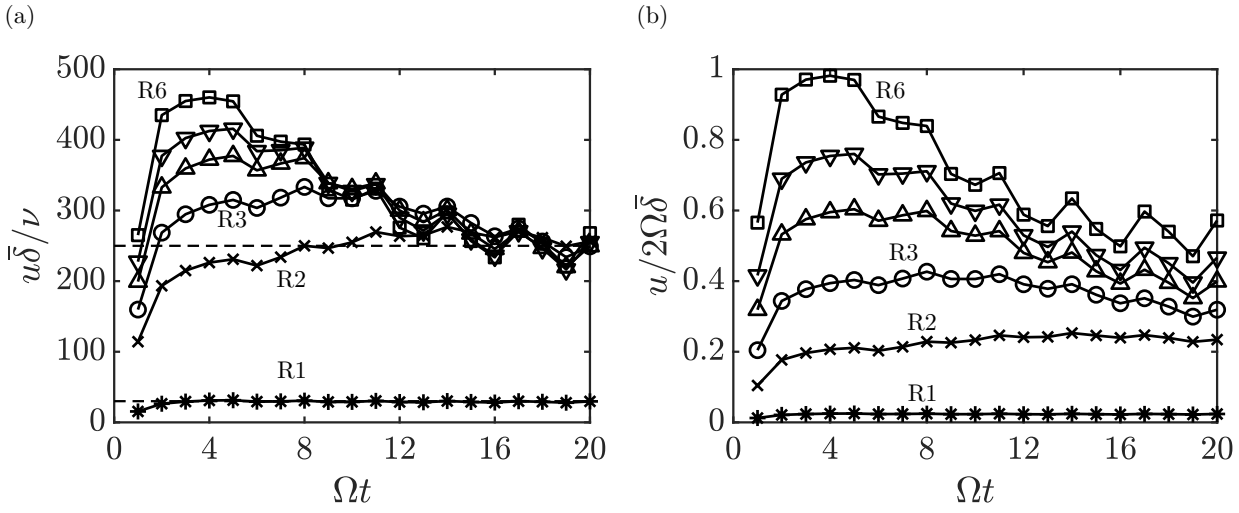

Fig. 4.4 Dimensionless r.m.s. velocity in the mid-plane. (a) A Reynolds number and (b) a Rossby number, both based on the mean blob size $\bar{\delta}$. Symbols are defined in table 4.1.

velocity in the saturated state,

$$\tilde{Ro} = \frac{v_0}{2\Omega\bar{\delta}}, \qquad \overline{Ro} = \frac{u}{2\Omega\ell_\perp}, \tag{4.1}$$

($\tilde{Ro}$ defined for R2–6 only). Here $\ell_\perp$ is the perpendicular integral scale of the flow, which is of order $\bar{\delta}$, and is calculated in §4.2.2. A summary of the runs is presented in table 4.1, where the Ekman number $E = \nu/2\Omega\bar{\delta}^2$ is defined using prescribed quantities.

The $\overline{Ro}$ values in table 4.1 are averages in time and space in the saturated state, the spatial averages are computed in separate regions of space: the 'buoyancy/turbulence' b and 'wave' w regions (defined in §4.2.2). We note $\overline{Ro}_w$ is similar to $\tilde{Ro}$, whereas $\overline{Ro}_b$ tends to be larger due to a higher kinetic energy and smaller integral length scales. These diagnostics show the general trend of increasing Rossby number from R1–6, however we

will explore later how the length scales and Ro evolve with time, and vary with height above/below the initial buoyant cloud. Inertial wave packets are emitted at early times, and carry away a fraction of the energy of the buoyant cloud. Thus, we may expect the Rossby numbers in the waves to be smaller than those in the buoyancy/turbulence region, and this is true for R1–6.

4.2.2 Flow morphology

Isosurfaces

The transition between columnar structures and disorganised flow can qualitatively be seen through isosurfaces of the velocity or vorticity fields. Here we show images of the axial vorticity ω_z (figure 4.5) and the vorticity field $|\boldsymbol{\omega}|$ coloured by relative helicity (figure 4.6). Columnar cyclone/anti-cyclone pairs (see figure 4.5) propagate away from the buoyant cloud (see also Davidson & Ranjan, 2015), akin to the flow structures seen in dynamo simulations (Sreenivasan & Jones, 2011). Here inertial wave packets are launched for all simulations R1–6. These are the axially propagating and extending features evident in figure 4.5. This is confirmed by figure 4.6, as helicity is segregated into a pattern which is negative (positive) in the upper (lower) part of the box, a fundamental characteristic of inertial waves (chapter 2). As expected from the group velocity relation for low-frequency inertial waves, 'wider' features advance faster, and this is seen in figures 4.5 & 4.6. For larger Ro, the buoyancy field advects and diffuses more as the waves are launched (see figure 4.7). This leads to wave packets with a broader range of widths, and thus a wider range of propagation speeds, from R2–6. As gravity is along y, for R2–6 the columnar structures lean over slightly, increasingly with larger Ro. This is due to horizontal movement in the buoyancy field, similar to the inclined columns reported by Hide *et al.* (1968) and Lighthill (1970).

A striking feature for runs R3–6 is a region about the mid-plane of the box where the flow appears increasingly small-scale and disordered. This turbulence is forced by the buoyancy field, is vertically localised (in the buoyancy/turbulence region), and is most easily seen in figure 4.6 for runs R3 and R5. This region is characterised by a broadband velocity field (see below), increased energy in the small scales, and a more complex helicity distribution (i.e. not clearly segregated either side of the mid-plane). We introduce $z_b(t)$ and $z_w(t)$ as measures of the spatial extent of the buoyancy/turbulence region and the wave-field, respectively. The buoyancy/turbulence zone, $-z_b \rightarrow z_b$, is defined as the height where the horizontally averaged buoyancy falls to 5% of its maximum value. This is a robust choice as the buoyancy field is advected by the turbulence generated near the

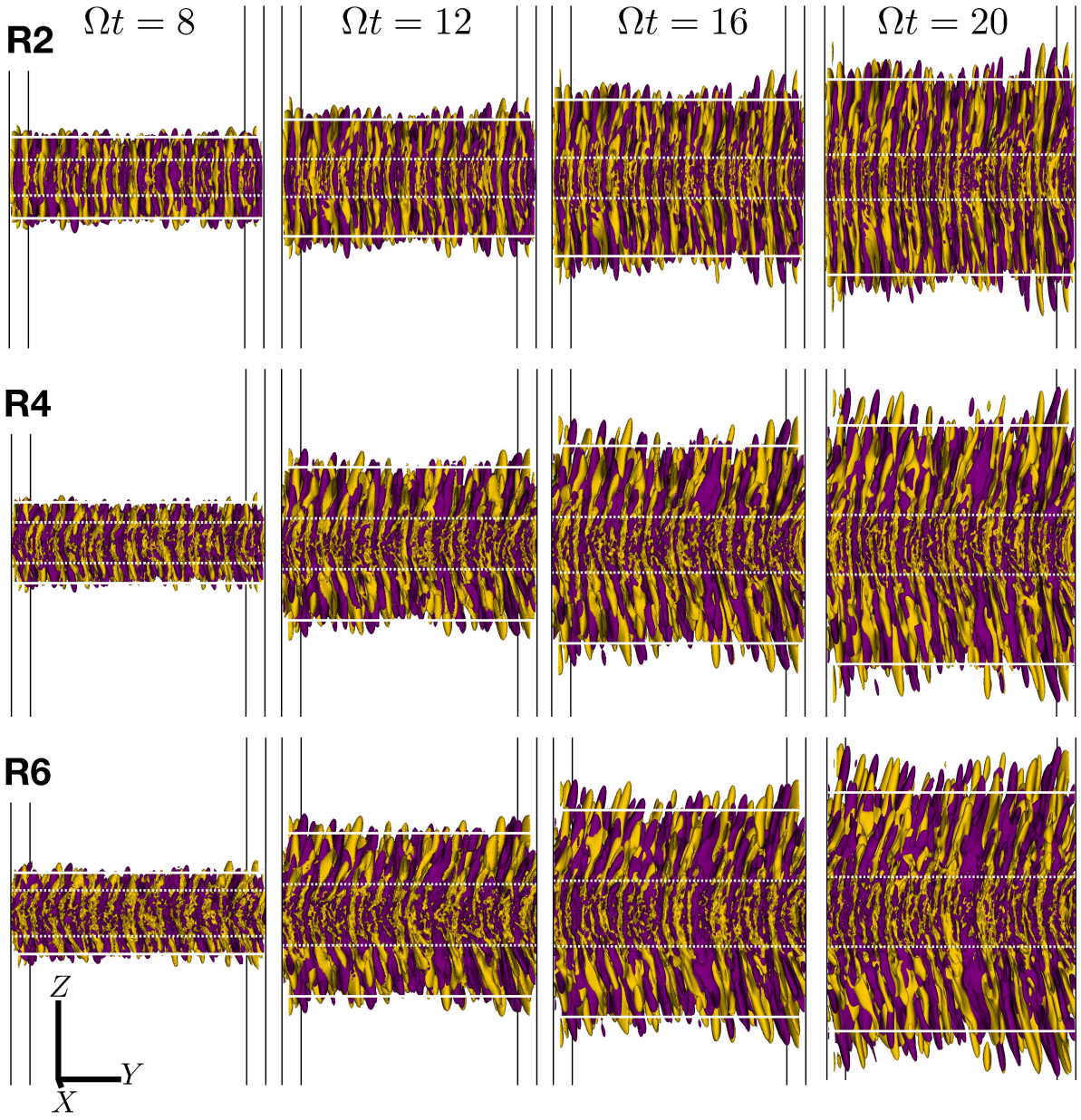

Fig. 4.5 Isosurfaces of axial vorticity for runs R2, R4 and R6 at 5% of the maximum value: dark purple is positive ω_z, light yellow is negative ω_z. The solid white horizontal lines indicate the extent of the wave packets $-z_w$ and z_w, and the dashed white lines bound the buoyancy/turbulence region $(-z_b, z_b)$.

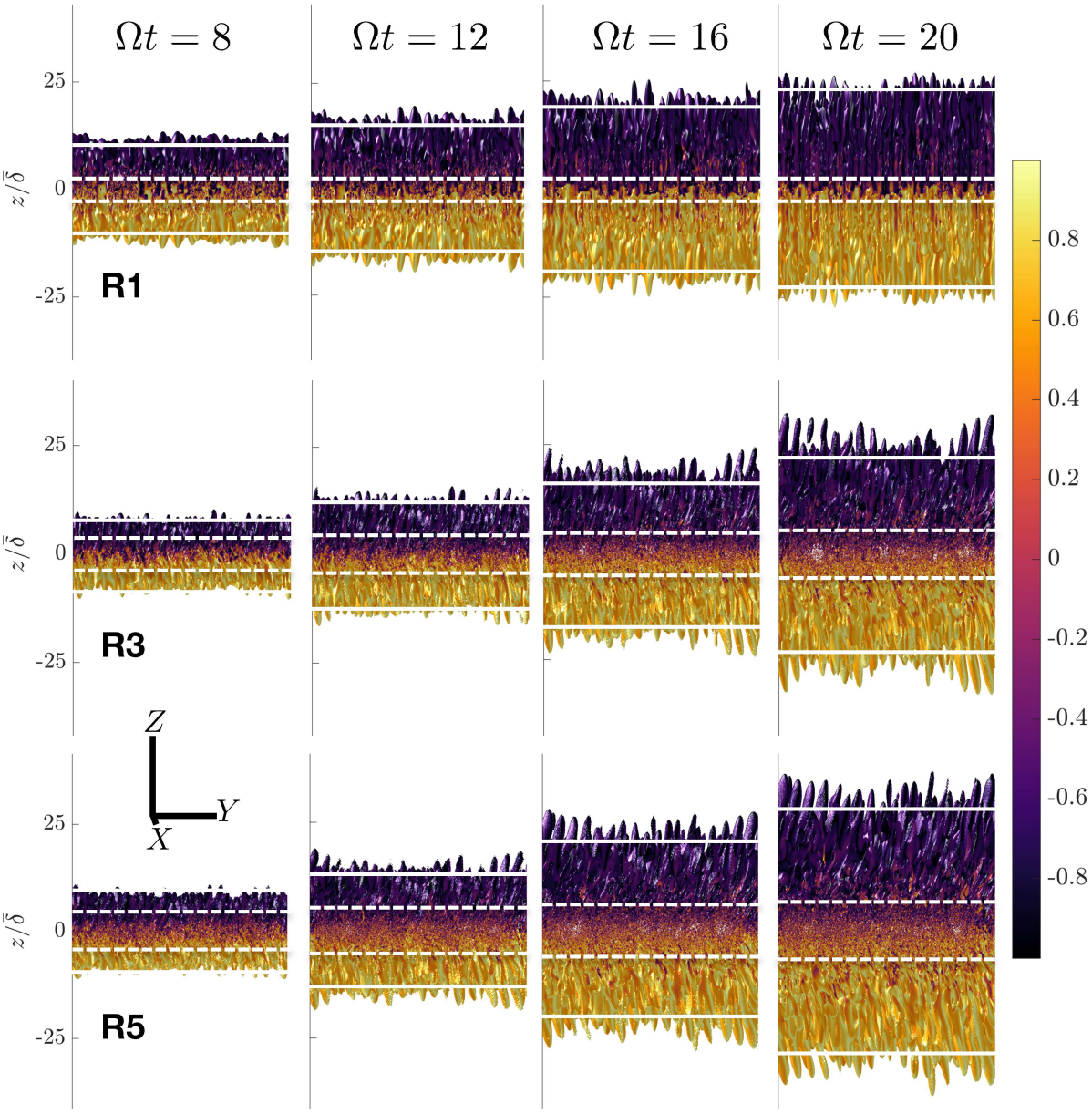

Fig. 4.6 Vorticity isosurfaces at 5% of the maximum value, coloured by relative helicity for runs R1, R3 and R5. The white dashed lines show the extent of the buoyancy/turbulence region $-z_b$ to z_b, the solid white lines show the extent of the wave field $-z_w$ and z_w.

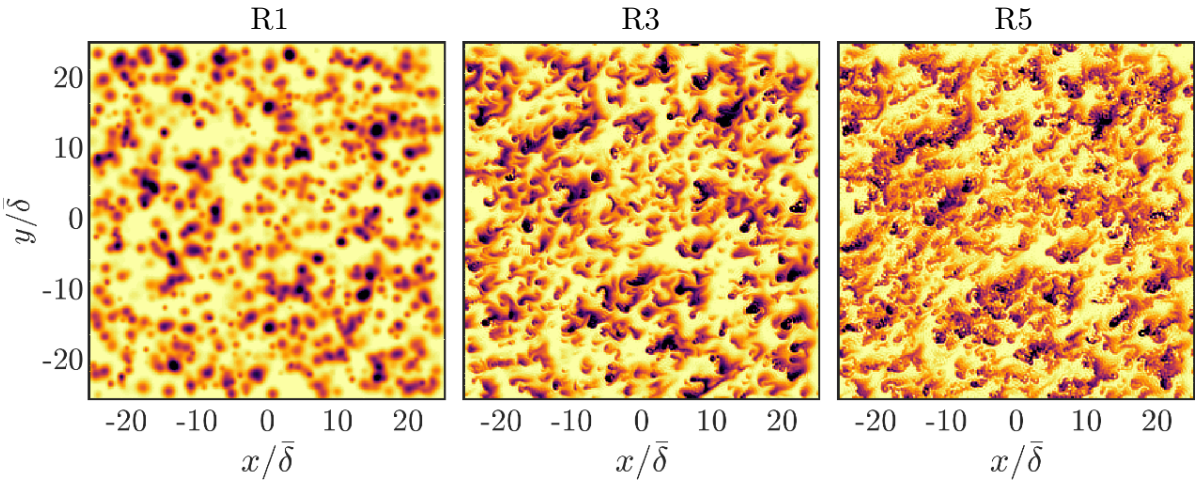

Fig. 4.7 Buoyancy field in the mid-plane at $\Omega t = 5$ for runs R1, R3 and R5, lighter colours correspond to more dense material.

mid-plane of the box. Analogously, the extent of the wave field z_w is defined as the point where the horizontally averaged velocity magnitude falls to 5% of its maximum value. The dashed white lines in figures 4.5 & 4.6 show the extent of the buoyancy/turbulence region, and the solid white lines indicate the extent of the wave-field.

Figure 4.7 shows the buoyancy field in the mid-plane of the box at $\Omega t = 5$ for runs R1, R3 and R5. The buoyancy field in R1 has advected a negligible amount, as expected at low-Ro, and there is little diffusion owing to the small Ekman number. However, for R3 and R6 there is a significant amount of advection and small scales are excited by the turbulence, and these small scales are preferentially diffusive.

Perpendicular spectra

Columnar structures formed by inertial wave propagation retain the perpendicular length scale of their source (Davidson, 2013*b*), for example the diameter of the buoyant blob or eddy from which the wave packet is launched. This can be seen through the group velocity of a low-frequency inertial wave packet $c_g \approx 2\Omega/k_\perp$, packets with a larger perpendicular length scale $\ell_\perp$ (smaller $k_\perp$) travel faster than packets with a smaller $\ell_\perp$ (larger $k_\perp$). Also, as we saw in the previous section, when the forcing is increased and the rotation weakened, we observe a disordered region about the mid-plane of the box where the flow is clearly incoherent. We expect the Rossby number in this turbulent region to be greater than the Rossby number of the waves launched initially, and we are interested in mapping the transition in space and time from the wave dynamics, characterised by a columnar morphology, to incoherent turbulence.

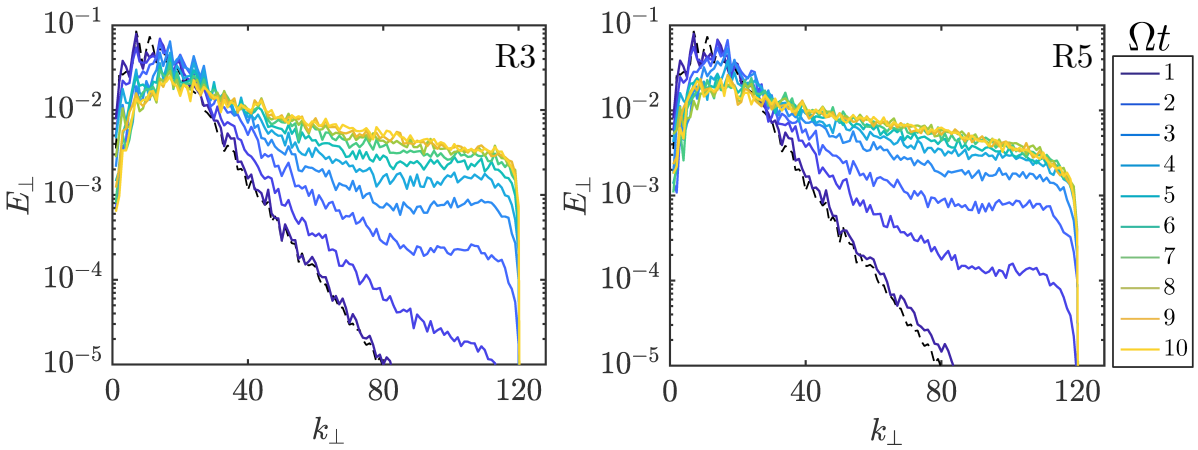

Fig. 4.8 Perpendicular spectra (normalised by their integral) in the mid-plane for $1 \leq \Omega t \leq 10$ (see legend), for runs R3 and R5. The black dashed line is the perpendicular spectrum of the initial buoyancy field.

To quantify these claims we compute perpendicular energy spectra at discrete heights in the box. Perpendicular spectra are defined as integrals of the Fourier modes of the perpendicular velocities over rings A of width 1 in the k_x-k_y plane

$$E_\perp(k_\perp) = \int_A \hat{u}_j \hat{u}_j \, \mathrm{d}A(k_\perp) \,. \tag{4.2}$$

Here $j = 1, 2$, $A(k_\perp) = \pi(k_{i+1}^2 - k_i^2)$ and $0 \leq k_i < k_{\max} - 1$. These spectra typically peak at $\pi/\ell_\perp$, where $\ell_\perp$ is the perpendicular integral scale of the flow (see §4.2.2). To the right of the peak of $E_\perp(k_\perp)$, we interpret $E_\perp(k_\perp)\mathrm{d}k_\perp$ as the perpendicular kinetic energy within the wavenumber range $k_\perp \to k_\perp + \mathrm{d}k_\perp$ (where here $\mathrm{d}k_\perp = 1$).

Perpendicular spectra (normalised by their integral) in the mid-plane of the box for runs R3 and R5 are shown in figure 4.8, for $1 \leq \Omega t \leq 10$. The dashed line shows the perpendicular spectrum of the initial buoyancy field, calculated analogously to the perpendicular velocity spectra. At $\Omega t = 1$, $E_\perp$ lies almost on top of the initial buoyancy spectrum, however the velocity field rapidly becomes broadband for both R3 and R5. It is in this sense that we characterise the flow as turbulent. We only present the spectra for R3 and R5 here for brevity, however these are representative of R2–6 (see figure 4.10).

It is of interest to compare $E_\perp(k_\perp)$ for R1–6. However if we hypothesise that the flow evolving in the buoyancy/turbulence region cares little about rotation, then making comparisons at the same Ωt may not be appropriate. So, we need an appropriate time to examine flow features and spectra in the mid-plane. Previous studies have shown that the peak of dissipation is a suitable time to compare turbulent quantities (Mininni & Pouquet, 2009*a*; Sahoo *et al.*, 2011). The dissipation is defined $\epsilon = \nu S_{ij} S_{ij}$ where S_{ij} is

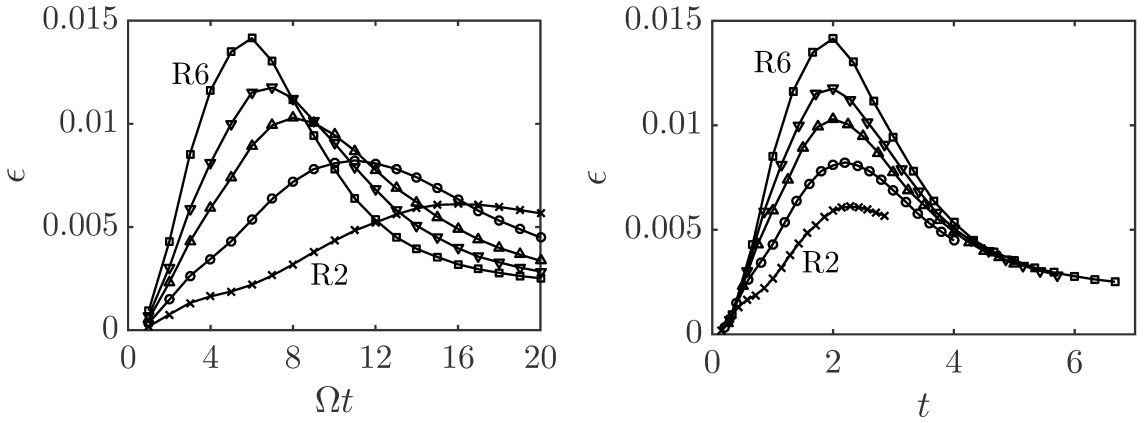

Fig. 4.9 Dissipation in the mid-plane as a function of Ωt and t respectively for runs R2–6. Symbols are defined in table 4.1.

the rate of strain tensor, this may be written in terms of the enstrophy and a divergence (Davidson, 2013*b*)

$$\epsilon = \nu|\boldsymbol{\omega}|^2 + \text{a divergence term}\,. \tag{4.3}$$

A common proxy for the dissipation, which we will term the dissipation here unless stated otherwise is

$$\epsilon \approx \nu|\boldsymbol{\omega}|^2\ . \tag{4.4}$$

This is averaged over the mid-plane of the box (for runs R2–6) and shown in figure 4.9. It is evident from figure 4.9 that the runs at higher Rossby number have had more time to advect and dissipate energy for the same Ωt. Therefore the turbulence in the buoyancy region becomes more developed in our simulations at larger Rossby numbers.

Runs with a higher Rossby number transition to turbulence at smaller Ωt. However for R3–6 the dynamics are similar. Figure 4.10 shows perpendicular spectra for all runs at 4 distinct times: (a) $\Omega t = 2$, (b) $\Omega t = 4$, (c) $t = \tau_{\text{peak}}$ and (d) $\Omega t = 20$ (the end of the simulation). At $\Omega t = 2$, the spectra for R1 and R2 are very close to the initial buoyancy spectrum whereas those for R5 and R6 have already begun to become broadband. As time progresses, at $\Omega t = 4$ the spectra for R3–6 are all broadband indicating the transition to turbulence. The spectra for runs R2–6 are all very similar at the peak of dissipation $t = \tau_{\text{peak}}$, and the curves are all at their most broadband point at this time. This suggests τ_{peak} is an objective time to compare runs R2–6. At the end of the runs, $\Omega t = 20$, the tails of the spectra for R3–6 have begun to fall back down, due to small-scale viscous dissipation.

Figure 4.11 shows energy spectra as a function of time at various heights for R1, R3 and R5. The first three heights are close to the buoyancy/turbulence region, and the

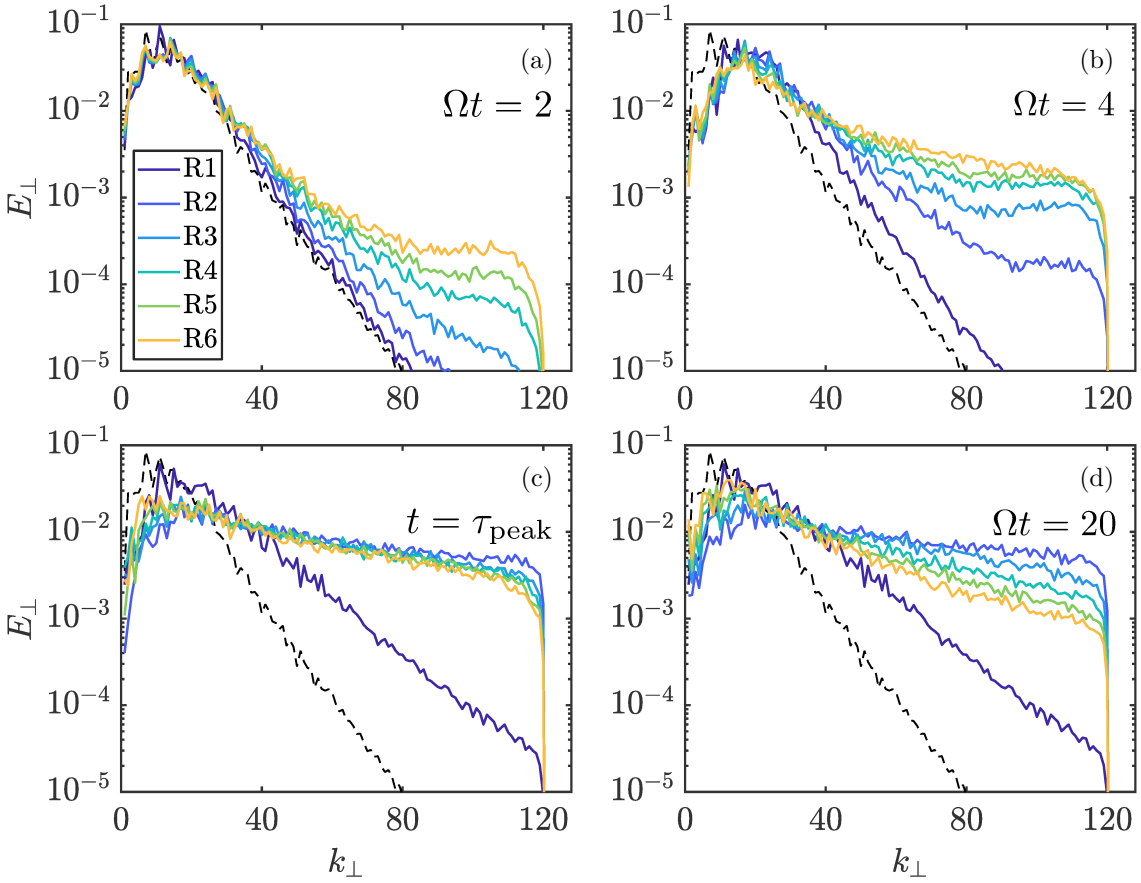

Fig. 4.10 Perpendicular spectra (normalised by their integral) in the mid-plane at (a) $\Omega t = 2$, (b) $\Omega t = 4$, (c) the peak of dissipation: τ_{peak}, and (d) at the end of the simulation, $\Omega t = 20$, for runs R1–6. The black dashed line is the perpendicular spectrum of the initial buoyancy field.

larger three are higher up in the wave-field. At the two largest heights, $z/\bar{\delta} \approx 15$, 20, the three plots look nearly identical, indicating that the dynamics in the wave-field are similar for the simulations presented. All of the energy lies under the green dashed line, which highlights energy travelling at the speed of low-frequency inertial waves, and this is to be expected in the wave-field. At the three smaller heights, $z/\bar{\delta} \approx 2$, 4, 6, there is a noteable difference between the simulations. For R1, much of the energy lies at low wavenumbers, and below the inertial wave group velocity line, suggesting that waves dominate the dynamics. However, for R3 and R5, a significant amount of high wavenumber energy is excited, which lies well above the line delineating energy transported by inertial waves. At $z/\bar{\delta} \approx 2$, inside the initial buoyant layer, the spectra are most broadband near the peak of dissipation in the mid-plane (vertical dashed line). For larger heights, $z/\bar{\delta} \approx 4$, 6,

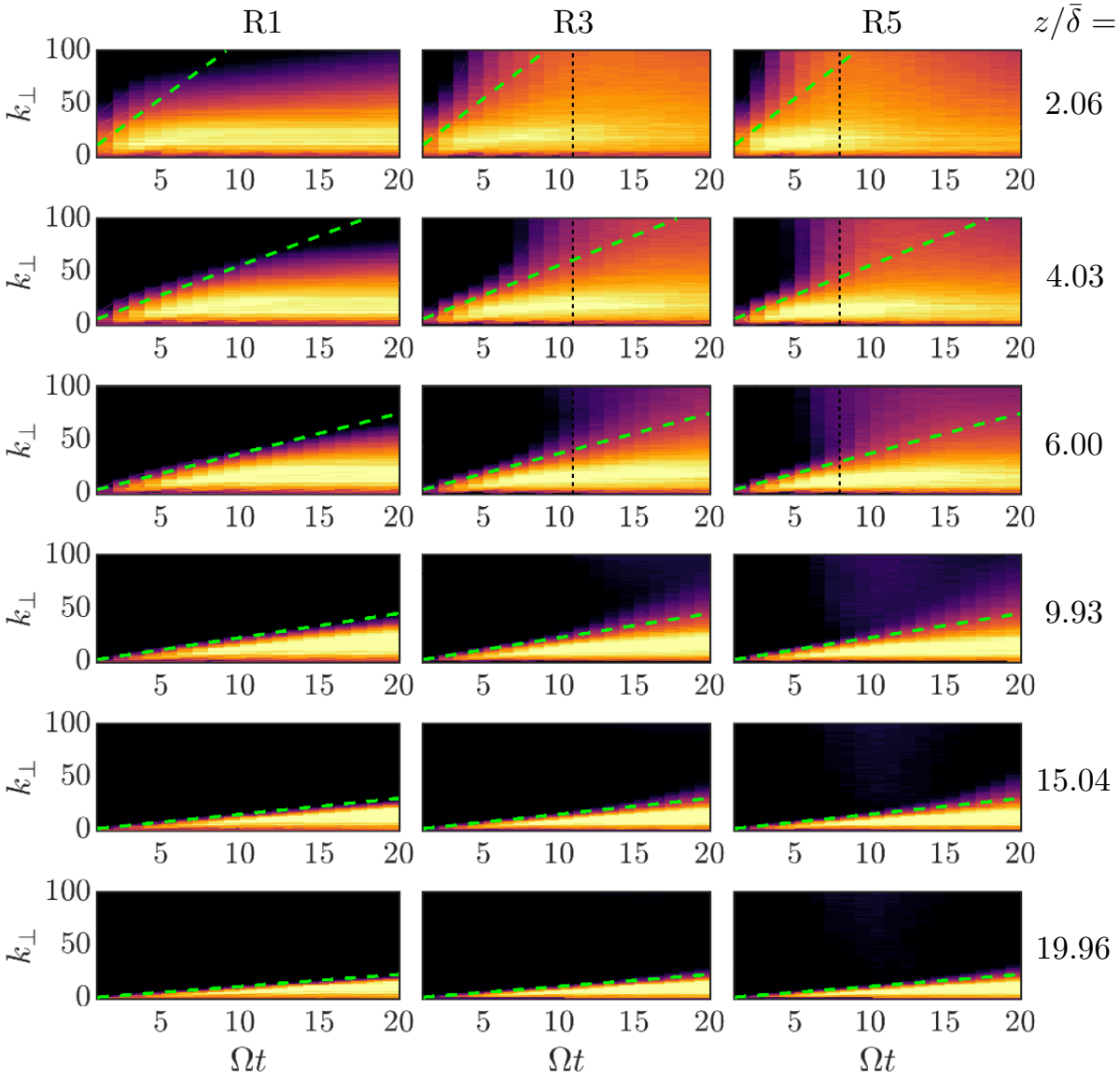

Fig. 4.11 Energy spectra $E_\perp(k_\perp, t)$ as a function of time at various heights $z/\bar{\delta}$ for R1, R3 and R5. The dashed green line highlights energy arriving at the group velocity of low-frequency inertial waves, and the vertical dashed black line shows the peak of dissipation in the mid-plane (shown only for smaller heights). Note that $z/\bar{\delta} = 2.06$ is within the initial buoyant layer ($-3 \leq z/\bar{\delta} \leq 3$).

the point at which the spectra are most broadband occurs later in time, and we interpret this as an imprint of the spread of the turbulent region to larger z with time.

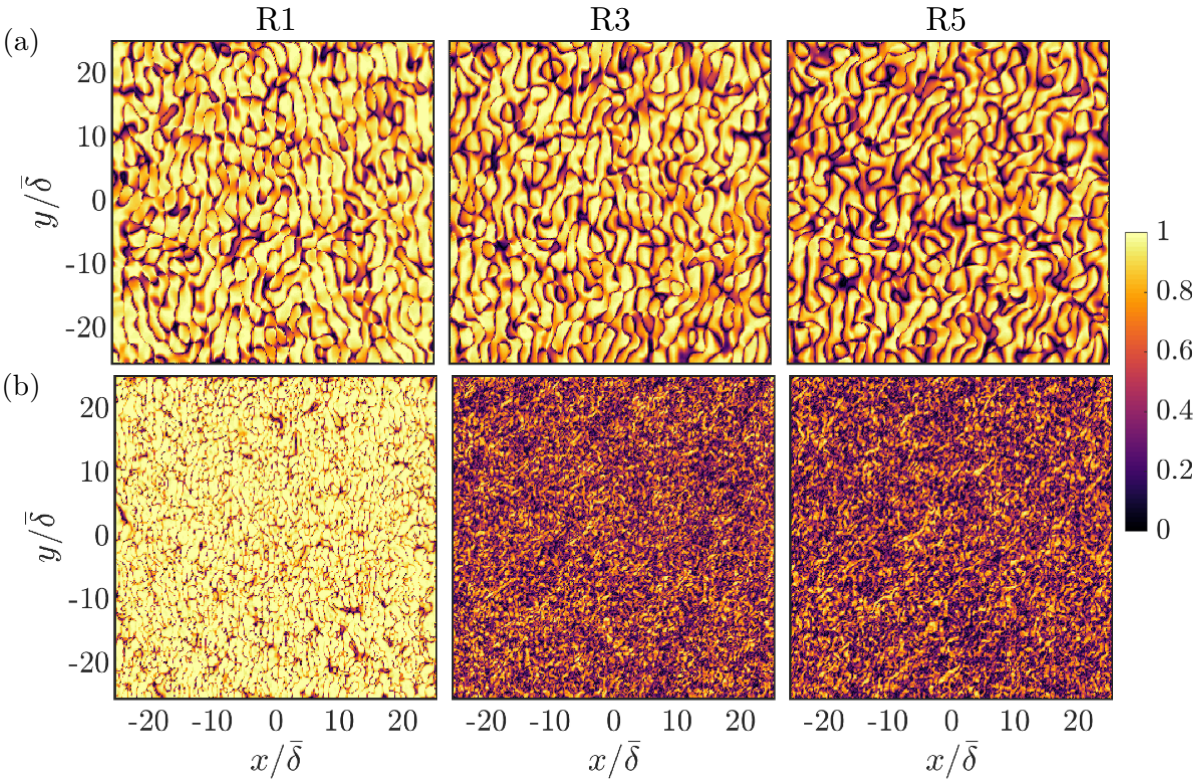

Fig. 4.12 Columnarity $C(x, y)$ in (a) the wave region and (b) the buoyancy/turbulence region for R1, R3 and R5 at $\Omega t = 16$.

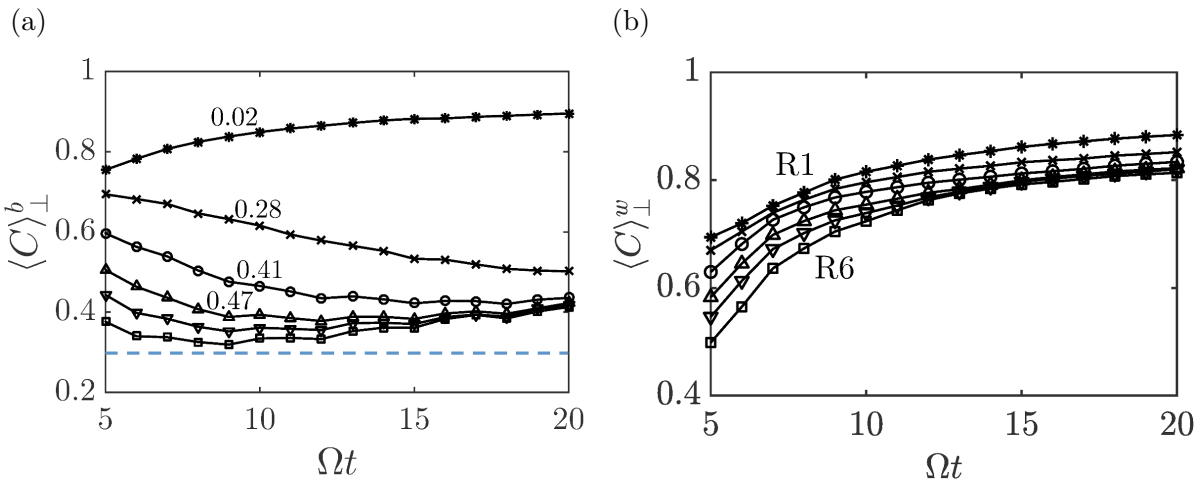

Fig. 4.13 Plane averaged columnarity in (a) the buoyancy/turbulence region and (b) the wave region. In (a) the dashed line is the time-averaged columnarity from a non-rotating simulation. Symbols are defined in table 4.1.

Columnarity

We define the columnarity of the flow as in Ranjan *et al.* (2018) (similar to Soderlund *et al.* (2012))

$$C(x, y) = \sqrt{\frac{\langle \omega_z \rangle_z^2}{\langle \omega_z^2 \rangle_z}}, \tag{4.5}$$

where $\langle\sim\rangle_z$ denotes averaging along z. In figure 4.12 we show a comparison of $C(x,y)$ in the wave-field and the buoyancy/turbulence region for R1, R3 and R5 at $\Omega t = 16$. The z-average is performed in two regions (a) $12 \leq z/\bar{\delta} \leq 18$ and (b) $-3 \leq z/\bar{\delta} \leq 3$. In the wave-field, the columnarity is strong for all the simulations, though we observe a slight weakening for R3 and R5 which may be due to the inclination of the columns at larger Rossby number. In the buoyancy/turbulence region the columnarity is nearly maximal for R1, and although the features are of a smaller scale, they are all of a similar size. However, for R3 and R5, there is a dramatic reduction in $C(x,y)$, the picture is more incoherent, and the features have a range of scales.

From (4.5), the quantity $\langle C\rangle_\perp$ can be derived by averaging in the transverse plane. Figure 4.13 shows the columnarity $\langle C\rangle_\perp$ computed in the buoyancy/turbulent region and in the wave region for runs R1–6 and $5 \leq \Omega t \leq 20$ (for $\Omega t < 5$ it is difficult to separate the two regions, although they are clearly identifiable at later times). For R1, we calculate $\langle C\rangle_\perp^b$ in the region $|z| < 3\bar{\delta}$ as there is no turbulence and the buoyancy field only fractionally evolves. The buoyancy region and the wave region have very high columnarity for R1. This reflects the fact that inertial waves are free to propagate at low Rossby number and the perpendicular length scales in the source region remain narrowly distributed about $\bar{\delta}$. Columnarity in the buoyancy/turbulence region for R2–6 decreases rapidly with increasing Rossby number. Four curves in (a) are labelled by Ro_b in the saturated state, and it is observed that the columnarity is greatly reduced for $Ro_b \sim 0.4$. The dashed line on the $\langle C\rangle_\perp^b$ plot is the time-averaged columnarity from a non-rotating run with the same initial conditions as R2–6. This shows that the columnarity of the flow in the buoyancy/turbulence region approaches the non-rotating value of 0.29 for larger Rossby numbers.

The columnarity in the wave-field, $\langle C\rangle_\perp^w$, is calculated in a layer with a thickness of $4\bar{\delta}$ that moves at the wave speed $\sim 2\Omega\bar{\delta}$. For all runs, the wave columnarity is high, suggesting that the dynamics in the wave-field are similar simulations R1–6. This is supported by the columnar structures seen in the vorticity isosurfaces shown in figures 4.5 & 4.6.

Length scales

A common method of measuring length scales in turbulence experiments is to integrate the two-point autocorrelations of velocity components, yielding a characteristic length of the region within which eddies are correlated. We are interested in the temporal change of the length scales parallel and perpendicular to the rotation vector, as it is well known that in rotating turbulence these two length scales behave in very different ways

(Staplehurst *et al.*, 2008). Consider a cloud of homogeneous non-rotating turbulence, to which we suddenly apply constant rapid rotation. We would like to monitor any growth of the axial length scale due to the propagation of inertial wave packets. Now inertial waves transfer information by the coordination of phase, for example in the ansatz $\sim \exp[\mathrm{i}(\boldsymbol{k}\cdot\boldsymbol{x} - \varpi t)]$ (Greenspan, 1968). However autocorrelations are almost completely devoid of phase information by their very construction (Bracewell, 1986), and it follows that we cannot expect to retrieve information relating to inertial wave propagation from classical integral scale measurements (Staplehurst *et al.*, 2008).

For these reasons, we do not compute axial integral length scales using autocorrelations. We can, however, visually monitor the axial growth of velocity structures (see figure 4.5), and the helicity distribution (figure 4.6) and this reinforces our conclusion that the axial growth is due to inertial wave packets. This is verified by the time-evolution of the plane-averaged r.m.s. velocities. Figure 4.14 shows u averaged over each perpendicular plane for $2 \leq \Omega t \leq 20$, the energy spreads to larger $z/\bar{\delta}$ with Ωt. We show the same quantity in figure 4.15, but now the height is normalised by Ωt, there is a satisfactory collapse of these data particularly within the wave-field.

The length scale which is important for the launching of wave packets, and to be used in the definition of Ro, is the length scale normal to the rotation axis. This perpendicular scale is often computed as (Mininni *et al.*, 2009; Mininni & Pouquet, 2009*b*; Sahoo *et al.*, 2011)

$$\ell_\perp = \frac{\pi \int k_\perp^{-1} E_\perp(k_\perp)\, \mathrm{d}k_\perp}{\int E_\perp(k_\perp)\, \mathrm{d}k_\perp}\,, \tag{4.6}$$

where $E_\perp(k_\perp)$ are perpendicular spectra (see §4.2.2). Applied to a sinusoidal field with single wavenumber k, this gives $\ell_\perp = \pi/k$, and for a sea of Gaussian eddies of size δ, $\ell_\perp \approx \delta$.

Figure 4.16 shows $\ell_\perp/\bar{\delta}$ as a function of $z/\bar{\delta}$ for times $2 \leq \Omega t \leq 20$. For all runs the shape of $\ell_\perp/\bar{\delta}$ is very similar at $\Omega t = 2$. For R1, the perpendicular scale within the buoyant cloud quickly settles at a value of $\ell_\perp/\bar{\delta} \approx 1.1$. For R2 however, we see the length scale in the buoyancy/turbulence region reduces, with a minimum of $\ell_\perp/\delta \approx 0.55$. There is a similar decrease in the perpendicular length scale for runs R3–6, although the dissipation of small-scale energy allows $\ell_\perp/\bar{\delta}$ to increase at later times in these runs. We interpret this reduction of the perpendicular length scale within the buoyancy/turbulence region in terms of the excitation of small-scale turbulence (see §4.2.2). Interestingly, the minima of $\ell_\perp(z = 0)$ for R3–6 roughly coincide with the peaks of dissipation seen in figure 4.9.

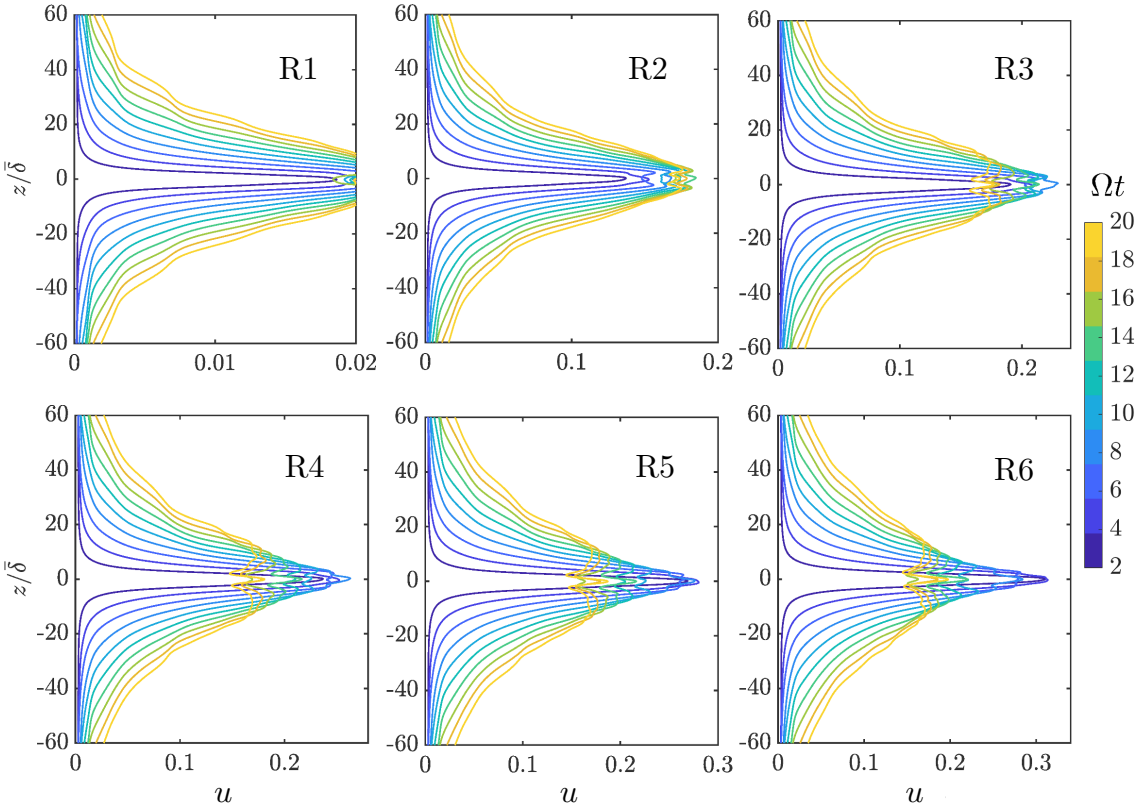

Fig. 4.14 Plane-averaged r.m.s. velocity for $2 \leq \Omega t \leq 20$.

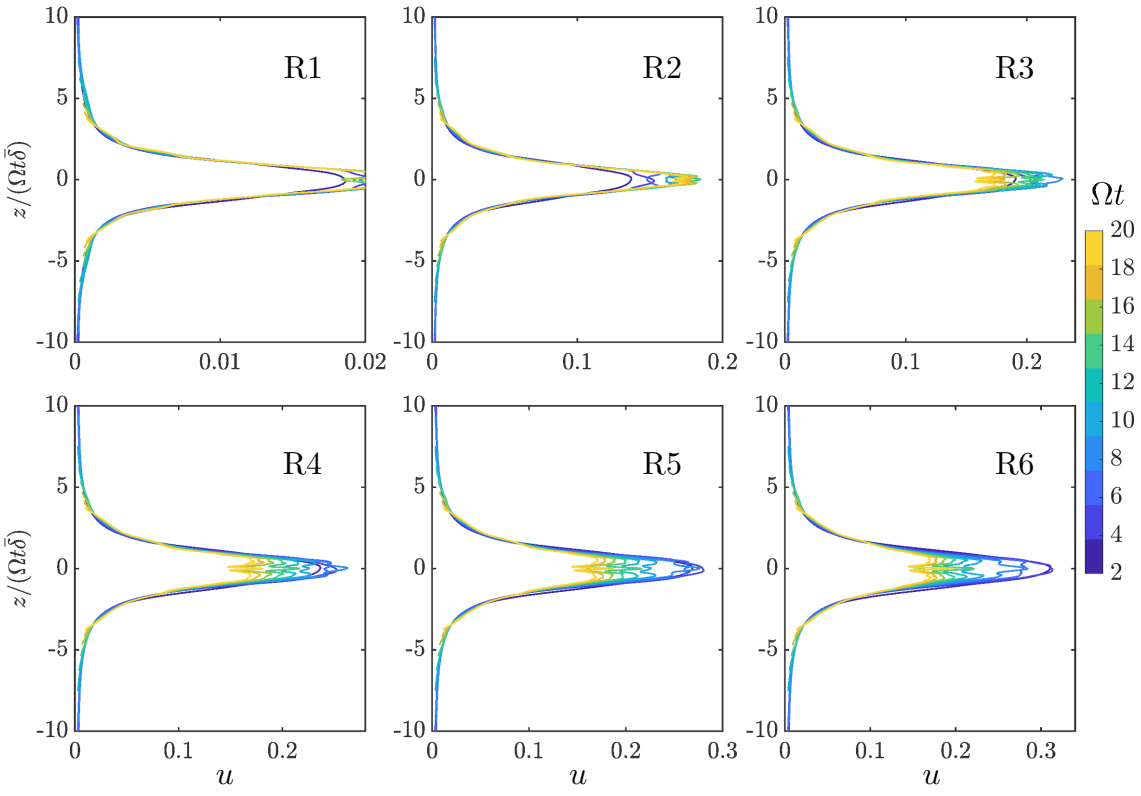

Fig. 4.15 As in figure 4.14, but now the left ordinate is normalised by Ωt.

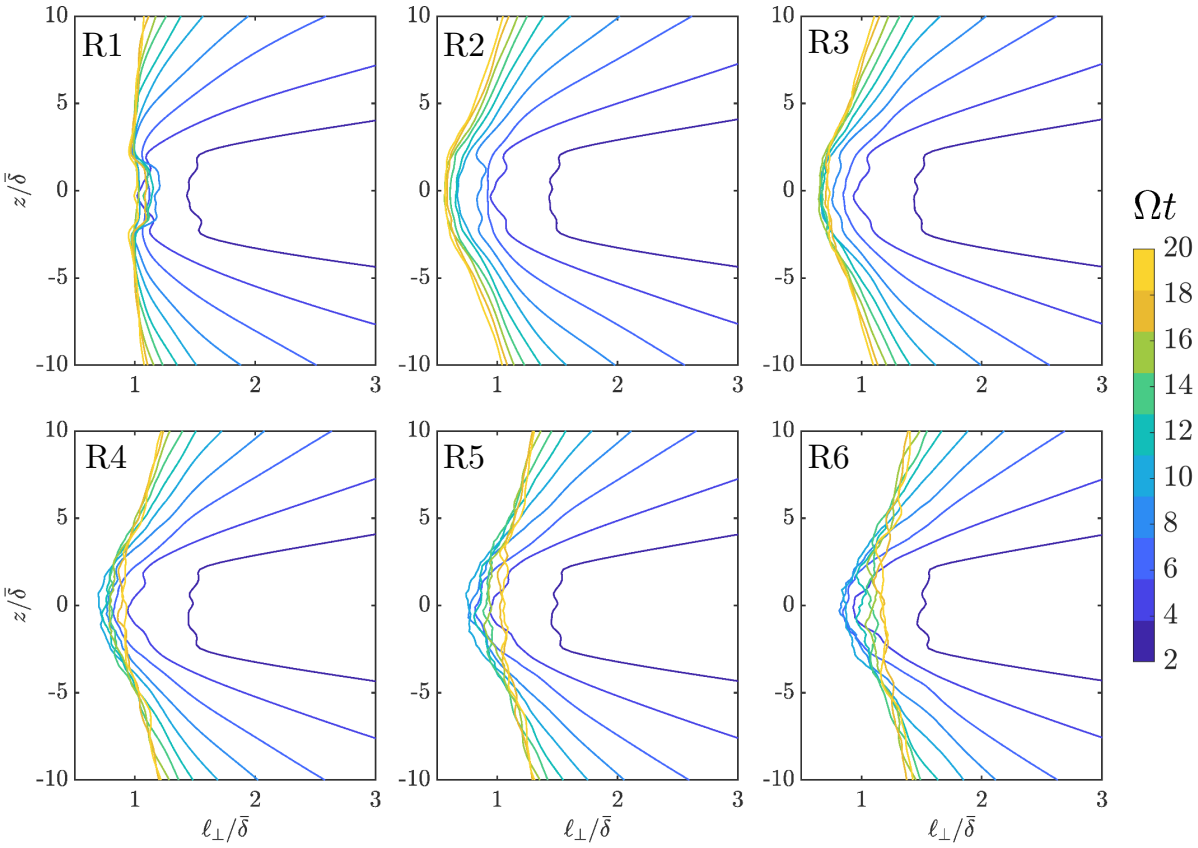

Fig. 4.16 The perpendicular length scale for $2 \leq \Omega t \leq 20$.

The temporal decline of $\ell_\perp/\bar{\delta}$ in the wave-field for all runs is expected. On inspection of the group velocity relation for low frequency inertial wave packets, we see that energy launched with a larger perpendicular length scale travels faster, and that $c_g \sim \Omega \ell_\perp^0$ where the superscript 0 denotes $\ell_\perp$ at the launch time. So, at a given z, the wave packets that arrive first are the broadest, and as time progresses narrower wave packets arrive.

Helicity

The isosurfaces of vorticity coloured by relative helicity (see figure 4.6) show that for all runs the helicity in the wave-field is segregated negative (positive) in the upper (lower) part of the box. However, for runs R2–6 the helicity distribution in the buoyancy/turbulence region is more complex. The turbulence in this region suggests that inertial waves are no longer the dominant feature of the flow, therefore we may expect less segregation of helicity.

Figure 4.17 shows the relative helicity $h_k^* = \boldsymbol{u} \cdot \boldsymbol{\omega}/|\boldsymbol{u}||\boldsymbol{\omega}|$ at $\Omega t = 16$ for runs R1, R3 and R5 in the plane $z = 3\bar{\delta}$, at the upper edge of the initial buoyant cloud. For R1, h_k^* is

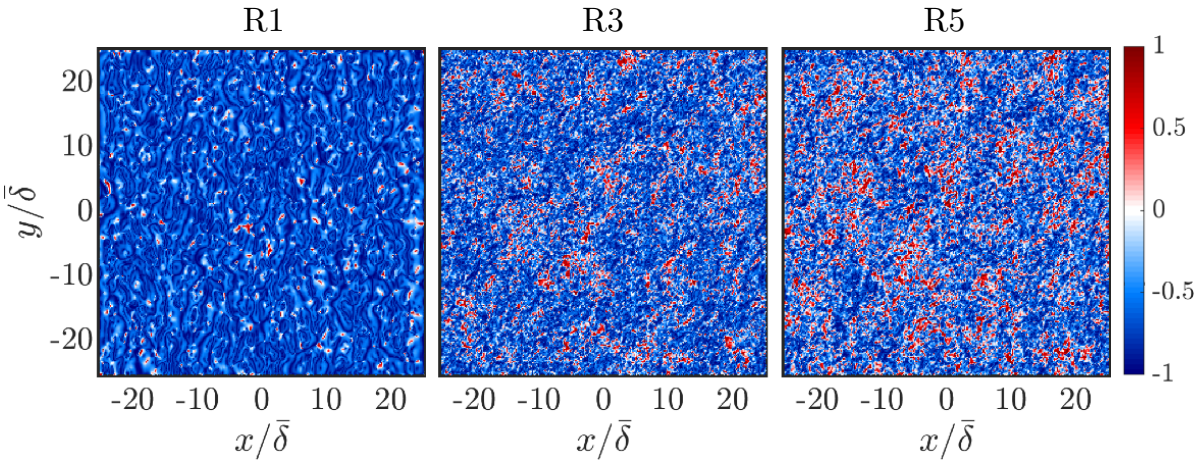

Fig. 4.17 Relative helicity at $\Omega t = 16$ in the plane $z = 3\bar{\delta}$ for runs R1, R3 and R5.

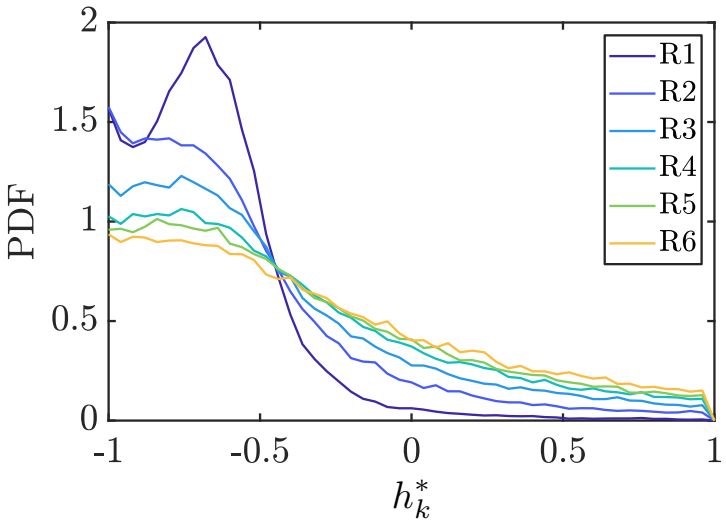

Fig. 4.18 Approximate probability density function of relative helicity h_k^* at $z = 3\bar{\delta}$ and $\Omega t = 16$.

almost entirely negative, indicating a high degree of helicity segregation. However, at larger Rossby number the helicity is progressively less segregated, due to the advancement of the turbulence to larger $|z|/\bar{\delta}$. This is clear from the approximate probability density function (PDF) of relative helicity at the same height $z = 3\bar{\delta}$ and the same time $\Omega t = 16$ (see figure 4.18). For R1 the PDF peaks at $h_k^* = -0.64$ and has a large positive skewness of 1.6. The PDFs for R2–6 are progressively less skewed, for R6 the skewness has reduced to 0.8.

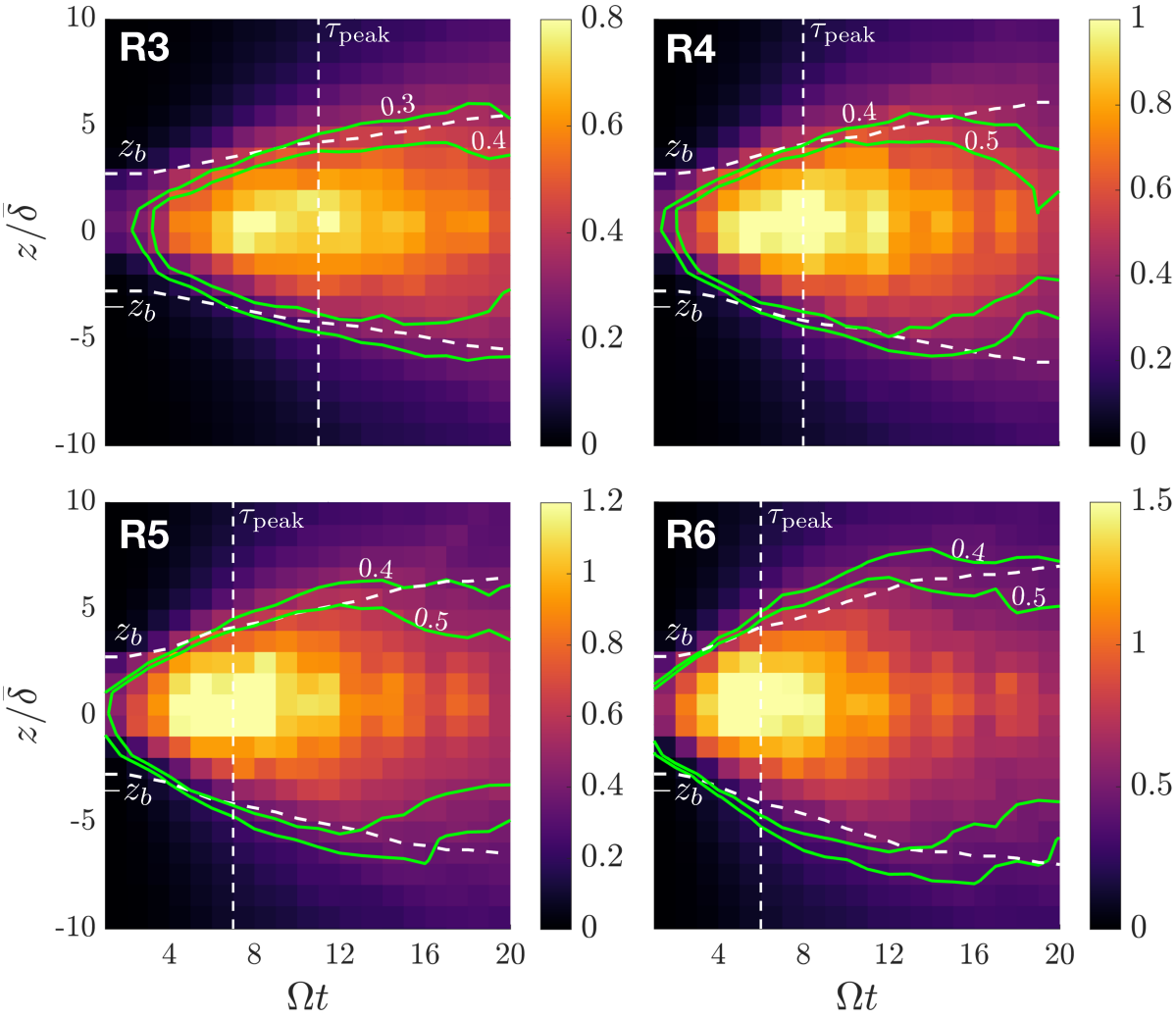

Fig. 4.19 Rossby number (colour scale) based on $\ell_\perp$ for $|z| < 10\bar{\delta}$ and $1 \leq \Omega t \leq 20$, the green contours are labelled by their value of Ro. The dashed white vertical lines indicate the time corresponding to the peak of dissipation, and the roughly horizontal dashed white lines show the extent of the buoyancy/turbulence region, $-z_b$ and z_b.

4.2.3 Transition Rossby number

Just as we can look at the perpendicular length scale through height and time, we can now examine $Ro = u/2\Omega\ell_\perp$. This quantity is derived from plane-averaged velocities and perpendicular length scales (§4.2.2), so it depends on $z/\bar{\delta}$ and time. Figure 4.19 shows the spatio-temporal variation of this Rossby number, indicated by the colour scale, for $1 \leq \Omega t \leq 20$ and $|z| < 10\bar{\delta}$, including green contours labelled by their Ro value. For R1 (not shown), at low-Ro, there is no turbulent region, and $Ro < 0.03$ everywhere at all times. This is expected as we are firmly in the linear regime and figure 4.6 (R1) shows no signs of transition to turbulence. As the initial buoyant perturbations are increased,

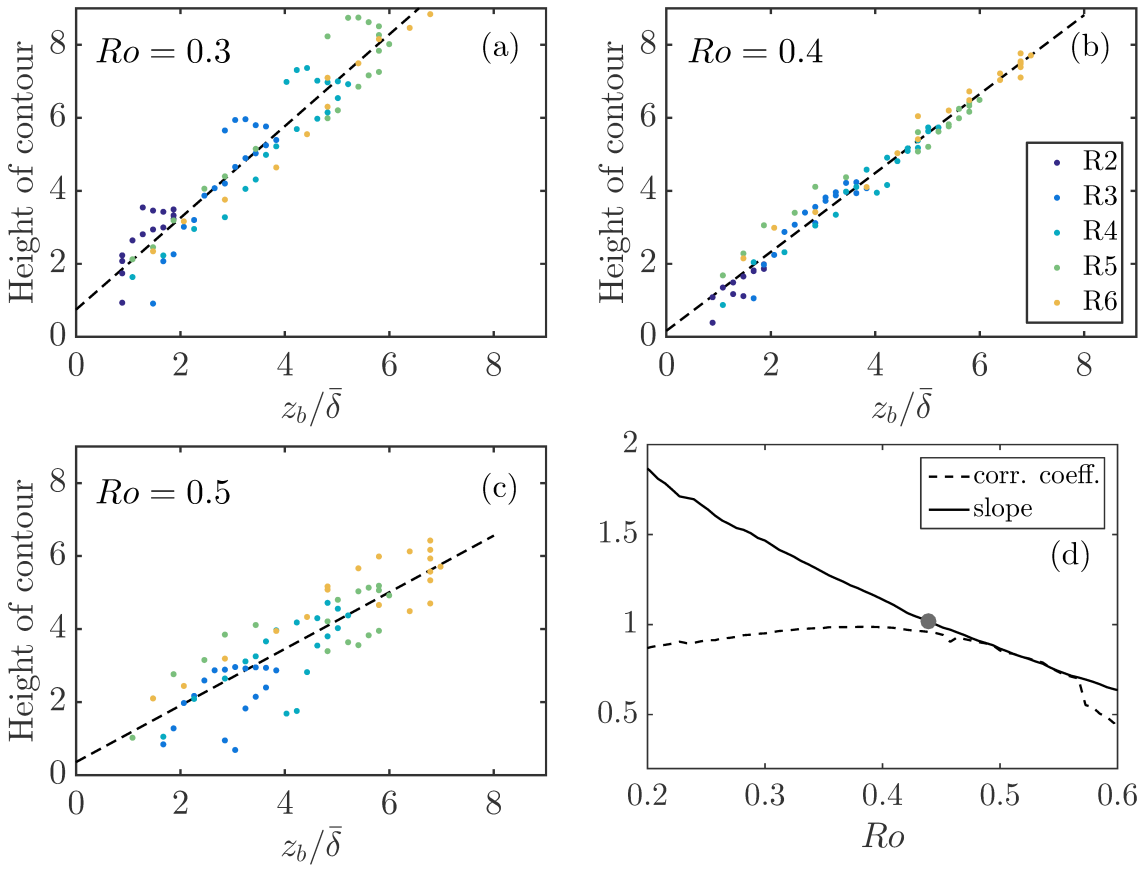

Fig. 4.20 (a-c) Comparison of the extent of the buoyancy/turbulence region $z_b/\bar{\delta}$ and the contour height for $Ro = 0.3$, 0.4, 0.5 respectively (see green contours figure 4.19) for runs R2–6. The dashed lines show the linear best fit. (d) The correlation coefficient and slope for values of $0.2 \leq Ro \leq 0.6$, the grey dot marks a slope of 1.

there is a region in the centre of the box where $Ro \gtrsim 0.4$, this is highlighted by the Ro contours. This is mimicked by the turbulent region we see in figures 4.5 & 4.6 in the centre of the box. The vertical white dashed lines mark the peak of dissipation in the mid-plane τ_{peak} for each run (see §4.2.2), this time approximately intersects the maximum Ro value for R2–6. The white dashed lines running from left to right show the buoyancy/turbulence region $\pm z_b$. Apart from early times, where $\pm z_b$ marks the initial cloud size, these lines approximately follow the Ro contours shown, $Ro = 0.3$, 0.4, 0.5. The value of the Ro contour which lies closest to $\pm z_b$ increases slightly from R3–6, but is always in the range $0.3 \leq Ro \leq 0.5$. This suggests that the buoyancy/turbulence region is approximately bounded by some critical Ro^{crit} value, within which rotation is not dominant and negligible energy is transported by inertial waves.

If we compare the extent of the cloud of turbulence $z_b/\bar{\delta}$ with the height of the $Ro = 0.4$ contour at each time $1 \leq \Omega t \leq 20$ for R2–6, we can see how good a match

this is. Figure 4.20 (a-c) compares $z_b/\bar{\delta}$ with the height of three sets of Ro contours, $Ro = 0.3$, 0.4, 0.5. Clearly for all three there is a positive correlation, and (a) and (c) are scattered slightly more than (b), the comparison at $Ro = 0.4$. Note that here we are looking not only for minimal scatter, but for a one-to-one correspondence: i.e. a linear relationship with a slope of unity. Therefore, we have computed the correlation coefficient between $z_b/\bar{\delta}$ and the contour heights, and the slope of the best linear fit for $0.2 \leq Ro \leq 0.6$, to find the critical Ro that best fits these data (see figure 4.20d). The correlation coefficient is greater than 0.9 for $0.25 \leq Ro \leq 0.48$, and peaks at $Ro = 0.39$. There is a drop to a correlation coefficient of 0.5 at $Ro = 0.6$ and this continues to decrease for larger Rossby numbers. The slope of the fit is always positive in the range $0.2 \leq Ro \leq 0.6$, however the value at slope one is $Ro = 0.43$. So if we give roughly equal weight to all $0.25 \lesssim Ro \lesssim 0.48$ based on the large positive correlation coefficient, then the optimum is $Ro^{\text{crit}} \sim 0.4$. This is supported by the visual comparison in figure 4.19. It is remarkable how close this critical value of Ro is compared with those found in the laboratory experiments of Staplehurst *et al.* (2008).

4.3 Discussion

4.3.1 Geodynamo simulations

In all the simulations presented here, low-frequency inertial waves are emitted from the buoyant cloud at early times, creating columnar cyclone/anti-cyclone pairs aligned with the rotation axis. The wave-field is maintained at low-Ro, and the columnar vortices extend linearly towards the top/bottom of the box. We note that the simulations stop before the wave-field (at low-Ro) has had sufficient time for nonlinear interactions to take place. For runs R2–6, with a larger initial buoyancy perturbation, we find that a region in the vertical centre of the box becomes turbulent. We have shown that the Rossby number, Ro, holds larger values within this turbulent region due to the combined effects of an increased r.m.s. velocity (figure 4.4), and a reduction in the perpendicular integral length scale (figure 4.16). We find that this turbulent region is approximately bounded by a critical Ro contour with the value $Ro^{\text{crit}} \sim 0.4$.

The critical Rossby number we find, $Ro^{\text{crit}} \sim 0.4$ is consistent with earlier estimates from rotating turbulence (Baqui & Davidson, 2015; Sreenivasan & Davidson, 2008; Staplehurst *et al.*, 2008). This may be due to the similar practices used in this work and by the turbulence community to estimate flow length scales. The transition seen here is similar to the transition observed in the dynamo simulations of Soderlund *et al.* (2012)

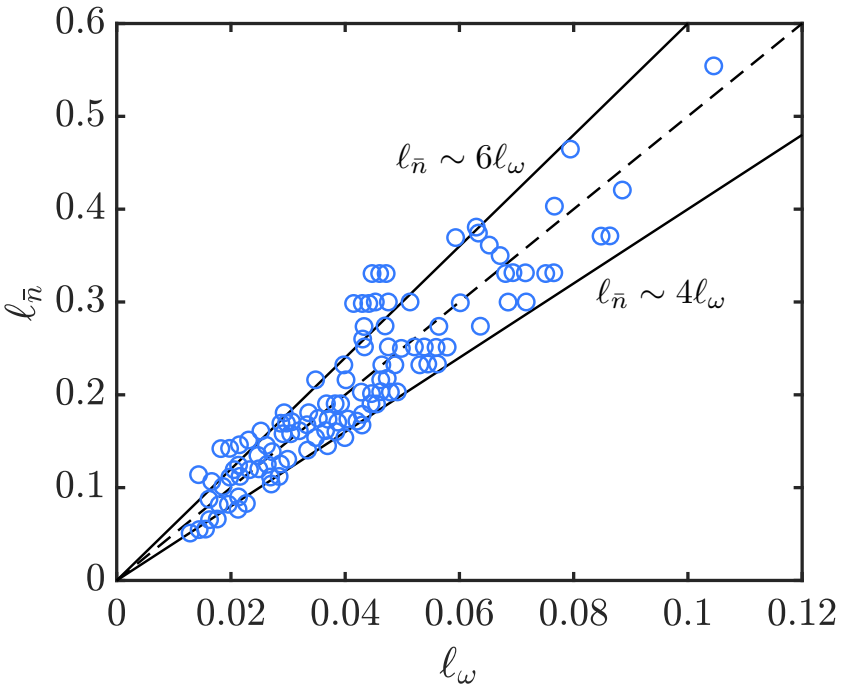

Fig. 4.21 The vorticity length scale ℓ_ω plotted against $\ell_{\bar{n}}$ for numerical dynamos in Uli Christensen's dataset, with some additions from Dormy *et al.* (2018). The solid lines are $\ell_{\bar{n}} = 4\ell_\omega$ and $\ell_{\bar{n}} = 6\ell_\omega$, and the dashed line is $\ell_{\bar{n}} = 5\ell_\omega$.

(§4.1), where a critical Rossby number of 0.1 is reported. This Rossby number is defined using the mean spherical harmonic degree in the time-averaged kinetic energy spectrum $\bar{n}$, as detailed in §4.1. The discrepancy between the value found here (and in rotating turbulence experiments), and the value observed across dynamo simulations (Christensen & Aubert, 2006; Kutzner & Christensen, 2002; Soderlund *et al.*, 2012, $Ro^{\text{crit}} \sim 0.1$), is likely caused by the definition of the length scale used in the local Ro.

The local Rossby number defined by Christensen & Aubert (2006) (and often used since) attempts to express the ratio of inertial to Coriolis forces at the scale of the convection. The dimensionless length-scale here is defined as $\ell_{\bar{n}} = \pi/\bar{n}$. The calculation to acquire this length scale involves radial averaging, so it does not take radial variations into account. Indeed, as the kinetic energy spectra do not fall off rapidly, this length scale is not found to characterise flow transitions (Schaeffer *et al.*, 2017). Furthermore, the kinetic energy spectrum as a function of degree happens to be rotationally invariant, requiring that $\ell_{\bar{n}}$ is an isotropic length-scale with respect to spherical surfaces. Now experiments and numerical simulations of rapidly rotating convection have revealed that the resulting flow is highly anisotropic, namely columnar and at lower Ekman numbers, sheet-like (Kageyama *et al.*, 2008; Sumita & Olson, 2000). Therefore the length scale,

related to $\ell_{\bar{n}}$, often used by geodynamo modellers to calculate the local Rossby number is almost certainly larger than the perpendicular integral length scale – the crucial column width or the size of buoyant plumes.

For the numerical dynamos in Uli Christensen's dataset (plus some additions), Dormy *et al.* (2018) calculated the vorticity length scale $\ell_\omega^2 = \langle \boldsymbol{u}^2 \rangle / \langle \boldsymbol{\omega}^2 \rangle$ (introduced in Oruba & Dormy, 2014), where the angle brackets denote time and volume averages. For the helical columnar convection exhibited in these simulations, we have the kinematic statement $\boldsymbol{\nabla} \times \boldsymbol{u} \sim u/\ell_\perp$ (Davidson, 2014), so that ℓ_ω is predominantly a measure of the column width. For this dataset we may consider the relationship between these two length scales $\ell_{\bar{n}}$ and ℓ_ω, as depicted in figure 4.21. There is an approximately linear relationship with $\ell_{\bar{n}} \sim 5\ell_\omega$, indicated by the dashed line (a linear regression gives $\ell_{\bar{n}} = 4.8\ell_\omega$). The solid lines $\ell_{\bar{n}} \sim 4\ell_\omega$ and $\ell_{\bar{n}} \sim 6\ell_\omega$ illustrate the sensitivity of the gradient of the fit. We return to the rotating turbulence estimate of the critical Rossby number $Ro^{\text{crit}} \sim 0.4$, and the transition in dynamo simulations which occurs at $Ro_{\bar{n}} \sim 0.1$, based on $\ell_{\bar{n}}$. Clearly this discrepancy of a factor of roughly 4 may be explained by the relationship shown in figure 4.21, where a factor of 5 is fits these data best. Indeed, Oruba & Dormy (2014) find that when the local Rossby number is based on this vorticity length, the transition between dipolar and multi-polar dynamos lies closer to 1.

Crucially, in the rotating turbulence experiments and simulations $Ro \sim 0.4$ has been identified as the point where inertial waves stop propagating. Moreover, the source of columnar structures in these studies is shown to be inertial wave propagation (Baqui & Davidson, 2015; Davidson *et al.*, 2006; Staplehurst *et al.*, 2008). This is corroborated by the results presented here for buoyancy driven rotating flows.

We have also shown for a set of dynamo simulations, that an appropriately defined convective scale Rossby number of $Ro \approx 0.5$ separates the two regimes of columnar and more three-dimensional convection. We suggest this cannot be a coincidence, and that columnar structures in dynamo simulations are sustained by the continual emission of inertial waves, originating from the buoyancy field (Davidson & Ranjan, 2015; Ranjan *et al.*, 2018). In addition, the loss of helical columnar convection when the forcing is increased ubiquitously leads to the collapse of the dipole field. We thus propose a purely hydrodynamic mechanism based on fast time-scale inertial wave propagation for the transition in flow structure and in turn, the inescapable dipole collapse.

The Prandtl number $Pr = 1$ for all these simulations, however the thermal Prandtl number is expected to be closer to 0.1 in Earth's outer core, and the compositional Prandtl number of ~ 100. Further, it is not known what fraction of the convective forcing is thermal or compositional, with estimates ranging from 50/50 thermal/compositional

to 80% compositional (Roberts & King, 2013). Therefore, investigations into the effect of varying Pr within the codensity formulation, or in so-called 'double-diffusive convection' (Bouffard *et al.*, 2017) on columnar structure formation may shed light on more realistic planetary core turbulence. For example, in the infinite Lewis number (the ratio of the thermal and compositional diffusivities) limit, buoyant plumes have a very thin filamentary structure and hence a small $\ell_\perp$.

We have neglected the magnetic field from the outset, motivated by results from previous work (Christensen & Aubert, 2006; Kutzner & Christensen, 2002; Soderlund *et al.*, 2012), however in Earth's core magnetic energy should be much greater than kinetic. Moreover, dissipation is expected to be almost entirely Ohmic, and the presence of a large scale field will cause anisotropy in velocity structures. Therefore, even though the mechanism for the transition is believed to be hydrodynamic in origin, the energy and length scales involved will be modified by the magnetic field. For example, Ohmic dissipation will stunt and morph magnetically modified helical waves from columnar structures into platelets, introducing another degree of anisotropy into the system. The combined decrease in both kinetic energy and (perpendicular) length scale will have an unpredictable effect on the local Ro. Under the influence of a magnetic field, the properties of inertial waves are modified, the resulting waves are termed magnetic-Coriolis waves (Bardsley & Davidson, 2016, 2017) (within which magnetostrophic waves are a subset). These magnetically modified waves have a slower group velocity, with intermediate waves travelling roughly half as fast as pure inertial waves, and magnetostrophic waves much slower. However, all such classes of waves segregate helicity in the same way as inertial waves.

4.3.2 M-dwarf stars

M-dwarf stars are young, low-mass stars, that are thought to be fully convective; that is, they convect throughout the majority of their radius. Importantly for us, measurements of their rotation periods suggest they rotate rapidly, and thus the dynamics of their interiors may be influenced by inertial wave propagation. This is in contrast to the Sun, where the central thermonuclear core and radiative zone occupy a large fraction of the solar radius, and the convection may only be strongly affected by rotation at the large-scales. By virtue of their rapid rotation and deep convection zone, it is thought that the dynamos of M-dwarf stars may operate in a broadly similar way to those of the planets (Brun & Browning, 2017). For example, figure 4.22 illustrates a reconstruction of the radial magnetic field of V734 Pegasi; the magnetic field is strong and dipolar. However, one important difference is the strong density stratification that is expected to

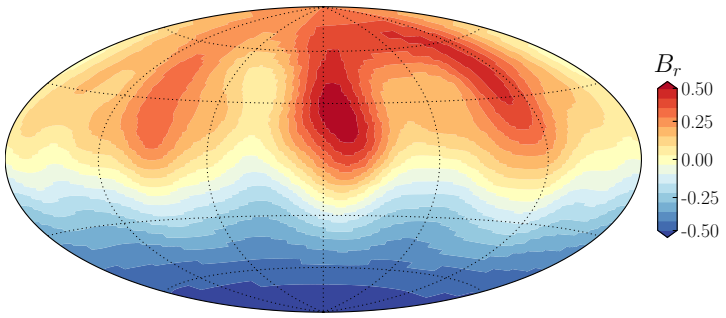

Fig. 4.22 Map of the radial magnetic field of the M-dwarf star V374 Pegasi reconstructed up to $n = 11$, from Gastine *et al.* (2013).

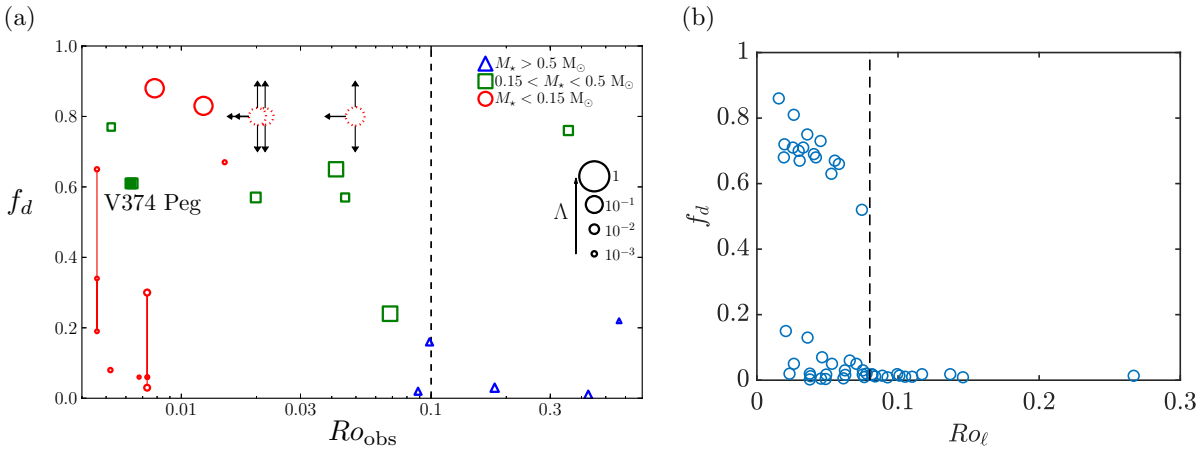

Fig. 4.23 Dipolarity – local Rossby number plot for (a) observations of M-dwarf stars from Gastine *et al.* (2013) and (b) anelastic dynamo models (Gastine *et al.*, 2012). In (a) the colours separate stars of different masses, larger symbols correspond to a stronger magnetic field, and the closed symbol highlights the M-dwarf V374 Pegasi featured in figure 4.22. In (b) the dashed line highlights $Ro_\ell = 0.08$.

be present in stellar interiors, so the Boussinesq approximation is no longer valid. The anelastic approximation is the next best thing, where the background thermodynamic variables are not constant, but may be radially stratified, and acoustic waves remain filtered out of the equations (Glatzmaier, 2013). The simulations discussed below are in the anelastic approximation. Another difference in the numerical modelling of stellar and planetary interiors is the outer boundary condition on the velocity field. Most geodynamo models opt for a no-slip condition, whereas models of stars use a stress-free condition, as is more relevant to the outer regions of a gaseous star.

There is some tentative evidence for a similar dipolar-multipolar transition in the observations and simulations of rapidly rotating M-dwarf stars (Gastine *et al.*, 2013). Figure 4.23a shows observational data for the dipolarity of M-dwarf stars of various

masses. The dipolarity is plotted against the 'observed' Rossby number $Ro_{\rm obs} = P/\tau_c$, where P is the rotation period and τ_c is the *empirical* turnover time of the convection, which is derived from a relationship between the X-ray emissions of the star and its rotation rate (Kiraga & Stepien, 2013). The empirical turnover time is therefore rather uncertain. The stars are grouped into three categories based on the mass of the star $M_\star$ (in units of the solar mass $M_\odot$), indicated in the legend. All early M-stars (with $M_\star > 0.5M_\odot$) observed are relatively slow rotators and lie in the multipolar regime. The observations of mid M-stars ($0.15M_\odot < M_\star < 0.5M_\odot$) display a possible dipolar-multipolar transition, with the exception of one outlier in the upper-right quadrant. Late M-stars ($M_\star < 0.15M_\odot$) appear to have two different morphologies. Some have a strong dipolar magnetic field, while others have weaker multipolar magnetic fields that exhibit significant time-variability (indicated by the lines connecting points in the bottom left).

In Gastine *et al.* (2013), these observations are compared to a suite of anelastic dynamo simulations with a variety of density contrasts across the shell, at $E = 10^{-4}$. A similar transition at $Ro_\ell \sim 0.1$ is reproduced in the anelastic simulations (figure 4.23b), up to moderate strengths of background density stratification (where Ro_ℓ is defined as in Christensen & Aubert (2006)). These models use stress-free boundary conditions, as may be appropriate for stellar applications, and this type of velocity condition has been shown to produce a 'bistability' in the magnetic field morphology. The bistability was first observed in the Boussinesq simulations of Simitev & Busse (2009), where the magnetic field was found to saturate in a dipolar or a multipolar state—for the same parameters—depending on the initial conditions of the simulation. We note the bistability is only observed when stress-free conditions on the velocity field are used. This phenomenon is also observed in the anelastic simulations, illustrated by the points to the left of $Ro_\ell = 0.08$ in figure 4.23b, where dipolar and multipolar dynamos are found. That said, no dipolar solutions were found for $Ro_\ell > 0.08$, indicating a similar transition as in the Boussinesq case.

The mechanism presented in this chapter—based on the suppression of inertial waves at $Ro \approx 0.5$—may be applicable to M-dwarf stars and to dynamo simulations with a moderate background density stratification. M-dwarfs with a mass $M_\star < 0.15M_\odot$ are at small $Ro_{\rm obs}$, and we do not expect to observe the transition here. Indeed, the red markers in figure 4.23a do not fit our picture. However, M-dwarfs with $M_\star > 0.15M_\odot$ (blue and green points in figure 4.23a) may show signs of a dipolar-multipolar transition with increasing $Ro_{\rm obs}$. One caveat here is that we do not know how $Ro_{\rm obs}$ and Ro_ℓ are related. Indeed, $Ro_{\rm obs}$ is derived from the empirical determination of τ_c, which is rather

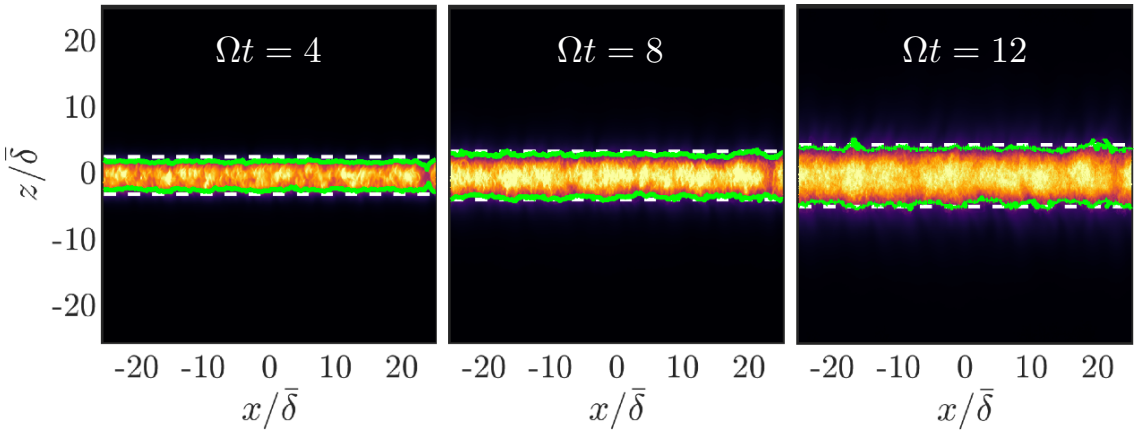

Fig. 4.24 The y-averaged Rossby number for simulation R5, at $\Omega t = 4$, 8, 12, where bright colours indicate larger $\langle Ro \rangle_y$. The green contour highlights $\langle Ro \rangle_y = 0.4$, and the white dashed lines bound the buoyancy/turbulence region.

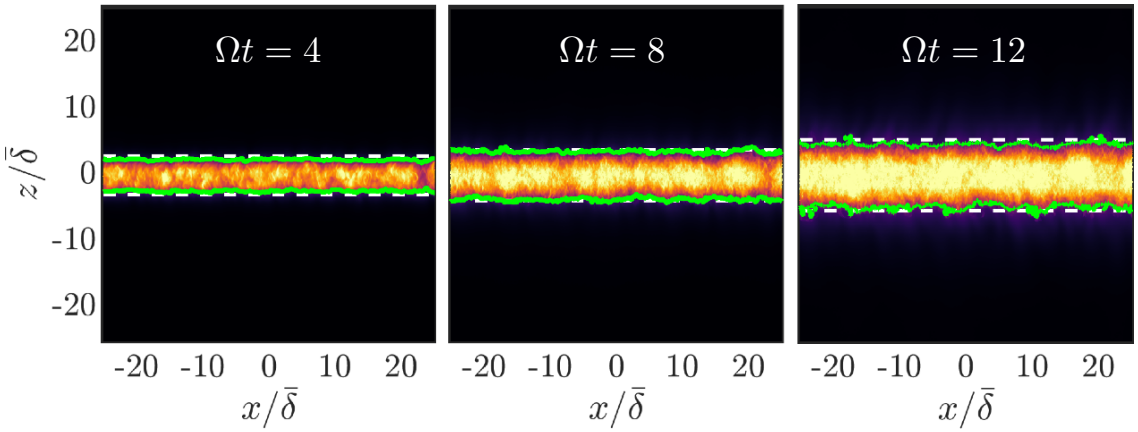

Fig. 4.25 As in figure 4.24, for simulation R6.

uncertain. However, the fact that observations are available, although uncertain, provides a unique opportunity for further work.

4.4 Summary

In this chapter we address the influence of nonlinear inertia on the maintenance of columnar structures by inertial wave propagation. Our simulations at moderate Rossby numbers reveal an abrupt transition in the morphology of flow structures at the critical threshold $Ro^{\mathrm{crit}} \approx 0.4$. To highlight the sharp transition in physical space, we show images of $\langle Ro \rangle_y$ for simulations R5 & R6 in figures 4.24 & 4.25, for three representative times. Lighter colours are larger $\langle Ro \rangle_y$, the green contour highlights $\langle Ro \rangle_y = 0.4$,

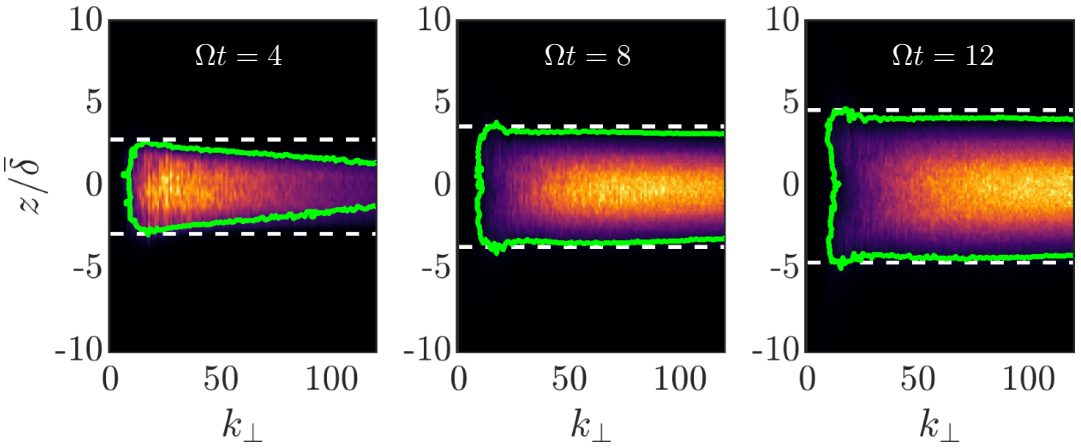

Fig. 4.26 Rossby number spectra for simulation R5 at each height, for $\Omega t = 4$, 8, 12, where brighter colours indicate larger $\mathcal{R}$. The colourmap shows $\mathcal{R}(k_\perp, z)$, the green line highlights $\mathcal{R} = 0.4$, and the dashed lines show the extent of the buoyancy/turbulence region.

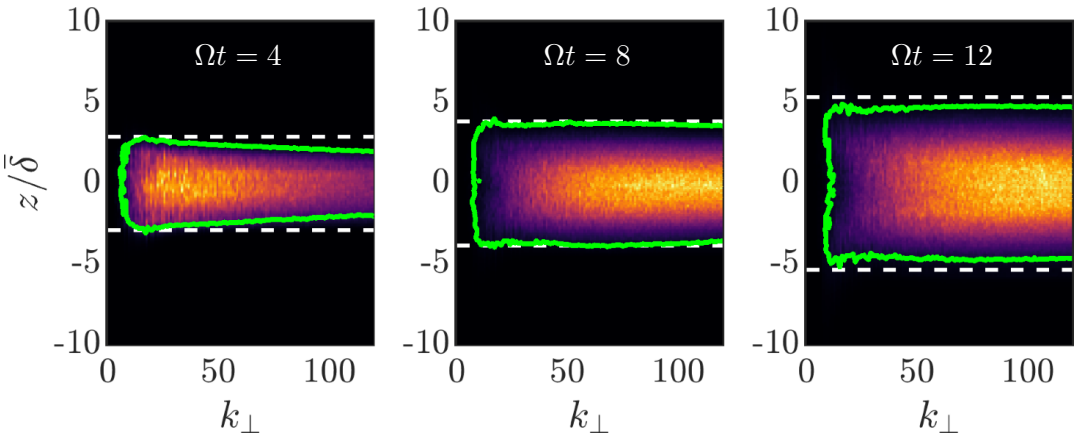

Fig. 4.27 As in figure 4.26, for simulation R6.

and the white dashed lines bound the buoyancy/turbulence region. The wave-field is at low-*Ro* throughout, and the Rossby number quickly increases at the edge of the buoyancy/turbulence region, within which the flow is incoherent.

The transition in spectral space is also distinctly abrupt, and this can be seen through the Rossby number spectra

$$\mathcal{R}(k_\perp) = \frac{(2E_\perp)^{1/2}\, k_\perp}{2\Omega}\,. \tag{4.7}$$

Figures 4.26 & 4.27 show $\mathcal{R}(k_\perp, z)$ (the colourmap) for R5 & R6, where the green contour highlights $\mathcal{R} = 0.4$, and the white dashed lines bound the buoyancy/turbulence region. Almost all the energy in the flow with $\mathcal{R} > 0.4$ is contained inside the buoyancy/turbulence region, within which the flow is turbulent. In the wave-field, however, $\mathcal{R} \ll 1$ and the

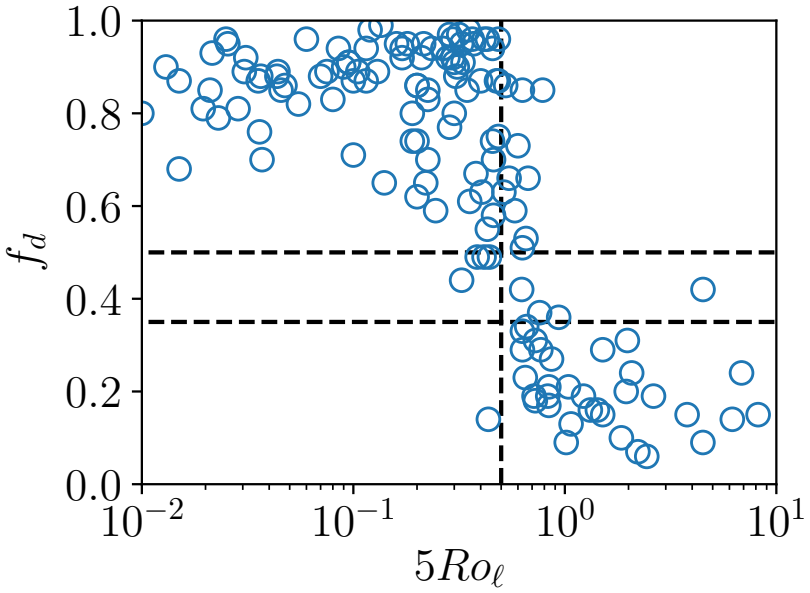

Fig. 4.28 Variation of f_d with $5Ro_\ell$ for the dynamos in Uli Christensen's dataset. The horizontal dashed lines highlight $f_d = 0.35$ and $f_d = 0.5$, and the vertical dashed line is at $5Ro_\ell = 0.5$.

transition at the boundary separating inertial wave packets and the turbulence is quite sharp.

There is a similar transition in flow morphology in geodynamo simulations, which occurs at a local Rossby number of $Ro_\ell \sim 0.1$ (Christensen & Aubert, 2006; Soderlund *et al.*, 2012). However, the length-scale used to define the local Rossby number overestimates the width of convective structures, lowering the value of Ro_ℓ with respect to Ro. By introducing a proxy for the perpendicular length-scale in these simulations, namely ℓ_ω, we have shown that the transition is shifted closer to $Ro \sim 0.5$ (figure 4.21). We have plotted the variation of f_d with $5Ro_\ell$ for 318 numerical dynamos from Uli Christensen's dataset in figure 4.28. The reduction in dipolarity at $Ro \approx 5Ro_\ell \approx 0.5$ describes the data well. This is consistent with the evidence presented here on the suppression of inertial wave propagation by the influence of nonlinear inertia. For increased buoyant forcing, the r.m.s. velocity increases and small length-scales in the flow are excited. Both of these effects impede the efficiency of inertial wave propagation, and this leads to incoherence in the velocity field. The disorganisation of the flow results in a disorganisation of the magnetic field, and the loss of dipolarity. Thus, we propose a purely hydrodynamic mechanism based on fast time-scale inertial wave propagation for the transition in flow structure, which is followed by the dipole collapse.

Chapter 5

Magnetic-Coriolis waves in a uniform transverse field

In this chapter, which contains work that is (at the time of writing) under review in McDermott & Davidson (2020), we address the influence of a large-scale magnetic field on the dispersion of inertial and MC wave packets from buoyant anomalies. The simulations presented here are all at low Rossby number, as is relevant for Earth's outer core. In contrast to the previous chapter, there is little influence from nonlinear inertia. The additional dynamics here are due to the addition of a transverse magnetic field, which reveals a spectrum of MC waves as described in chapter 2. We are interested in the properties of the modified wave packets, including their helicity and the induced emf due to the interaction with the large-scale field.

These simulations build on previous work by Davidson & Ranjan (2015) on the emf generated by a sea of inertial wave packets launched from a layer of buoyant anomalies. This earlier work considered the low magnetic Reynolds number case, where the magnetic fluctuations are not explicitly computed, but are derived from $\eta\boldsymbol{\nabla}^2\boldsymbol{b} = -(\boldsymbol{B}_0\cdot\boldsymbol{\nabla})\boldsymbol{u}$, a low-$Rm$ version of Ohm's law. It is not clear that the small-scales in Earth's core are characterised by $Rm \lesssim 1$. Using the estimates for Earth's core given in chapter 1, the magnetic Reynolds number based on $\ell = 10$ km is $Rm \sim 5$. Here, the full rotating MHD equations are solved, and we calculate the emf explicitly.

5.1 Introduction

The properties of monochromatic MC waves were explored in chapter 2. We noted that in the hydrodynamic case, inertial waves with $\boldsymbol{\Omega}\cdot\boldsymbol{k} \approx 0$ dominate the dispersion pattern, with a high energy density. This observation explains the initial formation of

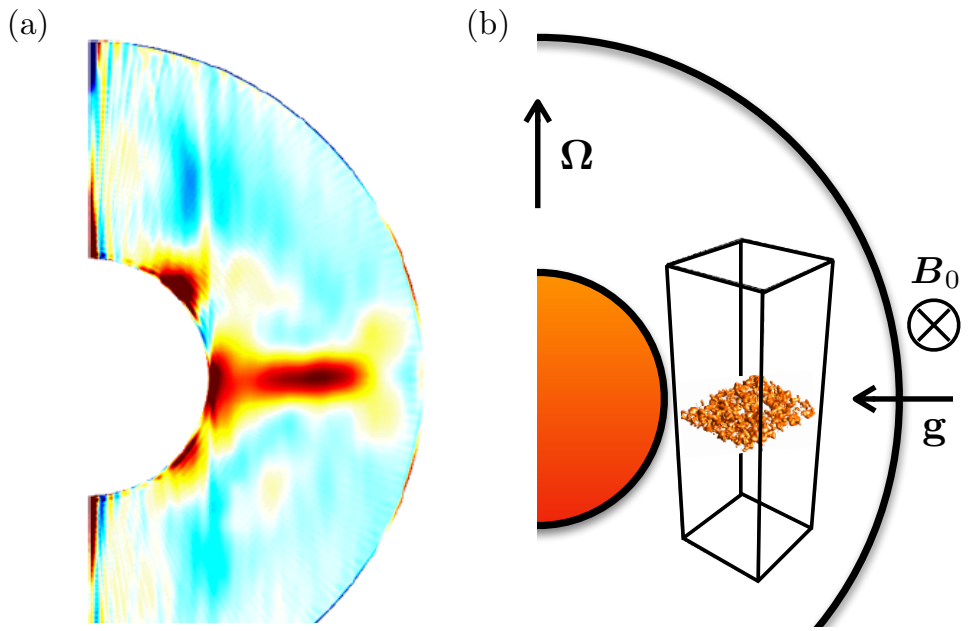

Fig. 5.1 The numerical set-up and its motivation. (a) An image from Sakuraba & Roberts (2009) showing an equatorially biased heat-flux. (b) We approximate the equatorial regions of a spherical shell with $\boldsymbol{\Omega} \perp \mathbf{g} \perp \boldsymbol{B}_0$, and the equatorially biased heat-flux is modelled as a layer of buoyant anomalies. This figure is a reproduction of figure 3.2.

columnar structures in a rapidly rotating fluid (Davidson *et al.*, 2006). In an electrically conducting fluid, any component of a large-scale field perpendicular to the rotation vector converts inertial waves into inertial-Alfvén waves. Inertial-Alfvén (IA) waves have an axial group speed of Ω/k, which is half the speed of a low-frequency inertial wave packet $2\Omega/k$. These waves have a component of their group velocity in the direction of the large-scale field, with a magnitude equal to the Alfvén velocity. There are other wave types which will play a role in the dispersion of energy: off-axis weakly modified inertial waves, intermediate MC waves, and magnetostrophic waves. However, the small group velocity of magnetostrophic waves renders them hard to detect on time-scales on the order of $10\Omega^{-1}$.

We perform DNS of a rapidly rotating Boussiesq fluid in a box elongated in the direction of the rotation vector, much like the set-up described in chapter 4. However, there is now a uniform transverse magnetic field $\boldsymbol{B}_0 = B_0\boldsymbol{e}_x$, that is orthogonal to both gravity $\mathbf{g} = g\boldsymbol{e}_y$ and the rotation vector $\boldsymbol{\Omega} = \Omega\boldsymbol{e}_z$. The motivation for this arrangement is illustrated in figure 5.1: where (a) is an equatorially biased heat-flux from a geodynamo simulation and (b) shows the box set-up with $\boldsymbol{\Omega} \perp \mathbf{g} \perp \boldsymbol{B}_0$. The case of an axial field yields trivial results, as inertial waves are only modified by transverse field components.

Bardsley (2019) showed that, with an axial field, after the passage of inertial wave packets, magnetostrophic waves can be observed in the dispersion pattern only on long time-scales, which we will not be able to reach with our simulations. We are interested in the regime of low Rossby number $Ro = u/2\Omega\delta$, while varying the relative strength of the large-scale field. As shown in chapter 2, we expect to observe a spectrum of modified wave-types in the presence of a large-scale magnetic field. All MC waves segregate kinetic helicity negative (positive) above (below) their source, as required for a helical wave dynamo. However, the effect of a large-scale magnetic field on the induced emf (and corresponding α-effect) is unclear. Where the linear diffusionless analysis of Bardsley & Davidson (2016) explored the dispersion pattern of MC waves launched from a buoyant blob, our simulations are better placed to investigate the (nonlinear) emf. Moreover, the MC waves have a component of their group velocity in the direction of the mean-field. Thus, with a transverse field, in the case of the buoyant cloud initial condition, we expect more horizontal mixing of wave packets compared to the hydrodynamic case.

5.2 Dispersion of waves from a single buoyant blob

Before looking at the dispersion of waves from a random sea of buoyant anomalies it is instructive to consider the case of a single buoyant blob. The set-up is as described above: $\boldsymbol{\Omega} = \Omega\boldsymbol{e}_z$, $\mathbf{g} = \mathrm{g}\boldsymbol{e}_y$ and $\boldsymbol{B}_0 = B_0\boldsymbol{e}_x$, in which rotation, gravity and a uniform magnetic field are mutually orthogonal. We numerically integrate the full rapidly rotating Boussinesq MHD equations from the initial conditions $\boldsymbol{u} = \boldsymbol{b} = \mathbf{0}$, with a single buoyant blob at the origin, which has an initially Gaussian profile $\rho' \sim \exp[-|\boldsymbol{x}|^2/\delta^2]$ (as described in chapter 3). Here $\boldsymbol{x}$ is the position vector and δ is the blob size. The ratio of Alfvén to inertial frequencies is expressed by the Lehnert number $Le = B_0/\Omega\delta$, and the Lundquist number $Lu = B_0\delta/\eta$ measures the ratio of the magnetic diffusion time-scale to the time-scale of Alfvén waves. Estimates of Le and Lu for the small-scales in Earth's outer core lie in the ranges $Le \sim 0.001 - 0.1$ and $Lu \sim 100 - 1000$ (see chapter 2). These estimates are very sensitive to the hidden azimuthal magnetic field strength (~ 3 mT, Gillet *et al.*, 2010), and the flow length-scale perpendicular to the rotation axis (~ 10 km, Davidson, 2014). Note that the transverse convective length scale in Earth's core was recently estimated at ~ 30 km (Guervilly *et al.*, 2019), which results in $Le \sim 0.01$. A parameter often referenced in the literature, which doesn't include a length scale, is the Elsasser number $\Lambda = LeLu$, and we expect $\Lambda \sim 10$ for Earth's dynamo. First, we set $Le = 0.1$ and $Lu = 160$ (so $\Lambda = 16$), as these choices illustrate the key wave

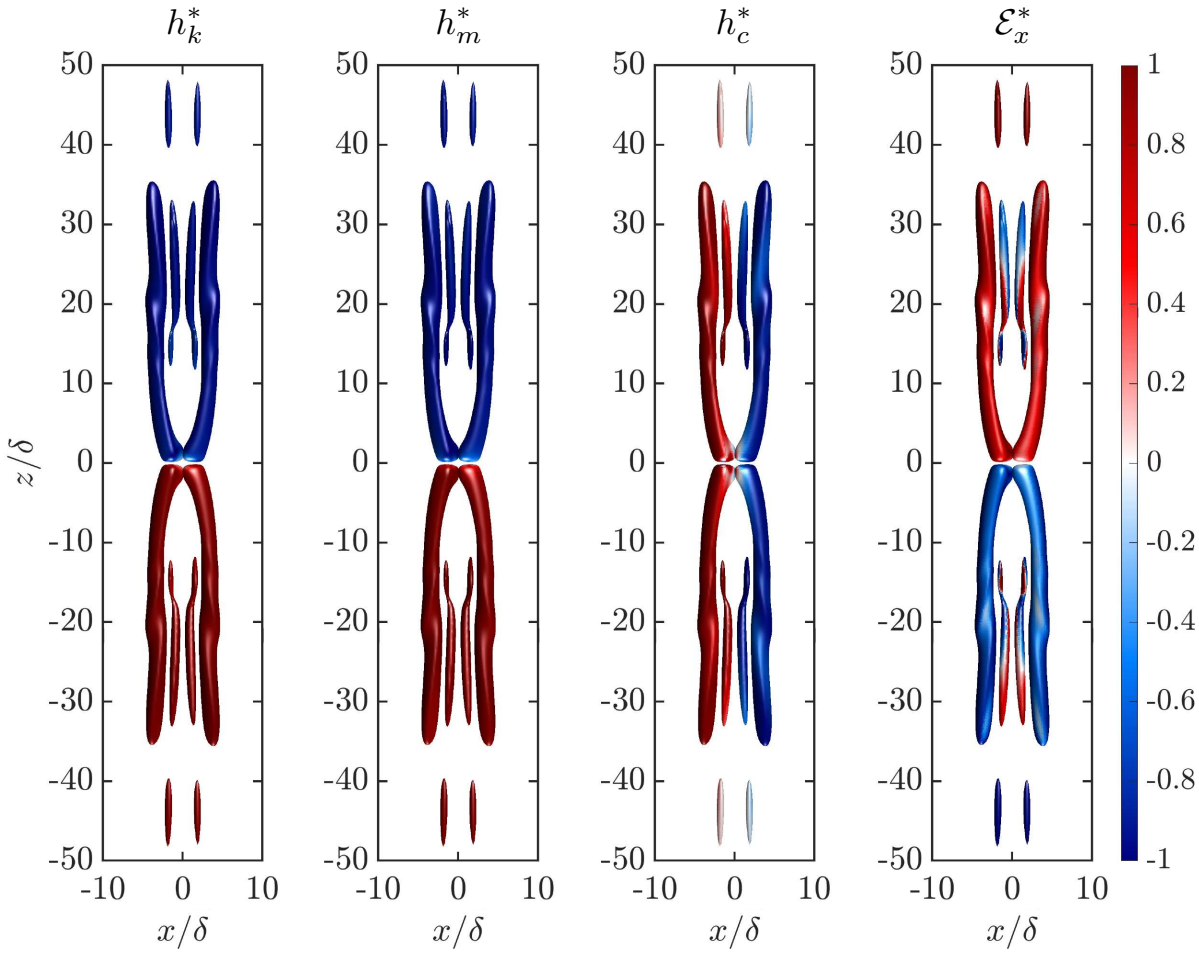

Fig. 5.2 Buoyant blob source at $Le = 0.1$. Axial velocity isosurfaces at $\Omega t = 30$ coloured by relative kinetic helicity h_k^*, relative magnetic helicity h_m^*, relative cross helicity h_c^* and the normalised emf in the x-direction $\mathcal{E}_x^*$ (left to right).

dynamics in a reasonable amount of simulation time. (See also simulation S4 with the same parameters later in §5.3).

We stop the simulation after $30\Omega t$ and inspect the dispersion pattern, as illustrated in figure 5.2. We show isosurfaces of $\pm u_z$ coloured by $h_k^* = h_k/|\boldsymbol{u}||\boldsymbol{\omega}|$, $h_m^* = h_m/|\boldsymbol{a}||\boldsymbol{b}|$, $h_c^* = h_c/|\boldsymbol{u}||\boldsymbol{b}|$ and the normalised emf in the x-direction: $\mathcal{E}_x^* = (\boldsymbol{u} \times \boldsymbol{b})_x/|\boldsymbol{u} \times \boldsymbol{b}|$. From (2.17), we expect to see axially elongated wave packets with a high energy density, that have moved horizontally to $\pm x/\delta \approx Le(\Omega t) \approx 3$. The isosurfaces shown in figure 5.2 are consistent with this prediction. As expected from the analysis above, kinetic and magnetic helicity are cleanly segregated negative (positive) above (below) the buoyant blob. The normalised fluctuating emf in the x-direction, $\mathcal{E}_x^*$, is segregated in the opposite way to h_k and h_m, with positive (negative) emf being transported above (below) the blob. The normalised emf has a smaller magnitude than the relative helicities, and h_k^*

and h_m^* are larger in magnitude than h_c^*. The buoyancy field itself does not appreciably evolve, owing to the low value of the Rossby number $Ro = u/2\Omega\delta \approx 0.01$, where u is the characteristic velocity magnitude.

The cross helicity and the emf are the dot product and cross product of $\boldsymbol{u}$ and $\boldsymbol{b}$. It follows that their values are closely related through $|h_c|^2 + |\boldsymbol{\mathcal{E}}|^2 = |\boldsymbol{u}|^2|\boldsymbol{b}|^2$. As the quantities are squared in this relation, even when the relative cross helicity holds a large value, say ≈ 0.75, the relative emf would be respectively ≈ 0.66. With the mean-field in the x-direction we expect $\mathcal{E}_x$ to dominate the other components of the emf, and this is what we observe for the current example (figure 5.2). The wave packets generated by a single blob are permitted to induce a strong emf, in spite of the relatively large degree of alignment between $\boldsymbol{u}$ and $\boldsymbol{b}$.

Now we explore the effect of varying the Lehnert number, or equivalently the mean field strength. In figure 5.3 we show the axial velocity at $\Omega t = 30$ with the field lines $\boldsymbol{B}_0 + \boldsymbol{b}$ superimposed, in the plane $y = 0$ for three Lehnert numbers $Le = 0.01$, 0.05, 0.1. (This choice of parameters is equivalent to the simulations initialised with a layer of buoyancy: S2, S3 and S4 introduced later in §5.3). For $Le = 0.01$ (left), the magnetic field barely effects the wave dispersion, so we see transient Taylor columns growing along $\boldsymbol{e}_z$, similar to those seen in purely hydrodynamic simulations (Davidson & Ranjan, 2015; McDermott & Davidson, 2019). Weaker petals of off-axis energy are also present, due to the isotropic source spectrum, however the energy density is highest on-axis. With a stronger uniform field (say $Le = 0.1$), there is evidently a considerable effect of the magnetic field on the wave dispersion. We see similar columnar structures, but now the energy is displaced laterally off-axis due to the component of $\boldsymbol{c}_g$ parallel to $\boldsymbol{B}_0$, see (2.17). Note that the dispersion pattern observed here is indistinguishable from the diffusionless analytical results of Bardsley & Davidson (2016), with a static buoyant blob at $Le = 0.1$ (see also the detailed comparison in chapter 3). It will be important to note that for the single blob case, the wave packets propagate horizontally away from each other, and do not interact. The horizontal propagation should not be mistaken for the slow evolution of magnetostrophic waves, whose time-scale is vastly greater than $30\Omega t$ — the dynamics shown occur on the fast time-scale.

A planetary core will inevitably be packed with buoyant anomalies, slowly migrating from the centre outwards under the influence of gravity. This is not dependent on whether the convection is driven thermally or compositionally. Each one of these buoyant blobs is obliged to emit a spectrum of MC waves, carrying varying degrees of helicity (kinetic, magnetic or cross). Similarly to the hydrodynamic case, it is the self-focusing waves launched with $\boldsymbol{k} \cdot \boldsymbol{\Omega} \approx 0$ which are particularly potent at creating columnar structures

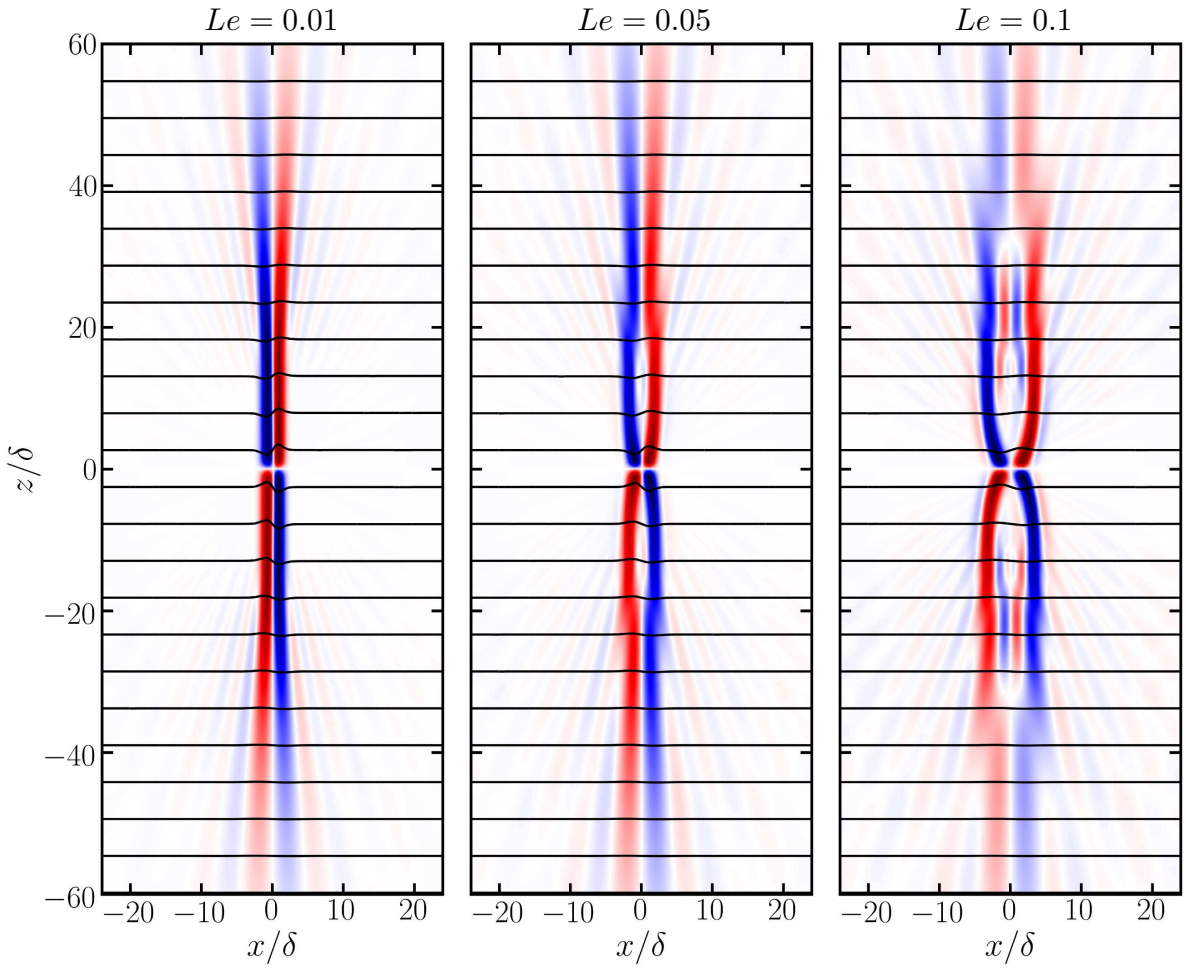

Fig. 5.3 u_z in the plane $y = 0$ at $\Omega t = 30$, gravity points into the page and the colour scale is saturated at ±85% of the maximum of $|u_z|$ in each pane. Blue (red) is negative (positive) u_z, the horizontal black lines are $\boldsymbol{B}_0 + \boldsymbol{b}$ and the Lehnert number increases from left to right. The perturbations to the field lines have been exaggerated by a factor of 10.

(figures 5.2 & 5.3), and in the presence of a uniform field it is the inertial and IA waves that assume this role. It is observed that in many of the published dynamo simulations, the r.m.s. radial velocity (Sakuraba & Roberts, 2009) and the temperature/density perturbations (Olson *et al.*, 1999; Schaeffer *et al.*, 2017) are concentrated near the equatorial plane (figure 5.1a). This observation motivates the initial conditions for the simulations presented in the next section.

5.3 Numerical simulations with a layer of buoyant anomalies

Table 5.1 Simulation parameters and estimated local values for Earth's outer core.

	Run	Le	Lu	Ro	$\Lambda = LeLu$
Not Earth-like Le	S1	10^{-8}	1.6×10^{-5}	2.8×10^{-3}	10^{-13}
Earth-like Le	S2	0.01	16	2.7×10^{-3}	0.16
	S3	0.05	78	1.9×10^{-3}	3.9
Marginal Le	S4	0.1	160	1.4×10^{-3}	16
	S5	0.2	310	1.0×10^{-3}	62
Not Earth-like Le	S6	0.5	780	7.9×10^{-4}	390
	Earth	$0.001 - 0.1$	$100 - 1000$	$\sim 1 \times 10^{-4}$	~ 10

We now describe six numerical simulations (labelled S1-6) which are initiated with the buoyant cloud initial condition (figure 5.1b). Using the average velocity in the mid-plane of the box u_0 we define: the Rossby number $Ro_0 = u_0/2\Omega\bar{\delta} \sim 0.005 - 0.01$ and the Reynolds number $Re = u_0\bar{\delta}/\nu \sim 20 - 50$. (We note that these numbers are smaller in the wave-field.) As $Pm = 1$, the magnetic Reynolds number is $Rm = Re$, while the Ekman number is $E = \nu/2\Omega\bar{\delta}^2 \approx 2 \times 10^{-4}$.

We vary Le from the basically hydrodynamic value of 10^{-8} through to $Le = 0.5$ by increasing the strength of the applied field, with the exact values given in table 5.1. Also reported are estimated values for the small scales in Earth's outer core. We also list the Lundquist number, defined as $Lu = B_0\bar{\delta}/\eta$, which is expected to be large in planetary cores. We introduce an 'average over the wave packets' which we will use consistently in the remainder of the paper, which is taken over the region $|\boldsymbol{u}| + |\boldsymbol{b}| > 0.05 \times \max(|\boldsymbol{u}| + |\boldsymbol{b}|)$. Using this average we define a velocity scale u, and the corresponding values of $Ro = u/2\Omega\bar{\delta}$ for our simulations are given in table 5.1. These decrease from S1–6 as a result of kinetic energy being converted to magnetic energy for larger B_0 and enhanced Ohmic dissipation. We will first qualitatively describe the results of simulations S1–6, then examine features of them in detail.

Figures 5.4 & 5.5 show isosurfaces of the axial velocity at ± 2 standard deviations, coloured by h_k^*, $|h_c^*|$ and $\mathcal{E}_x^*$ at $\Omega t = 30$. Column four in figures 5.4 & 5.5 displays a y-average (denoted $\langle\sim\rangle_y$) where the colour intensity is controlled by $\langle|u_z|\rangle_y$ and the hue is set by $\langle\mathcal{E}_x^*\rangle_y$. For $Le < 0.1$ (S1–3), the buoyant layer in the vertical centre of the box emits

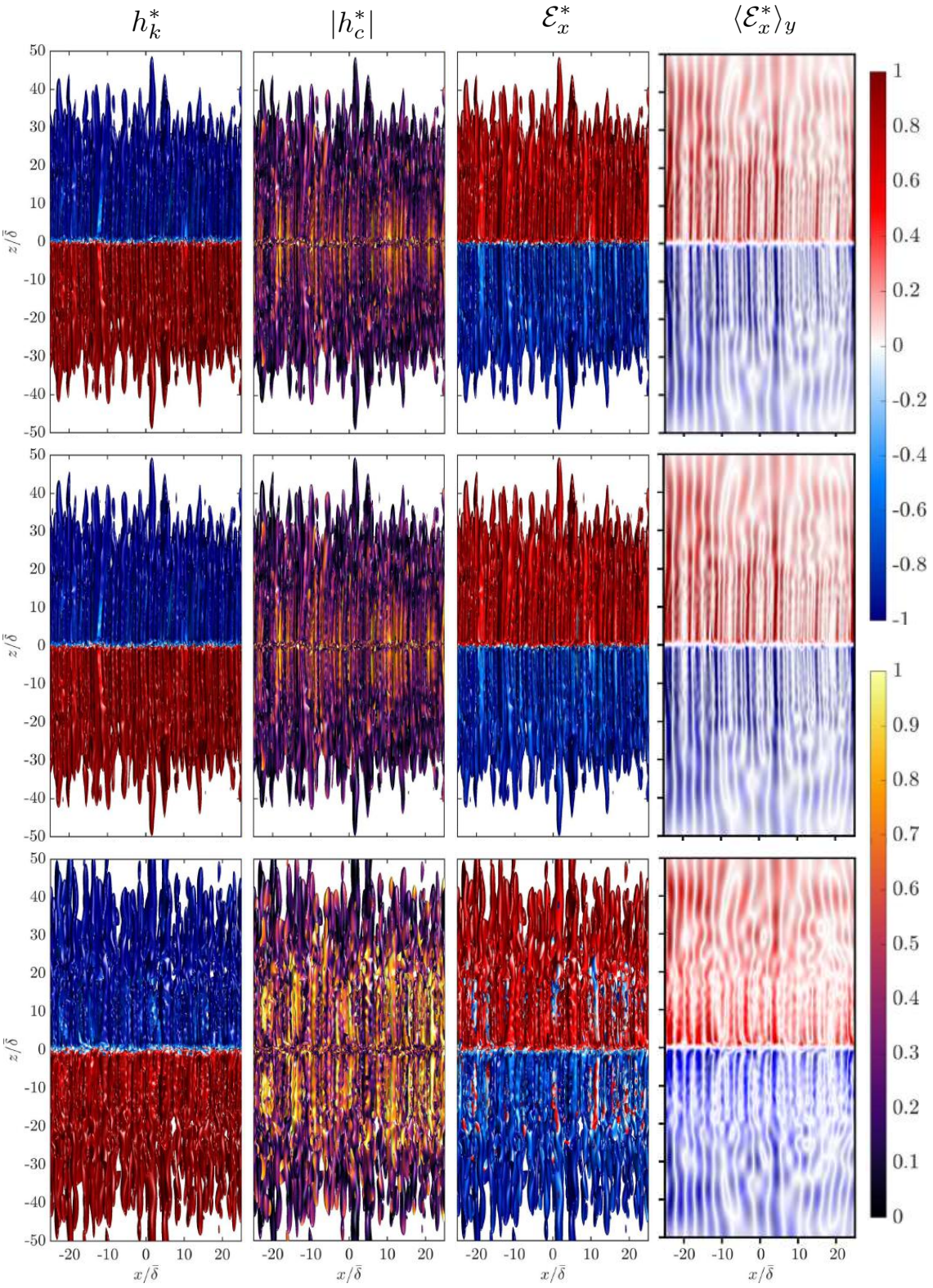

Fig. 5.4 Axial velocity isosurfaces coloured by relative kinetic helicity h_k^*, relative cross helicity magnitude $|h_c^*|$ (see second colour-bar) and normalised emf in the x-direction $\mathcal{E}_x^*$ (left to right). Isosurfaces shown for S1-3 (top to bottom), at $\pm$ two standard deviations of u_z and $\Omega t = 30$. Column 4 shows a y-average where the colour intensity is controlled by $\langle |u_z| \rangle_y$ and the hue is set by $\langle \mathcal{E}_x^* \rangle_y$. Note the top/bottom of the box are at ± 75 $z/\bar{\delta}$.

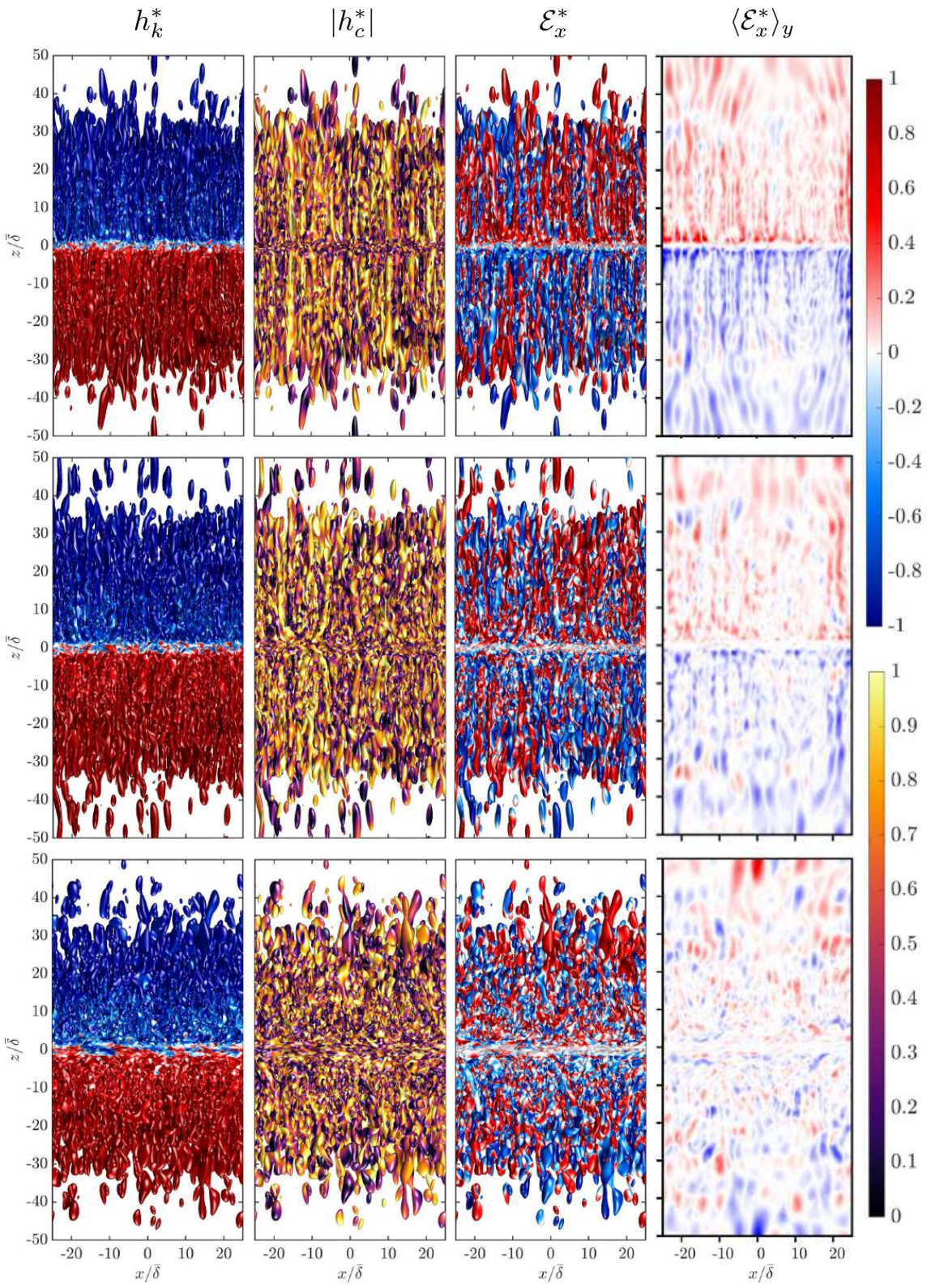

Fig. 5.5 Same as figure 5.4, for S4-6 (top to bottom).

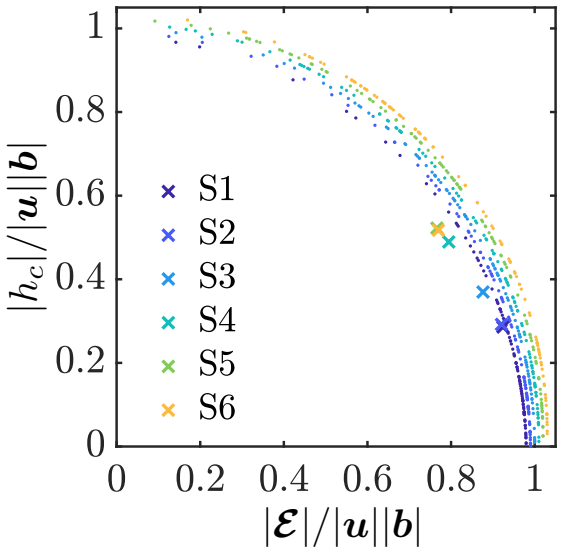

	$\lvert\mathcal{E}_x\rvert/\lvert\boldsymbol{\mathcal{E}}\rvert$	$\lvert h_{c,x}\rvert/\lvert h_c\rvert$
S1	0.84	0.45
S2	0.84	0.47
S3	0.80	0.51
S4	0.68	0.61
S5	0.60	0.76
S6	0.51	0.96

Fig. 5.6 The relation between cross helicity and the induced emf for a random selection of points within the wave packets at $\Omega t = 20$. All points for each simulation lie on the unit circle, but they have been shifted slightly for clarity. The crosses indicate the mean values over the wave packets, and the markers for S1 and S2 and for S5 and S6 are nearly on top of one another. The r.m.s. values of the ratios $|\mathcal{E}_x|/|\boldsymbol{\mathcal{E}}|$ and $|h_{c,x}|/|h_c|$ are listed to the right.

a spectrum of wave packets which form columnar structures aligned with the rotation axis. These structures are very similar to those seen in figures 5.2 & 5.3 for the single blob case. Those columnar structures in figure 5.4 resemble weakly modified inertial waves for S1 and S2; in fact the images for S1 and S2 (at $Le = 10^{-8}$ and $Le = 0.01$) are almost identical. This is our first observation: that on timescales on the order of one week, MC waves in the regime $Le \lesssim 0.01$ are not strongly affected by the mean-field, and behave much the same as inertial waves. For S3 ($Le = 0.05$), the wave-field remains largely coherent in the axial direction, as expected for a small value of Le. There is an increase in $|h_c^*|$ for wave packets with a slower axial group velocity, however the normalised emf remains strong and well segregated.

We tentatively identify inertial wave packets travelling at roughly the speed of low frequency inertial waves, but in regions where we observe increased levels of cross helicity, IA wave packets must also be present. Intermediate MC waves must be present, however they are more difficult to classify as they have varying degrees of cross helicity, though at low-Le these wave packets will be broadly columnar in structure by virtue of (2.16). Simulation S4 is in the same regime ($Le = 0.1$) as the individual blob example shown in figure 5.2. A closer inspection of figure 5.5 reveals that the wave packet morphology observed in figure 5.2 is present in the buoyant layer case, where wave packets elongate

along the rotation axis meanwhile migrating along magnetic field lines, yet for multiple blobs the wave packets overlap in space. For S4–6 ($Le \geq 0.1$), the picture exhibited for S1–3, columnar inertial/IA wave packets carrying intense positive (negative) $\mathcal{E}_x^*$ above (below) the buoyant layer becomes more complex. However, the y-average shown in column four of figures 5.4 & 5.5 remains strongly positive (negative) above (below) the buoyant layer for $Le \lesssim 0.1$.

The wave packets become less coherent in the direction of the rotation axis as the uniform field strength is increased (figure 5.5). For larger mean field strengths there is faster propagation in the direction of the imposed field. For S4, at $Le = 0.1$, although there is enhanced cross helicity, the normalised emf appears to be mostly positive (negative) above (below) the source and of moderate magnitude; indeed the y-average is very coherent. This follows from the argument on pp. 101, which states that wave packets can induce a large emf in spite of carrying a lot of cross helicity. We plot the relationship between $|h_c|$ and $|\boldsymbol{\mathcal{E}}|$ for a random selection of points within the wave packets in figure 5.6, the crosses indicate the mean values over the wave packets. The points for each simulation have been shifted slightly for clarity, but they all lie on the unit circle. The mean relative emf decreases with increasing Le (and the relative cross helicity increases). The same is true for the ratios $|\mathcal{E}_x|/|\boldsymbol{\mathcal{E}}|$ and $|h_{c,x}|/|h_c| = |u_x b_x|/|h_c|$ listed to the right in figure 5.6, $\mathcal{E}_x$ becomes less dominant and $h_{c,x}$ becomes more dominant with increasing Le. This may be explained by considering the increasing tension in the mean-field lines as B_0 increases. For a stronger mean-field, fluid motions perpendicular to the field lines become increasingly resisted by the Lorentz force. As the imposed field is in the x-direction, u_x becomes more dominant with larger field strengths, $|h_{c,x}|/|h_c|$ increases and $|\mathcal{E}_x|/|\boldsymbol{\mathcal{E}}|$ decreases.

For $Le \geq 0.2$ (S5 and S6) the emf is weaker, less organised and appears to be uncorrelated with the kinetic helicity. The kinetic and magnetic helicities remain mostly segregated for larger mean field strengths, but the segregation of the emf is no longer so clean, and this results in a weakening of $\langle \mathcal{E}_x^* \rangle_y$ (column four).

A uniform magnetic field has a detrimental effect on the relative kinetic and magnetic helicity transported by the wave packets. This is shown at $\Omega t = 30$ in figure 5.7, where $\langle h_k^* \rangle = \langle h_k \rangle / \langle \boldsymbol{u}^2 \rangle^{1/2} \langle \boldsymbol{\omega}^2 \rangle^{1/2}$ and $\langle h_m^* \rangle = \langle h_m \rangle / \langle \boldsymbol{a}^2 \rangle^{1/2} \langle \boldsymbol{b}^2 \rangle^{1/2}$ denote the relative kinetic and magnetic helicity, where the angle brackets denote an average in planes perpendicular to the rotation vector. These quantities are remarkably similar for S1 at $Le = 10^{-8}$ and S2 at $Le = 0.01$ (which is Earth-like) even at the late time shown. This supports our qualitative observation above, that the dynamics in S1 and S2 are alike. The curves for S2–6 display a slight decrease in both relative kinetic and magnetic helicity, indicating

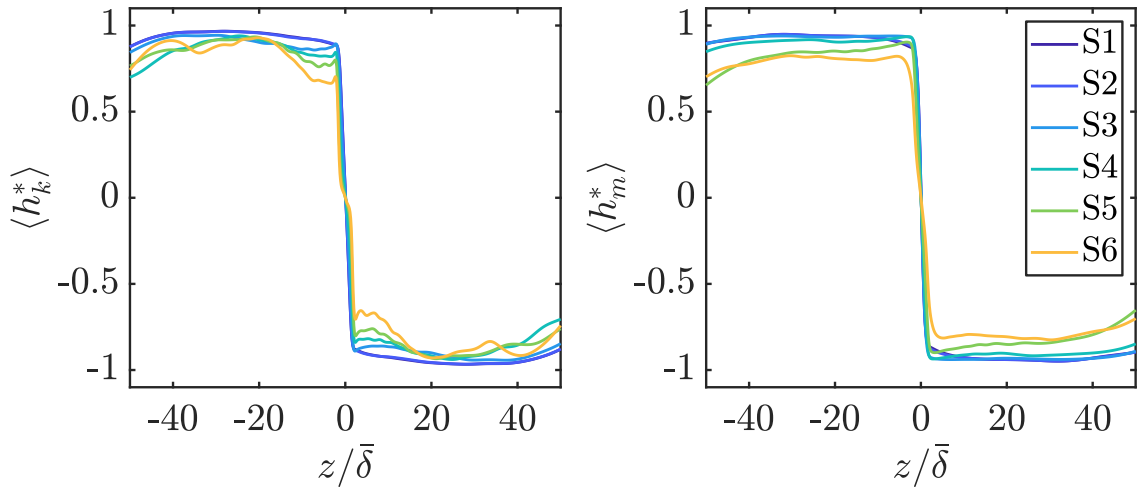

Fig. 5.7 Relative helicity averaged in planes perpendicular to the rotation vector at $\Omega t = 30$: (a) kinetic helicity (b) magnetic helicity. The curves for S1 and S2 lie almost on top of each other.

that these fields become less aligned with a stronger influence of the imposed magnetic field. The relative helicity is closely related to the average angle between the vector fields, and this is what we will examine next.

To look at how the relative helicities vary with Le, we have calculated approximate probability density functions (PDFs) of the associated angles. The relative kinetic helicity h_k^* is related to the angle between $\boldsymbol{u}$ and $\boldsymbol{\omega}$, say $\phi \in [0, 180°)$, such that $\phi = \cos^{-1}(h_k^*)$. Similar relations hold for the relative magnetic helicity: $\beta = \cos^{-1}(h_m^*)$, and the relative cross helicity: $\theta = \cos^{-1}(h_c^*)$. The PDFs of these angles, $P(\phi)$, $P(\beta)$ and $P(\theta)$, calculated over the wave packets, are shown in figure 5.8 at $\Omega t = 30$. Again, our first observation is that there is little difference between the PDFs for S1 and (the Earth-like) S2 for ϕ, β and θ. However, as Le is increased, $P(\phi)$ and $P(\beta)$ are less polarised, and the alignment between $\boldsymbol{u}$ and $\boldsymbol{\omega}$ and between $\boldsymbol{a}$ and $\boldsymbol{b}$ is marginally decreased (figures 5.8a,b). The most dramatic effect is in $P(\theta)$, where the PDF is quite sharply peaked for S1 and S2 at $\theta \approx 85°$, indicating that $\boldsymbol{u}$ and $\boldsymbol{b}$ are nearly perpendicular throughout the waves. This tells us that in the regime of low-Le: the normalised emf $|\boldsymbol{\mathcal{E}}^*| = |\sin\theta| \sim 1$, thus the waves are very efficient at inducing an emf. For S2 and S3, at $Le = 0.01$ and $Le = 0.05$, which are reasonable estimates for the small scales in Earth's outer core, $P(\theta)$ has a pronounced peak near 90°. With a stronger mean magnetic field, the PDF is broader but still peaks near $\theta \sim 90°$.

Now, figures 5.8c,d show there is a large difference in the alignment of the velocity and magnetic fields for the single blob case and the multiple blob (buoyant layer) case. With one blob there is clearly more frequent alignment between $\boldsymbol{u}$ and $\boldsymbol{b}$ than when there

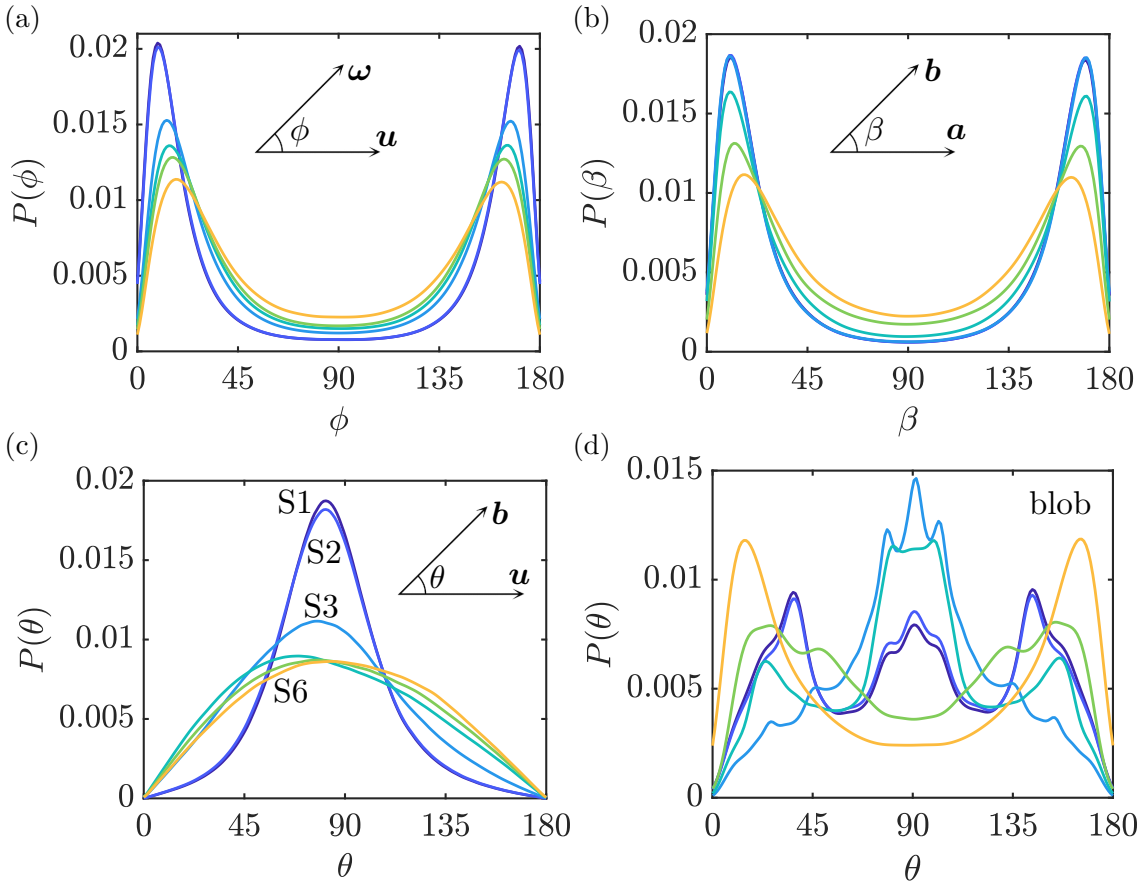

Fig. 5.8 Approximate PDFs of the angle between vector fields at $\Omega t = 30$. (a) velocity and vorticity (b) the magnetic field and its vector potential (c) velocity and the magnetic field. The colours are as indicated in figure 5.7 and are highlighted in (c). For comparison (d) shows $P(\theta)$ for the blob case.

are wave packets emitted from multiple neighbouring blobs. A simple explanation of this phenomena is as follows. Consider a two wave system with wave vectors $\boldsymbol{k}_1$ and $\boldsymbol{k}_2$, frequencies ϖ_1 and ϖ_2 and magnitudes $\hat{\boldsymbol{b}}_1$ and $\hat{\boldsymbol{b}}_2$,

$$\boldsymbol{b} = \hat{\boldsymbol{b}}_1 \cos(\boldsymbol{k}_1 \cdot \boldsymbol{x} - \varpi_1 t) + \hat{\boldsymbol{b}}_2 \cos(\boldsymbol{k}_2 \cdot \boldsymbol{x} - \varpi_2 t)\,, \tag{5.1}$$

where $|\boldsymbol{k}_1| \approx |\boldsymbol{k}_2|$ and $\varpi_1 \approx \varpi_2$ so that the waves are propagating information at approximately the same speed. Using (2.14), we can write an expression for the velocity field for the two waves

$$\boldsymbol{u} = -\frac{\varpi_1}{\varpi_{B,1}}\hat{\boldsymbol{b}}_1 \cos(\boldsymbol{k}_1 \cdot \boldsymbol{x} - \varpi_1 t) - \frac{\varpi_2}{\varpi_{B,2}}\hat{\boldsymbol{b}}_2 \cos(\boldsymbol{k}_2 \cdot \boldsymbol{x} - \varpi_2 t)\,. \tag{5.2}$$

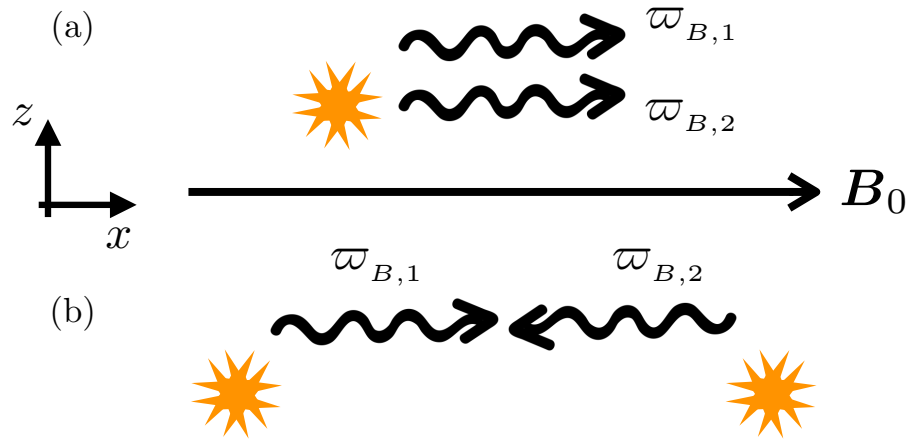

Fig. 5.9 Two wave cartoon, wiggly arrows indicate waves. (a) Single blob case (b) Two blob case.

We are interested in the induced emf, which is maximal when $\boldsymbol{u}$ and $\boldsymbol{b}$ are perpendicular, so we expand $\boldsymbol{u} \times \boldsymbol{b}$ to find

$$\begin{aligned} \boldsymbol{u} \times \boldsymbol{b} = &- \frac{\varpi_1}{\varpi_{B,1}} (\hat{\boldsymbol{b}}_1 \times \hat{\boldsymbol{b}}_2) \cos(\boldsymbol{k}_1 \cdot \boldsymbol{x} - \varpi_1 t) \cos(\boldsymbol{k}_2 \cdot \boldsymbol{x} - \varpi_2 t) \\ &+ \frac{\varpi_2}{\varpi_{B,2}} (\hat{\boldsymbol{b}}_1 \times \hat{\boldsymbol{b}}_2) \cos(\boldsymbol{k}_1 \cdot \boldsymbol{x} - \varpi_1 t) \cos(\boldsymbol{k}_2 \cdot \boldsymbol{x} - \varpi_2 t) \,. \end{aligned} \tag{5.3}$$

The conditions on the waves' respective wavevectors and frequencies mean the cosine terms have approximately the same argument, reducing them to $\cos^2(\sim)$ terms. Averaging this expression we find

$$\langle \boldsymbol{u} \times \boldsymbol{b} \rangle \approx \frac{\bar{\varpi}}{2} \left(\frac{1}{\varpi_{B,2}} - \frac{1}{\varpi_{B,1}} \right) (\hat{\boldsymbol{b}}_1 \times \hat{\boldsymbol{b}}_2) \,, \tag{5.4}$$

where $\bar{\varpi} = (\varpi_1 + \varpi_2)/2$. Now consider figure 5.9, which shows the two cases of wave packets propagating along the mean-field in the same direction ($\boldsymbol{k}_1 \approx \boldsymbol{k}_2$, for a single source) and toward one another ($\boldsymbol{k}_1 \approx -\boldsymbol{k}_2$, for two neighbouring sources). Evidently

$$\langle \boldsymbol{u} \times \boldsymbol{b} \rangle \approx \begin{cases} 0 & \text{if } \ \boldsymbol{k}_1 \approx \boldsymbol{k}_2 \,, \\ \frac{\bar{\varpi}}{|\bar{\varpi}_B|} (\hat{\boldsymbol{b}}_1 \times \hat{\boldsymbol{b}}_2) & \text{if } \ \boldsymbol{k}_1 \approx -\boldsymbol{k}_2 \,, \end{cases} \tag{5.5}$$

where $\bar{\varpi}_B = (|\varpi_{B,1}| + |\varpi_{B,2}|)/2$. Thus, spatially overlapping wave packets which propagate along field lines toward one another are permitted to generate a significant emf in the monochromatic case, and this can only happen in the multiple blob cases. However, MC wave packets emitted from a single source propagate along the mean-field away from one

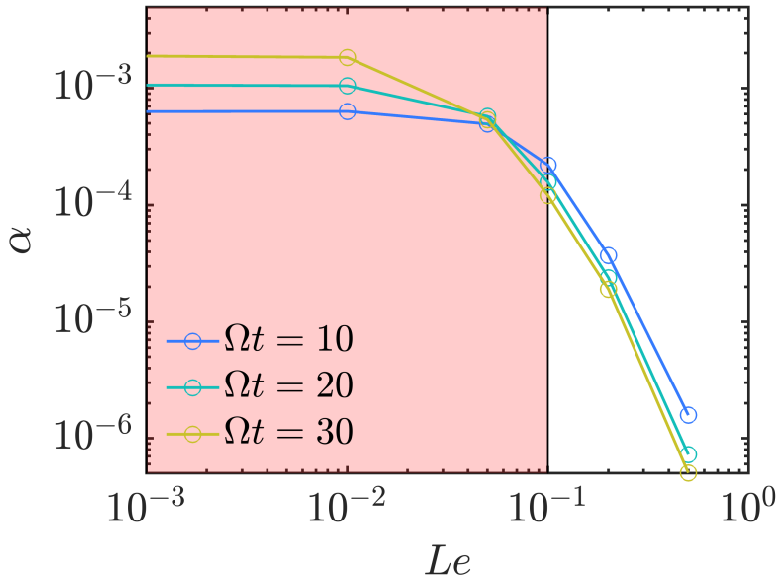

Fig. 5.10 Average α for simulations S2–6. The shaded box highlights the range of Earth-like Le and the points for S1 ($Le = 10^{-8}$) have approximately the same values as for S2, and are omitted for clarity.

another, and so never interact (see figure 5.9). This explains the difference between the alignment of $\boldsymbol{u}$ and $\boldsymbol{b}$ for the single blob and the multiple blob cases.

5.4 Implications for dynamo simulations and planetary cores

Figures 5.4 shows that the y-averaged emf in the direction of $\boldsymbol{B}_0$ is well segregated positive (negative) above (below) the buoyant source for Earth-like values of Le. Further, we have shown above that the environment in which there are many buoyant sources (arguably a more natural situation than a single isolated source) is beneficial to the generation of a mean emf. Now, we look at the variation of $\alpha = \langle \mathcal{E}_x \rangle / B_0$ across the simulations with a buoyant layer. We have calculated the average α over the wave packets restricted to the top half of the box (as α tends to be skew-symmetric about the mid-plane), and this is shown for three times in figure 5.10. It is clear from figure 5.10 that α remains strong for a broad range of field strengths up to $Le = 0.1$; dropping to 10 % of the value for S1 at $Le = 0.1$.

The physical interpretation of the observed decrease in α is that as B_0 increases there is increased lateral mixing between wave packets, as observed in figure 5.5. The horizontal displacement in the direction of the mean-field of a wave packet, denoted

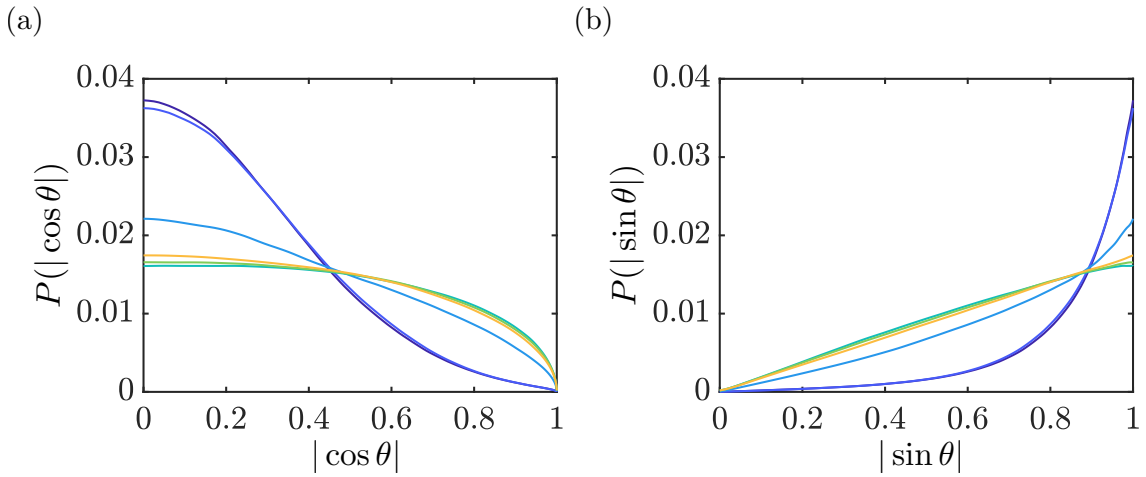

Fig. 5.11 Approximate PDFs of $|\cos\theta|$ and $|\sin\theta|$ for simulations S1–6. The colours are consistent with the previous figures, and the curves for S1 and S2 are very close together.

Δ, can be expressed as $\Delta/\bar{\delta} = (\Omega t)Le$. Therefore, at $30\Omega t$ (as in figure 5.5), the wave packets in S5 and S6 (at $Le = 0.2\,, 0.5$) have been significantly displaced. Now, the two inertial wave packets above (or indeed below) a buoyant blob have opposite signed u_z and ω_z (see figure 5.3). Thus, when there is a substantial amount of cross-mixing (as for $Le \geq 0.2$), there is cancellation in the components of the velocity field in the overlapping region, and the magnitude of the r.m.s. velocity is reduced. This is also true for MC wave packets, and the resulting decrease in the velocity and magnetic field perturbations is consistent with the observed reduction in α (figure 5.10).

It is also interesting to take a closer look at the PDFs of $|\cos\theta|$ and $|\sin\theta|$ (θ being the angle between $\boldsymbol{u}$ and $\boldsymbol{b}$ defined earlier). Figure 5.11 shows the PDFs throughout the wave packets at $\Omega t = 30$. Evidently we have a strong emf for $|\cos\theta| \approx 0$ and $|\sin\theta| \approx 1$, which is the most likely scenario for all the simulations. For S1 and S2 (at $Le = 10^{-8}$, 0.01), these are clearly the most pronounced parts of the PDF, indicating a strong induced emf. For S4–6, $|\cos\theta| \approx 0$ and $|\sin\theta| \approx 1$ are still the most pronounced parts of the PDF, but these values are approximately half as likely as for S1 and S2. These observations are independent of the magnitude of the kinetic energy, unlike the explanation above.

Recent numerical dynamo simulations have highlighted the presence of rapid time-scale inertial and hydromagnetic waves (Aubert, 2019; Ranjan *et al.*, 2018; Schaeffer *et al.*, 2017). Aubert (2019) observes "quasi-geostrophic Alfvén waves" propagating along the cylindrical radial magnetic field, launched from a buoyant plume. The description of these fast time-scale, localised events is very reminiscent of the wave packets observed in our simulations (and in Bardsley & Davidson, 2016). The convective structures outside the tangent cylinder in the extreme simulation of Schaeffer *et al.* (2017) are characterised

by Lehnert numbers in the range $0.01 - 0.1$. The flow is chaotic in space and time, quasi-geostrophic, and highly helical — fast time-scale MC wave packets like those observed in figures 5.4 & 5.5 (S2–4) are good candidates for the maintenance of these flow structures. As planetary dynamo simulations progress to increasingly turbulent states, it is expected that the propagation of wave packets will play an ever more important role in the dynamics, and possibly the dynamo mechanism (Davidson & Ranjan, 2015).

The magnetic field inside the core will certainly be heterogeneous, with the possibility of having regions of the core where the magnetic field is much weaker/stronger than the average. The more dipolar numerical simulations often exhibit an azimuthal mean-field which has opposite signs in each hemisphere, which is relatively weak outside of the tangent cylinder, and goes to zero at the equator (Roberts & King, 2013; Schaeffer *et al.*, 2017). This type of anti-symmetric mean-field would change our results in two main ways. The helicity distribution would remain negative (positive) above (below) the source. However the induced emf would now be positive both above and below, as required for an α^2 dynamo. Second, our results suggest that a weaker azimuthal field in the regions of the equatorial plane would be beneficial for the generation and propagation of kinetic helicity and the emf, although the dispersion relation of a wave packet may evolve along its path (Bardsley & Davidson, 2017). As the wave packets enter regions of stronger field at higher latitudes, they would be subject to enhanced Ohmic dissipation, reducing the likelihood of cancellation by reflections at the core-mantle boundary.

This picture is consistent with the cartoon outlined in figure 1.10 for an α^2 dynamo driven by helical convection/waves. Using ray theory, Bardsley & Davidson (2017) deduced the effect of an axially varying anti-symmetric mean-field on MC wave dispersion. They concluded that even though IA waves are de-focused by the slow variation of B_0, the fact that Le is small in Earth's core implies that the intermediate MC waves disperse more or less axially, and this is what we observe for a sea of MC wave packets for $Le < 0.1$. It is the fact that the time-scales τ_Ω, τ_A and $\tau_u = \ell/u$ are ordered such that $30\,\tau_\Omega \lesssim \tau_A \ll \tau_u$, which suggests that inertial/MC wave packets continually launched from a chaotic buoyancy field would be particularly effective at maintaining elongated flow structures and driving an α-effect.

5.5 Summary

Fast time-scale MC wave packets propagating through a uniform transverse mean-field generate a significant α-effect at Earth-like values of the Lehnert number. Further, the y-averaged induced emf remains well segregated positive (negative) above (below) the

wave source for $Le \lesssim 0.1$. For mean-fields with a larger magnitude the induced emf is reduced, and the α-effect is less influential. The wave packets in our simulations that transport a high energy density are well described by three groups: weakly modified inertial ($c_{gz} \sim 2\Omega/k$), inertial-Alfvén ($c_{gz} \sim \Omega/k$, $\boldsymbol{k} \cdot \boldsymbol{\Omega} \approx 0$) and intermediate MC wave packets (fast and columnar at low-Le). Our simulations cannot run for sufficiently many rotation times for the signature of magnetostrophic waves to become distinct.

For Earth-like values of the Lehnert number ($Le < 0.1$), we find that on time-scales of the order of weeks:

i The wave packets are coherent and columnar (figure 5.4).

ii In spite of a preferential alignment between $\boldsymbol{u}$ and $\boldsymbol{b}$, the wave packets induce a sizeable emf, which is greater when there are multiple neighbouring sources.

iii MC wave packets generate a spatially organised α-effect, where the average α remains strong for a broad range of field strengths up to $Le = 0.1$

iv The horizontally averaged $\mathcal{E}_x$ is well correlated with $-\langle h_k \rangle$.

The inertial/MC wave dynamo model of Davidson (2014) requires kinetic helicity that is sufficiently intense, and that is distributed negative (positive) in the north (south) outside the tangent cylinder. The model suggests that such a helical flow could set up an α^2 dynamo cycle as described in figure 1.10, where the velocity field principally acts on the horizontal components of the mean-field. However, this model does not explicitly take into account the dynamic effect of a mean magnetic field. The work presented here, in particular the points outlined above, suggest that such a model is indeed feasible in Earth's core, even for upper estimates of the toroidal field strength. (We note that our results are essentially the same if we model the local cylindrical radial field B_r as $B_0 \boldsymbol{e}_y$, yielding an α_{yy}.)

In Jault (2008), the axisymmetric motions launched by a jerk of the inner sphere, which travel rapidly along the rotation axis and migrate outwards at the radial Alfvén speed are certainly similar to the propagation of IA wave packets (see also the recent experiments by Tigrine *et al.*, 2019). It has been noted by Jault (2008) that numerical dynamos with large-scale Lehnert numbers less than $\sim 3 \times 10^{-2}$ are broadly quasi-geostrophic. Using the average mean spherical harmonic degree in the kinetic energy spectrum of the dynamos in the dataset of Christensen & Aubert (2006), this translates to a 'local' Lehnert number of ~ 0.2. This is consistent with the isosurfaces presented in figures 5.4 & 5.5 — the flow is reasonably columnar in S4 and becomes less columnar in S5–6.

In recent (more turbulent) geodynamo simulations (Aubert, 2019; Schaeffer *et al.*, 2017), buoyant anomalies outside the tangent cylinder have the potential to launch wave packets like those observed here. Ranjan *et al.* (2018) showed that the time derivative of axial velocity is a good indicator for localised wave-fronts, we corroborate this finding. This approach could be combined with analysis of the local energy density ratio and relative helicities to search for MC wave packets emitted from buoyant blobs/plumes in dynamo simulations.

Chapter 6

Conclusions

We now review the conclusions of this thesis, with a focus on the role of helical dispersive waves in dynamo simulations and in Earth's outer core. We ask what role inertial and magnetic-Coriolis waves may have in dynamo simulations and planetary cores – in the maintenance of quasi-geostrophic flow structures, and in magnetic field generation. Lastly, suggestions for future research are outlined.

The results we present in this thesis are numerical solutions of idealised problems. In chapter 4 we investigate the influence of nonlinear inertia on columnar structure formation by inertial wave propagation. The change in the dynamics from low-to-moderate Rossby number is linked to the dipolar-multipolar transition observed in dynamo simulations. The influence of a large-scale magnetic field on inertial wave propagation is presented in chapter 5. Here, inertial waves are modified into a spectrum of MC waves, and the dispersion pattern is not so simply described. At Earth-like Lehnert numbers we find that MC wave packets propagate energy mostly along the rotation axis, similarly to inertial wave packets. All resulting waves distribute kinetic helicity so that it is negative (positive) above (below) the wave-source, as is required for the helical wave dynamo model. Moreover, we find that the α-effect due to the wave packets is coherent for Earth-like Lehnert numbers.

6.1 A physical mechanism for the dipolar-multipolar dynamo transition

In chapter 4 and McDermott & Davidson (2019) we explored the influence of nonlinear inertia on the propagation of inertial wave packets. At low Rossby number, there is a large time-scale separation between the evolution of the buoyancy field and the dispersion

of energy by inertial wave packets. The buoyant anomalies emit inertial wave packets which propagate toward the top/bottom of the box at a speed close to $2\Omega/k$. The wave packets generate columnar flow structures which distribute kinetic helicity so that it is negative (positive) above (below) the buoyant source. The above confirms the linear inviscid theory laid out in Davidson (2013*b*) and chapter 2.

At moderate Rossby number, when nonlinear inertia is as important as the Coriolis acceleration, inertial waves are suppressed. This is evidenced from simulations R3–6 presented in chapter 4, which are initiated with a buoyancy field of greater magnitude. The potential energy in the buoyancy field is converted to kinetic energy, and inertial wave packets begin to disperse away from the buoyant layer. The wave packets are characterised by a small Rossby number. However, the Rossby number in the neighbourhood of the buoyant layer grows toward 1, and the flow in this region undergoes a turbulent transition where small length scales are excited. Later in time there are two distinct regions of flow: the inertial wave packets propagating toward the top and bottom of the box at low Rossby number, and the turbulent region where the buoyancy field is advected and the Rossby number is approximately unity.

By measuring the perpendicular integral length-scale of the velocity field as a function of z (the direction of the rotation vector) and time, we calculated $Ro(z,t)$. Investigating the value of $Ro(z,t)$ at the boundary between the turbulent region and the wave-field, we found that the two regions are delineated by $Ro^{\text{crit}} \approx 0.4$ (figure 6.1). This critical Rossby number, separating regions of inertial wave packets ($Ro < 0.4$) and turbulence ($Ro > 0.4$) is consistent with earlier rotating tank experiments (Staplehurst *et al.*, 2008).

6.1.1 Rotating turbulence

The rotating tank experiments of Davidson *et al.* (2006) are inhomogeneous, in that the velocity fluctuations are excited by a localised grid stroke at the top of a tank. In these experiments, the grid stroke excites eddies with a Rossby number of $O(1)$, and they observe the dynamics as the turbulence decays and the Rossby number falls. When the Rossby number is small enough, columnar structures emerge from the cloud of turbulence and extend toward the bottom of the tank. The fronts travel at the group speed of low-frequency inertial waves (based on the grid size), which identifies the columnar structures as inertial wave packets. Staplehurst *et al.* (2008) repeated these experiments with an inhomogeneous set-up, where $Ro \sim O(1)$ turbulence is initiated with a single grid stroke passing through the whole depth of the tank. Again, the turbulence decays and the Rossby number falls. They observe that the axial integral scale begins to increase

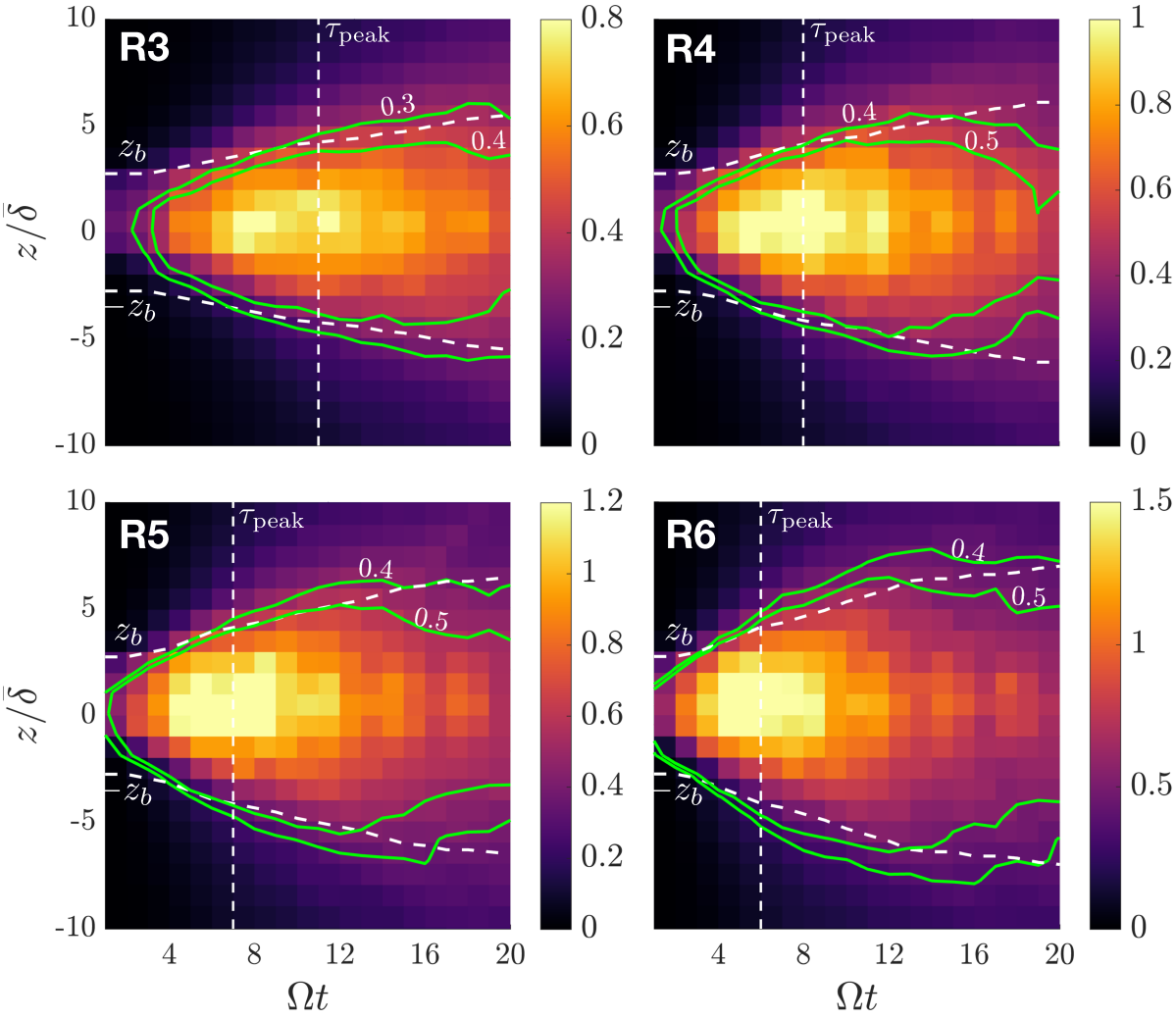

Fig. 6.1 Reproduction of figure 4.19, highlighting the transition between turbulence and inertial wave packets at $Ro^{\text{crit}} \approx 0.4$.

at a linear rate, consistent with low-frequency inertial wave propagation, at the time when $Ro \approx 0.4$. This observation is consistent with our value of Ro^{crit}.

Our numerical experiments initiated with a layer of buoyancy (chapter 4) are similar to these rotating tank experiments, with one difference. As potential energy in the buoyant layer is converted to kinetic energy in the flow, the Rossby number is initially small, but increasing. Whereas, in Davidson *et al.* (2006) and Staplehurst *et al.* (2008), the Rossby number is initially moderate, and decreasing—so inertial wave packets are launched only once the turbulence has sufficiently decayed. In our buoyancy-driven simulations, inertial wave packets are emitted from the outset, as the Rossby number is initially small. However, as the Rossby number in the neighbourhood of the buoyant

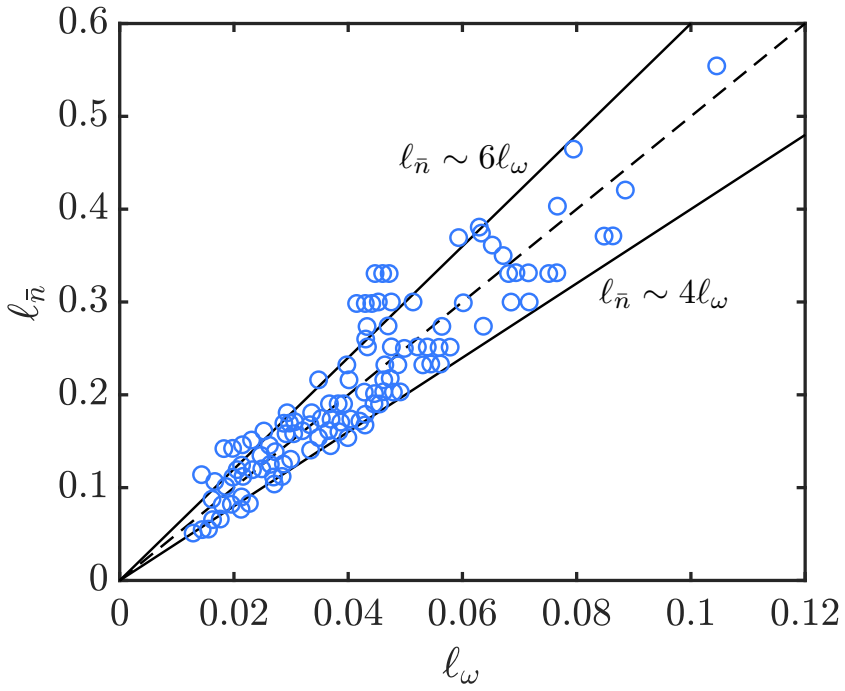

Fig. 6.2 Reproduction of figure 4.21, showing the relationship between $\ell_{\bar{n}}$ and ℓ_ω. Data from Uli Christensen's dataset with some additions from Dormy *et al.* (2018).

layer grows to reach the critical value, we identify a turbulent transition, and inertial wave packets in this region are suppressed.

6.1.2 Numerical dynamos

The mechanism that we observe in our numerical experiments may provide an explanation for a well-documented transition in numerical simulations of planetary dynamos. The transition from steady dipolar to fluctuating multipolar dynamos is a transition in fluid flow and magnetic field morphology. With weak convective driving (resulting in a low Rossby number) the velocity structures are columnar and helical, and they generate a dipolar magnetic field aligned with the rotation axis. As the convection is forced more strongly (resulting in a moderate Rossby number) the velocity field becomes less coherent and the magnetic field is disorganised. The collapse of the dipole has been previously linked to a *local* Rossby number, i.e. the Rossby number on the length-scale of the columnar convection (Kutzner & Christensen, 2002). The spherical simulations agree that the transition occurs at a 'local' Rossby number $Ro_\ell \approx 0.1$, where the characteristic length-scale is derived from the mean spherical harmonic degree in the kinetic energy spectrum (Christensen & Aubert, 2006).

In chapter 4 (see also McDermott & Davidson, 2019; Staplehurst *et al.*, 2008), we describe a mechanism through which columnar flow structures are created by inertial wave packets at low-Ro, and are suppressed at $Ro^{\text{crit}} \approx 0.4$ by turbulent flow. The discrepancy between Ro_ℓ at the transition in spherical simulations and our value of Ro^{crit} may be reconciled by considering the length-scales in each definition. The important length-scale is the characteristic width of the convection columns perpendicular to the rotation axis, which is difficult to access in simulations that use spherical harmonics. We can readily measure the perpendicular length-scale of the turbulence and/or wave packets, as described in chapter 4. An alternative measure when using spherical coordinates, is to consider the ratio of the r.m.s. velocity and the r.m.s. vorticity: $\ell_\omega = (\langle \boldsymbol{u}^2 \rangle / \langle \boldsymbol{\omega}^2 \rangle)^{1/2}$ (Oruba & Dormy, 2014), which may be constructed from the standard output of geodynamo simulations. It is readily shown that, for the helical columnar convection exhibited in many of these simulations, ℓ_ω is primarily a measure of the column width. Furthermore, we estimate the relationship between $\ell_{\bar{n}}$ (derived from the mean spherical harmonic degree in the kinetic energy spectrum) and ℓ_ω as $\ell_{\bar{n}} \approx 5\ell_\omega$ (figure 6.2). The discrepancy between $Ro_\ell \approx 0.1$ at the dipolar-multipolar dynamo transition and our value of $Ro^{\text{crit}} \approx 0.4$ is accounted for by the relationship between $\ell_{\bar{n}}$ and ℓ_ω.

In summary:

- We argue that the axial coherence of the velocity field in dynamo simulations is sustained by the dispersion of low-frequency inertial waves (or magnetically modified waves) from buoyant anomalies.
- We have shown that when $Ro \geq Ro^{\text{crit}} \approx 0.4$, inertial wave packets are suppressed, in line with previous rotating tank experiments (Staplehurst *et al.*, 2008).
- For the helical columnar convection exhibited in dynamo simulations, we have the kinematic result $\boldsymbol{\omega} = \boldsymbol{\nabla} \times \boldsymbol{u} \approx u/\ell_\perp$. Thus, the length-scale $\ell_\omega = (\langle \boldsymbol{u}^2 \rangle / \langle \boldsymbol{\omega}^2 \rangle)^{1/2}$ may be used as a proxy for $\ell_\perp$.
- The relationship $\ell_{\bar{n}} \approx 5\ell_\omega$, observed in dynamo simulations (figure 6.2), resolves the discrepancy between the dipolar-multipolar transition at $Ro_\ell \approx 0.1$ (based on $\ell_{\bar{n}}$), and our $Ro^{\text{crit}} \approx 0.4$ (based on $\ell_\perp$).

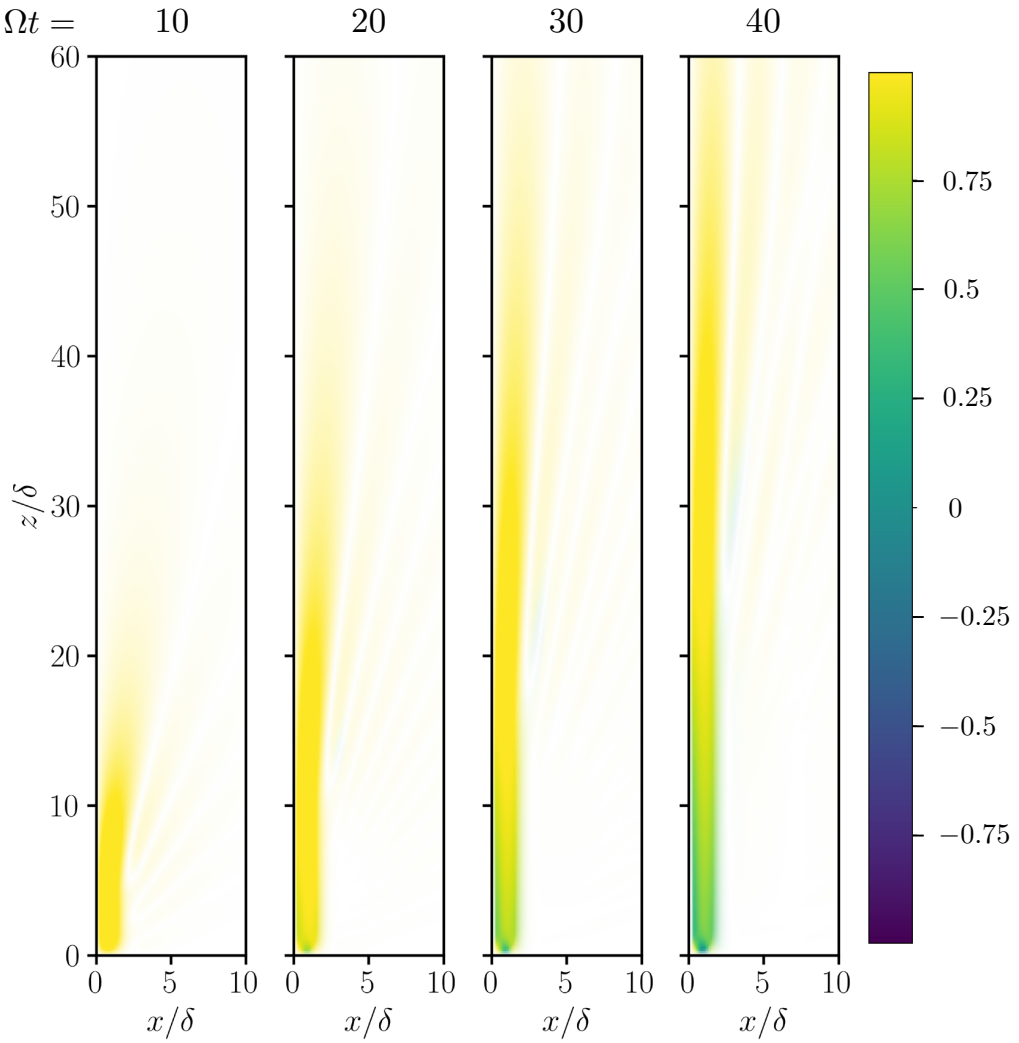

Fig. 6.3 Wave packets disperse away from a buoyant blob at $Le = 0.01$. The colour intensity is controlled by $|u_z|$ and the hue is set by $\lambda = (\boldsymbol{u}^2 - \boldsymbol{b}^2)/(\boldsymbol{u}^2 + \boldsymbol{b}^2)$ (colourbar). We show only the upper right quadrant for brevity.

6.2 The helicity characteristics and induced emf of magnetic-Coriolis wave packets

In chapter 5 and McDermott & Davidson (2020) we explore the effects of a uniform transverse magnetic field on the wave dispersion. In contrast to the simulations presented in chapter 4, we consider the Earth-like regime of low Rossby number, so nonlinear inertia is negligible. The parameter that is systematically varied is the Lehnert number Le, the ratio of the Alfvén and inertial frequencies, which is thought to lie in the range $Le = 0.001 - 0.1$ in Earth's outer core. In the presence of an ambient magnetic field,

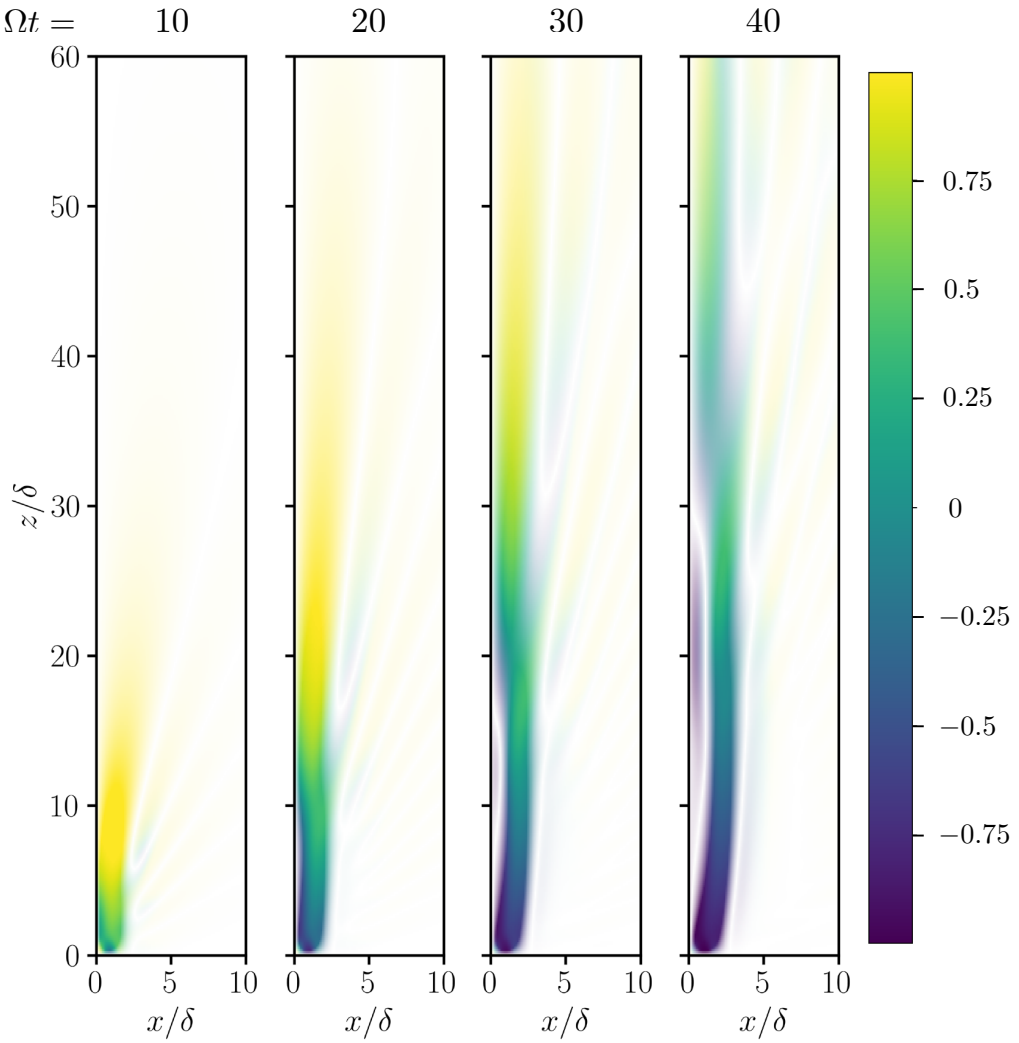

Fig. 6.4 As in figure 6.3, but here $Le = 0.05$.

inertial waves are modified into magnetic-Coriolis (MC) waves, which can be grouped into four categories based on the group velocity, wave frequency, helicity characteristics, and magnetic to kinetic energy ratio. The four categories of MC waves are: weakly-modified inertial, inertial-Alfvén (IA), intermediate MC, and magnetostrophic. We observe the former three wave-types in our simulations, and we do not identify magnetostrophic wave packets, as they evolve on a time-scale that is much longer than our simulations reach.

In chapter 3, we compared the numerical solution of the buoyant blob problem with a diffusion-less analytical result at $Ro \to 0$ (Bardsley, 2019). We use small but non-zero diffusivities in the DNS, the nonlinear inertial and Lorentz terms are included, and the buoyancy field evolves through an advection-diffusion equation. The solutions are almost identical at $Le = 0.1$ and $\Omega t = 30$; this result lends support to the approach used in

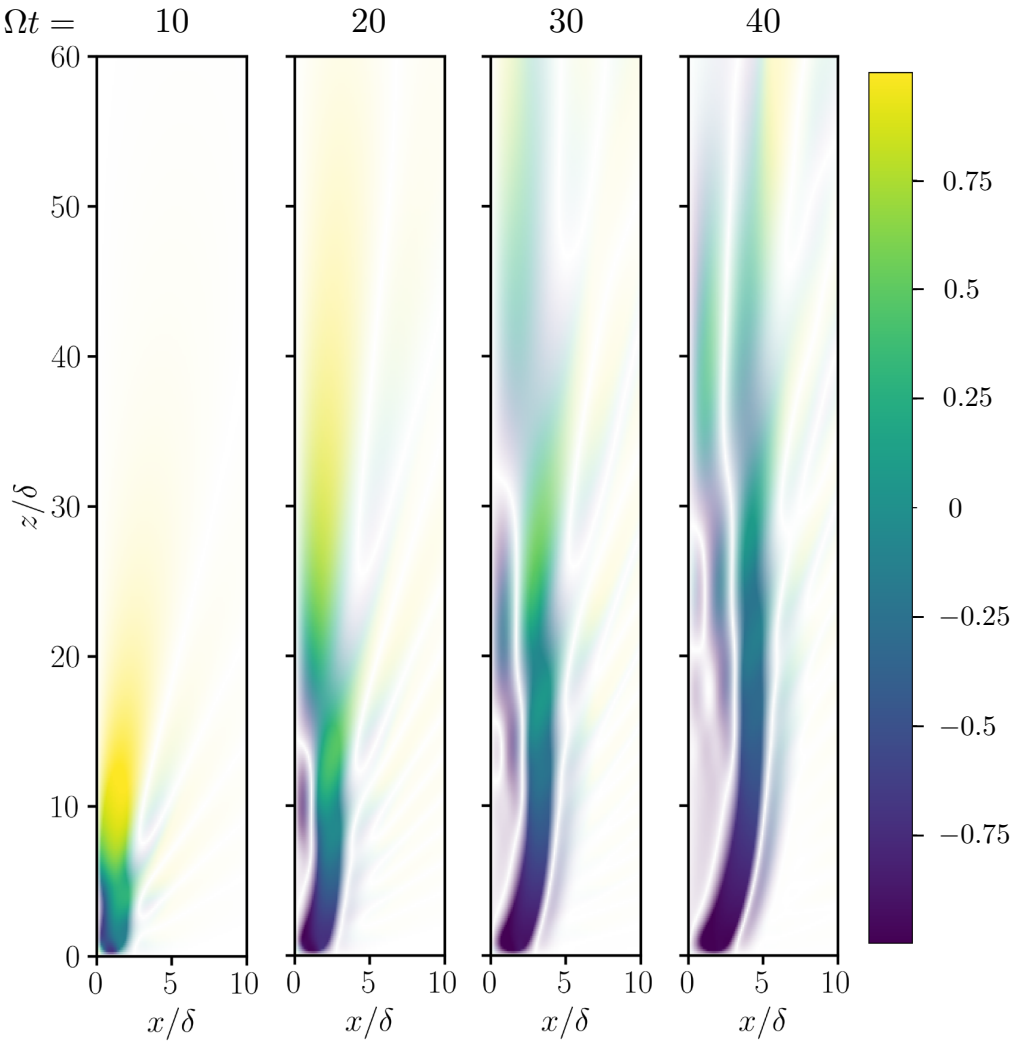

Fig. 6.5 As in figure 6.3, but here $Le = 0.1$.

Bardsley & Davidson (2016) and Bardsley & Davidson (2017). However, the DNS is better equipped to study nonlinear phenomena such as magnetic induction through the α-effect, which we explore in chapter 5.

When the Lehnert number is $Le \leq 0.01$, the wave packets are almost identical in structure to inertial wave packets, and the majority of the energy carried by the wave packets is kinetic. This is clear in figure 6.3, where the colour intensity is controlled by $|u_z|$ and the hue is set by $\lambda = (\boldsymbol{u}^2 - \boldsymbol{b}^2)/(\boldsymbol{u}^2 + \boldsymbol{b}^2)$. Thus, for inertial waves $\lambda = 1$ (bright yellow), for IA waves $\lambda = 0$ (turquoise), and for magnetostrophic waves $\lambda = -1$ (dark blue). When $Le = 0.05$ (figure 6.4), the dynamics are a little different. Inertial wave packets disperse kinetic energy in the fluid column above the buoyant blob, and they are followed by IA wave packets with an axial group speed $\sim \Omega/k$. Due to the tension

in the ambient field lines, the IA wave packets are displaced laterally in the x-direction at the Alfvén speed. The lateral displacement is more pronounced in figure 6.5, where $Le = 0.1$, and the displacement of the turquoise IA wave packet at $\Omega t = 40$ is clearly $Le\,\Omega t \approx 4$. Less energetic off-axis inertial waves and intermediate MC waves are present, however these waves are harder to distinguish, as their axial group speed is similar to the IA wave packets that have a high energy density.

6.2.1 Coherent emf at low Lehnert number

Simulations S1–6 (chapter 5) are initiated with a buoyant layer which contains mutliple wave-sources, resulting in a sea of wave packets. The full spectrum of MC wave packets segregate kinetic helicity negative (positive) above (below) their source, with respect to the rotation vector, and that is what we observe in our simulations. This is apparent in figure 6.6, where the colour intensity is controlled by the y-average of $|u_z|$ and the hue is set by the y-average of the relative kinetic helicity. The ambient magnetic field modifies the structure of the wave packets, and alters their group velocity in the axial and horizontal directions, however the relative helicity is mostly unchanged.

The wave packets interact with the ambient field and induce an emf, with a related α-effect. The fluctuating emf in the direction of the ambient field, $\mathcal{E}_x$, is coherent for Earth-like values of the Lehnert number ($Le < 0.1$), as evidenced by figure 6.7. This figure is similar to figure 6.6, but the hue is set by the y-average of $\mathcal{E}_x^*$. At $Le = 0.01$, the emf is organised and is well correlated with $-h_k$, as expected from classical mean-field theory. In contrast to the helicity, increasing the Lehnert number reduces the coherence of the induced emf (figure 6.7). Although, for Earth-like values of the Lehnert number ($Le < 0.1$), the emf induced by the wave packets is well-organised.

The fact that the kinetic helicity has a large relative value and is cleanly segregated negative (positive) above (below) the buoyant layer lends support to the helical wave dynamo model (Davidson, 2014, section 1.2.3). Further, the coherence of the induced emf for Earth-like values of the Lehnert number compounds the idea that an α^2 dynamo driven by helical waves, as introduced in 1.2.3, is feasible. The model relies on the spatial distribution of buoyant sources being sufficiently biased towards the equatorial plane. Our investigations have not tried to explain why this spatial distribution of buoyancy may come about, but observations of an equatorially biased heat-flux have guided the set-up of our model problems. At Earth's core conditions, if such a spatial bias were to come about, then the evidence we have presented suggests MC wave packets on the fast time-scale have the potential to drive a dynamo (as outlined in figure 1.10).

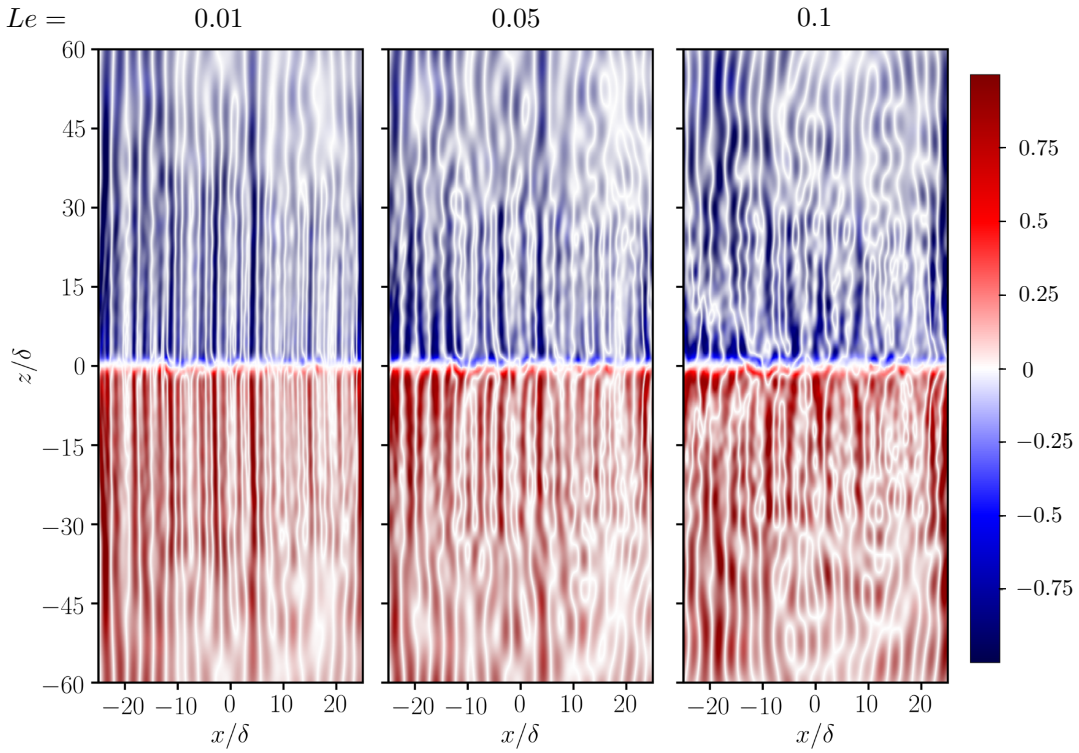

Fig. 6.6 Coherence of kinetic helicity carried by the wave packets. The colour intensity is controlled by the y-average of $|u_z|$ and the hue is set by the y-average of h_k^* (colourbar).

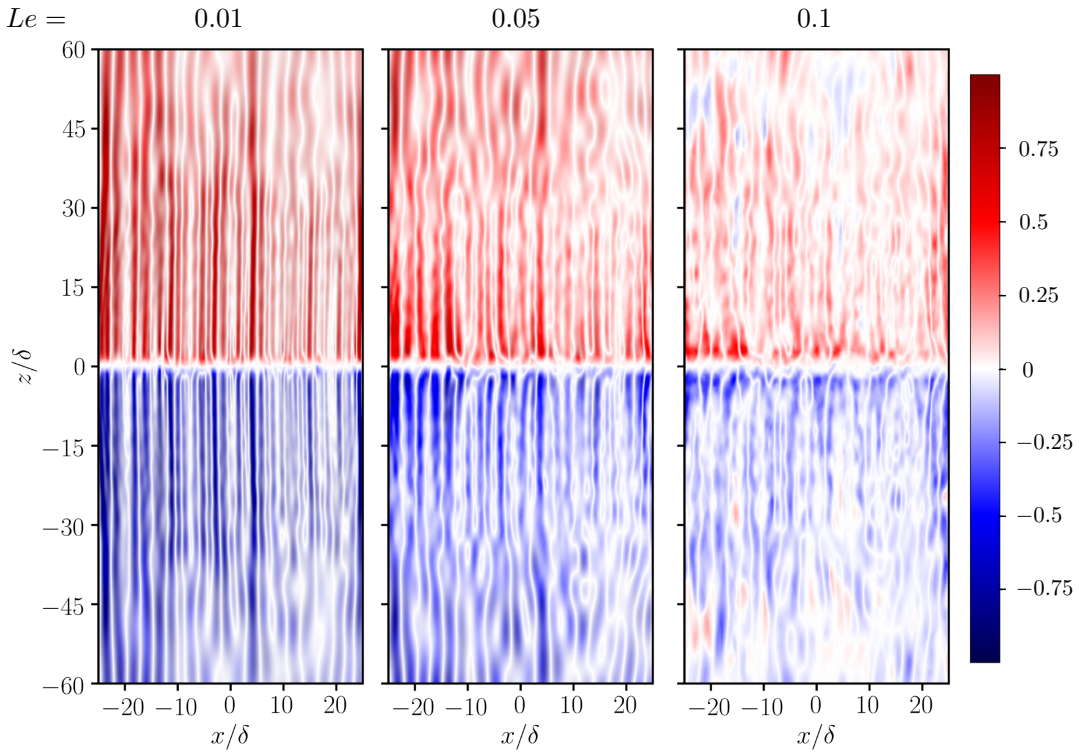

Fig. 6.7 Coherence of the emf induced by the wave packets. The colour intensity is controlled by the y-average of $|u_z|$ and the hue is set by the y-average of $\mathcal{E}_x^*$ (colourbar).

6.3 Future work

We end this thesis with a discussion of some possible avenues for future research. In each previous chapter we have discussed numerical simulations of the geodynamo in a spherical shell, and these simulations are perhaps the most useful tool to explore the role of wave packets in Earth's core. The methods used by Ranjan *et al.* (2018) to identify inertial wave packets in a moderately forced dynamo simulation could be further applied in efforts to identify magnetically modified wave packets. They found that $\partial_t u_z$ is a useful diagnostic for propagating wave fronts, and we corroborate this finding. Correlations between the buoyancy field near the equatorial plane and $\partial_t u_z$ far afield in the northern or southern hemisphere provide a connection between the wave-source and the wave packets. The "QG-MAC" waves identified in Aubert (2018) have a strikingly similar signature to IA wave packets emitted from a buoyant blob. He writes "we can typically observe spatially localized, alternating patterns of azimuthal flow acceleration ... propagating in the cylindrical radial direction from the tip of convective plumes ... propagate outwards at velocities that generally match the local Alfvén velocity". Further inspection of geodynamo simulations on the time-scale Ω^{-1} could shed light on the generation of helical columnar flow structures by MC wave packets supported by the large-scale field. The role of MC wave packets in the dynamo mechanism may be more difficult to untangle from the complex convective dynamics.

Concerning the dipolar-multipolar dynamo transition, we believe that we have provided convincing evidence that the suppression of inertial wave packets at the critical threshold, $Ro^{\text{crit}} \approx 0.4$, results in the loss of columnar flow structures (McDermott & Davidson, 2019). The simulations in chapter 4 are purely hydrodynamic, as previous work suggested that magnetic forces do not strongly effect the convection in the dynamos that undergo the transition (e.g. Christensen & Aubert, 2006; Soderlund *et al.*, 2012). However, the recent simulations by Menu *et al.* (2020), which exhibit a stronger magnetic field, may point to a destabilisation mechanism due to a strong Lorentz force. The dynamics at all relevant scales in Earth's core are likely characterised by $Ro \ll 1$, so any explanation of geomagnetic reversals cannot rely on a transition due to nonlinear inertia. A mechanism that includes the Lorentz force may offer an explanation, and a carefully selected set of model problems, similar to those presented in chapters 4 and 5, may be a good starting point.

Furthermore, the seemingly universal relationship between the Christensen & Aubert (2006) length-scale and the vorticity length, $\ell_{\bar{n}} \approx 5\ell_\omega$, may have a fundamental explanation. Using coordinate transforms, the velocity field output from a dynamo simulation could be expressed on a Cartesian grid to calculate the length-scale $\ell_\perp$, and provide a

comparison to $\ell_{\bar{n}}$ and ℓ_ω. This procedure could be done for volumes inside and outside the tangent cylinder, as the dynamics differ greatly between the two regions (Schaeffer *et al.*, 2017).

We briefly mentioned some observations of M-dwarf stars, and anelastic dynamo simulations, at the end of chapter 4. Further work could include hydrodynamic DNS initiated with a buoyant layer, with density stratification, to investigate the effect on inertial or inertia-gravity wave packets launched in that environment. Wave packets launched by turbulent eddies in the presence of rotation and density stratification were investigated in Ranjan (2015). With stress-free boundary conditions, the simulations of stellar dynamos often exhibit a strong zonal wind. It may be interesting to study the effect of a uniform horizontal flow on the dispersion of inertial wave packets from buoyant anomalies, where the dispersion relation of the waves is altered by the advective speed. Again, this could be accomplished through DNS in a periodic box.

The simulations presented in chapter 5 include a uniform transverse applied field. The magnetic field within Earth's outer core is certainly heterogeneous, and the effects of a spatially varying field (and Alfvén wave velocity) are of considerable interest. Using techniques from ray tracing, Bardsley & Davidson (2017) studied the effect of a slowly varying ambient magnetic field on the dispersion of MC waves from localised disturbances. They found that there is a 'wave ceiling', at which the axial group velocity approaches zero, and the wave packets would be subject to intense Ohmic dissipation. It is unlikely that this behaviour could be simulated in a periodic box, as some wave packets would penetrate the top and bottom boundaries after long integration times, however model problems in a spherical shell may yield interesting results.

Finally, Alfvén-like waves are receiving increased attention regarding the geodynamo, whether they be inertial-Alfvén waves, torsional waves or the axisymmetric waves simulated by Jault (2008). A pre-requisite for the latter two wave-types, is quasi-geostrophy, and as we have argued throughout this thesis, quasi-geostrophy in rapidly rotating turbulent convection is maintained by inertial or fast MC wave packets. The first experimental observations of torsional Alfvén waves were recently reported by Tigrine *et al.* (2019), using liquid sodium in a rotating spherical shell. Complementing the experiments were numerical simulations at similar parameters, which have some crossover with our simulations in chapter 5. The initial formation of geostrophic structures in the simulations looks very similar to the propagation of inertial-Alfvén wave packets in our buoyant blob simulations. Importantly, although diffusion is strong in the lab experiments, the magnetic Prantl number is as small as in planetary cores. This is a regime which numerical simulations cannot reach.

References

Alfvén, H. 1942 Existence of electromagnetic-hydrodynamic waves. *Nature* **150** (3805), 405–406.

Aubert, J. 2018 Geomagnetic acceleration and rapid hydromagnetic wave dynamics in advanced numerical simulations of the geodynamo. *Geophysical Journal International* **214** (1), 531–547.

Aubert, J. 2019 Approaching Earth's core conditions in high-resolution geodynamo simulations. *Geophysical Journal International* **219** (1), 137–151.

Aurnou, J. M. & Olson, P. L. 2001 Experiments on Rayleigh–Bénard convection, magnetoconvection and rotating magnetoconvection in liquid gallium. *Journal of fluid mechanics* **430**, 283–307.

Baqui, Y. B. & Davidson, P. A. 2015 A phenomenological theory of rotating turbulence. *Physics of Fluids* **27** (2), 025107.

Bardsley, O. P. 2019 Dispersive waves in Earth's outer core. PhD thesis, University of Cambridge.

Bardsley, O. P. & Davidson, P. A. 2016 Inertial–Alfvén waves as columnar helices in planetary cores. *Journal of Fluid Mechanics* **805**, R2.

Bardsley, O. P. & Davidson, P. A. 2017 The dispersion of magnetic-Coriolis waves in planetary cores. *Geophysical Journal International* **210** (1), 18–26.

Bouffard, M., Choblet, G., Labrosse, S. & Wicht, J. 2019 Chemical convection and stratification in the Earth's outer core. *Frontiers in Earth Science* **7**, 99.

Bouffard, M., Labrosse, S., Choblet, G., Fournier, A., Aubert, J. & Tackley, P. J. 2017 A particle-in-cell method for studying double-diffusive convection in the liquid layers of planetary interiors. *Journal of Computational Physics* **346**, 552–571.

Bracewell, R. N. 1986 *The Fourier transform and its applications*, 2nd edn. McGraw-Hill.

Brachet, M. E., Meiron, D. I., Orszag, S. A., Nickel, B. G., Morf, R. H. & Frisch, U. 1983 Small-scale structure of the Taylor–Green vortex. *Journal of Fluid Mechanics* **130**, 411–452.

Brown, W. J., Mound, J. E. & Livermore, P. W. 2013 Jerks abound: An analysis of geomagnetic observatory data from 1957 to 2008. *Physics of the Earth and Planetary Interiors* **223**, 62–76.

Brun, A. S. & Browning, M. K. 2017 Magnetism, dynamo action and the solar-stellar connection. *Living Reviews in Solar Physics* **14** (1), 4.

Busse, F. H. 1975 A model of the geodynamo. *Geophysical Journal International* **42** (2), 437–459.

Calkins, M. A., Julien, K., Tobias, S. M. & Aurnou, J. M. 2015 A multiscale dynamo model driven by quasi-geostrophic convection. *Journal of Fluid Mechanics* **780**, 143–166.

Canuto, C. 1988 *Spectral methods in fluid dynamics*. Berlin: Springer-Verlag.

Christensen, U. R. & Aubert, J. 2006 Scaling properties of convection-driven dynamos in rotating spherical shells and application to planetary magnetic fields. *Geophysical Journal International* **166** (1), 97–114.

Dallas, V. & Tobias, S. M. 2016 Forcing-dependent dynamics and emergence of helicity in rotating turbulence. *Journal of Fluid Mechanics* **798**, 682–695.

Davidson, P. A. 2005 *Turbulence : an introduction for scientists and engineers*. Oxford University Press.

Davidson, P. A. 2013*a* Scaling laws for planetary dynamos. *Geophysical Journal International* **195** (1), 67–74.

Davidson, P. A. 2013*b* *Turbulence in rotating, stratified and electrically conducting fluids*. Cambridge University Press.

Davidson, P. A. 2014 The dynamics and scaling laws of planetary dynamos driven by inertial waves. *Geophysical Journal International* **198** (3), 1832–1847.

Davidson, P. A. 2016 Dynamos driven by helical waves: scaling laws for numerical dynamos and for the planets. *Geophysical Journal International* **207** (2), 680–690.

Davidson, P. A. 2017 *Introduction to magnetohydrodynamics*, 2nd edn. Cambridge University Press.

Davidson, P. A. & Ranjan, A. 2015 Planetary dynamos driven by helical waves–II. *Geophysical Journal International* **202** (3), 1646–1662.

Davidson, P. A. & Ranjan, A. 2018 Are planetary dynamos driven by helical waves? *Journal of Plasma Physics* **84** (3), 735840304.

Davidson, P. A. & Siso-Nadal, F. 2002 On the structure of small-scale motion in the core of the earth. *Geophysical & Astrophysical Fluid Dynamics* **96** (1), 49–76.

Davidson, P. A., Staplehurst, P. J. & Dalziel, S. B. 2006 On the evolution of eddies in a rapidly rotating system. *Journal of Fluid Mechanics* **557**, 135–144.

Deguen, R., Alboussière, T. & Brito, D. 2007 On the existence and structure of a mush at the inner core boundary of the Earth. *Physics of the Earth and Planetary Interiors* **164** (1-2), 36–49.

Dickinson, S. C. & Long, R. R. 1983 Oscillating-grid turbulence including effects of rotation. *Journal of Fluid Mechanics* **126**, 315–333.

Dormy, E., Oruba, L. & Petitdemange, L. 2018 Three branches of dynamo action. *Fluid Dynamics Research* **50** (1), 011415.

Driscoll, P. & Olson, P. 2009 Effects of buoyancy and rotation on the polarity reversal frequency of gravitationally driven numerical dynamos. *Geophysical Journal International* **178** (3), 1337–1350.

Dziewonski, A. M. & Anderson, D. L. 1981 Preliminary reference Earth model. *Physics of the earth and planetary interiors* **25** (4), 297–356.

Finlay, C. C. & Jackson, A. 2003 Equatorially dominated magnetic field change at the surface of Earth's core. *Science* **300** (5628), 2084–2086.

Finlay, C. C., Olsen, N., Kotsiaros, S., Gillet, N. & Tøffner-Clausen, L. 2016 Recent geomagnetic secular variation from Swarm and ground observatories as estimated in the CHAOS-6 geomagnetic field model. *Earth, Planets and Space* **68** (1), 112.

Fornberg, B. 1998 *A practical guide to pseudospectral methods*, , vol. 1. Cambridge university press.

Foulger, G. R., Natland, J. H., Presnall, D. C. & Anderson, D. L. 2005 *Plates, plumes and paradigms*. Geological Society of America.

Garcia, F., Oruba, L. & Dormy, E. 2017 Equatorial symmetry breaking and the loss of dipolarity in rapidly rotating dynamos. *Geophysical & Astrophysical Fluid Dynamics* **111** (5), 380–393.

Gastine, T., Duarte, L. & Wicht, J. 2012 Dipolar versus multipolar dynamos: the influence of the background density stratification. *Astronomy & Astrophysics* **546**, A19.

Gastine, T., Morin, J., Duarte, L., Reiners, A., Christensen, U. R. & Wicht, J. 2013 What controls the magnetic geometry of M dwarfs? *Astronomy & Astrophysics* **549**, L5.

Gilbert, W. 1600 *De magnete*. London: Peter Short.

Gillet, N., Jault, D., Canet, E. & Fournier, A. 2010 Fast torsional waves and strong magnetic field within the Earth's core. *Nature* **465**, 74–77.

Glatzmaier, G. A. 2013 *Introduction to modeling convection in planets and stars: Magnetic field, density stratification, rotation*. Princeton University Press.

Godeferd, F. S. & Moisy, F. 2015 Structure and dynamics of rotating turbulence: A review of recent experimental and numerical results. *Applied Mechanics Reviews* **67** (3).

Gómez, D. O., Mininni, P. D. & Dmitruk, P. 2005 Parallel simulations in turbulent MHD. *Physica Scripta* **2005** (T116), 123.

Greenspan, H. P. 1968 *The theory of rotating fluids*. Cambridge University Press.

Griffiths, D. J. 2014 *Introduction to electrodynamics*, 4th edn. Pearson Custom Library.

Gubbins, D. 2001 The Rayleigh number for convection in the Earth's core. *Physics of the Earth and Planetary Interiors* **128** (1-4), 3–12.

Gubbins, D. 2004 *Time series analysis and inverse theory for geophysicists*. Cambridge University Press.

Guervilly, C., Cardin, P. & Schaeffer, N. 2019 Turbulent convective length scale in planetary cores. *Nature* **570** (7761), 368–371.

Halley, E. 1701 A new and correct chart shewing the variations of the compass in the western & southern oceans as observed in ye year 1700 by his Maties command by Edm. Halley.

Henderson, P. & Henderson, G. 2009 *The Cambridge handbook of earth science data*. Cambridge University Press.

Hide, R. 1966 Free hydromagnetic oscillations of the Earth's core and the theory of the geomagnetic secular variation. *Philosophical Transactions of the Royal Society of London. Series A, Mathematical and Physical Sciences* **259** (1107), 615–647.

Hide, R., Ibbetson, A. & Lighthill, M. J. 1968 On slow transverse flow past obstacles in a rapidly rotating fluid. *Journal of Fluid Mechanics* **32** (2), 251–272.

Holme, R., Olsen, N. & Bairstow, F. L. 2011 Mapping geomagnetic secular variation at the core–mantle boundary. *Geophysical Journal International* **186** (2), 521–528.

Hopfinger, E. J., Browand, F. K. & Gagne, Y. 1982 Turbulence and waves in a rotating tank. *Journal of Fluid Mechanics* **125**, 505–534.

Hori, K., Jones, C. A. & Teed, R. J. 2015 Slow magnetic Rossby waves in the Earth's core. *Geophysical Research Letters* **42** (16), 6622–6629.

Ibbetson, A. & Tritton, D. J. 1975 Experiments on turbulence in a rotating fluid. *Journal of Fluid Mechanics* **68** (4), 639–672.

Jackson, A. & Finlay, C. 2015 5 - Geomagnetic secular variation and its applications to the core. In *Treatise on geophysics*, pp. 137–184. Elsevier.

Jackson, A., Jonkers, A. R. T. & Walker, M. R. 2000 Four centuries of geomagnetic secular variation from historical records. *Philosophical Transactions of the Royal Society of London A: Mathematical, Physical and Engineering Sciences* **358** (1768), 957–990.

Jacquin, L., Leuchter, O., Cambon, C. & Mathieu, J. 1990 Homogeneous turbulence in the presence of rotation. *Journal of Fluid Mechanics* **220**, 1–52.

Jault, D. 2008 Axial invariance of rapidly varying diffusionless motions in the Earth's core interior. *Physics of the Earth and Planetary Interiors* **166** (1-2), 67–76.

Kageyama, A., Miyagoshi, T. & Sato, T. 2008 Formation of current coils in geodynamo simulations. *Nature* **454** (7208), 1106–1109.

King, E. M. & Buffett, B. A. 2013 Flow speeds and length scales in geodynamo models: the role of viscosity. *Earth and Planetary Science Letters* **371**, 156–162.

Kiraga, M. & Stepien, K. 2013 ASAS photometry of ROSAT sources. II. New variables from the ASAS North Survey. *arXiv preprint arXiv:1304.3236* .

Kutzner, C. & Christensen, U. R. 2002 From stable dipolar towards reversing numerical dynamos. *Physics of the Earth and Planetary Interiors* **131** (1), 29 – 45.

Lesieur, M. 1987 *Turbulence in fluids: stochastic and numerical modelling*. Nijhoff Boston, MA.

Lighthill, M. J. 1970 The theory of trailing Taylor columns. *Mathematical Proceedings of the Cambridge Philosophical Society* **68** (2), 485–491.

Lighthill, M. J. 1978 *Waves in fluids*. Cambridge University Press.

Maffioli, A. P. L. 2012 The evolution of a stratified turbulent cloud. PhD thesis, University of Cambridge.

Malkus, W. V. R. 1967 Hydromagnetic planetary waves. *Journal of Fluid Mechanics* **28** (4), 793–802.

McDermott, B. R. & Davidson, P. A. 2019 A physical conjecture for the dipolar–multipolar dynamo transition. *Journal of Fluid Mechanics* **874**, 995–1020.

McDermott, B. R. & Davidson, P. A. 2020 On the helicity characteristics and induced emf of magnetic-Coriolis wave packets. *Geophysical Journal International* ggaa373.

Menu, M. D., Petitdemange, L. & Galtier, S. 2020 Magnetic effects on fields morphologies and reversals in geodynamo simulations. *Physics of the Earth and Planetary Interiors* **307**, 106542.

Mininni, P. D., Alexakis, A. & Pouquet, A. 2009 Scale interactions and scaling laws in rotating flows at moderate Rossby numbers and large Reynolds numbers. *Physics of Fluids* **21** (1), 015108.

Mininni, P. D. & Pouquet, A. 2009*a* Finite dissipation and intermittency in magnetohydrodynamics. *Physical Review E* **80** (2), 025401.

Mininni, P. D. & Pouquet, A. 2009*b* Helicity cascades in rotating turbulence. *Physical Review E* **79** (2), 026304.

Mininni, P. D. & Pouquet, A. 2010 Rotating helical turbulence II. Intermittency, scale invariance, and structures. *Physics of Fluids* **22** (3), 035106.

Mininni, P. D., Rosenberg, D., Reddy, R. & Pouquet, A. 2011 A hybrid MPI–OpenMP scheme for scalable parallel pseudospectral computations for fluid turbulence. *Parallel Computing* **37** (6-7), 316–326.

Mitchell, A. C. 1946 Chapters in the history of terrestrial magnetism. *Terrestrial Magnetism and Atmospheric Electricity* **51** (3), 323–351.

Moffatt, H. K. 1970 Dynamo action associated with random inertial waves in a rotating conducting fluid. *Journal of Fluid Mechanics* **44** (4), 705–719.

Moffatt, H. K. 1978 *Magnetic field generation in electrically conducting fluids*. Cambridge University Press.

Moffatt, H. K. & Loper, D. E. 1994 The magnetostrophic rise of a buoyant parcel in the Earth's core. *Geophysical Journal International* **117** (2), 394–402.

Nimmo, F. 2015 8.02 - Energetics of the Core. In *Treatise on Geophysics*, 2nd edn. (ed. Gerald Schubert), pp. 27–55. Oxford: Elsevier.

Olson, P. & Christensen, U. R. 2006 Dipole moment scaling for convection-driven planetary dynamos. *Earth and Planetary Science Letters* **250** (3-4), 561–571.

Olson, P., Christensen, U. R. & Glatzmaier, G. A. 1999 Numerical modeling of the geodynamo: mechanisms of field generation and equilibration. *Journal of Geophysical Research: Solid Earth* **104** (B5), 10383–10404.

Orszag, S. A. & Patterson Jr, G. S. 1972 Numerical simulation of three-dimensional homogeneous isotropic turbulence. *Physical Review Letters* **28** (2), 76.

Oruba, L. & Dormy, E. 2014 Transition between viscous dipolar and inertial multipolar dynamos. *Geophysical Research Letters* **41** (20), 7115–7120.

Parker, E. N. 1955 Hydromagnetic dynamo models. *The Astrophysical Journal* **122**, 293.

Pouquet, A., Lee, E., Brachet, M. E., Mininni, P. D. & Rosenberg, D. 2010 The dynamics of unforced turbulence at high Reynolds number for Taylor–Green vortices generalized to MHD. *Geophysical and Astrophysical Fluid Dynamics* **104** (2-3), 115–134.

Pozzo, M., Davies, C., Gubbins, D. & Alfe, D. 2012 Thermal and electrical conductivity of iron at Earth's core conditions. *Nature* **485** (7398), 355–358.

Pozzo, M., Davies, C., Gubbins, D. & Alfè, D. 2014 Thermal and electrical conductivity of solid iron and iron–silicon mixtures at Earth's core conditions. *Earth and Planetary Science Letters* **393**, 159–164.

Proudman, J. 1916 On the motion of solids in a liquid possessing vorticity. *Proc. R. Soc. Lond. A* **92** (642), 408–424.

Ranjan, A. 2015 Inertial waves in rotating turbulence. PhD thesis, University of Cambridge.

Ranjan, A. 2017 Segregation of helicity in inertial wave packets. *Phys. Rev. Fluids* **2**, 033801.

Ranjan, A. & Davidson, P. A. 2014 Evolution of a turbulent cloud under rotation. *Journal of Fluid Mechanics* **756**, 488–509.

Ranjan, A., Davidson, P. A., Christensen, U. R. & Wicht, J. 2018 Internally driven inertial waves in geodynamo simulations. *Geophysical Journal International* **213** (2), 1281–1295.

Roberts, P. H. & King, E. M. 2013 On the genesis of the Earth's magnetism. *Reports on Progress in Physics* **76** (9), 096801.

Rogallo, R. S. 1981 Numerical experiments in homogeneous turbulence. *NASA SA Technical Memorandum 81315* .

Sahoo, G., Perlekar, P. & Pandit, R. 2011 Systematics of the magnetic-Prandtl-number dependence of homogeneous, isotropic magnetohydrodynamic turbulence. *New Journal of Physics* **13** (1), 013036.

Sakuraba, A. & Roberts, P. H. 2009 Generation of a strong magnetic field using uniform heat flux at the surface of the core. *Nature Geoscience* **2** (11), 802–805.

Sano, M., Wu, X. Z. & Libchaber, A. 1989 Turbulence in helium-gas free convection. *Physical Review A* **40** (11), 6421–6430.

Schaeffer, N., Jault, D., Nataf, H-C. & Fournier, A. 2017 Turbulent geodynamo simulations: a leap towards Earth's core. *Geophysical Journal International* **211** (1), 1–29.

Schwaiger, T., Gastine, T. & Aubert, J. 2019 Force balance in numerical geodynamo simulations: a systematic study. *Geophysical Journal International* **219** (1), S101–S114.

Sheyko, A., Finlay, C. C., Favre, J. & Jackson, A. 2018 Scale separated low viscosity dynamos and dissipation within the Earth's core. *Scientific reports* **8** (1), 1–7.

Sheyko, A., Finlay, C. C. & Jackson, A. 2016 Magnetic reversals from planetary dynamo waves. *Nature* **539** (7630), 551–554.

Simitev, R. D. & Busse, F. H. 2009 Bistability and hysteresis of dipolar dynamos generated by turbulent convection in rotating spherical shells. *Europhysics Letters* **85** (1), 19001.

Soderlund, K. M. 2011 Investigating transitions in planetary dynamo models. PhD thesis, University of California, Los Angeles.

Soderlund, K. M., King, E. M. & Aurnou, J. M. 2012 The influence of magnetic fields in planetary dynamo models. *Earth and Planetary Science Letters* **333**, 9–20.

Soderlund, K. M., King, E. M. & Aurnou, J. M. 2014 Corrigendum to "the influence of magnetic fields in planetary dynamo models" [Earth Planet. Sci. Lett. 333–334 (2012) 9–20]. *Earth and Planetary Science Letters* **392**, 121 – 123.

Sreenivasan, B. & Davidson, P. A. 2008 On the formation of cyclones and anticyclones in a rotating fluid. *Physics of Fluids* **20** (8), 085104.

Sreenivasan, B. & Jones, C. A. 2011 Helicity generation and subcritical behaviour in rapidly rotating dynamos. *Journal of Fluid Mechanics* **688**, 5–30.

St. Pierre, M. G. 1996 On the local nature of turbulence in Earth's outer core. *Geophysical & Astrophysical Fluid Dynamics* **83** (3-4), 293–306.

Staplehurst, P. J., Davidson, P. A. & Dalziel, S. B. 2008 Structure formation in homogeneous freely decaying rotating turbulence. *Journal of Fluid Mechanics* **598**, 81–105.

Starchenko, S. V. & Jones, C. A. 2002 Typical velocities and magnetic field strengths in planetary interiors. *Icarus* **157** (2), 426 – 435.

Steenbeck, M., Krause, F. & Rädler, K-H 1966 Berechnung der mittleren Lorentz-Feldstärke für ein elektrisch leitendes medium in turbulenter, durch Coriolis-Kräfte beeinflußter Bewegung. *Zeitschrift für Naturforschung A* **21** (4), 369–376.

Sumita, I. & Olson, P. 2000 Laboratory experiments on high Rayleigh number thermal convection in a rapidly rotating hemispherical shell. *Physics of the Earth and Planetary Interiors* **117** (1-4), 153–170.

Taylor, G. I. 1922 The motion of a sphere in a rotating liquid. *Proc. R. Soc. Lond. A* **102** (715), 180–189.

Tigrine, Z., Nataf, H-C, Schaeffer, N., Cardin, P. & Plunian, F. 2019 Torsional Alfvén waves in a dipolar magnetic field: experiments and simulations. *Geophysical Journal International* **219** (1), S83–S100.

Tobias, S. 2019 The turbulent dynamo. *arXiv preprint arXiv:1907.03685* .

Vallis, G. K. 2017 *Atmospheric and oceanic fluid dynamics*. Cambridge University Press.

Weiss, N. O. & Proctor, M. R. E. 2014 *Magnetoconvection*. Cambridge University Press.

de Wijs, G. A., Kresse, G., Vočadlo, L., Dobson, D., Alfe, D., Gillan, M. J. & Price, G. D. 1998 The viscosity of liquid iron at the physical conditions of the Earth's core. *Nature* **392** (6678), 805–807.

Yarom, E. & Sharon, E. 2014 Experimental observation of steady inertial wave turbulence in deep rotating flows. *Nature Physics* **10** (7), 510–514.

Yeung, P. K., Zhai, X. M. & Sreenivasan, K. R. 2015 Extreme events in computational turbulence. *Proceedings of the National Academy of Sciences* **112** (41), 12633–12638.

Yeung, P. K. & Zhou, Y. 1998 Numerical study of rotating turbulence with external forcing. *Physics of Fluids* **10** (11), 2895–2909.

Zhang, K. & Fearn, D. R. 1993 How strong is the invisible component of the magnetic field in the Earth's core. *Geophysical Research Letters* **20** (19), 2083–2086.

A1 - Algorithms

PSDNS

The PSDNS code described in chapter 3 solves the rotating Boussinesq equations with a modified Rogallo scheme (Rogallo, 1981). Here we briefly describe the algorithm for this method, as implemented by Yeung & Zhou (1998) and Maffioli (2012). We start with the governing momentum equation written in spectral space

$$\left(\partial_t + \nu k^2\right)\hat{u}_i = -\mathrm{i}k_i\hat{\tilde{p}} - \mathrm{i}k_j\widehat{u_i u_j} - 2\epsilon_{i3k}\Omega\hat{u}_k + \hat{\mathcal{B}}\delta_{iq}\,, \tag{1}$$

where $\tilde{p}$ is the modified pressure, $\mathcal{B} = cg$ is the buoyancy and gravity is in the direction q. To eliminate pressure from these equations we dot (1) with $\mathrm{i}k_i$ followed by multiplication by $\mathrm{i}k_j$ and use continuity $k_i\hat{u}_i = 0$ to gain an expression for $-\mathrm{i}k_i\hat{\tilde{p}}$,

$$-\mathrm{i}k_i\hat{\tilde{p}} = \frac{k_i k_j}{k^2}\left(\hat{G}_j + 2\epsilon_{j3l}\Omega\hat{u}_l - \delta_{jq}\hat{\mathcal{B}}\right), \tag{2}$$

where $\hat{G}_j = \mathrm{i}k_i\widehat{u_j u_i}$. Substituting (2) into (1) results in a projection of the nonlinear, Coriolis and buoyancy terms normal to the wavevector $\boldsymbol{k}$,

$$\left(\partial_t + \nu k^2\right)\hat{u} = -P_{ij}\left[\hat{G}_j - \delta_{jq}\hat{\mathcal{B}} + 2\epsilon_{j3l}\Omega\hat{u}_l\right], \tag{3}$$

where $P_{ij} = \delta_{ij} - k_i k_j/k^2$ is the tensor which applies the projection. This renders the solution incompressible, with $\boldsymbol{\nabla}\cdot\boldsymbol{u} = 0$ satisfied exactly in spectral space.

Following Rogallo (1981), we introduce modified velocities $\hat{V}_i = \exp\left(\nu k^2\Delta t\right)\hat{u}_i$ (using integrating factors for the viscous terms) to obtain the following equation for the coefficients of V_i

$$\partial_t\hat{V}_i = -\exp\left(\nu k^2 t\right)P_{ij}\left[\hat{G}_j - \delta_{jq}\hat{\mathcal{B}}\right] - 2P_{ij}\,\epsilon_{j3l}\Omega\hat{V}_l\,. \tag{4}$$

As the rotation vector is in the z-direction, the Coriolis term may be simplified

$$\partial_t \hat{V}_i = -\exp\left(\nu k^2 t\right) P_{ij}\left[\hat{G}_j - \delta_{jq}\hat{\mathcal{B}}\right] - \frac{2\Omega k_3}{k^2} K_{ij}\hat{V}_j\,, \tag{5}$$

where K_{ij} is the skew-symmetric matrix

$$K_{ij} = \begin{bmatrix} 0 & -k_3 & k_2 \\ k_3 & 0 & -k_1 \\ -k_2 & k_1 & 0 \end{bmatrix}.$$

In order to decouple (5), one of two methods may be used

1. Use the eigenvalues of the matrix K_{ij} to diagonalise the Coriolis term.
2. Introduce a pair of auxiliary variables based on a helical decomposition (Lesieur, 1987).

The code opts for the second method, and defines

$$\begin{aligned} \beta_+ &= \frac{1}{k_{12}}\left(\mathrm{i}k_2\hat{V}_1 - \mathrm{i}k_1\hat{V}_2 - k\hat{V}_3\right), \\ \beta_- &= -\frac{1}{k_{12}}\left(\mathrm{i}k_2\hat{V}_1 - \mathrm{i}k_1\hat{V}_2 + k\hat{V}_3\right), \end{aligned} \tag{6}$$

where $k_{12} = \sqrt{k_1^2 + k_2^2}$ and $k = |\boldsymbol{k}|$. Adding and subtracting the auxiliary variables (6) and using continuity yeilds the inverse expressions

$$\begin{aligned} \hat{V}_1 &= -\frac{\mathrm{i}k_2}{2k_{12}}\left(\beta_+ - \beta_-\right) + \frac{k_1 k_3}{2kk_{12}}\left(\beta_+ + \beta_-\right), \\ \hat{V}_2 &= \frac{\mathrm{i}k_1}{2k_{12}}\left(\beta_+ - \beta_-\right) + \frac{k_2 k_3}{2kk_{12}}\left(\beta_+ + \beta_-\right), \\ \hat{V}_3 &= -\frac{k_{12}}{2k}\left(\beta_+ + \beta_-\right), \end{aligned} \tag{7}$$

which will be needed to reform the modified velocities. Re-expressing (5) in terms of the auxiliary variables (6), we find the resulting equations are de-coupled

$$\left(\frac{\partial}{\partial t} \mp \frac{2\mathrm{i}\Omega k_3}{k}\right)\beta_\pm = \pm\frac{\exp(\nu k^2 t)}{k_{12}}\Big[-\mathrm{i}k_2 P_{1j}\,\hat{H}_j + \mathrm{i}k_1 P_{2j}\,\hat{H}_j \pm k P_{3j}\,\hat{H}_j\Big], \tag{8}$$

where $\hat{H}_j = \hat{G}_j - \delta_{jq}\hat{\mathcal{B}}$. Note that the buoyancy term is simply subtracted from the component of the convective term in the direction of gravity, making it relatively simple

to implement in the code. The LHS suggests the use of integrating factors for the Coriolis terms, $\exp\left(\mp\frac{2\mathrm{i}\Omega k_3}{k}\right)$. Multiplying (8) through by the factors, we can write

$$\frac{\partial}{\partial t}\left[\beta_\pm \exp\left(\mp\frac{2\mathrm{i}\Omega k_3}{k}\right)\right] = \pm\exp\left(\mp\frac{2\mathrm{i}\Omega k_3}{k}\right)\frac{\exp(\nu k^2 t)}{k_{12}}\times \left[-\mathrm{i}k_2 P_{1j}\,\hat{H}_j + \mathrm{i}k_1 P_{2j}\,\hat{H}_j \pm k P_{3j}\,\hat{H}_j\right]. \tag{9}$$

The above equations (9) are numerically integrated over a small timestep $\Delta t = t_{n+1} - t_n$ to solve for the auxiliary variables, from which the modified velocities may be calculated, to finally form the true velocities at the next time-point. The time-stepping procedure is described in the next section.

Time advance

The time advancement scheme chosen by Yeung & Zhou (1998) is a Runge-Kutta order-2 method, which is a two-stage predictor-corrector method. Writing (9) symbolically as

$$\partial_t\left(F_\pm \beta_\pm\right) = F_\pm \hat{C}_\pm \tag{10}$$

where $F_\pm = \exp\left(\mp\frac{2\mathrm{i}\Omega k_3}{k}\right)$ are the Coriolis integrating factors and

$$\hat{C}_\pm = \pm\frac{\exp(\nu k^2 t)}{k_{12}}\left[-\mathrm{i}k_2 P_{1j}\,\hat{H}_j + \mathrm{i}k_1 P_{2j}\,\hat{H}_j \pm k P_{3j}\,\hat{H}_j\right].$$

At the next time point t_{n+1}, the predictor estimate of the auxiliary variables is (Canuto, 1988)

$$\beta^*_\pm\left(t_{n+1}\right) = F_\pm^{-1}\left[\beta_\pm\left(t_n\right) + \Delta t\,\hat{C}_\pm\left(t_n\right)\right], \tag{11}$$

which is simply a forward Euler step. The corrector step to complete one timestep of (10) is

$$\beta_\pm\left(t_{n+1}\right) = F_\pm^{-1}\left[\beta_\pm\left(t_n\right) + \frac{\Delta t}{2}\hat{C}_\pm\left(t_n\right)\right] + \frac{\Delta t}{2}\hat{C}^*_\pm. \tag{12}$$

Here, $\hat{C}^*_\pm$ is computed from the predictor estimate of the velocity field $\hat{u}^*_i$, which is retrieved from the predictor modified velocities $\hat{V}^*_i$, calculated using (7) from the predictor auxiliary variables $\beta^*_\pm$. Notice that the collection of terms in square brackets in (12) is known at the predictor stage, where they are stored, so that the inverse of the integrating factors need not be computed at the corrector stage.

GHOST

The GHOST code (Gómez *et al.*, 2005) described in chapter 3 solves the rotating MHD equations with an imposed mean-field. The governing equations in spectral space are

$$\left(\partial_t + \nu k^2\right)\hat{u}_i = -\mathrm{i}k_i\hat{\Pi} + \mathrm{i}k_j(\widehat{b_i b_j} - \widehat{u_i u_j}) - 2\epsilon_{i3k}\Omega\hat{u}_k + \hat{\mathcal{B}}\delta_{iq}\,, \tag{13}$$

$$\left(\partial_t + \eta k^2\right)\hat{a}_i = \epsilon_{ijk}\widehat{u_j b_k}\,, \tag{14}$$

$$\left(\partial_t + \kappa k^2\right)\hat{\mathcal{B}} = -\mathrm{i}k_j\widehat{\mathcal{B}u_j}\,. \tag{15}$$

where b_i is the total magnetic field including the fluctuations and the mean-field, and a_i is the solenoidal magnetic vector potential. These equations are supplemented by the divergence-free conditions $\mathrm{i}k_i\hat{u}_i = \mathrm{i}k_i\hat{b}_i = 0$. The code uses an order-2 Runge-Kutta time-stepping scheme, which will be described at the end of this section.

In the first sub-step the field arrays are simply copied into auxiliary arrays, but in the second sub-step the following operations complete one timestep.

1. Get the magnetic field from the vector potential: $\hat{b}_i = \mathrm{i}\epsilon_{ijk}k_j\hat{a}_k$
2. Build the arrays $\mathrm{i}k_j\widehat{u_i u_j}$ and $\mathrm{i}k_j\widehat{b_i b_j}$ by transforming to real space to form the products, transforming back to Fourier space, and multiplying by $\mathrm{i}k_j$
3. Add the Coriolis, buoyancy, Lorentz and nonlinear inertia terms and multiply the resulting arrays by the projection tensor P_{ij} to project them perpendicular to the wavevector
4. Form $\epsilon_{ijk}\widehat{u_j b_k}$ and project it normal to the wavevector
5. Form $\mathrm{i}k_j\widehat{\mathcal{B}u_j}$
6. Calculate the Laplacian terms $k^2\hat{u}_i$, $k^2\hat{a}_i$ and $k^2\hat{\mathcal{B}}_i$
7. Step each equation forward in time using the Runge-Kutta second sub-step below

The Runge-Kutta order-2 time-step is

$$f^*(t_n) = f(t_n)\,, \tag{16}$$

$$f(t_{n+1}) = f^*(t_n) + \frac{\Delta t}{2}\left(N^*(t_n) - L^*(t_n)\right)\,, \tag{17}$$

where N denotes the RHS of the equations and L represents the Laplacian terms. Here f may be $\hat{u}$, $\hat{b}$ or $\hat{\mathcal{B}}$.